SLAC-R-1053

NEW SCIENCE OPPORTUNITIES ENABLED BY LCLS-II X-RAY LASERS

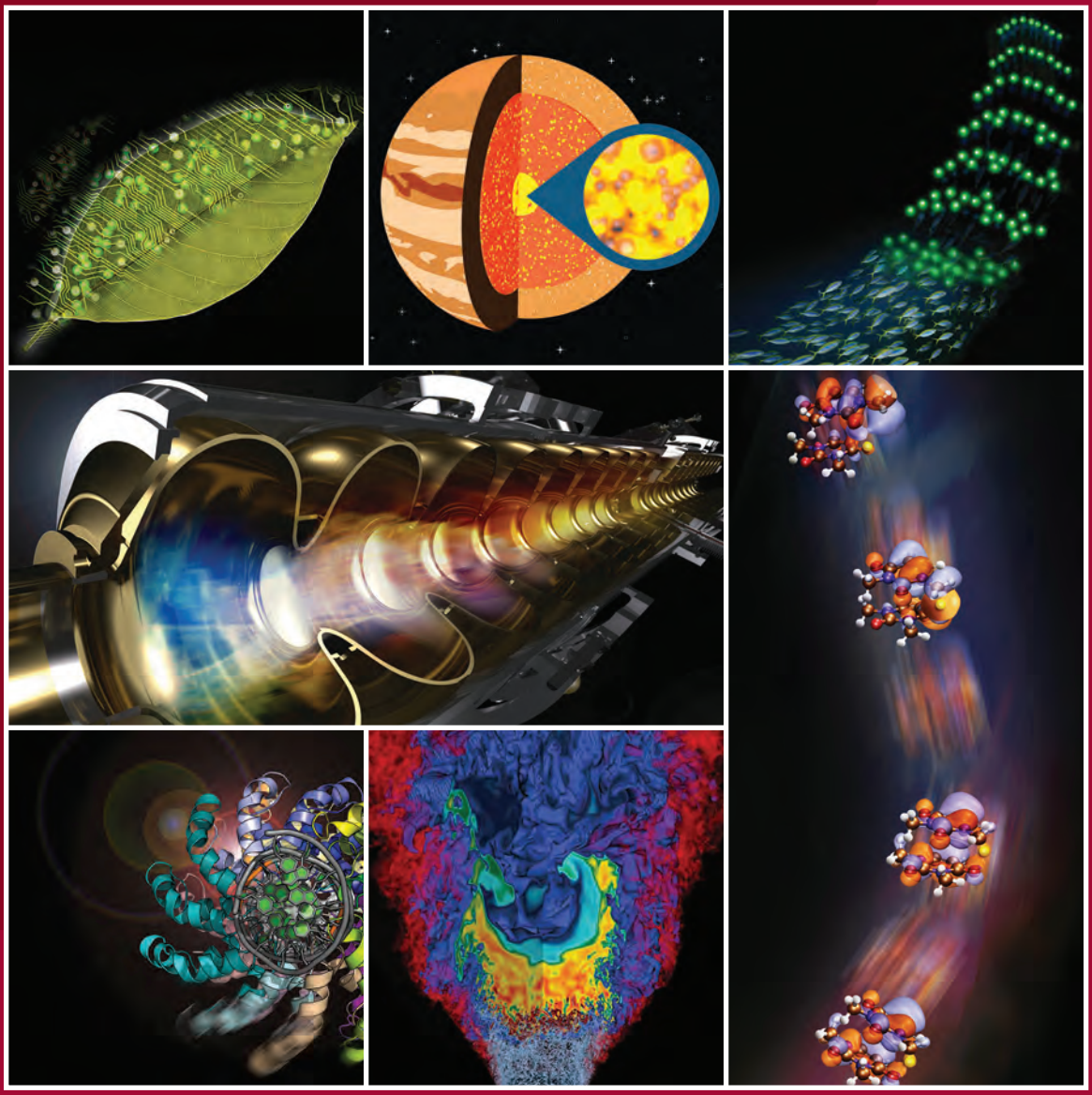

June 1, 2015

LCLS
SLAC NATIONAL ACCELERATOR LABORATORY
U.S. DEPARTMENT OF ENERGY
Office of Science

Preface

This document attempts to capture the most compelling new science opportunities that are enabled by the unique capabilities of the new LCLS-II X-ray laser facility, namely: soft and tender X-rays (0.25 to 5 keV) at high repetition rates (up to 1 MHz) and hard X-rays (up to 25 keV) at 120 Hz. Many compelling areas of science have been identified by the scientific community, through a series of workshops over the past several years, where LCLS-II offers the potential to significantly advance our understanding. This document is not intended to be comprehensive of all the science to be pursued at the future LCLS facility. In particular, it does not capture important ongoing science that will continue to exploit the existing capabilities of the present LCLS facility. Nevertheless, this document will help to establish a scientific foundation for the new facility (encompassing present LCLS capabilities and new LCLS-II capabilities), and will inform LCLS strategic planning and investments over the next 5-10 years.

The emphasis of this document is on identifying broad scientific opportunities, elucidating their potential impact, and providing a first-order link between these opportunities and LCLS-II capabilities. Brief descriptions are provided for various experimental approaches to be used, and novel new approaches to be developed, along with select examples of required optics and instruments. However, this document is not intended to capture all the optics and instrumentation requirements. Similarly it does not provide a detailed plan for instrumentation design or for any associated research and development that might be required. Balancing the scientific opportunities and impact, with instrumentation needs, available resources, and infrastructure, will be part of the LCLS planning process which this document will help to inform.

Published by:
SLAC National Accelerator Laboratory
2575 Sand Hill Road
Menlo Park, CA 94025

Work supported in part by Department of Energy contract DE-AC02-76SF00515

This document was prepared as an account of work sponsored by the United States Government. While this document is believed to contain correct information, neither the United States Government nor any agency thereof, nor any of their employees, nor any of their contractors, subcontractors, or their employees, makes any warranty, express or implied, or assumes any legal liability or responsibility for the accuracy, completeness, or any third party's use or the results of such use of any information, apparatus, product, or process disclosed, or represents that its use would not infringe privately owned rights. Reference herein to any specific commercial product, process, or service by its trade name, trademark, manufacturer, or otherwise, does not necessarily constitute or imply its endorsement, recommendation, or favoring by the United States Government or any agency thereof or its contractors or subcontractors. The views and opinions of authors expressed herein do not necessarily state or reflect those of the United States Government or any agency thereof or its contractors or subcontractors.

Cover graphics courtesy of:
Susan Brand, LBNL Public Affairs Creative Services
SLAC Office of Communications

Contributors

P. Abbamonte[53] F. Abild-Pedersen[35] P. Adams[17] M. Ahmed[17] F. Albert[18] R. Alonso Mori[35]
P. Anfinrud[27] A. Aquila[35] M. Armstrong[18] J. Arthur[35] J. Bargar[35] A. Barty[6,7] U. Bergmann[35]
N. Berrah[46] G. Blaj[35] H. Bluhm[17] C. Bolme[19] C. Bostedt[35] S. Boutet[35] G. Brown[35,37]
P. Bucksbaum[35,37] M. Cargnello[37] G. Carini[35] A. Cavalleri[25,52,55] V. Cherezov[56] W. Chiu[3]
Y. Chuang[17] D. Cocco[35] R. Coffee[35] G. Collins[18] A. Cordones-Hahn[17] J. Cryan[35] G. Dakovski[35]
M. Dantus[22] H. Demirci[35] P. Denes[17] T. Devereaux[35,37] Y. Ding[35] S. Doniach[37] R. Dörner[15]
M. Dunne[35] H. Durr[35] T. Egami[57] D. Eisenberg[43] P. Emma[35] C. Fadley[17,41] R. Falcone[17,40]
Y. Feng[35] P. Fischer[17] F. Fiuza[35] L. Fletcher[35] L. Foucar[21] M. Frank[18] J. Fraser[45] H. Frei[17]
D. Fritz[35] P. Fromme[2] A. Fry[35] M. Fuchs[54] P. Fuoss[1] K. Gaffney[35] E. Gamboa[35] O. Gessner[17]
S. Ghimire[35] A. Gleason[19] S. Glenzer[35] T. Gorkhover[35] A. Gray[39] M. Guehr[35] J. Guo[17] J. Hajdu[60]
S. Hansen[33] P. Hart[35] M. Hashimoto[35] J. Hastings[35] D. Haxton[17] P. Heimann[35] T. Heinz[35,37]
A. Hexemer[17] J. Hill[4] F. Himpsel[58] P. Ho[1] B. Hogue[2] Z. Huang[35] M. Hunter[35] G. Hura[17]
N. Huse[25,52] Z. Hussain[17] M. Ilchen[8,37] C. Jacobsen[1] C. Kenney[35] J. Kern[17,35] S. Kevan[17] J. Kim[35]
H. Kim[36] P. Kirchmann[35] R. Kirian[2] S. Kivelson[37] C. Kliewer[33] J. Koralek[35] G. Kovácsová[21]
A. Lanzara[17,40] J. LaRue[35] H. Lee[35] J. Lee[35] W. Lee[35] Y. Lee[35,37] I. Lindau[37] A. Lindenberg[35,37]
Z. Liu[34] D. Lu[35] U. Lundstrom[37] A. MacDowell[17] W. Mao[35,37] J. Marangos[14] G. Marcus[35]
T. Martinez[35,37] W. McCurdy[17,41] G. McDermott[17,45] C. McGuffey[44] H. Michelsen[33] M. Minitti[35]
S. Miyabe[32] S. Moeller[35] R. Moore[35] S. Mukamel[42] K. Nass[21] A. Natan[35] K. Nelson[23] S. Nemšák[9]
D. Neumark[17,40] R. Neutze[12] A. Nilsson[35,38] D. Nordlund[35] J. Norskov[35,37] S. Nozawa[29]
H. Ogasawara[35] H. Ohldag[35] A. Orville[4] D. Osborn[33] T. Osipov[35] A. Ourmazd[59] D. Parkinson[17]
C. Pellegrini[35,43] G. Phillips[31] T. Rasing[30] T. Raubenheimer[35] T. Recigno[17] A. Reid[35] D. Reis[35,37]
A. Robert[35] J. Robinson[35] D. Rolles[16] J. Rost[24,37] S. Roy[17] A. Rudenko[16] T. Russell[47]
R. Sandberg[19] A. Sandhu[50] N. Sauter[17] I. Schlichting[21] R. Schlögl[10] W. Schlotter[35] M. Schmidt[59]
J. Schneider[6,7] R. Schoenlein*[17,35] M. Schoeffler[15] A. Scholl[17] Z. Shen[35] O. Shpyrko[44] T. Silva[26]
S. Sinha[44] D. Slaughter[17] J. Sobota[35] D. Sokaras[35] K. Sokolowski-Tinten[51] S. Southworth[1]
J. Spence[2] C. Stan[35] J. Stohr[35] R. Stroud[45] V. Sundstrom[20] C. Taatjes[33] A. Thomas[48] M. Trigo[35]
Y. Tsui[49] J. Turner[35] A. van Buuren[18] S. Vinko[55] S. Wakatsuki[35,37] J. Wark[55] P. Weber[5]
T. Weber[17] M. Wei[11] T. Weiss[35,37] P. Wernet[13] W. White[35] P. Willmott[28] K. Wilson[17]
W. Wurth[6,7,52] V. Yachandra[17] J. Yano[17] D. Yarotski[19] L. Young[1] Y. Zhu[4] D. Zhu[35] P. Zwart[17]

---

[1]Argonne National Laboratory
[2]Arizona State U.
[3]Baylor College Medicine
[4]Brookhaven National Laboratory
[5]Brown U.
[6]Center for Free Electron Laser Science
[7]DESY
[8]European XFEL
[9]Forschungszentrum Jülich
[10]Fritz-Haber-Institut - MPG
[11]General Atomics
[12]Goetheburg U.
[13]Helmholtz-Zentrum Berlin
[14]Imperial College London
[15]Institut für Kernphysik, Goethe U. Frankfurt
[16]Kansas State U.
[17]Lawrence Berkeley National Laboratory
[18]Lawrence Livermore National Laboratory
[19]Los Alamos National Laboratory
[20]Lund U.
[21]Max Planck Inst. for Medical Research
[22]Michigan State U.
[23]MIT
[24]MPI Physics Complex Systems Dresden
[25]MPI Structural Dynamics
[26]National Institute Standards and Tech.
[27]National Institutes Health
[28]Paul Scherrer Institute
[29]Photon Factory, Japan
[30]Radboud U.
[31]Rice U.
[32]RIKEN Center for Advanced Photonics
[33]Sandia National Laboratories
[34]SIMIT, CAS, Shanghai Tech Univ.
[35]SLAC National Accelerator Laboratory
[36]Sogang U.
[37]Stanford U.
[38]Stockholm U.
[39]Temple U.
[40]U. California, Berkeley
[41]U. California, Davis
[42]U. California, Irvine
[43]U. California, Los Angeles
[44]U. California, San Diego
[45]U. California, San Francisco
[46]U. Connecticut
[47]U. Massachusetts Amherst
[48]U. Michigan
[49]U. Alberta
[50]U. Arizona
[51]U. Duisburg-Essen
[52]U. Hamburg
[53]U. Illinois
[54]U. Nebraska Lincoln
[55]U. Oxford
[56]U. Southern California
[57]U. Tennessee
[58]U. Wisconsin-Madison
[59]U. Wisconsin-Milwaukee
[60]Uppsala U.

*corresponding author

Table of Contents

1.0 Executive Summary and Overview 3

2.0 Science Opportunities 9

2.1 Fundamental Dynamics of Energy & Charge in Atoms & Molecules 9

2.1.1 Fundamental charge migration & coherent light/matter interaction 10

2.1.2 Directed energy conversion, excited-states, & non Born-Oppenheimer dynamics 15

2.1.3 Advanced combustion and aerosol chemistry 33

2.2 Catalysis, Photo-catalysis, Environmental & Coordination Chemistry 44

2.2.1 Towards a predictive understanding of photo-catalysis 45

2.2.2 Tracking heterogeneous chemistry in real time under working conditions 52

2.3 Quantum Materials 63

2.3.1 Understanding and controlling emergent phenomena in materials with interacting degrees of freedom 63

2.3.2 Understanding and controlling nonequilibrium spin states at fundamental length and time scales 79

2.4 Nanoscale Heterogeneity, Fluctuations and Dynamics of Functional Materials 89

2.4.1 Spontaneous Fluctuations and Nanoscale Heterogeneity 89

2.4.2 Materials Dynamics, Energy Transport, and Phase Transitions at the Nanoscale 99

2.5 Matter in Extreme Environments 109

2.5.1 Warm and Hot Dense Matter: Laboratory Astrophysics 110

2.5.2 Dynamic compression, shock and impact physics 118

2.6 Revealing Biological Function on Natural Length and Time Scales 125

2.6.1 Understanding the dynamics of biological complexes & molecular machines 127

2.6.2 Dynamics, structure and function of biological assemblies in near-native environments 135

2.6.3 Understanding the relationships between electronic structure & biological function 139

3.0 New Experimental Approaches 148

3.1 Multidimensional X-ray Spectroscopy 148

3.2 Heterogeneous Ensembles: Fluctuations, Structure and Function 155

3.3 X-ray Cinematic Micro-Tomography with Chemical Imaging 161

4.0 Instrumentation 164

4.1 X-ray Optics & Beamlines 164

4.2 Lasers 170

4.3 Detectors 175

4.4 Diagnostics 177

5.0 Overview of LCLS-II 181

5.1 Unique LCLS-II Capabilities 182

5.2 Overview: Linacs, Undulators/FELs 182

5.3 Operating Modes 185

5.4 Future Options/Capabilities 186

Appendix 1: X-ray Interactions and Non-Disruptive Probing 189

1.0 Executive Summary and Overview

Since their discovery by Röntgen in 1895, X-rays have revolutionized our fundamental understanding of matter and, thereby, redefined chemistry, physics, biology, and many related fields of science and technology. The broad scientific importance of X-rays is reflected in the fact that 22 Nobel Prizes in physics, chemistry, and medicine have been awarded for work that involved X-rays. Scientists generally utilize X-rays in one of three ways: *X-ray scattering,* which exploits the short wavelengths of X-rays to resolve the structure of matter at the atomic scale; *X-ray spectroscopy,* which provides chemical specificity to characterize the local bonding and structural environment of specific atoms, and *X-ray imaging* which utilizes the penetrating capabilities of X-rays to reveal the unseen interior of complex matter. The development of synchrotron-based X-ray sources over the past 40 years has ushered in a modern age of X-ray science (leading to five Nobel Prizes since 1997) by harnessing high-energy electron accelerator technology to provide X-ray beams that are intense, highly directional, and tunable over a wide wavelength range. Synchrotron sources have developed into large regional scientific centers, servicing thousands of experiments per year, and X-rays are being applied in such disparate science areas as environmental science, astrophysics, and art history.

The recent emergence of X-ray lasers, more than one hundred years after Röntgen's original discovery, portends another revolution in X-ray science that will transform the field for the 21st century. *X-ray free-electron lasers* (X-ray FEL), enabled by developments in electron accelerator technology, generate X-ray beams many orders of magnitude brighter than the brightest synchrotron source. X-ray FELs generate ultrafast pulses that can be as short as 1 femtosecond (10^{-15} of a second) and can approach full spatial and temporal coherence. The pulsed nature of the X-rays invite their use as a probe of sample dynamics on a fast time scale appropriate for observing atomic motions. The very high intensity can create a significant data set from a single X-ray pulse. Whereas previous X-ray sources, including synchrotron sources, have primarily engaged in studies of static structures, X-ray FELs are by their nature suited for studying dynamic systems at the time and length scales of atomic interactions.

The first X-ray FEL to generate hard X-rays, the Linac Coherent Light Source (LCLS), began operation in 2009 and has dramatically exceeded performance expectations. This facility was created using an existing electron accelerator which limits its pulse rate to 120 Hz. It generates X-rays by amplifying spontaneous noise in the electron beam (the so-called SASE process), which limits the temporal coherence of the pulses. Nevertheless, LCLS has already had a significant impact on many areas of science, including: resolving the structures of macromolecular protein complexes that were previously inaccessible; capturing bond formation in the elusive transition-state of a chemical reaction; revealing the behavior of atoms and molecules in the presence of strong fields; observing quantum vortices in superfluid helium; and probing extreme states of matter from the structure of supercooled water to metals shock-heated to 10,000 degrees. The early success of LCLS, along with the promise of more X-ray laser science to come, makes a compelling case that a next-generation facility is essential. This need is widely recognized by the international science community, and has been cited in several BES reports.

The 2007 BES report *Directing Matter & Energy: Five Grand Challenges for Science & the Imagination*[1] identified fundamental open questions that underpin energy science. The report further cited the need for new observational tools and facilities to help address these grand challenges. The 2009 BES report *Next-Generation Photon Sources for Grand Challenges in Science and Energy*[2] recognized specific areas of energy science where next-generation X-ray light sources would have the greatest impact. Most recently, the *Report of the BESAC Subcommittee on Future X-ray Light Sources* (2013)[3] specifically stated:

> *...an exciting window of opportunity exists for the U.S. to provide a revolutionary advance in X-ray science by developing and constructing an unprecedented X-ray light source. This new light source*

should provide high repetition rate, ultra-bright, transform limited, femtosecond X-ray pulses over a broad photon energy range with full spatial and temporal coherence.

LCLS-II represents just such an advance in X-ray laser technology and will be a transformative tool for energy science. It will qualitatively change the way in which X-ray *scattering*, *spectroscopy and imaging* will be used in the future, to observe in ways never before possible, how natural and artificial systems function, spanning multiple decades of time scales (down to the attosecond regime) and multiple spatial scales (down to the atomic regime). LCLS-II will further enable powerful new ways to capture rare chemical events, characterize fluctuating heterogeneous complexes, and reveal underlying quantum phenomena in matter using nonlinear, multidimensional, and coherent X-ray techniques that are only possible with a true X-ray laser.

This next-generation facility will be based on advanced superconducting accelerator technology (continuous-wave RF) and tunable magnetic undulators. It will support the latest seeding technologies to provide fully coherent X-rays (at the spatial diffraction limit *and* at the temporal transform limit) in a uniformly-spaced train of pulses with programmable repetition rates of up to 1 MHz and tunable photon energies from 0.25 to 5 keV. It will also provide coherent X-ray pulses at photon energies greatly exceeding those presently available at LCLS, up to 25 keV at 120 Hz.

It is important to note that the revolution in X-ray laser science coincides with a renaissance in conventional synchrotron X-ray sources. In particular, new storage-ring lattice designs with lower electron-beam emittance now enable the generation of diffraction-limited soft and hard X-ray beams with substantially higher brightness. The properties of X-rays from upgraded synchrotrons will begin to approach those of a continuous source at the spatial diffraction limit, with broad incoherent bandwidth, and long pulses with low peak intensities at hundreds of MHz repetition rate. Thus, synchrotron sources will continue to complement X-ray laser facilities by providing access to many thousands of users annually and serving many tens of experiments simultaneously.

LCLS-II Science Opportunities Document Outline & Overview

In a pending BES report, the original five grand challenges for science and the imagination[1]:

- *How do we control material processes at the level of electrons?*
- *How do we design and perfect atom- and energy-efficient synthesis of revolutionary new forms of matter with tailored properties?*
- *How do remarkable properties of matter emerge from complex correlations of the atomic or electronic constituents and how can we control these properties?*
- *How can we master energy and information on the nanoscale to create new technologies with capabilities rivaling those of living things?*
- *How do we characterize and control matter away – especially very far away – from equilibrium?*

will be augmented with five transformative opportunities for discovery science:

- *Mastering hierarchical architectures and beyond-equilibrium matter*
- *Beyond ideal materials and systems: understanding the critical roles of heterogeneity, interfaces and disorder*
- *Harnessing coherence in light and matter*
- *Revolutionary advances in models, mathematics, algorithms, data, and computing*
- *Exploiting transformative advances in imaging capabilities across multiple scales*

Section 2 of this document describes six broad areas of science in which the unique capabilities of LCLS-II will be essential to achieving further advances on the original grand challenges and will address critical knowledge gaps at the new scientific frontiers of matter and energy, as summarized in the five transformative opportunities above.

Fundamental Dynamics of Energy & Charge

Charge migration, redistribution and localization, even in simple molecules, are not well understood at the quantum level. These processes are central to complex processes such as photosynthesis, catalysis, and bond formation/dissolution that govern all chemical reactions. Indirect evidence points to the importance of quantum coherences and coupled evolution of electronic and nuclear wavefunctions in many molecular systems. However, we have not been able to directly observe these processes to date, and they are beyond the description of conventional chemistry models. High-repetition-rate soft X-rays from LCLS-II will enable new dynamic molecular reaction microscope techniques that will directly map charge distributions and reaction dynamics in the molecular frame. New nonlinear X-ray spectroscopies offer the potential to map quantum coherences in an element-specific way for the first time.

Experimental Approaches:

- Dynamic molecular reaction microscope
- Time-resolved photoemission spectroscopy
- Time-resolved Hard X-ray scattering
- New nonlinear X-ray spectroscopies

Catalysis & Photo-catalysis

Understanding catalysis and photo-catalysis is essential for directed design of new systems for chemical transformation and solar energy conversion that are efficient, chemically selective, robust, and based on earth-abundant elements. LCLS-II will reveal the critical (and often rare) transient events in these multi-step processes, from light harvesting, to charge separation, to charge migration and subsequent accumulation at catalytically active sites. Time-resolved, high-sensitivity, element-specific spectroscopy enabled by LCLS-II will provide the first direct view of charge dynamics and chemical processes at interfaces, making it possible to pinpoint where charge carriers are lost (within a molecular complex or device) — a crucial bottleneck for efficient solar energy conversion. Such approaches will capture rare chemical events in operating catalytic systems across multiple time and length scales. The unique LCLS-II capability for simultaneous delivery of hard and soft X-ray pulses opens the possibility to follow chemical dynamics (via spectroscopy), concurrent with structural dynamics (substrate scattering) during heterogeneous catalysis.

Experimental Approaches:

- Time-resolved resonant inelastic X-ray scattering and absorption spectroscopy
- Time-resolved X-ray photoelectron spectroscopy
- Simultaneous soft X-rays (spectroscopy) and hard X-rays (scattering)
- X-ray photon correlation spectroscopy
- New nonlinear X-ray spectroscopies

Emergent Phenomena in Quantum Materials

There is an urgent technology need to understand and ultimately control the exotic properties of new materials – ranging from superconductivity to ferroelectricity to magnetism. These properties emerge from the correlated interactions of the constituent matter components of charge, spin, and phonons, and are not well described by conventional band models that underpin present semiconductor technologies. Fully coherent X-rays from LCLS-II will enable new high-resolution spectroscopy approaches that will map the collective excitations that define these new materials in unprecedented detail. Ultrashort X-ray pulses and optical fields will facilitate new coherent light-matter approaches for manipulating charge,

spin, and phonon modes to both advance our fundamental understanding and point the way to new approaches for materials control.

Experimental Approaches:

- Time-resolved and high-resolution resonant inelastic X-ray scattering
- Time-resolved X-ray dichroism and coherent scattering/imaging
- Time- and spin-resolved hard X-ray photoemission
- X-ray photon correlation spectroscopy

Nanoscale Materials Dynamics, Heterogeneity & Fluctuations

The properties of functional materials are often defined by interfaces, heterogeneity, imperfections, and fluctuations of charge and/or atomic structure. Models of ideal materials often break down when trying to describe the properties that arise from these complex, non-equilibrium conditions. Ultrashort X-ray pulses from LCLS-II will provide element-specific snapshots of materials dynamics to characterize transient non-equilibrium and meta-stable phases. Programmable trains of soft X-ray pulses at high repetition rates will characterize spontaneous fluctuations and heterogeneities at the nanoscale across many decades of time, while coherent hard X-ray scattering will provide unprecedented spatial resolution of material structure, its evolution, and relationship to functionality under operating conditions.

Experimental Approaches:

- X-ray photon correlation spectroscopy
- Time-resolved X-ray scattering

Matter in Extreme Environments

Unpredictable material phases and properties also emerge under extreme conditions of temperature, pressure, and applied fields. Understanding the behavior of matter under these extreme conditions is essential to improve the function of materials in extreme environments, such as those required for fusion energy, and to advance our understanding of planets and stars in the universe. LCLS-II capabilities for generating soft and hard X-ray pulses simultaneously will enable the creation and probing of extreme conditions that are far beyond our present reach. Penetrating hard X-ray pulses will allow the unique characterization of unknown structural phases. The unprecedented spatial and temporal resolution will enable direct comparison with theoretical models relevant for inertial-confinement fusion and planetary science.

Experimental Approaches:

- Time-resolved X-ray scattering
- Time-resolved X-ray Thomson scattering/X-ray spectroscopy
- Simultaneous soft X-rays (spectroscopy) and hard X-rays (scattering)

Revealing Biological Function

Biological function is profoundly influenced by dynamic changes in protein conformations and by interactions with molecules and other complexes — processes that span many decades in time. Such dynamics are central to the function of biological enzymes, cellular ion channels comprised of membrane proteins, and macromolecular machines responsible for transcription, translation and splicing, to name just a few examples. X-ray crystallography at modern synchrotrons has transformed the field of structural biology by routinely resolving simple macromolecules at the atomic scale. LCLS has already demonstrated a major advance in this area by resolving the structures of macromolecules that were previously inaccessible by using the new approaches of *serial nano-crystallography* and *diffract-before-destroy* with high-peak-power X-ray pulses. The high repetition rate of LCLS-II portents another major advance by revealing biological *function* through its unique capability to follow the dynamics of macromolecules and interacting complexes *in real time* and *in native environments*. Advanced solution

scattering and coherent imaging techniques will characterize, at the sub-nanometer scale, the conformational dynamics of heterogeneous ensembles of macromolecules – both spontaneous fluctuations of isolated complexes and conformational changes that may be initiated by the presence of specific molecules, environmental changes, or by other stimuli. The unique LCLS-II capability for generating two-color hard X-ray pulses will enable entirely new phasing schemes for nano-crystallography, and will resolve atomic-scale structural dynamics of biochemical processes that are often the first step leading to larger-scale protein motions.

Experimental Approaches:

- Time-resolved X-ray scattering
- Time-resolved resonant inelastic X-ray scattering/spectroscopy

Section 3 of this document describes a few of the qualitatively new experimental approaches that are enabled by the capabilities of LCLS-II (in addition to the more developed approaches indicated above).

Multidimensional X-ray spectroscopy refers to a broad class of new methods that exploit coherent X-ray/matter interactions and incorporate sequences of X-ray pulses to generate experimental signals that are a function of multiple time delays and/or photon energies. In these techniques, X-rays are used both as a pump, to prepare element-specific non-equilibrium states of matter (in gas, liquid, or condensed phase), and as a probe of the time-evolution of these non-stationary states. As demonstrated in recent decades in the area of optical wave-mixing with amplified continuous-wave, mode-locked optical lasers, a high-repetition-rate, tunable ultrafast X-ray laser will be essential to fully realize the tremendous scientific potential of multidimensional nonlinear X-ray techniques. These tools rely on the simultaneous combination of high peak power, high average power, tunability, and temporal and spatial coherence. Moreover, extracting scientific insight from multidimensional spectroscopy requires an ability to trade off peak power, average power, pulse duration, and bandwidth to enhance the nonlinear signals of interest and discriminate them from a multitude of other effects. The LCLS-II X-ray laser has the versatility to access the few-femtosecond time scales characteristic of electronic motion and quantum coherences in atoms and molecules, as well as the high spectral resolution to map the low-energy collective modes that define correlated materials.

Heterogeneous Ensembles: Fluctuations, Structure & Function describes new approaches for revealing structure and function of macromolecular machines at the nanoscale, exploiting the high repetition rate of LCLS-II. We presently lack the tools necessary for dynamic imaging of such biological machines – in operation, in native solution environments. Small-angle and wide-angle X-ray scattering (SAX/WAX) in solution are presently being used to great advantage in combination with X-ray crystallography. However, the full potential of these approaches remains unrealized because of rotational averaging, owing to long exposure times – effectively projecting the scattering information from three-dimensional objects onto one dimension, thereby preventing unambiguous structure determination. Faster exposure times available from LCLS-II will eliminate the restriction of rotational averaging, thereby projecting the X-ray scattering information onto two dimensions – providing orders of magnitude of additional information that will enable structure determination in entirely new ways. In addition, the high repetition rate of LCLS-II will generate approximately 10^{10} scattering images per day. This unprecedented data volume (from solution ensemble samples or from single-particle scattering), combined with pattern-recognition algorithms and advanced computational approaches, will qualitatively transform our ability to extract information about heterogeneity (non-identical particles), spontaneous dynamics, and statistical rare events which are central to the way biological complexes function in native environments.

High-speed Chemically-Selective Imaging refers to the potential for exploiting the high average coherent power from LCLS-II for three-dimensional imaging with chemical specificity over a wide range of length and time scales with continuous observation of chemical and structural processes. Applications range

from analysis of combustion chemistry applied to fuel jets and flames, to analysis of chemical flow through porous media, to polymer processing.

Section 4 highlights some of the unique enabling beamline and endstation instrumentation – optics, detectors, lasers, and endstations – that will be needed to capitalize on the most important science opportunities described in Section 2. Development of instrumentation for LCLS-II is in the early stages, and this effort will be organized as part of the ongoing operation of the LCLS facility. Recent LCLS-II scientific workshops provide a starting point for defining and prioritizing the instrumentation needs. LCLS will continue to engage the scientific community for their input and feedback as plans for instrumentation development are refined.

Section 5 provides a brief description of the LCLS-II X-ray laser, focusing on the unique capabilities, objective performance parameters, operating modes, and potential future options and capabilities. These are motivated by the science opportunities described in Section 2 and informed by recent LCLS-II scientific workshops. A more complete technical description can be found in the LCLS-II Final Design Report.[4]

References:

1. "Directing Matter and Energy: Five Challenges for Science and the Imagination," (http://science.energy.gov/~/media/bes/pdf/reports/files/gc_rpt.pdf, 2007).
2. "Next-Generation Photon Sources for Grand Challenges in Science and Energy," (http://science.energy.gov/~/media/bes/pdf/reports/files/ngps_rpt.pdf, 2009).
3. "Report of the BESAC Subcommittee on Future X-ray Light Sources," (http://science.energy.gov/~/media/bes/besac/pdf/Reports/Future_Light_Sources_report_BESAC_approved_72513.pdf, 2013).
4. "LINAC Coherent Light Source II (LCLS-II) Project Final Design Report - LCLSII-1.1-DR-0251-R0," (SLAC National Accelerator Laboratory, https://slacspace.slac.stanford.edu/sites/lcls/lcls-2/fdr/pages/default.aspx, 2015).

2.0 Science Opportunities

2.1 Fundamental Dynamics of Energy & Charge in Atoms & Molecules

Synopsis

All chemistry employs electron motion to carry out a reaction, but the fundamental dynamics of moving electrons have always been hidden because they are just too fast to detect. The typical momentum of an electron in a chemical bond is high enough to carry it across a small molecule in a fraction of a femtosecond. The motion of nuclei on the other hand proceeds on the timescale of many femtoseconds. The most powerful and widely used approximations in chemistry (and more than a few Nobel Prize achievements) actually take advantage of this so-called "separation of time scales" to help reduce complex many-body quantum processes of electron and nuclear motion to more tractable forms that lead to simple predictive models. Yet these approximations cannot resolve the chemistry of some of our most urgent problems such as light harvesting by molecules and the transformation of light energy into chemical bonds.

In addition, many of our great challenges in energy science, materials science, and bioscience require new insights that lie beyond this femtosecond barrier, require us to view the electrons as they interact with each other and with nuclei. Examples of these challenge problems are the role of coherence in photochemistry; the details of charge migration during radiation damage; and the initial dynamics of charge migration that lead to charge transfer in electrochemistry and in catalysis.

In this section we will examine some of the opportunities for research enabled by LCLS-II in this area. The fundamental message is that LCLS-II will lead to new progress in this science, which will in turn transform our understanding of chemical change.

Introduction

Energy transfer in chemistry is carried by electrons, and initiated by electron motion. Lighting a flashlight or a candle, charging a battery, growth of a plant – all are electron-initiated processes. The defining characteristic that separates these chemical processes from other materials processes (freezing, evaporation, bending, cracking, etc.) is that in chemistry, the electrons change their state. It is therefore not surprising that a new instrument that is capable of detecting and imaging electron motion in matter will be a wonderful new tool for chemistry. Here we summarize some of the transformative new science opportunities enabled by LCLS-II.

A great example of the importance of electron motion is photo-absorption in molecules, which is the fundamental mechanism by which solar energy is captured. This drives a wealth of chemical processes which play important roles for life on earth – from photosynthesis, to vision, to vitamin D production in humans. A single solar photon absorbed by a molecule delivers as much energy to a single electron as a flashlight battery – several electron volts. One long-standing question that can be addressed with the unique capabilities of LCLS-II is how energy gained by the absorption of a photon is converted into charge migration and charge transfer, and ultimately into stored chemical energy that can be available for applications. Unless this energy is selectively channeled into chemical bonds on femtosecond time scales and Angstrom length scales, it will be lost to heat. In green plants this loss is about two-thirds, so there is much interest in understanding how the electron energy can be harnessed more efficiently.

The central issue here is coupling: first between the external energy source (sunlight for example) and the electrons in a molecule; and then between the electrons and the atomic nuclei. Ultimately storage is

accomplished by re-organization of the atoms, which move in response to changes in the distribution of electron charge around them.

Our current understanding of photochemistry is based on a number of approximations that simplify the process but at the same time limit our insight about the early stages. The two most important approximations are the Franck-Condon (FC) approximation, which assumes that no nuclear motion occurs during the initial act of photo-absorption; and the Born-Oppenheimer approximation (BOA), which assumes that only nuclear positions, and not nuclear motion, determine the electronic energy levels in the molecule. Both of these approximations break down at critical points, such as at the moment of photo-absorption, or at special points of electronic state degeneracy that must occur during non-radiative relaxation following molecular excitation. These points of degeneracy are places where the motions of the electrons and the nuclei have a particularly strong effect on each other.

Solar energy conversion is only one example of charge transfer, which is also critical for the inner workings of batteries, catalysts, combustion, corrosion, and many other chemical processes. The time scales for these reactions can vary by factors of more than a million, due to myriad electron pathways that can change on femtosecond time scales due to collisions or as a result of slight changes in atomic arrangement. The shortest time scales of interest are now accessible because of the combination of high intensity and ultrashort X-ray pulses at LCLS-II.

The strong fields generated in a focused X-ray laser beam are of particular fundamental interest on the molecular scale. Ordinary sunlight or conventional X-ray sources interact with molecules fairly weakly, by the simple measure that the motion initiated by absorption of a single photon is completely concluded before the next absorption event. X-ray lasers break this rule. The collective effect of multiple X-ray photons concentrate the energy so that the extreme conditions in the target can mimic the interiors of large planets or stars. They also lead to nonlinear processes such as photon harmonic generation.

Finally, LCLS II offers a wealth of new opportunities due to its transversal and longitudinal coherence properties. Ordinary sources of light such as sunlight or synchrotron X-rays have no longitudinal coherence, meaning that the separation of successive absorption events is much longer than the effective duration of a single photon. These conventional sources also have almost no transverse coherence, which means that nearby absorption or scattering events in the target are more widely spaced than the transverse area of a single photon. These concepts of photon area and duration have precise definitions, which place the number of photons in a coherent volume (photon degeneracy) at LCLS to be more than ten billion. This is an extreme jump compared to a number closer to one for synchrotrons. Laser spectroscopy over the past half-century has developed a catalog of coherent methods to take advantage of this high photon degeneracy, but they have never been accessible at X-ray wavelengths before the advent of the X-ray free electron lasers. Furthermore, such methods can make optimal use of high repetition rate and stable coherent properties that can be available at LCLS-II.

2.1.1 Fundamental charge migration & coherent light/matter interaction

Ultrafast electrons and core-hole dynamics

One of the triumphs of LCLS has been the ability to create element specific core vacancies (core holes) with high probability, and on a fast enough time scale to use them to initiate dynamics. This has been an important entry point for the more general study of charge transfer and all its applications from photochemistry to catalysis. An important limitation of LCLS has been its low repetition rate and relative lack of stability. This places a tremendous premium on the ability to perform so-called single shot experiments, where each laser pulse is nearly an experiment unto itself. However, with the high repetition rate and greater stability of LCLS-II many of these methods may be replaced with more powerful multi-pulse multi-delay methods. These can begin to address more general and more critical

scientific questions that were not previously possible, such as understanding the fundamentals of photochemistry and the light-harvesting process in both natural and artificial systems.

In order to answer these questions scientists would like to measure all aspects of charge motion. One example that is especially accessible with ultrafast X-rays is the charge redistribution following inner-shell core electron photoionization, often leading to Auger relaxation and subsequent valence-shell electron dynamics. LCLS-II should be able to track hole/electron dynamics evolving into charge transfer and chemical transformation, both in gas phase and ultimately with liquids, solutions, and other areas of condensed phase chemistry.

Liquid phase multidimensional core-hole migration studies will explore the relevance of electron coherences in condensed phase chemistry. A key goal is to define how electrons retain coherence in systems that are embedded in an ambient environment. Although such systems are not isolated, nonetheless it is thought that low-coherence subspaces still exist and that these can be the source of some high efficiency and control in photochemistry.

The high repetition rate means that small signal methods such as lock-in detection can be employed that do not rely on saturating the initial excitation. In addition to repetition rate, the length of the X-ray pulse can be sufficiently short to support multi-pulse delay studies before the onset of Auger relaxation. Therefore pulses in the range of 1-5 fs are highly desirable. A ~1 fs X-ray pulses synchronized with a ~1 fs X-ray/UV/vis pulse would be ideal for transient absorption measurements, or for studies where the signal is provided by transient Auger spectra. We stress that the pulse duration, pulse energy, rep-rate, stability, diagnostics, and synchronized laser capability from LCLS II will be transformative in enabling these measurements.

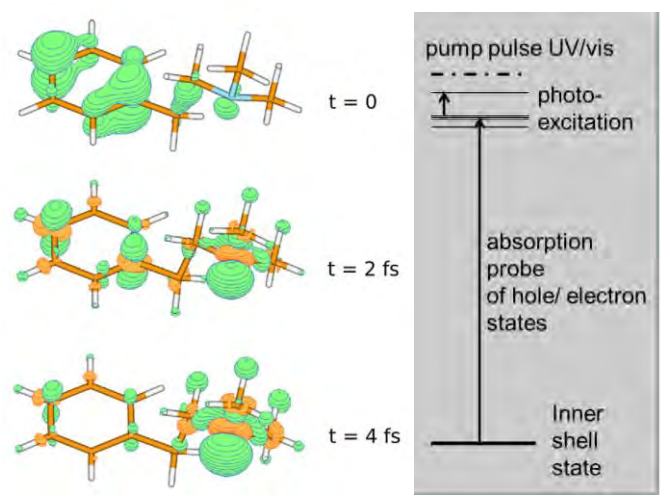

Figure 1: Left: Frontier orbitals of charge dynamics in 2-phenylethyl-N,N-dimethylamine initiated by a valence-shell hole.[1]
Right: Measurement scheme for site-specific probing of valence charge dynamics via transitions from inner-shell states.

The basic technique of valence shell probing is illustrated in Figure 1. Initial photoionization creates a charge disturbance in a molecule associated with a valence hole. This highly non-stationary state leads to rapid electron migration before the heavier atoms can move significantly. The evolution of charge in this valence-hole state can be monitored at a specific location with a second X-ray pulse tuned to a different energy to be sensitive to a particular atomic species.

Valence electronic wavepacket dynamics

Complementing studies of charge dynamics driven by core-hole excitations, nonlinear X-ray techniques enabled by LCLS-II hold tremendous promise for following the flow of charge through the creation of coherent non-stationary *valence electronic wavepackets* that are initially localized on specific atomic

sites, and evolve on ultrafast time scales (in the absence of a core hole). This new approach – Stimulated X-ray Raman Spectroscopy, SXRS – is analogous to stimulated Raman techniques now widely employed in the visible and infra-red regime to create coherent *vibrational wavepackets* in matter. A more complete description of the SXRS process is provided in Section 3.1.

The potential impact of SXRS studies of charge dynamics is illustrated in Figure 2 which shows recent SXRS simulations of ultrafast energy transfer dynamics in a Zn/Ni porphyrin heterodimer which are of interest as model components in artificial light harvesting and photosynthetic complexes.[2]

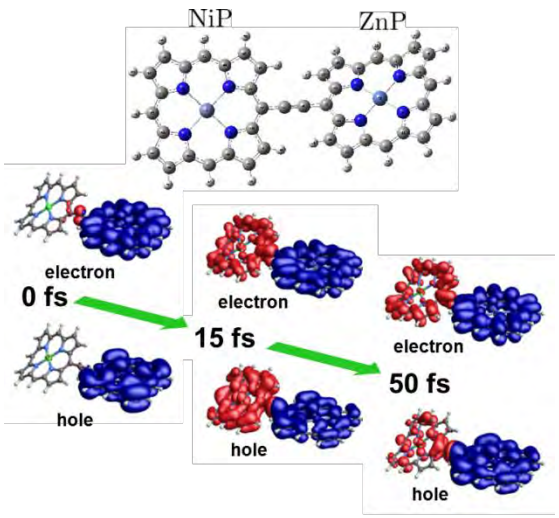

Figure 2: Excitation energy transfer simulation in Zn/Ni porphyrin heterodimer. The X-ray pump pulse is resonant with the Zn L_3-edge, and creates a localized valence excitation (wavepacket) via SXRS. Evolution of electron and hole densities (isosurfaces) are calculated from the non-stationary valence superposition states prepared via SXRS.[2]

In this example, an intense attosecond pulse resonant with the Zn $L_{2,3}$ absorption edge (~1.01 keV) excites a core electron into a virtual superposition of unoccupied valence orbitals, and subsequently stimulates emission from occupied valence orbitals to fill the core hole. This stimulated process creates a coherent valence wavepacket of charge in the vicinity of the Zn atom, on time scales much faster than any nuclear motion. Thus, this is a powerful approach for separating coupled valence-electronic and nuclear degrees of freedom, and for revealing excitation energy transfer effects (co-propagation of the electron and hole wavepackets), and quantum coupling between the valence systems of the Zn and Ni monomers.[2] A second X-ray pulse probes the evolution of electronic wavepackets through transient X-ray absorption, photoelectron spectroscopy, or a second SXRS interaction – all of which provide element specificity (e.g. tuning to the Ni resonance). Related nonlinear X-ray wave-mixing techniques, such as Core-hole Correlation Spectroscopy, are sensitive probes of coupling between the valence systems at different atomic sites in a molecule (as discussed in Section 3.1). These approaches are uniquely enabled by the combination of tunable X-ray pulses with high peak power, and at high repetition rate provided by LCLS-II.

Dynamics of energy flow in larger molecules, molecular ions and clusters

Energy deposition and energy flow is extremely important in clusters and large molecules, for X-ray diffraction studies, chemical processing, and also in order to understand the basic mechanisms of radiation damage. LCLS, the world's first general research tool for high intensity X-ray studies, has already made a number of important discoveries in this area. In focused beam experiments at LCLS, we have discovered some general rules for strong X-ray absorption. We have discovered, for example, that in some cases sequential ionization to high charge states dominates, so that the highest charge state of ionization is limited by the energy delivered by a single photon.[3] In other cases we have found that nonlinear cooperative X-ray absorption can dominate, resulting from excitation to intermediate excited states and from radiative relaxation during absorption.[4]

Negative ions represent a special class of systems and accurate descriptions of the structure and dynamics of negative ions provide critical tests of fundamental atomic, molecular and chemical science. Due to the excess negative charge, electron correlation effects assume a prominent role in anions. This makes them an ideal testing ground of correlation phenomena, exposing inaccuracies or discrepancies in fundamental ab-initio calculations, thereby providing detailed insight into strongly correlated systems in general. The role of the extra electron in anions gives rise to different properties compared to their counterpart neutral or positive ions making anions intriguing to study. Negative ions are also important in many physical processes occurring in chemistry, stellar atmospheres, molecular clouds, and plasma physics.

In clusters such as C_{60} we see that energetic coulomb explosions occur because of the mutual repulsion of highly charged carbons.[5] But when the cluster also contains a large hydrogen fraction along with heavier atoms, such as methane clusters, then the mobile protons can neutralize high ionization rates so that the state of carbon ionization is dramatically reduced.[6, 7] Finally, very recent studies of time-resolved X-ray diffraction from clusters are showing evidence for transient plasma states with unusual properties as the hot electrons equilibrate, first with each other, and much later with the ions.[8]

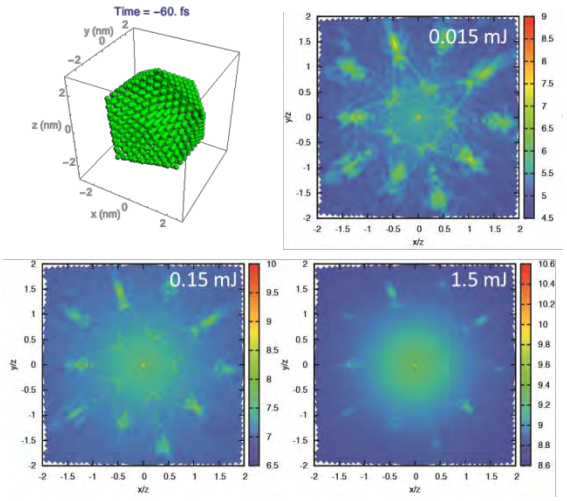

Figure 3: X-ray scattering Monte-Carlo/Molecular-Dynamics simulation of radiation damage in a 5.2 nm 7-shell argon cluster with 30 fs pulses at 8 keV and pulse energies of 0.015 mJ, 0.15 mJ, and 1.5 mJ. (P. Ho, C. Knight, L. Young unpublished)

LCLS-II will have the ability to map all of these transient phenomena in detail. The higher photon energies available in the warm linac portion will extend the range of parameters available in cluster imaging studies. The high repetition rate superconducting linac FEL could reveal the earliest stages of structural changes following strong X-ray absorption.

Role of quantum coherences and evolution in chemical processes: strong field, high intensity, short-pulse frontier

Optimal control with X-rays can extend the scientific reach beyond that attained with incoherent X-rays. Accelerator-based sources offer additional possibilities to manipulate the light pulse by sculpting the electron beam. One way to formulate optimal control in the X-ray domain is separating the light-matter interactions that depend on the pulse envelope from interactions that depend only on the photon energy.

Optimal control has become a versatile tool in combination with pulse shapers to synthesize waveforms for a number of important applications in laser-matter interactions. Now that we have the opportunity for many eV of coherent bandwidth, the sculpting of X-ray pulses is appealing.

A straightforward approach already demonstrated in LCLS is to shape the electron beam upstream of the undulators. Electron beam shaping also provides an elegant means to implement feedback loops to search for X-ray pulse shapes that optimize an experimental goal, such as the suppression or enhancement of

fragmentation channels. LCLS-II substantially improves electron beam control by replacing the noisy pulsed warm linac with a cw superconducting linac.

A well-controlled electron beam can then lead to well-controlled X-rays, particularly if the X-rays can be produced in a way that does not add excessive noise, such as seeding, self-seeding, or so-called "Echo" methods. In fact having spent so much effort to tame the electron beam, it would be most impractical for LCLS-II to still rely solely on the stochastic process of SASE to produce X-rays, thus removing most of the hard-won advantages of stability. Furthermore, the manipulation of the X-ray beam using e-beam based approaches is an important science goal in its own right, and would open up many new fundamental science applications.

Current simulations suggest that pulses of 0.5fs duration are possible.[9] The coherent bandwidth associated with such pulses will enable programs such as impulsive Raman scattering and coherent multidimensional spectroscopy, described later in this section.

2.1.2 Directed energy conversion, excited-states, & non Born-Oppenheimer dynamics

Light absorption in a molecule excites valence electrons, and the subsequent molecular dynamics determines how the photon energy is channeled – often very selectively, into changed chemical bonds, migration of electrical charge, nuclear motion, heat, or other energetic degrees of freedom.

Excited electronic states also play an important role in chemistry induced by high energy ionizing particles. In organic matter, such energy is efficiently converted into a shower of lower energy electrons which may induce electronically excited states leading to bond breakage via dissociative electron attachment (DEA). The stunning demonstration by Sanche and coworkers[10] in 2000 that single- and double-strand breaks in DNA can by triggered by low-energy electron collisions led to a revived interest in "electron-driven chemical processes" – particularly low-energy DEA in biologically relevant species, from water to DNA bases.

Understanding and controlling molecular dynamics in the electronic excited state remains a fundamental science challenge, in large part because we lack the requisite tools to probe these processes – simultaneously at the atomic level and on natural femtosecond time scales.

New capabilities for understanding reaction dynamics at LCLS-II

LCLS-II will provide qualitatively new probes of energy and charge flow and how they work in simple and complex molecular systems. The high repetition rate of LCLS-II in the soft X-ray range will enable sophisticated coincidence measurement schemes for kinematically complete experiments *while the reaction occurs*. This approach measures simultaneously the momenta of all the constituent components of a complex (typically via pulsed ionization and TOF spectroscopy of the charged fragments), from which the transient charge distribution may be reconstructed *in the molecular frame*. Moreover, coincidence capabilities with high repetition rate offer important new approaches for capturing rare transient events. The stability and precision of LCLS-II in pulse timing, spectrum and intensity will enable transient spectroscopy (e.g. using photoelectrons or X-ray absorption) with unprecedented sensitivity to discern small changes in electronic configurations and molecular structure. Hard X-rays at 25 keV photon energy will provide a qualitative advance in our ability to resolve transient atomic structure of reacting complexes at the sub-Å scale.

Photoexcitation

How is energy, absorbed from light, selectively converted into chemical energy in molecular systems?

A few examples illustrate the diversity of molecular energy conversion processes following interaction with light. Many molecules undergo a major structural change, localized around few bonds[11]. Prominent examples include: azobenzene;[12, 13] stilbene;[14, 15] rhodopsin – responsible for the first step in vision[16-18] and for proton pumping in bacteria;[19, 20] and green fluorescent protein – used as fluorescent marker in genetics.[21] In contrast, light energy absorbed by nucleobases and related classes of molecules is selectively channeled away from bond changes and large structural motion into other dissipative channels – thus contributing to the photo-protection of our genetic code, by inhibiting ultraviolet induced dimerization of bases in the DNA strand.[22-24] Light excitation can also trigger the emergence of chirality (right-handed vs. left-handed structure) in a molecule.[25] This form of symmetry breaking is fundamental in chemistry, and biology as the chemical properties and biological function of two molecular enantiomers are often completely different.

Dynamics are key to addressing this question, since excess photon energy must be rapidly channeled to desirable pathways (e.g. coordinated rearrangement of specific chemical bonds or migration of electrical charge) or else it will be dissipated into undesirable or even destructive channels. Thus, detailed

knowledge of the concerted motion of electrons and nuclei that occurs in the *electronic excited state* on the fundamental time scale of femtoseconds is essential to understanding, and ultimately controlling these processes.

Photoexcitation and photoconversion: Current understanding and knowledge gaps of excited molecular states

Our current understanding of chemistry in electronically excited states is based largely on *adiabatic* potential energy surfaces (PES) that are a consequence of the Born-Oppenheimer approximation (BOA) – namely the assumption that the electronic structure (comprised of light, fast electrons) responds essentially instantaneously to motions of the slower heavier nuclei, thereby justifying separate consideration of the electronic and nuclear wavefunctions.[26] However, this assumption breaks down at crossing regions of the potential energy surfaces where the electronic states are degenerate, or nearly degenerate.[27-29] In such regions, the characteristic time scale for electronic motion is given roughly by the inverse of the energy spacing ($1/\Delta E$) of the eigenstates. Thus in crossing regions (as $\Delta E \rightarrow 0$) the response of the electronic structure slows to the nuclear motion timescale, and close lying adiabatic states become strongly coupled. In these regions, quantum wavepackets transfer rapidly and efficiently from one adiabatic state to another, thereby determining the pathways and branching of chemical reactions. The topology of these interactions regions may be points or seams of conical intersections[30-32] depending on the dimensionality of the potential energy landscape.[33, 34] While experimental and theoretical efforts in recent decades demonstrate that non Born-Oppenheimer behavior is ubiquitous in polyatomic molecules, we nevertheless lack an experimental ability to directly observe molecular dynamics in these non Born-Oppenheimer regions, and similarly lack an adequate theoretical description of these effects in more complex molecules.

The importance of understanding photochemistry and non-BOA processes in isolated molecules lies in part on the very close interplay of experiments with theory, thereby providing foundational knowledge and principles that can then be applied to more complex systems. Current theoretical approaches are limited in their ability to predict nuclear dynamics during chemical transformations, and rely on compromising approximations even for small molecules. Conventional treatments of electronic structure and couplings based on Hartree-Fock methods crudely approximate electron interactions by mean field potentials. More elaborate approaches, such as the full configuration interaction, become computationally intractable for increasing molecular size. For photoexcited electronic states, both electron correlation and non-Born-Oppenheimer dynamics play a crucial role and render calculations extremely challenging.[35, 36]

The nucleobase thymine provides an illustrative example of the scientific challenges and opportunities to advance our understanding of photochemistry and energy conversion in electronic excited states. Figure 4 shows a representation of the potential energy surface for thymine in the electronic excited state. Light absorption launches a molecular vibrational wavepacket in the Franck-Condon region from which it relaxes to points of degeneracy with two lower lying states. For the two reaction coordinates g and h (b) the degeneracy is linearly lifted, showing the conical intersection. The exact shape of the potential-energy surface is highly controversial, leading to conflicting predictions about both the nuclear relaxation on the PES and the non-BOA transitions to other electronic states.

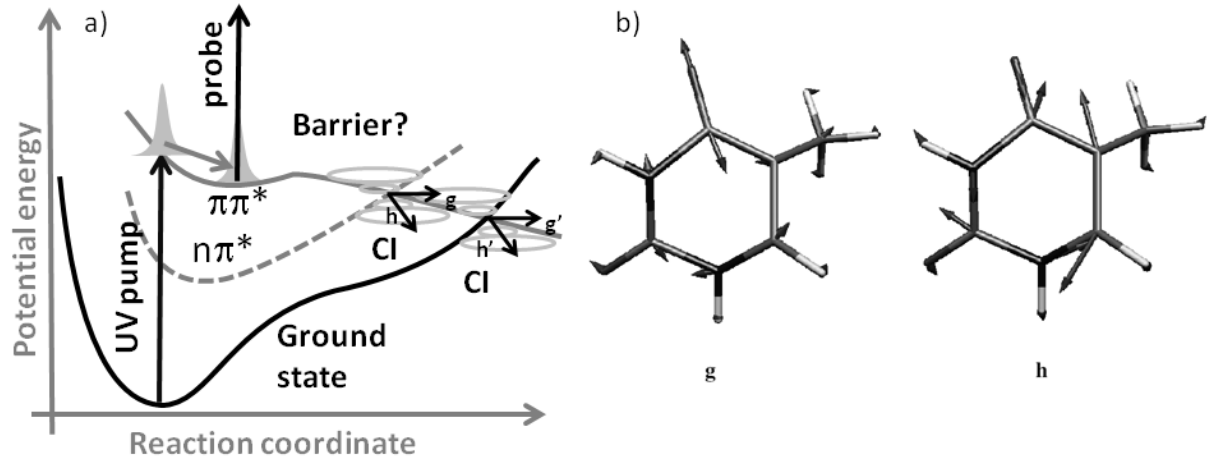

Figure 4: Reaction path from the Franck-Condon region to conical intersections connecting with the ground and nπ* states. The presence of a barrier along the relaxation coordinate is a subject of debate in the literature. (b) Reaction coordinates g and h with vectors indicating the direction of motion of certain atoms within the thymine molecule (from ref. 37). These two vectors span the space for the conical intersection ππ*-nπ*. Both the predicted gradient and barrier depend sensitively on the *ab-initio* approach chosen.[38]

Time-resolved X-ray spectroscopy in isolated molecules can address several key scientific questions that will inform theoretical development:

What are the nuclear dynamics on photoexcited states?
Measuring changes in the nuclear geometry will determine the gradients on the photoexcited PES and provide important input to refine the accuracy of *ab-initio* methods dealing with electron correlation in different ways. Furthermore, for isomerization reactions, it provides important information on the reaction path and the PES shape towards the photoinduced isomer.

What are the electronic dynamics following light excitation?
Measuring the electronic dynamics after photoexcitation will allow us to address transient changes of electronic structure associated with non-BOA coupling. This will test the quality of different non-BOA simulation approaches from classical like surface hopping among adiabatic states[36] to more complex quantum full spawning[39] approaches.

What is the extent of the electronic wavefunction over the molecule?
The extend of an electronic wavefunction over the molecule is directly related to electron correlation.[40] Measuring it can help designing more sophisticated quantum chemistry methods.

Experiments on valence excited states are generally initiated by an optical pulse, with the exception of X-ray Raman excitation, discussed below. Ultrafast X-rays probe the evolution of nuclei and electrons of photoexcited molecules with element specificity and site selectivity provided by core-hole methods with detection via photoelectron, Auger electron, photo-ion, photo-absorption and -emission spectroscopies. LCLS II with its high repetition rate will enable completely new routes for dilute gas phase targets such photoemission and multi-particle correlation spectroscopy.

X-ray pulses with moderate peak power and high average power at high repetition from LCLS II are particularly well suited for photoemission spectroscopy in low pressure samples of isolated molecules – where the challenging combination of linear probe interaction and high counts rates are required. **Molecular reaction microscopes** utilize multi-particle coincidence (MPC) techniques which detect the simultaneous arrival of several photo-ions or electrons or even both emerging from a *single* molecule in

the interaction region. This tight constraint absolutely requires a high repetition rate source and up to now *static* versions of these measurements are successfully performed at synchrotrons. Implementation of MPC together with an optical pulse will lead to detailed information on the *dynamics* of the photoexcited state. Multi-photo-ion coincidence measures the momentum of molecular fragments, from which molecular isomerization pathways can be deduced. Applied to the ring opening of cyclohexadiene performed without coincidence at the LCLS,[41] a much more detailed picture of the nuclear rearrangements and gradients of the photoexcited state follows. MPC of ions and electrons offers the opportunity of photoelectron imaging in the molecular frame as suggested by Krasniqi et al.,[42] providing a complementary rout to probe nuclear dynamics.

Nonlinear, time resolved X-ray methods have been pioneered by recent theoretical development[43] as discussed in Section 3, and offer powerful approaches to probe valence charge distributions and correlations over a molecule. Stimulated X-ray Raman scattering (SXRS) creates coherent superposition of valence electronic states (electronic wavepacket) localized on a specific atomic site, via impulsive resonant X-ray excitation. The evolution of this wavepacket throughout the molecule may be probed (e.g. at another atomic site) by a time-delayed X-ray pulse. Core-hole correlation spectroscopy is a wave-mixing scheme that is sensitive to valence charge correlations between different atomic sites on a molecule. Both of these provide information about the spatial extent of electronic wavefunctions through the molecule, for instance by transient shifts in core photoelectron lines. The spatial shape of wavefunctions is a sensitive probe of electron interactions as comparative approaches between mean field and highly correlated methods show (see ref. 40 and references therein).

Light induced chirality

Handedness or chirality is an important property of molecules, determining their biological function. For example, the right handed form of the amino acid penicillamine presents a cure for rheumatoid arthritis and heavy metal intoxications, while the left handed enantiomer is poisonous. The pharmaceutical industry invests billions of dollars each year in drug control and discovery where chirality can determine the benefit versus toxicity of a compound. The 2001 Nobel Prize in chemistry was awarded for the production of single enantiomer drugs and chemicals.[44] *Where does life on earth come from and why does nature choose to build it with a certain handedness?*[45] It remains unclear how the racemic balance of enantiomers (equal quantities of the right- and left-handed versions a molecule) breaks down, and how one enantiomers almost completely dominates in nature.[46, 47]

LCLS-II offers an important opportunity to advance our understanding of chirality by steering the handedness in which a molecule emerges as a chiral object in the transient electronic excited state. Excited state dynamics allow even achiral molecules to show a handedness. Photoionized CO molecules exhibit strong chiral signals when a symmetry-braking coordinate frame is defined by the molecular axis, the angular momentum of the circular polarized photon, and the vector momentum of the photoelectron.[48] As another example, the planar and therefore achiral molecule HFCO turns into a chiral umbrella-like structure upon $n \rightarrow \pi^*$ excitation with an optical pulse.[25] Absorbed photon energy excites the electron into a new orbital, with the consequence that the nuclei have to adjust. With a certain time period (~10 ps) the molecule oscillates from left-handed to right-handed (i.e. the umbrella is oriented up or down respectively). The same tools which are used to investigate chirality (e.g. circular polarization) might also initiate the symmetry breaking from which chirality emerges.

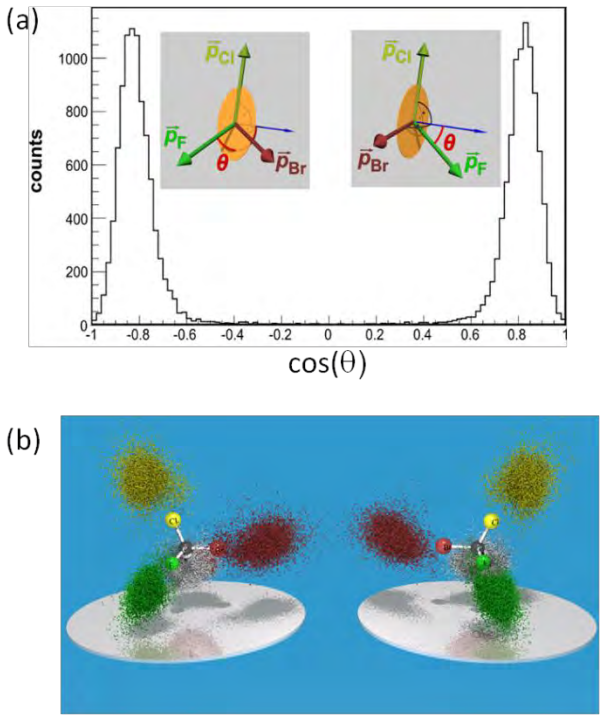

Figure 5: (a) Chirality angle cos(θ), defined by momentum vectors of three particles (see insets), separating the two enantiomers of racemic CHBrClF. (b) linear momentum distribution of right/left handed CHBrClF, (from ref. 49).

Understanding chirality requires sensitive tools for distinguishing different enantiomers. More than 100 years ago, circular dichroism (CD) was established. The probability for one enantiomer absorbing a right circular polarized (RCP) photon differs slightly from a photon with opposite helicity. The "conventional" CD signal is small (10^{-5}), but has the advantage of being insensitive to molecular orientations. Much stronger effects ($\sim 10^{-1}$) are observed in the ionization dynamics of molecules. Both the probability creating specific ionic fragments (breaking certain bonds) and even more important CD effects in the photoelectron angular distributions (PECD), have been subject of research only in the last 10 years. These new methods need additional theory input to relate the CD effects to the geometrical structure (right/left handed) of an unknown structure. A very interesting approach utilized the well-known technique of Coulomb Explosion Imaging. The molecule becomes multiple ionized, by absorption of a high energetic photon or a short laser pulse, and subsequently fragments into many charged particles. The momenta of all charged particles are then measured in coincidence. In Figure 5 the results for CHBrClF, the textbook example of a chiral molecule, are shown following absorption of a 710 eV photon.[49] Depending on the initial handedness of the molecule the cross product of three momentum vectors is either positive or negative. This relates to the absolute configuration of the molecule, whether it was right or left handed. LCLS-II offers a unique opportunity to apply these techniques to molecules in the electronic excited state, where control technique may be applied to influence the emergent chirality.

Charge-driven processes & dissociative electron attachment dynamics in polyatomic molecules

Excited electronic states play an important role in chemistry induced by low-energy electrons that result from the interaction of high energy photons or ionizing particles with organic matter. Resonant collisions between low-energy electrons and molecules can efficiently channel electronic energy into nuclear motion either though excitation of vibrational or dissociative modes. In dissociative electron attachment (DEA), an electron attaches to molecule to form a transient anion. The addition of this extra electron can disrupt the bonds that hold the molecule together, resulting in fragmentation. If the fragmentation time is shorter than the time it takes the electron to auto-detach, the collision can result in the formation of a stable negative ion plus neutral fragment(s). Because the time of attachment of the incident electron to the molecule cannot be established by conventional methods, there have never been experiments on DEA

analogous to the pump-probe experiments in photodissociation that directly probe the molecular dynamics.

DEA is an important process in gaseous electronics since the presence of an electron-attaching species in a low-temperature gaseous discharge leads to anion formation that can profoundly affect the properties of the discharge. DEA studies in the1970s and 1980s focused on measuring total cross sections.[50] A revival if interest in DEA came from the discovery that low energy electrons created from ionizing radiation trigger DNA strand breaks.[10] This led to the new focus on post-attachment dynamics of DEA, where modern momentum imaging techniques are used to characterize the angular distributions of the anion fragments, and theoretical calculations guide in the interpretation of the results.[51]

A recurring theme of DEA studies in polyatomic molecules over the past few years is the importance of conical intersections (seams of intersection) between excited negative ion states and the key role they play in channeling energy into specific anion fragment channels.[52, 53] The presence of conical intersections in excited-state photochemistry and their manipulation to alter branching ratios in a pump-probe framework is well established. Similar dynamical studies are, in principle, possible with transient anions produced by DEA, but the practical difficulties associated with producing short pulses of monoenergetic electrons has to date precluded time-dependent studies of DEA in a pump-probe context. In the case of transient negative ion states, the seams of intersecting surfaces may actually be located in the electronic continuum. The dynamics of dissociation take place on the time-scale of tens to hundreds of femtoseconds. Therefore, slow kinetic energy electron pulses of a few tens of femtoseconds would be needed for such experiments and this is not possible with conventional techniques.

LCLS-II provides an important opportunity to advance our understanding of non Born-Oppenheimer dynamics in charge-driven chemistry. Short pulses of monoenergetic electrons may be created by inner-shell photoionization of an inert gas atom using X-ray pulses tuned 2-8 eV above an inner-shell ionization threshold to produce photoelectrons in the appropriate energy range for DEA studies. To minimize space-charge and other detrimental collisional effects the target DEA molecules should be located as close as possible to the photoelectron source. This may be achieved by mixing the inert and target gases in a jet source. The combination of high rep-rate and ultrafast X-ray pulses provided by LCLS-II could thus be used to bring DEA experiments into the time domain.

In an experiment that produces the metastable molecular anion using an ultrafast X-ray pulse, the anion could be probed afterwards with a delayed, ultrashort UV pulse to photoexcite the anion and thus alter the course of the fragmentation to change the products. Such an experiment would effectively determine how long it takes the molecule to reach a conical intersection that controls the course of the dissociation. This type of experiment could be the first direct probe of DEA dynamics. Theoretical calculations of the molecular dynamics on the anion potential surface would be able to predict the time delay at which the probe pulse would find the system at the conical intersection or beyond it on a particular potential surface.

The angular distributions of anions produced in DEA can give insight into the nature of the dissociation dynamics following electron attachment. When the observed distributions differ markedly from the theoretical predictions of the axial recoil approximation, it signals a more complicated dynamics that can involve internal geometric changes of the initially formed transient anions or intersections with other anion states through conical intersections that can feed different product final states. Taking DEA studies into the time domain will provide a level of insight into anion dynamics that is not possible with current methods.

Molecular structure determination in the electronic excited state

Accurate determination of the transient nuclear geometries of molecules in the electronic excited states is still in its infancy. The higher X-ray photon energies, higher flux, and shorter pulses provided by

LCLS-II, will lead to many breakthroughs in the study of excited-state molecular dynamics using hard X-ray scattering.

One scientific frontier that the observation of structural dynamics will open is what, exactly, is the meaning of 'molecular structure'. The quantum description of a wave packet propagating on a potential energy surface during the reaction has associated with it a spatial shape, including maxima and minima. How is structure defined for such an object? Is it possible to image the intricate details of a wave packet? Can one follow different parts of the wave packet when it splits into components, for example at a conical intersection? How would one approach these questions from an experimental and from a theoretical point of view? And, finally, what can we learn about the molecules from the observation of such transient wave packets?

With the photon flux available from LCLS II it will be possible to investigate many chemical reaction systems. One particularly promising application is the structural dynamics associated with charge transfer reactions. A major open question is in the facilitation of charge transfer by conformational changes, particularly when the molecular backbone has multiple vibrational degrees of freedom. Further intriguing questions revolve around the breaking of symmetry in photochemical reactions, and about the opportunity inherent in the control of chemical reactions by differentially affecting the chemical reaction pathways. An experimental challenge is posed by the desire to observe, with ultrafast time resolution, the structural dynamics of bimolecular reactions: if it were possible to selectively observe those reacting partners that are at a particular point in their approach, then it might be possible to explore the dynamics of an additional large class of chemical reactions. Most likely, such an approach would require investigations at the single-particle level, a frontier that LCLS-II is uniquely suited to conquer.

Recent experiments from LCLS in 1,3, cyclohexadiene[54, 55] (as shown in Figure 6) provide an illustrative example – and a glimpse of what will be possible with LCLS-II. Cyclohexadiene is a model complex for understanding non Born-Oppenheimer processes, and is closely related to the photo-dynamics responsible for the formation of vitamin D. Ultrafast hard X-ray scattering studies at 8 keV followed changes in the scattering pattern on the few-percent level, at momentum-transfer of $\boldsymbol{q}$~4 Å^{-1}, over the course of the ring-opening. Already at this level, quantitative comparison with theoretical predictions is possible.

Hard X-ray pulses at 25 keV from LCLS-II will qualitatively change our ability to reveal ultrafast structural dynamics in a wide range of molecules, with potential momentum-transfer range exceeding 20 Å^{-1}. At this level, it will be possible to explore the structural changes immediately upon optical excitation. This will allow us to explore the very first steps of the electrocyclic reaction, during the brief moment in time where the pathways of the molecular motions determine the stereo-specificity of the reaction.[56] In spite of intense investigations spanning many decades, the processes taking place in this time range remain shrouded in mystery.[57]

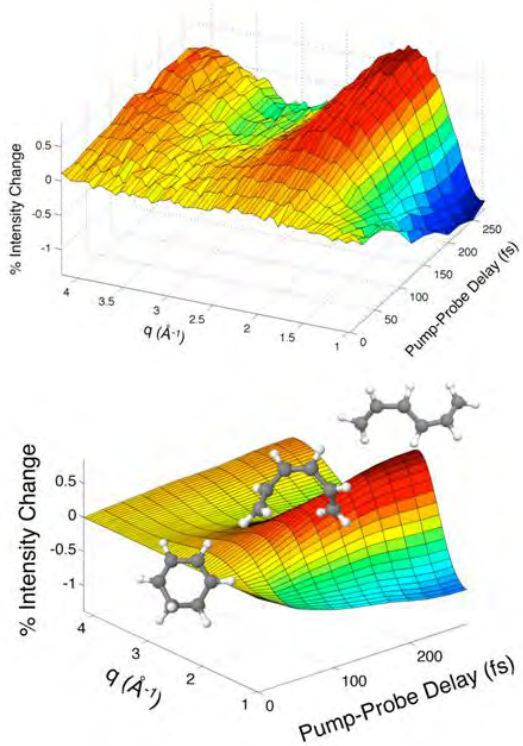

Figure 6: Molecular structure dynamics of photo-excited 1,3-cyclohexadiene using hard X-ray scattering. (Top) Experimentally measured time-dependent pump-probe signal, defined as the percent difference in scattering patterns as a function of pump-probe delay time. (Bottom) Optimized theoretical signal as a function of time and momentum transfer $\boldsymbol{q}$.[54, 55]

Colliding molecular beams – reactive scattering in the electronic ground state

The high repetition rate of LCLS-II enables a paradigm shift for the study of chemical transformations in the *electronic ground state* by enabling multi-dimensional stroboscopic X-ray imaging of chemical reactions that are not amenable to conventional pump-probe schemes. This unique approach holds the promise of directly characterizing the elusive transition-state between reactants and product for the first time.

The concept of "Femtosecond Serial X-ray Spectroscopy" combines the well-defined reaction conditions of crossed molecular beam experiments with the high fidelity of coincident imaging techniques to map chemical reaction pathways onto a multi-dimensional space of correlated observables. By stitching together thousands of femtosecond X-ray correlation spectra, a complete, femtosecond time-resolved map of the entire reaction pathway emerges. The technique bears conceptual similarities with, for example, serial X-ray crystallography and fluctuation scattering techniques, in which the statistical sampling of a sufficiently large ensemble of target orientations is employed to gain a complete real-space image of a particular specimen. The key difference, however, is that serial spectroscopy samples along the time axis, not along any spatial orientations, i.e., it uses high-repetition rate spectroscopic sampling to generate a *complete picture of chemical dynamics* along one or more reaction coordinates rather than a complete image of an object in real-space.

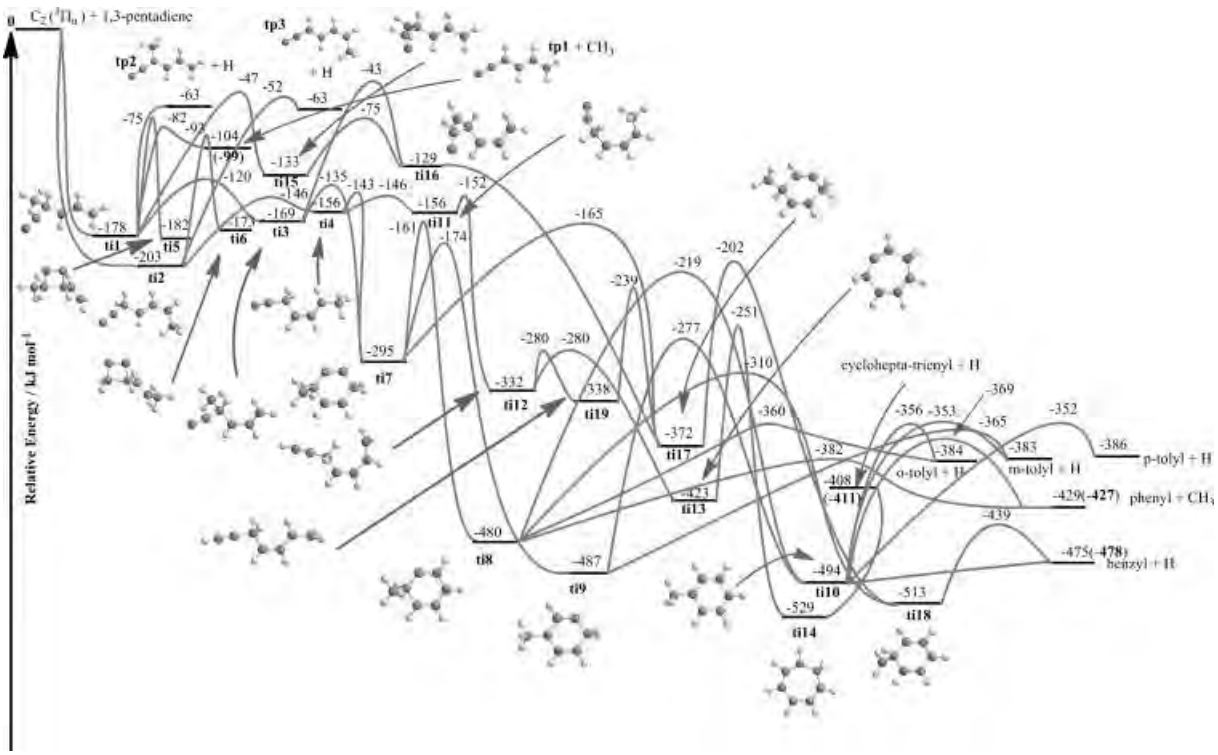

Figure 7: Calculated potential energy surface for the reaction of triplet dicarbon with 1,3-pentadiene. Intermediates are labeled as **ti** and products as **tp** along with the energies relative to the separated reactants in kJ/mol.[58] Femtosecond serial X-ray spectroscopy may provide the first universal tool to directly observe complex reaction dynamics that are currently only accessible to theoretical modeling.

Reactive scattering experiments have reshaped our understanding of chemical transformations by combining well-defined reaction conditions with sensitive product characterization techniques in order to provide the, so-far, most stringent tests for *ab initio* based descriptions of chemical reaction dynamics.[59] This approach has led to seminal advances in characterizing the impact of precursor kinetic[60] and internal[61] energies,[62] molecular orientation[63] and stereochemistry,[64, 65] spin-orbit states,[66] isomerism,[67] and isotopic constitution[68], as well as quantum pathway interferences[69] on chemical reactivity. However, virtually all reactive scattering studies are based on the fundamental concept that only the precursors and the reaction products are experimentally accessible, while the decisive moments and transient configurations that connect them (transition-states) remain largely inaccessible. The path from reactants to products has to be modeled by demanding theoretical calculations, resulting in a "black box" region of chemical dynamics studies that shrouds significant complexity even for moderately sized molecules, as illustrated by the potential energy surfaces for the reaction of triplet di-carbon with 1,3-pentadiene shown in Figure 7.

Since the advent of "femtochemistry",[70] one of the holy grails of the AMO community has been to "watch chemistry as it happens", i.e. to look inside the black box of chemical reactions. To date, however, the vast majority of ultrafast molecular dynamics studies have concentrated on unimolecular relaxation dynamics after photo-induced excitation. While pump-probe studies can sample transient molecular configurations on timescales reaching the attosecond regime, there is a much broader realm of chemical systems and dynamics that are not amenable to this approach. For example, only a few pioneering studies have managed to monitor dynamics associated with the *formation* of a chemical bond rather than a bond cleavage.[71-73]

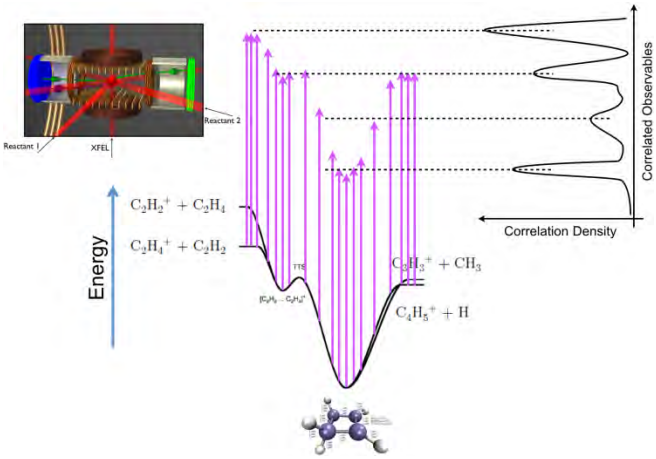

Figure 8: Concept of serial femtosecond X-ray spectroscopy. The temporal evolution of a chemical reaction is mapped onto a multi-dimensional phase space of correlated observables using a high-repetition rate FEL in combination with coincident imaging of reactive scattering events. (Showcase potential energy surface from Palm *et al.*[74])

A high repetition rate X-ray laser in combination with state-of-the-art momentum imaging techniques will be a powerful new tool to monitor chemical reactions on their most fundamental timescales and without the need for pump-probe schemes. Figure 8 illustrates the concept of femtosecond serial X-ray spectroscopy using the model potential energy surfaces of the reactive scattering between acetylene ions and ethylene. Two molecular beams containing the reactants collide at the interaction point of a reaction microscope.[75] X-ray pulses probe the interaction region with repetition rates up to 1 MHz, and resulting photoelectrons, fragment ions, and X-ray fluorescence are characterized by coincident momentum imaging in a similar fashion as in conventional synchrotron studies, with ~10^4 times enhancement in time resolution. The highly differential measurements provide a fingerprint of the transient molecular configuration(s) at the moment that the femtosecond X-ray pulse illuminates the sample. The probability with which a specific molecular configuration is detected scales inversely with the configuration's lifetime. The measurements, therefore, result in multi-dimensional correlation density maps that represent the population density distributions of transient species, i.e., their characters *and* the timescales the molecules reside in the specific configurations during the reaction.

Typical crossed molecular beam experiments can achieve collision frequencies in the range of 10^{13} per second.[76] The rate of reactive collisions can easily exceed 10^{10} per second,[59] corresponding to one reaction every 1,000 X-ray laser shots with ~100 fs pulse length. At a pulse repetition rate of 1 MHz, this corresponds to a pulse exposure rate of chemical reactions on the order of ~1 kHz. For a 10^{-2} coincidence detection efficiency, this results in a 10 Hz count rate, enabling the recording of correlation density maps with 10's of thousands of entries within an hour. This simple estimate clearly demonstrates that experiments of this kind are enabled only by X-ray lasers with pulse repetition rates ≥100 kHz.

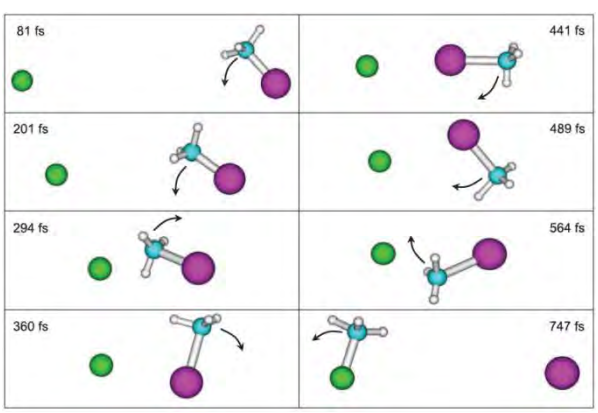

Figure 9: Simulated trajectory for the indirect roundabout reaction mechanism of Cl^- and CH_3I that proceeds via CH_3 rotation.[77]

Figure 9 depicts an interesting candidate for a femtosecond serial X-ray spectroscopy study. A gas-phase crossed molecular beam imaging study by Wester and co-workers[77] demonstrated that the classic nucleophilic substitution reaction $Cl^- + CH_3I \rightarrow CH_3Cl + I^-$ is more complex than previously assumed. Based on trajectory simulations (Figure 9), the group argued that, in addition to the expected direct substitution, an indirect "roundabout" reaction mechanism contributes at high collision energies. In this reaction scheme, the incoming chlorine anion does not immediately attach to the backside of the CH_3I reaction partner but instead strikes its side (Figure 9, ~300 fs), inducing a molecular rotation around the heavy iodine atom. Only after a full rotation of the CH_3I reactant (~600-700 fs) does the Cl^- eventually attach to the back of the carbon atom and leads to the ejection of an I^- anion. The entire roundabout reaction mechanism proceeds within ~400 fs between the first collision and the departure of the iodine fragment. The simulations also indicated the existence of other roundabout variants with intermediate lifetimes on the order of 1-4 ps. No direct observation of this mechanism is feasible with conventional reactive scattering techniques. The technique outlined above would be a game changer, allowing to map all transient configurations with femtosecond precision and the fidelity of coincidence imaging that has already enabled the successful monitoring of electronic dynamics during the photo-induced dissociation of CH_3I at LCLS.[78]

Experimental Approaches and Impact of LCLS-II

Photoelectron, photoabsorption/emission and velocity map imaging at LCLS II

Probing photoinduced dynamics with X-rays has the clear advantage of high local sensitivity within the molecules. As mentioned above, the element and site selectivity due to the high binding energies of core electrons allow for this local sensitivity. The introduction of powerful femtosecond X-ray pulses at free electron lasers allowed for real first applications in ultrafast X-ray probing.

LCLS II will introduce the next major technical improvement. The facility will operate at repetition rates of several kHz up to 1 MHz, resulting in a high X-ray flux distributed over many more pulses compared to LCLS I. In addition, the high repetition rate will go hand-in-hand with a much higher stability of the source. We expect that the intensity, the spectral content as well as the temporal jitter with respect to an optical pump pulse will be much better than at a low repetition rate FEL.

Higher repetition rate and increased stability will have a profound impact on X-ray probe methods. Typically, one tries to avoid nonlinear effects in the probe process because those can alter the traces of molecular dynamics in the photoelectron/photoemission or photoabsorption spectra. In addition, for photoelectron and Auger measurements, too many X-ray probe photons per pulse will induce space charge in the interaction region, which leads to rather unpredictable shifts in the electron kinetic energies. Distributing X-ray probe photons over a larger number of pulses by increasing the repetition rate therefore has the advantage of avoiding nonlinear and space charge effects. At low repetition rate sources, the flux per pulse needs to be attenuated, whereas all photons can be used at a higher repetition rate source with the same average flux. Experiments will benefit from this in terms of signal-to-noise ratio and overall time needed to acquire pump-probe spectra.

While improving the experimental features for photoabsorption and photoelectron measurements, LCLS II will enable photoemission measurements in the gas phase, which so far has not been possible. For typical emission spectrometer setups with an angular efficiency of 10^{-5} and an emission yield in the soft X-ray of 10^{-3}, one can estimate that one needs 10^{14} photons in the X-ray domain to detect one emission photon in a typical (10^{14} molecules/cm^3) gas phase target. These 10^{14} photons need to be delivered without inducing nonlinear effects and only at repetition rates above 100 kHz.

The increased stability of LCLS II will benefit any type of X-ray probe. For absorption and photoelectron spectroscopy, spectral jitter is a clear issue at LCLS, resulting in an inefficient use of photons when

combined with a monochromator. With higher spectral stability, spectra will be collected much faster, or with much higher accuracy over similar measurement times. In the long run it will be very attractive to reduce any jitter such that one can avoid the complications of single shot diagnostics and analysis. LCLS-II has the potential to be used in a similar way as a normal laboratory-based high repetition laser source where averaging and lock-in detection are powerful data-acquisition techniques.

A COLTRIMS dynamic molecular reaction microscope at LCLS II

The key challenge of atomic physics, cluster physics and physical chemistry today lies in the multi-particle nature of these systems. The properties and dynamics of these systems, their interaction with the environment and their interaction with light cannot be understood without treating the correlations between the electrons and between the electrons and the nuclei explicitly.

The unique intensities, photon energies and pulse structure of LCLS-II allows breaking such systems apart by single or multiple photoionization followed by Auger cascades and ionic fragmentation even in a time controlled manner. This power of LCLS-II as a tool to drive multiple ionization together with the grand challenge outlined above call for a combination of LCLS-II with a state-of-the-art spectrometer as, illustrated in Figure 10, that detects not only one of the many fragments or scattered particles (like traditional electron spectroscopy or X-ray scattering) but completely traces the correlations between all fragments (ions and electrons) from each individual molecule or cluster in coincidence. The X-ray and laser driven fragmentation of a molecule by photons preserves all the entanglement between the particles in the bound state or in a time evolving transition state and transfers it in a coherent way into the continuum, where it can be measured with the coincidence technique proposed here.

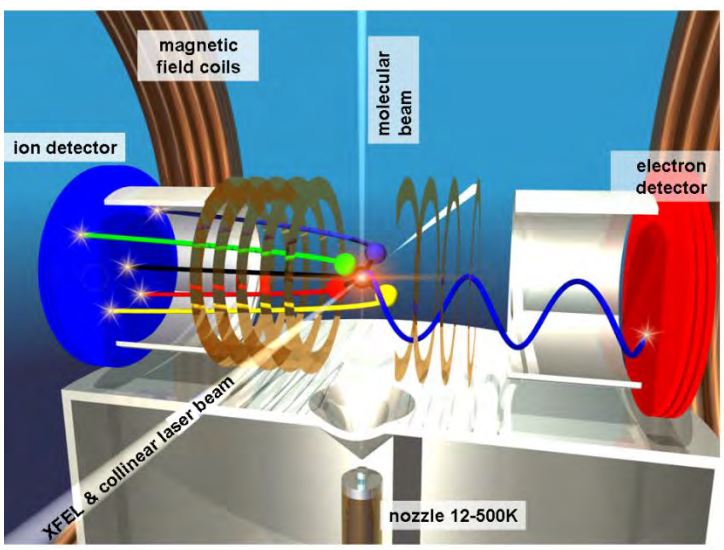

Figure 10: Artist view of a COLd Target Recoil Ion Momentum Spectroscopy (COLTRIMS) setup. Only one molecule is ionized in one particular LCLS II pulse. The ion and electron momenta are fully characterized in coincidence.

Dynamic Molecular Reaction Microscope - Selected Examples:

Time resolved photoelectron diffraction in fixed in space molecules

Photoelectrons emitted from well localized inner shells are ideal for "illuminating molecules from within".[79] The photoelectron wave launched at a specific site in the molecule is diffracted in the actual molecular structure at the instant of photo absorption. To record such diffraction patterns, the electrons need to be detected in coincidence with the fragment ions. This multiple coincidence allows fixing the gas phase molecule in space by analyzing the emission direction of the fragment ions. Figure 11 shows a recent non-time resolved example. The C K-shell photoelectrons emitted from methane clearly reflect the positions of the H atoms in the molecular reference frame.

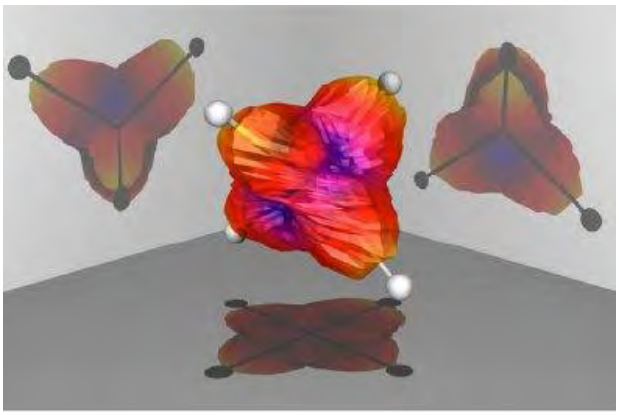

Figure 11: Photoelectron emission from Carbon K-shell of methane.[80]

This technique can be taken to the time domain by pumping the molecule with the tunable optical laser system provided at the end station. Such pump-probe experiments become feasible only since the intensity of the LCLS-II in its very small focus is sufficient to saturate the probe step.

Multiphoton inner-shell processes

Nonlinear X-ray physics can be addressed with this instrument in an unprecedented manner. For atomic inner-shell processes the ion recoil momentum for each charge state carries the information about the sequence of ionization steps. The combined information on the angular distribution of the different charge-state ions together with the corresponding distribution of the photoelectrons will allow unraveling the angular momentum coupling of the photons.

Multiple inner-shell ionization

Molecules that contain several atoms of one species can be K-shell ionized multiple times by several one-photon absorption processes during the same X-ray pulse. The energetics and dynamics of such multiple core holes distributed on different sites are highly sensitive to the chemical environment. A COLTRIMS Reaction Microscope allows for measuring the energy and angular distribution of all the photoelectrons from the different sites in the body-fixed frame of the molecule. In addition, the Auger electrons can be measured. Their energy, together with the kinetic energy release (KER) of heavy fragments, can be used to pin down the initial and final states of the fragmentation pathways for a given photoelectron angular distribution. It is particularly interesting to have the LCLS-II beam split into two time-delayed pulses. As the K-shell holes decay on a few femtosecond timescale, the electrons from the time delayed probe pulse will reflect the evolution of the energy levels and molecular dynamics. Electronic relaxation and bond breaking taking place in such an X-ray pump/X-ray probe scheme can be traced through the angular and energy distribution of the photoelectrons. Obtaining significant statistics for this kind of experiment, while maintaining the proper correlation and identification of all the fragments and electrons resulting from a single molecular explosion, will only become feasible with the introduction of LCLS-II high repetition rates.

X-ray driven ultrafast molecular dynamics

The X-rays can be used to excite inner-shell electrons to empty orbitals in a molecule. These excited states can be highly repulsive and ultrafast dissociation sets in before the system can undergo Auger decay. This process can be studied for the first time in the time domain by using two identical (or even different "color") X-ray pulses with varying time delay.

X-ray pump - laser probe studies

LCLS-II X-ray pulses can be used to selectively excite a K-shell electron from a well-defined site in a molecule to a bound empty orbital. This pump step initiates molecular and electronic dynamics. In some cases this step will even induce chirality in a system where the ground state is non chiral. A circularly

polarized pulse of the femtosecond optical laser can then be used to peel off electrons from the excited orbital by tunnel ionization. Such strong field tunnel ionization maps the orbital to the detector where its time and spatial evolution can be measure in coincidence with the ionic fragments and the Auger electrons. The targets to be irradiated are single atoms, molecules or clusters in a supersonic gas beam. Examples include simple diatomic gases like N_2 or CO, rare gas and molecular clusters, hydrocarbons, benzene and azobenzene, small chiral molecules, water in the gas phase and small water clusters. Figure 5 shows the chiral CHClBrF as an example.

Experiments with molecular/cluster ions will especially benefit from the progress in COLTRIMS at LCLS-II, since the sample is typically delivered at a very low number density (around 1e6 molecules/cm^3). Synchrotron experiments show that the high repetition rate provides ideal conditions to study the electronic ground state of these systems.[81] Excited state phenomena like non-linear absorption of anion systems which as well as their ultrafast dynamics after XUV or X-ray excitation will be studied using the high repetition rate at LCLS II.

Transient molecular structure determination

The determination of the nuclear geometry in photo-excited states is still in its infancy. Technical challenges persist on several fronts. Foremost among them is the limited range of scattering angles that can be accessed with the currently available fundamental beam of LCLS (the third harmonic is yet too weak to perform the experiment). With fundamental energies reaching 25 keV, LCLS II will extend the range of diffraction angles by a factor ~3. Coupled with sample cell and detector geometries that more fully detect the radiation scattered into all angles, this may allow us to reach momentum transfer values up to 20 Å^{-1}, sufficient for highly accurate structure determination and detailed comparison with theory.

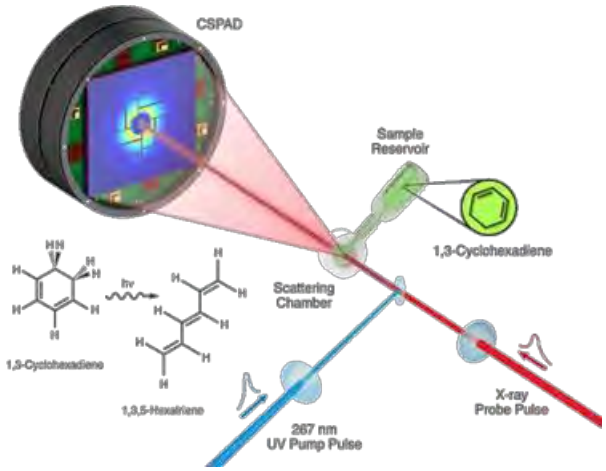

Figure 12: Experimental arrangement for the measurement of molecular photo-excited dynamics using hard X-ray scattering: A laser pulse excites the gas phase molecular sample, here 1,3-cyclohexadiene, to an electronically excited state from where the reaction proceeds. After an adjustable delay time, an X-ray probe pulse is scattered off the molecular sample, giving a diffraction pattern that encodes the transient molecular structure.[54,55]

A systematic problem with past experiments has been the unavailability of an experimentally determined time zero: immediately upon excitation, the molecular structure has not changed. Consequently, there is no signature of time zero in the diffraction image. LCLS II will enable us to make inroads on this problem, as the higher time-averaged photon flux will permit the mapping of the electronic excitation: the electron motions are sufficiently fast to serve as a start signal for the clock of molecular structural dynamics.

Recently, ultrafast electron diffraction[82-85] has emerged as a strong contender to probe real-time molecular structural dynamics. Electron scattering/diffraction techniques have unique benefits for structural studies: offering increased scattering cross sections and easily attainable wide-angle (>30 Å^{-1}) momentum-transfer range. However, sufficiently intense (in terms of electrons/pulse) electron beams are extremely hard to generate and the overall time resolution these beam can achieve are ultimately limited by space charge

effects. Using relativistic electron energies, it may even be possible to achieve time resolutions that approach those offered by the LCLS X-ray source,[86] although an experimental implementation of MeV electrons in a gas diffraction experiment remains outstanding. The major problem of electron diffraction, assuming sufficiently intense electron beams can be generated, is that the Rutherford scattering cross section that governs electron diffraction[87] scales as $1/q^4$, requiring dramatic sensitivity to discern differential changes in scattering intensities at momentum-transfer up to 20 $Å^{-1}$.

References

1. S. Lünnemann, A. I. Kuleff, and L. S. Cederbaum, "Ultrafast charge migration in 2-phenylethyl-N,N-dimethylamine," Chem. Phys. Lett. **450**, 232 (2008).
2. J. D. Biggs, Y. Zhang, D. Healion, and S. Mukamel, "Watching energy transfer in metalloporphyrin heterodimers using stimulated X-ray Raman spectroscopy," Proceedings of the National Academy of Sciences **110**, 15597 (2013).
3. L. Young, E. P. Kanter, B. Krässig, Y. Li, A. M. March, S. T. Pratt, et al., "Femtosecond electronic response of atoms to ultra-intense X-rays," Nature **466**, 56 (2010).
4. B. Rudek, S.-K. Son, L. Foucar, S. W. Epp, B. Erk, R. Hartmann, et al., "Ultra-efficient ionization of heavy atoms by intense X-ray free-electron laser pulses," Nat Photon **6**, 858 (2012).
5. B. F. Murphy, T. Osipov, Z. Jurek, L. Fang, S. K. Son, M. Mucke, et al., "Femtosecond X-ray-induced explosion of C_{60} at extreme intensity," Nat Commun **5**, 4281 (2014).
6. N. Timneanu, B. Iwan, J. Andreasson, M. Bergh, M. Seibert, C. Bostedt, et al., "Fragmentation of clusters and recombination induced by intense and ultrashort X-ray laser pulses," Proc. SPIE, Int. Soc. Opt. Eng. **8777**, 87770J (9 pp.) (2013).
7. B. Erk, D. Rolles, L. Foucar, B. Rudek, S. W. Epp, M. Cryle, et al., "Ultrafast Charge Rearrangement and Nuclear Dynamics upon Inner-Shell Multiple Ionization of Small Polyatomic Molecules," Physical Review Letters **110**, 053003 (2013).
8. C. Bacellar, A. Chatterley, J. Cryan, M. Ziemkiewicz, O. Gessner, C. Bernando, et al., "X-ray pump / X-ray probe femtosecond coherent diffractive imaging of electron dynamics in pristine and embedded xenon clusters," in *45th Annual Meeting of the APS Division of Atomic, Molecular and Optical Physics*(Madison, WI, 2014), p. Abstract: T7.00002.
9. J. Rosenzweig, G. Andonian, A. Fukasawa, E. Hemsing, G. Marcus, A. Marinelli, et al., "Breaking the Attosecond, Angstrom and TV/m Field Barriers with Ultra-fast Electron Beams," Conf.Proc. **C100523**, THPEC015 (2010).
10. B. Boudaiffa, P. Cloutier, D. Hunting, M. A. Huels, and L. Sanche, "Resonant formation of DNA strand breaks by low-energy (3 to 20 eV) electrons," Science **287**, 1658 (2000).
11. *Photochromism: molecules and systems* (Elsevier, Amsterdam ; Boston, 2003).
12. M. Alemani, M. V. Peters, S. Hecht, K.-H. Rieder, F. Moresco, and L. Grill, "Electric Field-Induced Isomerization of Azobenzene by STM," J. Am. Chem. Soc. **128**, 14446 (2006).
13. M. Comstock, N. Levy, A. Kirakosian, J. Cho, F. Lauterwasser, J. Harvey, et al., "Reversible Photomechanical Switching of Individual Engineered Molecules at a Metallic Surface," Phys. Rev. Lett. **99** (2007).
14. R. J. Sension, S. T. Repinec, A. Z. Szarka, and R. M. Hochstrasser, "Femtosecond laser studies of the cis-stilbene photoisomerization reactions," The Journal of Chemical Physics **98** (1993).
15. D. H. Waldeck, "Photoisomerization dynamics of stilbenes," Chem. Rev. **91**, 415 (1991).
16. D. Polli, P. Altoè, O. Weingart, K. M. Spillane, C. Manzoni, D. Brida, et al., "Conical intersection dynamics of the primary photoisomerization event in vision," Nature **467**, 440 (2010).
17. Q. Wang, L. A. Peteanu, R. W. Schoenlein, R. A. Mathies, and C. V. Shank, "Vibrationally coherent photochemistry in the femtosecond primary event of vision," Science **266**, 422 (1994).
18. R. Schoenlein, L. Peteanu, R. Mathies, and C. Shank, "The first step in vision: femtosecond isomerization of rhodopsin," Science **254**, 412 (1991).
19. R. Mathies, C. Brito Cruz, W. Pollard, and C. Shank, "Direct observation of the femtosecond excited-state cis-trans isomerization in bacteriorhodopsin," Science **240**, 777 (1988).
20. S. Schenkl, F. van Mourik, G. van der Zwan, S. Haacke, and M. Chergui, "Probing the Ultrafast Charge Translocation of Photoexcited Retinal in Bacteriorhodopsin," Science **309**, 917 (2005).

21. G. Groenhof, M. Bouxin-Cademartory, B. Hess, S. P. de Visser, H. J. C. Berendsen, M. Olivucci, et al., "Photoactivation of the Photoactive Yellow Protein: Why Photon Absorption Triggers a Trans-to-Cis Isomerization of the Chromophore in the Protein," J. Am. Chem. Soc. **126**, 4228 (2004).
22. C. T. Middleton, K. de La Harpe, C. Su, Y. K. Law, C. E. Crespo-Hernández, and B. Kohler, "DNA Excited-State Dynamics: From Single Bases to the Double Helix," Annu. Rev. Phys. Chem. **60**, 217 (2009).
23. C. E. Crespo-Hernández, B. Cohen, P. M. Hare, and B. Kohler, "Ultrafast Excited-State Dynamics in Nucleic Acids," Chem. Rev. **104**, 1977 (2004).
24. W. J. Schreier, T. E. Schrader, F. O. Koller, P. Gilch, C. E. Crespo-Hernandez, V. N. Swaminathan, et al., "Thymine Dimerization in DNA Is an Ultrafast Photoreaction," Science **315**, 625 (2007).
25. R. Berger, "Molecular parity violation in electronically excited states," PCCP **5**, 12 (2003).
26. M. Born, and R. Oppenheimer, "Zur Quantentheorie der Molekeln," Annalen der Physik **389**, 457 (1927).
27. H. Köppel, W. Domcke, and L. S. Cederbaum, "Multimode MolecularDynamics Beyond the Born-Oppenheimer Approximation," Advances in Chemical Physics **57**, 59 (1984).
28. G. Herzberg, *Molecular Spectra and Molecular Structure: Infrared and Raman spectra of polyatomic molecules* (R.E. Krieger Pub. Co., 1991).
29. D. Yarkony, "Diabolical conical intersections," Reviews of Modern Physics **68**, 985 (1996).
30. E. Teller, "The Crossing of Potential Surfaces," The Journal of Physical Chemistry **41**, 109 (1937).
31. W. Domcke, D. Yarkony, and H. Köppel, eds. *Conical intersections electronic structure, dynamics & spectroscopy. World Scientific, River Edge, N.J.; London* (World Scientific, River Edge, N.J.; London, 2004).
32. B. G. Levine, and T. J. Martínez, "Isomerization Through Conical Intersections," Annu. Rev. Phys. Chem. **58**, 613 (2007).
33. G. J. Atchity, S. S. Xantheas, and K. Ruedenberg, "Potential energy surfaces near intersections," The Journal of Chemical Physics **95** (1991).
34. T. J. Martínez, "Physical chemistry: Seaming is believing," Nature **467**, 412 (2010).
35. F. Plasser, M. Barbatti, A. A. Aquino, and H. Lischka, "Electronically excited states and photodynamics: a continuing challenge," Theoretical Chemistry Accounts **131**, 1 (2012).
36. J. C. Tully, "Perspective: Nonadiabatic dynamics theory," The Journal of Chemical Physics **137**, 22A301 (2012).
37. J. J. Szymczak, M. Barbatti, J. T. Soo Hoo, J. A. Adkins, T. L. Windus, D. Nachtigallová, et al., "Photodynamics Simulations of Thymine: Relaxation into the First Excited Singlet State," The Journal of Physical Chemistry A **113**, 12686 (2009).
38. H. R. Hudock, B. G. Levine, A. L. Thompson, H. Satzger, D. Townsend, N. Gador, et al., "Ab Initio Molecular Dynamics and Time-Resolved Photoelectron Spectroscopy of Electronically Excited Uracil and Thymine," The Journal of Physical Chemistry A **111**, 8500 (2007).
39. M. Ben-Nun, J. Quenneville, and T. J. Martínez, "Ab Initio Multiple Spawning: Photochemistry from First Principles Quantum Molecular Dynamics," The Journal of Physical Chemistry A **104**, 5161 (2000).
40. A. I. Kuleff, S. Lünnemann, and L. S. Cederbaum, "Ultrafast reorganization of the hole charge created upon outer-valence ionization of porphyrins," Chem. Phys. **399**, 245 (2012).
41. V. S. Petrovic, M. Siano, J. L. White, N. Berrah, C. Bostedt, J. D. Bozek, et al., "Transient X-Ray Fragmentation: Probing a Prototypical Photoinduced Ring Opening," Phys. Rev. Lett. **108** (2012).
42. F. Krasniqi, B. Najjari, L. Strueder, D. Rolles, A. Voitkiv, and J. Ullrich, "Imaging molecules from within: Ultrafast angstrom-scale structure determination of molecules via photoelectron holography using free-electron lasers," Phys. Rev. A **81** (2010).
43. S. Mukamel, D. Abramavicius, L. Yang, W. Zhuang, I. V. Schweigert, and D. V. Voronine, "Coherent Multidimensional Optical Probes for Electron Correlations and Exciton Dynamics: From NMR to X-rays," Acc. Chem. Res. **42**, 553 (2009).
44. K. B. Sharpless, "Searching for New Reactivity (Nobel Lecture) Copyright© The Nobel Foundation 2002. Adapted with the permission of the editors from "Coelacanths and Catalysis": K. B. Sharpless, Tetrahedron 1994, 50, 4235," Angewandte Chemie International Edition **41** (2002).
45. J. S. Siegel, "Homochiral imperative of molecular evolution," Chirality **10**, 24 (1998).
46. J. Bailey, "Circular Polarization in Star- Formation Regions: Implications for Biomolecular Homochirality," Science **281**, 672 (1998).
47. E. Rubenstein, W. A. Bonner, H. P. Noyes, and G. S. Brown, "Supernovae and life," Nature **306**, 118 (1983).

48. T. Jahnke, T. Weber, A. L. Landers, A. Knapp, S. Schossler, J. Nickles, et al., "Circular dichroism in K-shell ionization from fixed-in-space CO and N-2 molecules," Phys. Rev. Lett. **88**, 073002 (2002).
49. M. Pitzer, M. Kunitski, A. S. Johnson, T. Jahnke, H. Sann, F. Sturm, et al., "Direct Determination of Absolute Molecular Stereochemistry in Gas Phase by Coulomb Explosion Imaging," Science **341**, 1096 (2013).
50. L. G. Christophorou, and J. K. Olthoff, *Fundamental Electron Interactions with Plasma Processing Gases* (Springer US, Boston, MA, 2004).
51. H. Adaniya, B. Rudek, T. Osipov, D. J. Haxton, T. Weber, T. N. Rescigno, et al., "Imaging the Molecular Dynamics of Dissociative Electron Attachment to Water," Phys. Rev. Lett. **103** (2009).
52. D. J. Haxton, H. Adaniya, D. S. Slaughter, B. Rudek, T. Osipov, T. Weber, et al., "Observation of the dynamics leading to a conical intersection in dissociative electron attachment to water," Phys. Rev. A **84** (2011).
53. A. Moradmand, D. S. Slaughter, D. J. Haxton, T. N. Rescigno, C. W. McCurdy, T. Weber, et al., "Dissociative electron attachment to carbon dioxide via the $^2\Pi_u$ shape resonance," Phys. Rev. A **88** (2013).
54. M. P. Minitti, J. M. Budarz, A. Kirrander, J. S. Robinson, D. Ratner, T. J. Lane, et al., "Imaging Molecular Motion: Femtosecond X-Ray Scattering of the Ring Opening in 1,3- Cyclohexadiene," Phys. Rev. Lett., in press (2015).
55. M. P. Minitti, J. M. Budarz, A. Kirrander, J. Robinson, T. J. Lane, D. Ratner, et al., "Toward structural femtosecond chemical dynamics: imaging chemistry in space and time," Faraday Discuss. **171**, 81 (2014).
56. R. B. Woodward, and R. Hoffmann, "The Conservation of Orbital Symmetry," Angewandte Chemie International Edition in English **8**, 781 (1969).
57. S. Deb, and P. M. Weber, "The Ultrafast Pathway of Photon-Induced Electrocyclic Ring-Opening Reactions: The Case of 1,3-Cyclohexadiene," Annu. Rev. Phys. Chem. **62**, 19 (2011).
58. B. B. Dangi, D. S. N. Parker, R. I. Kaiser, D. Belisario-Lara, and A. M. Mebel, "An experimental and theoretical investigation of the formation of C_7H_7 isomers in the bimolecular reaction of dicarbon molecules with 1,3-pentadiene," Chem. Phys. Lett. **607**, 92 (2014).
59. Y. T. Lee, "Molecular Beam Studies of Elementary Chemical Processes (Nobel Lecture)," Angew. Chem. Int. Ed. Engl. **26**, 939 (1987).
60. T. N. Kitsopoulos, M. A. Buntine, D. P. Baldwin, R. N. Zare, and D. W. Chandler, "Reaction Product Imaging: The $H+D_2$ Reaction," Science **260**, 1605 (1993).
61. T. Wang, J. Chen, T. Yang, C. Xiao, Z. Sun, L. Huang, et al., "Dynamical Resonances Accessible Only by Reagent Vibrational Excitation in the F + HD→HF + D Reaction," Science **342**, 1499 (2013).
62. T. Turner, O. Dutuit, and Y. T. Lee, "The effects of collision energy and vibrational excitation on H^{+2}, HD^++He reactions," J. Chem. Phys. **81**, 3475 (1984).
63. D. H. Parker, K. K. Chakravorty, and R. B. Bernstein, "Reactive asymmetry of methyl iodide. The crossed-beam reaction of oriented methyl iodide with rubidium," J. Phys. Chem. **85**, 466 (1981).
64. F. Wang, J.-S. Lin, and K. Liu, "Steric Control of the Reaction of CH Stretch–Excited CHD_3 with Chlorine Atom," Science **331**, 900 (2011).
65. F. Wang, K. Liu, and T. P. Rakitzis, "Revealing the stereospecific chemistry of the reaction of Cl with aligned $CHD_3(v1 = 1)$," Nat Chem **4**, 636 (2012).
66. F. Dong, S.-H. Lee, and K. Liu, "Direct determination of the spin-orbit reactivity in $Cl(2p_{3/2},2p_{1/2})+H_2/D_2HD$ reactions," J. Chem. Phys. **115**, 1197 (2001).
67. Y.-P. Chang, K. Długołęcki, J. Küpper, D. Rösch, D. Wild, and S. Willitsch, "Specific Chemical Reactivities of Spatially Separated 3-Aminophenol Conformers with Cold Ca^+ Ions," Science **342**, 98 (2013).
68. Y. Ogi, H. Kohguchi, and T. Suzuki, "Deuterium isotope effects in the polyatomic reaction of $O(1D_2)+CH_4 \rightarrow OH+CH_3$," Phys. Chem. Chem. Phys. **15** (2013).
69. D. Dai, C. C. Wang, S. A. Harich, X. Wang, X. Yang, S. D. Chao, et al., "Interference of Quantized Transition-State Pathways in the $H+D_2 \rightarrow D+HD$ Chemical Reaction," Science **300**, 1730 (2003).
70. A. H. Zewail, "Femtochemistry: Atomic-scale dynamics of the chemical bond," J. Phys. Chem. A **104**, 5660 (2000).
71. N. F. Scherer, L. R. Khundkar, R. B. Bernstein, and A. H. Zewail, "Real-time picosecond clocking of the collision complex in a bimolecular reaction: The birth of OH from $H+CO_2$," J. Chem. Phys. **87**, 1451 (1987).
72. H. Öström, H. Öberg, H. Xin, J. LaRue, M. Beye, M. Dell'Angela, et al., "Probing the transition state region in catalytic CO oxidation on Ru," Science **347**, 978 (2015).

73. K. H. Kim, J. G. Kim, S. Nozawa, T. Sato, K. Y. Oang, T. W. Kim, et al., "Direct observation of bond formation in solution with femtosecond X-ray scattering," Nature **518**, 385 (2015).
74. H. Palm, C. Alcaraz, P. Millié, and O. Dutuit, "State-selected $C_2H_2^+ + C_2H_4$ reaction: Controlled by dynamics or statistics?," International Journal of Mass Spectrometry **249–250**, 31 (2006).
75. J. Ullrich, R. Moshammer, A. Dorn, R. D rner, L. P. H. Schmidt, and H. Schmidt-B cking, "Recoil-ion and electron momentum spectroscopy: reaction-microscopes," Rep. Prog. Phys. **66**, 1463 (2003).
76. M. S. Elioff, J. J. Valentini, and D. W. Chandler, "Subkelvin Cooling NO Molecules via "Billiard-like" Collisions with Argon," Science **302**, 1940 (2003).
77. J. Mikosch, S. Trippel, C. Eichhorn, R. Otto, U. Lourderaj, J. X. Zhang, et al., "Imaging Nucleophilic Substitution Dynamics," Science **319**, 183 (2008).
78. B. Erk, R. Boll, S. Trippel, D. Anielski, L. Foucar, B. Rudek, et al., "Imaging charge transfer in iodomethane upon x-ray photoabsorption," Science **345**, 288 (2014).
79. A. Landers, T. Weber, I. Ali, A. Cassimi, M. Hattass, O. Jagutzki, et al., "Photoelectron Diffraction Mapping: Molecules Illuminated from Within," Physical Review Letters **87**, 013002 (2001).
80. J. B. Williams, C. S. Trevisan, M. S. Schöffler, T. Jahnke, I. Bocharova, H. Kim, et al., "Imaging Polyatomic Molecules in Three Dimensions Using Molecular Frame Photoelectron Angular Distributions," Phys. Rev. Lett. **108**, 233002 (2012).
81. R. C. Bilodeau, N. D. Gibson, C. W. Walter, D. A. Esteves-Macaluso, S. Schippers, A. Müller, et al., "Single-Photon Multiple Detachment in Fullerene Negative Ions: Absolute Ionization Cross Sections and the Role of the Extra Electron," Physical Review Letters **111**, 043003 (2013).
82. R. C. Dudek, and P. M. Weber, "Ultrafast Diffraction Imaging of the Electrocyclic Ring-Opening Reaction of 1,3-Cyclohexadiene," The Journal of Physical Chemistry A **105**, 4167 (2001).
83. H. Ihee, V. A. Lobastov, U. M. Gomez, B. M. Goodson, R. Srinivasan, C. Y. Ruan, et al., "Direct imaging of transient molecular structures with ultrafast diffraction," Science **291**, 458 (2001).
84. C. J. Hensley, J. Yang, and M. Centurion, "Imaging of Isolated Molecules with Ultrafast Electron Pulses," Phys. Rev. Lett. **109** (2012).
85. R. J. D. Miller, "Femtosecond Crystallography with Ultrabright Electrons and X-rays: Capturing Chemistry in Action," Science **343**, 1108 (2014).
86. J. B. Hastings, F. M. Rudakov, D. H. Dowell, J. F. Schmerge, J. D. Cardoza, J. M. Castro, et al., "Ultrafast time-resolved electron diffraction with megavolt electron beams," Applied Physics Letters **89** (2006).
87. N. F. Mott, and H. S. W. Massey, *The theory of atomic collisions* (Clarendon Press ; Oxford University Press, Oxford [Oxfordshire]; New York, 1987).

2.1.3 Advanced combustion and aerosol chemistry

Combustion is now and will remain for many decades the most important means of energy utilization on earth. The enormous benefits of modern combustion technologies (e.g. reliable electricity, rapid transportation, heating and cooling etc.), are accompanied by negative consequences, such as the health effects of combustion particulates, photochemical smog, and anthropogenic climate change. It is increasingly important to utilize combustion with greater efficiency and fewer harmful impacts on the planet and its inhabitants. For example, in the transportation sector, new energy sources such as biomass-derived fuels offer an opportunity to optimize the fuel stream for new highly efficient engines, and to develop novel fuels that will help reduce greenhouse gas emissions and enhance national energy security. Climate change concerns create an urgent need for these solutions, reflected in the goal for 80% greenhouse gas emission reductions in the U.S. by 2050. Because of the inherent advantages, e.g., in transportability and energy density, of liquid hydrocarbons, it is likely that they will continue to be used as energy carriers via future energy technologies such as solar fuels. Accordingly, there is an increasing need for predictive models of engine combustion that are accurate from the scale of molecules and electrons through the macroscopic scale of engine cylinders.

The groundbreaking capabilities of LCLS-II will be instrumental to create the science base for predictive combustion models. With the promise of new detailed experiments, and the astonishing advances in computation, a concerted effort will be able to deliver truly rigorous science-based models of combustion, with genuine predictive power even for unexplored fuels and combustion strategies. Validating such models will entail ground-breaking experimental probes of combustion chemistry and physics, many of which could be realized with the high repetition rate, high average power, and coherent radiation promised by LCLS-II.

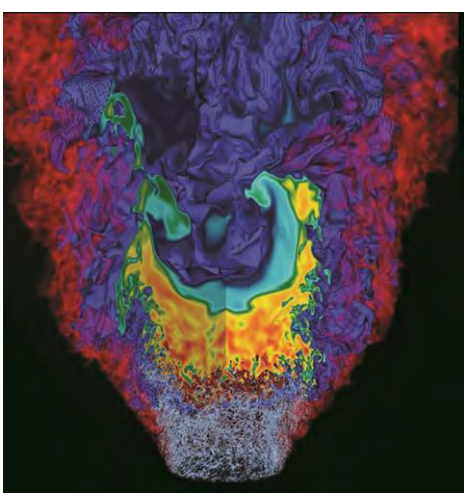

Figure 13. Illustration of the complexity of the combustion environment. Computer simulations of N_2O, NO, and OH species concentrations in a hydrogen flame (central radius ~2.5 cm).[1]

Challenges and Opportunities in Combustion Science

Because combustion relies on a complex interrelationship of chemistry and turbulent fluid mechanics, its processes exhibit inhomogeneities and correlations across a wide range of length and time scales as illustrated in Figure 13. The most powerful class of experimental methods for turbulent combustion is *dynamic imaging*, i.e. resolving the spatial and temporal distributions in a combustion process. Furthermore, because the coupling of chemical and fluid-dynamical phenomena lies at the heart of combustion's complexity, *chemically-specific* imaging is key for combustion investigations. LCLS-II X-ray lasers will image the fundamental chemistry and physics that govern the entire process of combustion, from fuel sprays to gas-phase combustion to particulate formation and evolution. The following presents

three critical areas in combustion science (fuel sprays, turbulent reacting flows, and particulate formation and oxidation) where these breakthrough capabilities can address problems that remain difficult or impossible to solve with other techniques. Finally, we discuss how the characteristics of LCLS-II will provide unprecedented new experimental capabilities to address these challenges.

Chemistry and Physics of Fuel Sprays

Combustion engines are undergoing radical changes, brought on largely by new scientific and technological discoveries using laser diagnostics. It is clear that most emerging engine technologies will use direct injection of liquid fuel into the combustion chamber. It is imperative to understand the entire spray, how it breaks up, mixes, vaporizes and burns, in order to develop fully predictive models for engine combustion. Although these processes control combustion efficiency and emissions formation in every type of direct-injected engine, they remain poorly understood, even at the level of fundamental fluid mechanics. Furthermore, many potentially important couplings of the spray fluid mechanics and chemical environment have simply not been explored. In order to make further progress, significant leaps are required.

As a simple example, it is speculated that under normal diesel engine operating conditions, a small fuel-rich flame is stabilized just downstream of the liquid jet, leading to soot formation at the tip of the flame[2]. However, in this region, the fuel/air ratio and the existence of a flame have never been measured. Furthermore, under very high levels of exhaust gas recirculation (EGR, used to lower NO production) this region of the spray appears to be completely changed, especially as it evolves downstream[3]. Again, the fuel/air ratio is unknown, as is the chemical effect of EGR entrainment, or the differing effects of fuel-bound or free oxygen. Exploring these issues demands information about the interior of sprays, with chemical detail never before available. Finally, the performance of injection, as for many aspects of engine combustion, is often governed by stochastic processes and statistically unlikely adverse events, such as wall or piston wetting, making temporal and spatial resolution important. In the combusting spray the chemical bonding environment of carbon, for example, moves from liquid fuel to vaporized fuel through the combustion process to carbon monoxide, carbon dioxide, or to particulate carbon (soot). Correlation of these chemical transformations with the physics of the spray will be a tremendous breakthrough that will become possible with LCLS-II.

Probing the mass transport, differential evaporation, and oxidative chemistry of fuel flows at the high pressures (~30 atm) and temperatures (~1000K) that are directly relevant to high-efficiency/low-pollution next generation engine designs is extremely challenging. Light scattering in a dense spray can confound optical methods, requiring strategies such as ultrafast ballistic imaging[4, 5] and X-ray absorption[6] to probe the critical spray formation region, where the liquid core initially breaks up. In fact, even with the current state of the art, spatial and temporal imaging of the fluid structures is at best incomplete. Imaging the interior of the spray with chemical specificity within is essentially impossible at present.

The revolutionary capabilities of LCLS-II present a very promising route to meet these challenges. The potential for time-resolved chemically-specific tomography of turbulent gas-phase reacting flows is discussed below (and in section 3.3). At the densities of an evaporating high-momentum fuel jet, transmission imaging near the carbon or oxygen K-edges is simply impossible because of the small penetration depths. Nevertheless, for fundamental fluid dynamics, single-pulse direct absorption tomography in the 2-3 keV region could permit unprecedented resolution of transient three-dimensional liquid structures with separation of droplet and liquid core features.

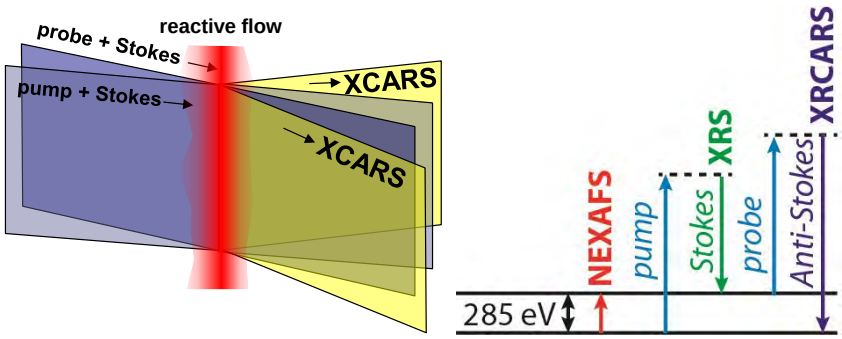

Figure 14. X-ray CARS diagram for chemically specific line imaging. Pump and probe photon energies are degenerate (k_p) and are co-linear with the Stokes pulses (k_S), thus generating two signals via SXRS ($k_{XCARS}=2k_p-k_S$).

The truly transformational aspects of LCLS-II, however, are in the ability to *chemically* resolve spatio-temporal structures. The coupling of the chemical nature of multiphase reacting flows with the fluid mechanics is largely unexplored. In principle, X-ray Raman scattering can provide similar chemical information to near-edge absorption spectroscopy, but cross sections for spontaneous Raman scattering are low. Here, the high power, coherence, and narrow bandwidth of LCLS-II X-ray pulses will enable stimulated X-ray Raman spectroscopies (SXRS)[7] that can bring many orders of magnitude increase in efficiency over spontaneous Raman. X-ray coherent anti-Stokes Raman spectroscopy (XCARS), as a version of SXRS, for example, along a line-imaging geometry[8] as shown in Figure 14, is a possible way to spatially resolve the changes in chemical bonding across the reacting spray, even for highly scattering environments. The changes in the molecular K-edge spectra are mapped onto the frequency offset of the XCARS signal. The temporal resolution will be determined by the amount of averaging required (as dictated by the available average power), but stimulated coherent X-ray Raman spectroscopy opens a unique window into the interior chemistry of a fuel spray. Because all the X-ray wavelengths can be chosen to transmit through the spray, and because the XCARS signal arises only from the area where the beams cross, chemical information is obtained at chosen locations within even a dense spray.

Cinematic Imaging of Reacting Flows

The stochastic nature of turbulent reacting flows is a critical factor in combustor design, and understanding turbulence-chemistry interactions is key to developing robust and efficient combustion strategies. Despite significant advances in 1D and 2D imaging of turbulent flames, many important observables are still not accessible with current imaging techniques. By its nature, the spatio-temporal structure of turbulence is not repeatable, and therefore comparisons between numerical simulations and experiments are currently performed on a statistical basis using conditionally averaged quantities (mixture fraction, local strain rate, dissipation rate, spatial scales, etc.). The relevant correlations between species concentrations and flow conditions are incompletely characterized, due to a lack of temporal resolution and the absence of information on the third spatial dimension. The ultimate goal of experimental reacting flows is to measure a complete 4D movies (space + time) of the fluid dynamics while simultaneously resolving molecular identities and concentrations. Achieving this goal will permit the use of experimentally-derived initial boundary conditions for numerical flame simulations. This approach will allow a direct comparison of the model to experiment and facilitate the development and validation of next-generation high-fidelity, large-eddy simulations (LES) and direct numerical simulations (DNS). and will be a revolutionary leap forward in understanding the coupling of chemistry and fluid dynamics that is at the heart of combustion in real devices.

The scientific challenge and impact for chemically resolving spatio-temporal structures in a combustion environment is illustrated in Figure 15. This shows LES calculations of the mixture fraction (mass fraction of fluid) for a *non-reacting* propane jet. Comparison of calculations at different temporal resolutions with single-shot laser Rayleigh scattering measurements show the significance of temporal resolution (~1 μs) and spatial resolution (~100 μm) for effective comparison with theory.[9] Critical to

advancing our predictive understanding is to achieve this spatio-temporal resolution with *chemical-selectivity*, and in a *reacting combustion environment* which is beyond present capabilities.

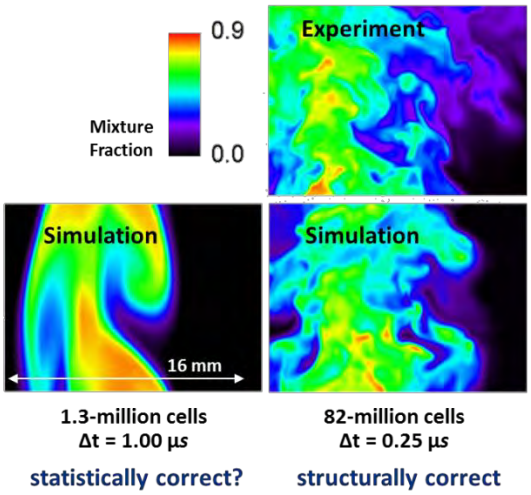

Figure 15. Non-reacting propane jet: comparison of mixture fraction (mass fraction of fluid) from LES calculations (at different temporal resolutions), with single-shot laser Rayleigh scattering.[9]

Although VUV radiation from synchrotrons has made major advances in our understanding of combustion chemistry (e.g., the discovery of enols, a new class of combustion intermediates[10]), the proposed experiments on turbulence-chemistry interactions require the capabilities of a high-repetition-rate X-ray laser. Direct 4D comparison with combustion models are not yet possible, and will require cinematic imaging experiments (high frame-rate imaging) to make a continuous "movie" of scalar and vector flame properties. Among the pressing needs for experimental measurements are 4D measurements of species, temperature, mixture fraction (fuel distribution), and scalar dissipation (rate of molecular mixing) spanning the full range of turbulence length scales. The following sections describe a few of the possible experimental imaging probes enabled by LCLS-II that will provide revolutionary new insights into turbulence-chemistry interactions and important phenomena, such as localized flame extinction and ignition.

The imaging tools for spatio-temporal interrogation of turbulent flames include single-pulse X-ray fluorescence imaging and single-pulse tomography using either fluorescence or direct absorption. The narrow bandwidth radiation (<100 meV) of LCLS-II will be critical in providing chemical speciation, as illustrated by recent time-averaged soft X-ray combustion studies at the ALS (see Section 3.3).[11] The combination of high repetition rate and high pulse energy from LCLS-II is critical and not available from synchrotrons or any envisioned table-top laser source.

Time-resolved X-ray fluorescence imaging will use the LCLS-II beams (formatted into a laser sheet) for excitation at the low-energy side of the carbon K-edge near 284 eV.[12] Red-shifted fluorescence (265 - 283 eV) arising from valence electrons filling the 1*s* core hole will be imaged perpendicular to the laser sheet [13]. The fluorescence will not be substantially absorbed by the flame due to its red-shift. Absorption cross sections of ~10^{-18} cm^2 per C atom, fluorescence quantum yields of ~$3x10^{-3}$, and 90% quantum efficiency imaging detectors will provide sufficient signal to noise for single-pulse imaging. Cinematic 2D images acquired every 10 microseconds (utilizing the 0.1-1 MHz LCLS-II repetition rate) will be fast enough to correlate structures from one frame to the next. Spectrally integrated fluorescence (265 - 283 eV) will enable imaging of the total carbon atom distribution, which when coupled with temperature measurements (from Rayleigh scattering) will provide spatio-temporal maps of mixture fraction.

Mixture fraction, ξ, is a central quantity in the theory and modeling of turbulent non-premixed and partially premixed combustion. The state of mixing between the fuel and oxidizer streams is quantified by

mixture fraction, and the *rate* of molecular mixing is given by the scalar dissipation rate, $\chi = 2D(\nabla\xi \cdot \nabla\xi)$, where D is the mixture-averaged mass diffusivity. Multi-dimensional mixture fraction measurements are required to determine the scalar dissipation rate. Optical laser-based measurements of mixture fraction in flames are a challenge because of spatial variations in temperature and chemical composition. Single-point and line measurements of mixture fraction are feasible using simultaneous Raman/Rayleigh/CO-LIF to measure all the major species concentrations and temperature[14]. However, this approach is not practical for multi-dimensional measurements of mixture fraction.

State-of-the-art methods for 2D mixture fraction imaging[15-17] are single-pulse measurements that do not provide insight into the temporal evolution of the 3D flame structure. This structure governs phenomena such as localized extinction and re-ignition. In addition, these techniques rely on measurements of multiple reactive species to construct a conserved scalar (a quantity that is neither consumed nor produced, e.g. mixture fraction).

X-ray fluorescence imaging of carbon will enable spatially and temporally resolved measurements of all carbon-containing species in the flame. Because X-ray fluorescence is largely an atomic process, this measurement will track the redistribution of carbon atoms that originated from the fuel, independent of chemical reactions that redistribute them in the flame. The concentration of carbon atoms is a true conserved scalar that cannot be directly measured with optical techniques. Spatially resolved carbon concentrations will be coupled with Rayleigh scattering to determine a carbon-based mixture fraction.

Quantitative visible/UV fluorescence imaging is complicated by spatially dependent fluorescence collisional quenching rates (i.e., converting signal to concentration requires concentration maps and quenching rates for all other species). By contrast, in X-ray fluorescence, the fluorescence lifetime is governed by the dominant Auger electron emission lifetime (~ 10 fs)[18]. This lifetime is three to four orders of magnitude shorter than the time between molecular collisions in an atmospheric pressure flame; therefore the X-ray image will be unaffected by collisional quenching, greatly simplifying quantitative interpretation.

Powerful multi-dimensional variants on this technique (as described in more detail in Section 3.1) will provide unprecedented detail for investigating turbulent reacting flows. Four-dimensional (space + time) imaging is possible by scanning the laser sheet to multiple different positions within the depth of field of a single imaging detector. In this way a full spatial and temporal map can be acquired with sufficient time resolution to follow the evolution of flame structures (using LCLS-II repetition rates up to 1 MHz). Chemical speciation could be achieved by tuning the excitation to near edge features characteristic of important functional groups, providing critical information on the relative concentrations of e.g. aromatic, aliphatic, carbonyl, or ether functionalities. The excitation light may also be tuned to the red side of the oxygen edge (543 eV) or the nitrogen edge (410 eV) to probe the distributions of species containing these atoms.

An second approach to 4D chemically resolved imaging is single pulse tomography—obtaining projections of the flame to reconstruct its spatial structure, with sufficient frame rate to follow its temporal structure. We envision two tomographic approaches applied at the carbon K-edge, based on fluorescence and absorption, each with its own strengths and challenges.

Fluorescence excitation tomography is a variant of planar fluorescence imaging described above. However, instead of forming a thin X-ray laser sheet, the beam is expanded to overlap a significant volume of the flame. Fluorescence is imaged at multiple viewing angles using an array of imaging detectors. Because fluorescence excitation is a linear process, the signal levels will be the same as in planar imaging. The extra expense of multiple cameras will enable full spatial and temporal

reconstruction of the flame structure. Chemical specificity would be achieved as described above for planar fluorescence imaging.

An alternative approach to fluorescence is spatially and chemically resolved absorption tomography at the carbon K-edge. This approach promises better signal-to-noise than fluorescence (due to the low quantum yield of fluorescence), but requires a sophisticated design to create an angular array of excitation beams (as described in Section 3.3). The 3D spatial structure of the flame can be tomographically reconstructed from the set of projected absorption images at various angles. This single-pulse tomography will deliver the desired 4D cinematic imaging at the 100 kHz repetition rate of LCLS-II. Chemical functional group speciation could be achieved by tuning the exciting radiation to appropriate near-edge features, as described above. This single-pulse tomographic approach would be a revolutionary capability not only for reacting flows, but also for imaging many irreproducible objects, and relies on the characteristics of LCLS-II radiation (simultaneously high repetition rate and pulse energy).

A key advantage of all these X-ray based techniques, compared to similar approaches in the UV-IR-optical regime, is that signals from these core electron spectroscopies will not be degraded by diminishing Boltzmann quantum level fractions at higher temperatures, nor by unfavorable Franck-Condon factors. The new multi-dimensional imaging capabilities will be instrumental in making progress in understanding ignition and extinction phenomena. Understanding the dynamics of these transient processes is increasingly important because the peak efficiency in many advanced combustion systems is obtained near their stability limits, where the risk of extinction and excess pollutant formation is also greater.

Aerosol Chemistry and Soot Formation

Soot has a substantial negative impact on human health,[19-21] air quality,[21] and global climate.[21-23] The growing concern over adverse health and environmental effects of small particles has prompted strict regulations of fine particulate emissions, has caused them to be a target of the President's recently released *Climate Action Plan* [24], and has intensified research on the control and impact of combustion-generated particles. There are significant limitations on our ability to control soot emissions or develop mitigation strategies, however, and overcoming these limitations will require addressing severe deficiencies in our understanding of particle formation and evolution during combustion [25].

These deficiencies are attributable in large part to a lack of sensitive, accurate, noninvasive measurements of the physical and chemical characteristics of soot during its development and evolution in combustors. Real progress in surmounting these deficiencies in our understanding of soot formation and evolution will necessitate overcoming experimental limitations and coupling experimental results with model development and validation. This progress is essential for development of effective soot emissions controls and environmental impact mitigation strategies.

Figure 16 summarizes the chemistry of soot formation and evolution in a flame. Soot formation is initiated by the production of hydrocarbon radicals during initial fuel oxidation.[26-28] These radicals lead to higher molecular-weight growth and polycyclic aromatic hydrocarbon (PAH) generation.[27] Large PAHs nucleate or grow to form incipient nanoparticles in the size range of 2-10 nm (shown in red in Figure 16)[29, 30]. Incipient particles grow by coagulation and surface growth to form larger particles. These particles lose hydrogen by pyrolysis and oxidation, and collisions of these carbon-rich particles form agglomerates rather than coagulating (shown in purple in Figure 16). Hydrogen loss and surface growth continues until these agglomerated particles become covalently bound aggregates of mostly carbonaceous particles with a fine structure resembling polycrystalline graphite (shown in green in Figure 16).[28] Oxidation of these graphitic particles is believed to proceed by reactions of O_2, O, and OH at "active" sites (i.e., defect or edge sites[31]) on the graphitic surface to form CO and CO_2.[32]

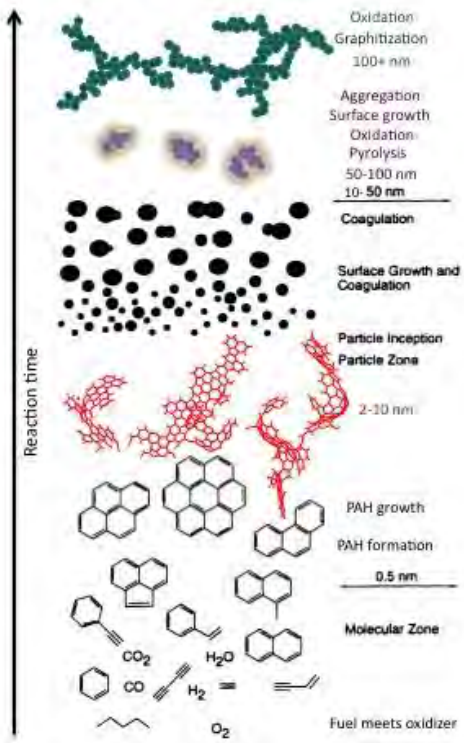

Figure 16. Schematic representation of soot formation and evolution in a flame. The molecular structures and particles are not drawn to scale. This figure is an update of the classic figure of soot formation from Bockhorn presented in 1994,[26] modified with molecular species predicted to initiate soot formation by Violi (personal communication) and extended to include aggregation, graphitization, and oxidation of mature graphitic soot.

Studies of soot chemistry require measurements of soot composition, size, morphology, and volume fraction. Despite many decades of development, most of the techniques available to provide such measurements are plagued by serious drawbacks. These techniques can be divided into either *ex situ* methods, which require extractive sampling of particles from the combustor, or *in situ* methods, which probe particles directly under combustion conditions. There is a wide range of *ex situ* techniques that have been used to study soot. These techniques can be extremely valuable in providing information about particle composition, size, and morphology. Unfortunately, they rely on extractive sampling, which (1) causes significant perturbations to the combustion system and (2) leads to condensation of gas-phase species onto the particles, complicating interpretation of the results. *In situ* techniques, on the other hand, avoid complications associated with extractive sampling and are much less invasive, but the number of available *in situ* techniques for studies of soot in combustors is very limited. In addition, these techniques often suffer from difficulties associated with signal interpretation (e.g. ref. 33), but using a combination of *in situ* techniques may allow these difficulties to be circumvented.

X-ray diagnostics can provide considerable information about particle chemical and physics characteristics. Hard X-ray techniques are particularly appealing because they may allow *in situ* measurements of combustion systems at elevated pressures, which is necessary for understanding combustion under engine-relevant conditions. Measurements made at LCLS-II will be transformational in advancing our understanding of combustion chemistry, particularly when coupled with laser-based *in situ* studies, *ex situ* measurements, theoretical work, and combustion modeling results.

Probing particle composition

Near-edge X-ray absorption fine structure (NEXAFS) spectroscopy is a powerful tool for probing particle composition and carbon electronic structure.[34-36] Figure 17 shows examples of NEXAFS spectra recorded on soot samples extracted from selected locations in a premixed flat flame. This figure demonstrates signatures of functional groups and carbon hybridization that change with particle evolution in the flame and can be used to study formation, oxidation, and graphitization in the flame. A probe was inserted in the

flame in order to collect these samples, however, and the spectra were recorded *ex situ*. Previous work by Frank et al. [11] has demonstrated that NEXAFS spectra can be collected *in situ* in a flame, but the flame must be under vacuum to allow propagation of the soft X-ray probe at the carbon K edge of ~285 eV.

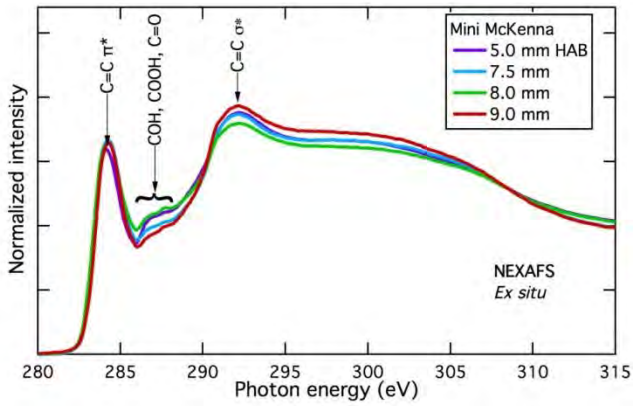

Figure 17. NEXAFS spectra recorded at the carbon K edge. Spectra were recorded on soot samples collected from an atmospheric ethylene-air premixed flat flame at selected heights above the burner (HABs). Signatures of functional groups are labeled.

Spontaneous X-ray Raman spectroscopy (XRS) offers the ability to probe the carbon K edge using hard X-rays in the flame under normal operating conditions and pressures. Figure 14 shows an energy-level diagram that compares XRS transitions with those of NEXAFS. Whereas NEXAFS is a direct transition from the 1s orbital to the lowest unoccupied molecular orbital at ~285 eV, the same transition is probed in XRS using a hard X-ray non-resonant probe photon energy and detecting the hard X-ray inelastically scattered Stokes signal. Figure 18 shows *in situ* XRS spectra recorded with the same flame configuration as that used to generate the soot probed by the NEXAFS spectra shown in Figure 17. These spectra were recorded on Beamline 6-2 at the Stanford Synchrotron Radiation Lightsource (SSRL) using the Si(111) monochromator, which delivered photons at ~6.5 keV with a flux of 2×10^{13} photons/s and energy resolution of 0.85 eV [37]. The detector was a Johann-type crystal spectrometer 40 spherically bent and diced Si(110) crystals positioned on a 1-m Rowland circle and subtending a solid angle of 1.9% of 4π sr.[37] The signal was recorded on a silicon drift detector that was used to reduce background by spectrally discriminating against diffuse scatter. Because both the incident beam and signal were in the hard X-ray regime, the experiment could be performed at atmospheric pressure without excessive loss of signal. The photon energy of the incident beam was scanned, and the detection wavelength was fixed.

The most striking features in the spectra shown in Figure 18 are those attributable to gas-phase CO and CO_2 in the flame. This result is similar to the measurements of NEXAFS spectra recorded in a low-pressure methane diffusion flame by Frank et al. [11]. The underlying features of the soot particles and precursors are difficult to discern in these spectra, and extracting them from the gas-phase interference will require more averaging. The XRS cross section is extremely low, however, and each of these spectra requires considerable signal averaging. The high repetition rate of LCLS-II and its associated increase in average flux, will significantly shorten XRS data collection periods and will open the door for pump-probe experiments for, e.g., isolating the signals of the soot particles from the gas-phase species. Another advantage is that XRS can be performed simultaneously with hard X-ray techniques to probe of soot particle size and morphology as discussed on page xx.

The results displayed in Figure 18 demonstrate the feasibility of probing these transitions using X-ray coherent anti-Stokes Raman spectroscopy (XCARS), which can offer orders of magnitude more signal than XRS [7]. This increase in signal is attributable to the spatial coherence of the XCARS photons, which are scattered into a small solid angle rather than the randomly scattered XRS photons. In addition, XRS depends linearly on incident photon flux whereas XCARS depends on the third order susceptibility and is nonlinearly dependent on photon flux. LCLS-II will provide high photon flux and phase coherence when self-seeded and will thus enable implementation of XCARS.

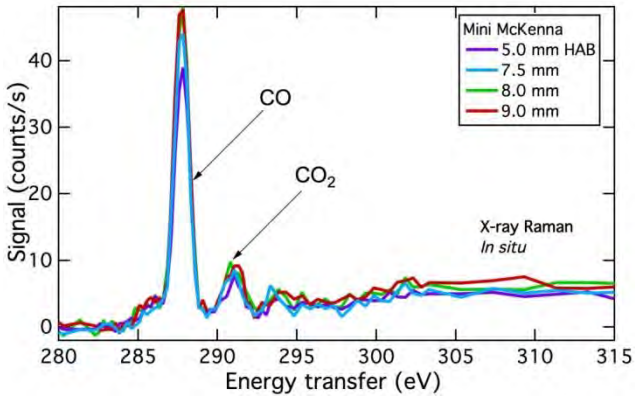

Figure 18. XRS spectra recorded at the carbon K edge. Spectra were recorded *in situ* in the flame produced by the same burner as used for the NEXAFS spectra in Figure 17.

Further details about composition can be derived from X-ray photoelectron spectroscopy (XPS) and will be a good complement to XRS and XCARS measurements. Although *ex situ* XPS measurements have been made on soot [38], this diagnostic has never been deployed for *in situ* measurements in a flame. High-intensity X-ray sources coupled with differentially pumped electrostatic lens systems make it possible to conduct ambient pressure ($<10^{-2}$ atm) X-ray photoelectron spectroscopy (APXPS) measurements under *in situ* conditions and elevated temperatures [39]. These measurements require the detector operating distance to be close to the sample in order for the ejected photoelectrons to be measured; at near atmospheric pressures, however, this approach could provide a unique *in situ* methodology for probing soot chemistry.

Probing particle size and morphology

Particle formation chemistry controls incipient particle size and morphology. These characteristics are not readily measurable; the particles are too small to be measured at laser wavelengths and too easily perturbed by probes to be measured by *ex situ* techniques. Loh et al.[40] used diffractive imaging to produce images of isolated particles at LCLS in order to probe the morphology and fractal dimension of individual artificial soot particles. The high repetition rate of LCLS-II will enable us to probe the morphology of individual incipient particles *in situ* in a flame for the first time. The density of incipient particles is small, which will allow us to sample continuously to generate statistics on these particles. These measurements will be complemented by *in situ* measurements of particle size using small-angle X-ray scattering (SAXS)[41-44] and particle fine structure using wide-angle X-ray scattering (WAXS).[43] The LCLS-II upgrade will also provide the ability to shrink the incident X-ray beam spot and hence increase the spatial resolution of the *in situ* SAXS measurements in different regions of the flame for studies of combustion chemistry. The truly unique aspect of this work is that multiple photon energies at the LCLS-II may allow the simultaneous combination of *in situ* spectroscopy (X-ray Raman) and *in situ* scattering/imaging of soot to get information on both the structure and the chemistry at the same position in the flame. The LLNL (van Buuren) and Sandia (Michelsen) groups are conducting the first proof of principle experiment to determine the viability of the combined X-ray Raman/ SAXS approach.

References

1. J. B. Bell, M. S. Day, and M. J. Lijewski, "Simulation of nitrogen emissions in a premixed hydrogen flame stabilized on a low swirl burner," Proceedings of the Combustion Institute **34**, 1173 (2013).
2. J.E. Dec, "A Conceptual Model of DI Diesel Combustion Based on Laser-Sheet Imaging," in *SAE Technical Paper 970873*(1997), p. DOI: 10.4271/970873.
3. M. Musculus, and L. Pickett, "Chapter 33: In-cylinder spray, mixing, combustion, and pollutant-formation processes in conventional and low-temperature-combustion diesel engines," in *Advanced Direct Injection Combustion Engine Technologies and Development: Volume : Diesel Engines*, H. Zhao, ed. (Woodhead Publishing Ltd., Cambridge, UK, 2009).

4. J. B. Schmidt, Z. D. Schaefer, T. R. Meyer, Roy, S., , S. A. Danczyk, and G. J.R., "Ultrafast time-gated ballistic-photon imaging and shadowgraphy in optically dense rocket sprays," Appl Optics **48**, B137 (2009).
5. M. A. Linne, M. Paclaroni, E. Berrocal, and D. Sedarsky, "Ballistic imaging of liquid breakup processes in dense sprays," Proc. Combust. Inst. **32**, 2147 (2009).
6. Wang Y, Liu X, Im K-S, Lee W-K, Wang J, and Fezzaa K, "Ultrafast X-ray study of dense-liquid-jet flow dynamics using structure-tracking velocimetry," Nature Phys **4**, 305 (2008).
7. S. Tanaka, and S. Mukamel, "Coherent X-ray Raman spectroscopy: A nonlinear local probe for electronic excitation," Physical Review Letters **89**, 043001 (2002).
8. C. Kliewer, "Quantitative one-dimensional imaging using picosecond dual-broadband pure-rotational CARS," submitted to Applied Optics, https://share.sandia.gov/crf/crfnews.php?id=307.
9. J. H. Frank, S. A. Kaiser, and J. C. Oefelein, "Analysis of scalar mixing dynamics in LES using high-resolution imaging of laser Rayleigh scattering in turbulent non-reacting jets and non-premixed jet flames," Proceedings of the Combustion Institute **33**, 1373 (2011).
10. C. A. Taatjes, N. Hansen, A. McIlroy, J. A. Miller, J. P. Senosiain, and S. J. Klippenstein, "Enols are common intermediates in hydrocarbon oxidation," Science **308**, 1887 (2005).
11. J. H. Frank, A. Shavorskiy, H. Bluhm, B. Coriton, E. Huang, and D. L. Osborn, "In situ soft X-ray absorption spectroscopy of flames," Applied Physics B: Lasers and Optics **117**, 493 (2014).
12. R. Manne, and J. Chem, Physics **52** (1970).
13. B. O. Ayoolan, R. Balachandran, J. H. Frank, E. Mastorakos, and C. F. Kaminski, "Spatially resolved heat release rate measurements in turbulent premixed flames," Combust Flame **144**, 1 (2006).
14. R. S. Barlow, and J. H. Frank, "Effects of turbulence on species mass fractions in methane/air jet flames," Proc. Combust. Inst **27**, 1087 (1998).
15. J. H. Frank, K. M. Lyons, D. F. Marran, M. B. Long, S. H. Stårner, and R. W. Bilger, "Mixture fraction imaging in turbulent nonpremixed hydrocarbon flames," Proc. Combust. Inst **25**, 1159 (1994).
16. M. B. Long, J. H. Frank, K. M. Lyons, D. F. Marran, and S. H. Starner, "A technique for mixture fraction imaging in turbulent nonpremixed flames," Ber. Bunsenges. Phys. Chem. **97**, 1555 (1993).
17. J. Fielding, J. H. Frank, S. A. Kaiser, M. D. Smooke, and M. B. Long, "Polarized/depolarized rayleigh scattering for determining fuel concentrations in flames," Proc. Combust. Inst. **29**, 2703 (2003).
18. A. J. Seen, and F. P. Larkins, "Ab initio studies of molecular x-ray-emission processes - Ethanol," Phys.B-At. Mol. Opt. Phys. **25**, 4811 (1992).
19. J. S. Lighty, J. M. Veranth, and A. F. Sarofim, "Combustion aerosols: Factors governing their size and composition and implications for human health," Journal of the Air & Waste Management Association **50**, 1565 (2000).
20. N. A. H. Janssen, G. Hoek, M. Simic-Lawson, P. Fischer, L. van Bree, H. ten Brink, et al., "Black carbon as an additional indicator of the adverse health effects of airborne particles compared with PM10 and PM2.5," Environmental Health Perspectives **119**, 1691 (2011).
21. E. J. Highwood, and R. P. Kinnersley, "When smoke gets in our eyes: The multiple impacts of atmospheric black carbon on climate, air quality, and health," Environment International **32**, 560 (2006).
22. IPCC, *Climate Change 2013: The Physical Science Basis. Working Group I Contribution to the Fifth Assessment Report of the Intergovernmental Panel on Climate Change* (Cambridge University Press, Cambridge, UK and New York, NY, 2013).
23. T. C. Bond, S. J. Doherty, D. W. Fahey, P. M. Forster, T. Berntsen, B. J. DeAngelo, et al., "Bounding the role of black carbon in the climate system: A scientific assessment," Journal of Geophysical Research **118**, 5380 (2013).
24. Whitehouse, "The President's Climate Action Plan," (http://www.whitehouse.gov/sites/default/files/image/president27sclimateactionplan.pdf, June 2013).
25. DOE, "Report of the Basic Energy Sciences Workshop on Basic Research Needs for Clean and Efficient Combustion of 21st Century Transporation Fuels ", O. o. Science, ed. (2006).
26. H. Bockhorn, *Soot Formation in Combustion: Mechanisms and Models* (Springer-Verlag, Berlin, 1994).
27. H. Richter, and J. B. Howard, "Formation of polycyclic aromatic hydrocarbons and their growth to soot - a review of chemical reaction pathways," Progress in Energy and Combustion Science **26**, 565 (2000).
28. K.-H. Homann, "Fullerenes and soot formation - New pathways to large particles in flames," Angewandte Chemie International Edition, 2434 (1998).

29. H. Wang, "Formation of nascent soot and other condensed-phase materials in flames," Proceedings of the Combustion Institute **33**, 41 (2011).
30. A. Violi, "Modeling of soot particle inception in aromatic and aliphatic premixed flames," Combustion and Flame **139**, 279 (2004).
31. J. R. Hahn, H. Kang, S. M. Lee, and Y. H. Lee, "Mechanistic study of defect-induced oxidation of graphite," Journal of Physical Chemistry **103**, 9944 (1999).
32. B. R. Stanmore, J. F. Brilhac, and P. Gilot, "The oxidation of soot: A review of experimnets, mechanisms, and models," Carbon **39**, 2247 (2001).
33. A. Braun, "Some comments on "Soot surface area evolution during air oxidation as evaluated by small angle X-ray scattering and CO2 adsorption"," Carbon **44**, 1313 (2006).
34. S. di Stasio, and A. Braun, "Comparative NEXAFS study on soot obtained from an ethylene/air flame, a Diesel engine, and graphite," Energy & Fuels **20**, 187 (2006).
35. H. A. Michelsen, A. V. Tivanski, M. K. Gilles, L. H. van Poppel, M. A. Dansson, and P. R. Buseck, "Particle formation from pulsed laser irradiation of soot aggregates studied with a scanning mobility particle sizer, a transmission electron microscope, and a scanning transmission x-ray microscope," Applied Optics **46**, 959 (2007).
36. A. Braun, A. Kubatova, S. Wirick, and S. B. Mun, "Radiation damage from EELS and NEXAFS in diesel soot and diesel soot extracts," Journal of Electron Spectroscopy and related Phenomena **170**, 42 (2009).
37. D. Sokaras, D. Nordlund, T.-C. Weng, R. Alonso Mori, P. Velikov, D. Wenger, et al., "A high resolution and large solid angle x-ray Raman spectroscopy end-station at the Stanford Synchrotron Radiation Lightsource," Review of Scientific Instruments **83**, 043112 (2012).
38. J.-O. Müller, D. S. Su, U. Wild, and R. Schlögl, "Bulk and surface structural investigations of diesel engine soot and carbon black," Physical Chemistry Chemical Physics **9**, 4018 (2007).
39. E. J. Crumlin, E. Mutoro, W. T. Hong, M. D. Biegalski, H. M. Christen, Z. Liu, et al., "In Situ Ambient Pressure X-ray Photoelectron Spectroscopy of Cobalt Perovskite Surfaces under Cathodic Polarization at High Temperatures," The Journal of Physical Chemistry C **117**, 16087 (2013).
40. N. D. Loh, C. Y. Hampton, A. V. Martin, D. Starodub, R. G. Sierra, A. Barty, et al., "Fractal morphology, imaging, and mass spectrometry of single aerosol particles in flight," Nature (London) **486**, 513 (2012).
41. J. P. Hessler, S. Seifert, and R. E. Winans, "Spatially resolved small-angle x-ray scattering studies of soot inception and growth," Proceedings of the Combustion Institute **29**, 2743 (2002).
42. J. B. A. Mitchell, S. di Stasio, J. L. LeGarrec, A. I. Florescu-Mitchell, T. Narayanan, and M. Sztucki, "Small angle x-ray scattering study of flame soot nanoparticle aggregation and restructuring," Journal of Applied Physics **105**, 124904 (2009).
43. F. Ossler, L. Vallenhag, S. E. Canton, J. B. A. Mitchell, J. L. Le Garrec, M. Sztucki, et al., "Dynamics of incipient carbon particle formation in a stabilized ethylene flame by in situ extended-small-angle- and wide-angle X-ray scattering," Carbon **51**, 1 (2013).
44. A. W. Kandas, I. G. Senel, Y. Levendis, and A. F. Sarofim, "Soot surface area evolution during air oxidation as evaluated by small angle X-ray scattering and CO2 adsorption," Carbon, 241 (2005).

2.2 Catalysis, Photo-catalysis, Environmental & Coordination Chemistry

Synopsis

Energy from the sun powers most of the earth, and the intelligent use of sunlight for our energy needs will be a critical component in addressing urgent challenges in energy production, transformation, and storage – with reduced impact on the environment. Making viable carbon-neutral fuel from sunlight with sufficient energy efficiency and selectivity involves a myriad of complex processes spanning many orders of length and time scales – down to atoms and femtoseconds. These include light harvesting, electron hole separation, charge localization and migration, catalysis driven by electrons or by heat, energy conversion and storage.

Energy conversion and chemical transformation in nature and industry relies almost entirely on chemical catalytic processes at interfaces between solids and liquids or gases. These include novel electro - or photo-catalysis processes to produce hydrogen and to convert emitted CO_2 to fuels, more efficient and stable fuel cell catalysts, and selective thermal heterogeneous catalytic processes for generation of methanol, higher alcohols, and hydrocarbons. The US chemical industry alone is responsible for about 10% of the U.S. industrial production and employs more than 1 million people. It has been estimated that more than 90% of all industrial chemicals are dependent on the availability of suitable catalysts, and that about 60% of all processes in the chemical industry rely on catalysis.

The capabilities of LCLS-II for time-resolved, in-situ, element-specific and interface-sensitive studies will transform our ability to study many phenomena associated with these grand challenges in catalysis and photo-catalysis. Understanding natural systems and man-made catalysts under their normal operating conditions, and across broad time- and length-scales will be critical to the design of robust, chemically selective, earth abundant and effective catalysts that will help us to meet pressing energy and environmental challenges.

Introduction

Efficient and selective transformation of light, heat, and electrochemical energy into stable chemical fuels requires the development of new catalysts. Despite tremendous efforts to date, catalyst development is dominated by trial-and-error approaches that have so far failed to provide competitive alternatives to using fossil-fuel feedstock for fuel production. In order to transform the energy production landscape, we need a better understanding of how catalysts control chemical activity, leading to more accurate theoretical models that can provide predictive guides leading to hypothesis-driven design and development of new chemistries and novel catalysts. Catalysis chemistry is complex, since even though local atomic properties govern the catalysis of isolated reactions, meso- and macro-scale properties govern the abundance and local environment of reactive sites, reactant and product transport, and catalyst aging. One approach to understanding catalysis involves model systems which single out fundamental chemical and physical processes that are still poorly understood (e.g. non-adiabatic dynamics and coupled charge-transfer) and contribute towards robust interpretation and development of theory and simulation. Another approach involves *operando* investigation of how the integration of chemical and physical phenomena dictates the performance of a functioning prototype, and for characterization of the salient local chemical properties that are present under reaction conditions. Both approaches yield advances toward predictive design and synthesis of new materials.

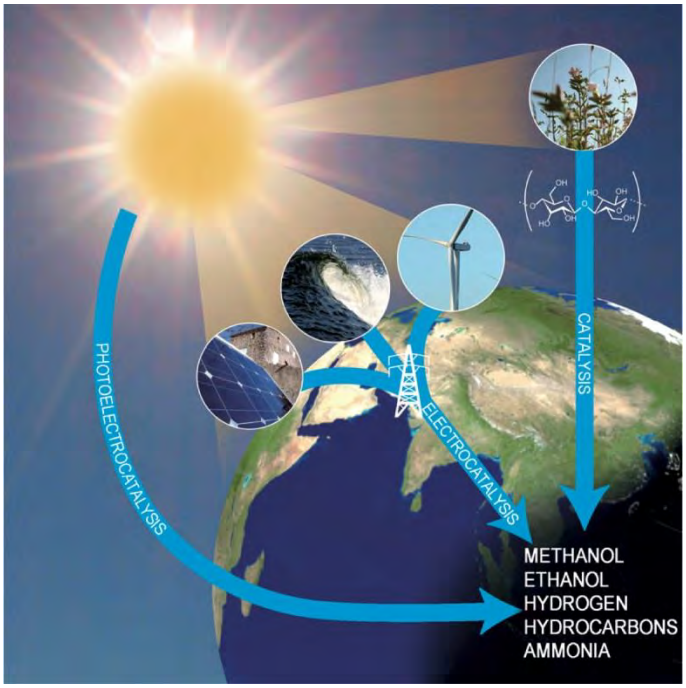

Figure 19. Illustration of the essential role of catalysis in the transformation of solar energy into a fuel. Right: direct solar-driven catalysis in natural photosynthesis. Middle: conversion of solar, wind, and tidal energy to electricity, for subsequent application in electro-catalytic processing. Left: integrated light harvesting and catalysis, e.g. as in solar-driven fuel cells.[1]

X-ray methods – *spectroscopy*, *scattering*, and *imaging* – provide powerful tools for characterizing catalysts and chemical reactions on length scales ranging from the atomic to the macroscopic. Element-specificity, and the X-ray spectral signatures of chemical bonding provide sensitivity to active sites in complex systems. The ability of X-rays to characterize surfaces and buried interfaces is particularly useful for studying chemical transformation and charge-transfer in heterogeneous catalysis. While most of our existing understanding is based on a time-averaged view of reactions at interfaces, X-ray lasers allow us to directly observe transformations and characterize reaction mechanisms across timescales (down to femtoseconds) and length scales (down to sub-nanometer) simultaneous with chemical specificity for the first time. The intrinsic properties of X-rays, coupled with new techniques, and the remarkable capabilities of LCLS-II (ultrafast time resolution, full transverse coherence, and high repetition rate) present potentially transformative new approaches to address fundamental and use-inspired questions in chemistry and catalysis.

2.2.1 Towards a predictive understanding of photo-catalysis

Electronic excited-state phenomena provide a compelling intersection of fundamental and applied research interests in the chemical sciences. Photocatalytic systems must perform three critical tasks: efficiently harvest photons, convert photon energy to a stable electrochemical potential through electronic excited-state charge separation and transport, and utilize this chemical potential to drive fuel production (see Figure 20). Optimization of each of these steps relies on our ability to understand and control fundamental physical and chemical phenomena associated with the non-adiabatic dynamics of electronic excited states. Section 2.1 discusses these challenges for isolated molecules, here the challenges are compounded by condensed-phase/solvent environment and coupling to other molecular elements. While transition state theory provides a powerful framework for understanding electronic ground-state reactions, we do not have the theoretical tools to predict electronic excited-state charge-transfer phenomena with sufficient fidelity to be of practical value.

The central events of excited state chemistry critically influence the performance of a photocatalyst. Stable charge separation and transport involve internal conversion, intersystem crossing, and conformational changes on the ultrafast time scale. The push toward cost effective materials and assembly

processes mean that these charges are being transported through defect rich or disordered materials where motion of charge is strongly coupled to static and dynamic deviations from ideal ordered structures. Understanding and modeling charge separation, transport, and localization in systems with strong interaction between electronic and nuclear structure, particularly for systems far from equilibrium, remains a significant challenge as these processes cannot be readily observed or calculated with standard experimental or theoretical methods.

Conventional chemistry models assume disparate time scales for evolution of electronic and atomic structure (Born-Oppenheimer approximation), but evidence points to the importance of coupled electronic/atomic structure (non-Born-Oppenheimer) in many systems. This has become a generally accepted aspect of photo-driven phenomena, but we lack the requisite tools to robustly disentangle the coupled motion of electrons and nuclei in many energy critical materials. New tools that enable direct observation of these central events will qualitatively advance our understanding of chemical dynamics in photocatalytic systems, and advance the development of design principles for directing molecular and materials synthesis. The challenging goal of controlling electronic excited-state dynamics provides a key connection between AMO physics (as discussed in Section 2.1) and physical- and materials-chemistry.

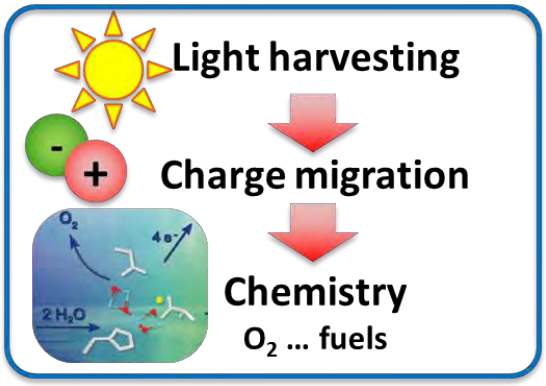

Figure 20. Illustration of essential steps in photo-catalysis

The significance of studying model systems extends beyond fundamental chemical physics. In materials with strong vibronic interactions (e.g. molecules and metal-oxide semiconductors), the charge carriers trap in self-induced local vibrational distortions (conformational changes) and defects. The energetics and dynamics of this process are critical to photocatalyst performance because they determine the mobility of charges and set an upper bound for the effective electrochemical potential of the photocatalyst. Ultrafast X-rays provide a unique opportunity to characterize the energetics and dynamics of the charge carriers, their spin and charge density, and the structural distortions that trap them.

Understanding how photogenerated carriers catalyze chemical reactions represents the most complex and challenging aspect of photogenerating fuels. The most important photocatalytic and electrochemical reactions, like CO_2 and N_2 reduction and H_2O oxidation, involve multiple electron transfers, often coupled with proton transfer. Multi-electron correlation and nuclear quantum effects cannot be disregarding when investigating photocatalysis, making solar fuels a compelling union of the fundamental and the practical.

The development and utilization of femtosecond resolution X-ray methods will play an important role in understanding, and ultimately controlling, the physics and chemistry of photocatalysis. Charge separation, charge transport, and catalysis are local phenomena. X-ray techniques can disentangle the coupled motion of electrons and nuclear dynamics with atomic resolution and chemical specificity, making them uniquely powerful for studying chemical dynamics.

The new capabilities of LCLS-II will complement and enhance the significant present attributes of LCLS – particularly for X-ray spectroscopy (e.g. resonant inelastic X-ray scattering, RIXS, see sidebar). For spectroscopy, tunability across the K-edges of lighter elements (C, N, O,…P, S, Cl) through the L-edges of the 3*d* and 4*d* transition-metals, combined with high average power (ability to trade off peak intensity and repetition rate) will enable ideal experimental conditions for catalysis studies. The initial applications of soft X-ray spectroscopy in this area highlight both the potential impact of ultrafast X-ray spectroscopy and the significant limits of a low repetition rate source. In addition, ultrafast X-rays at 25 keV will be invaluable for diffuse scattering studies of nuclear structure, enabling real space structures to be extracted from Fourier analysis of subtle difference scattering signals.

LCLS-II studies of model photo-catalysts and dynamics: will be a qualitative advance beyond time-resolved optical studies of photochemistry – which have been central to our current understanding of reaction mechanisms to date. While optical signatures of electronic and nuclear dynamics can be found for many systems, they generally fail to robustly observe ultrafast spin dynamics, cannot characterize changes in charge density with atomic specificity and resolution, and struggle to identify the nuclear degrees of freedom coupled to electronic excited state dynamics (unless the nuclear motions are Franck-Condon active and underdamped).

This set of constraints has impeded the interpretive value of many ultrafast optical measurements and makes the capabilities of ultrafast X-ray laser sources complementary and should prove decisive in many cases because chemistry is an atomically local phenomena and ultrafast X-ray spectroscopy and scattering provide a much more detailed picture of electronic excited-state phenomena. By combining the strengths of ultrafast optical spectroscopy with ultrafast X-ray methods we will stimulate the development of new fundamental concepts and theories to describe the processes that underlie photocatalysis.

Transition metal complexes possess all the critical ingredients of photocatalysts: strong optical absorption, the capacity to bind reactants, and the electronic structure to facilitate the electron transfer

Resonant Inelastic X-ray Scattering (RIXS)

RIXS measures the energy distribution of <u>occupied</u> and <u>unoccupied</u> molecular orbitals sensitive to the local chemistry of a metal center with high resolution. Time-resolved RIXS correlates orbital symmetry with spin multiplicity and reactivity in short-lived reaction intermediates. With the dramatic increase in average brightness at LCLS-II, high-resolution RIXS with femtosecond resolution will be used to map how frontier orbital energies drive charge separation and transfer in complex functioning systems.

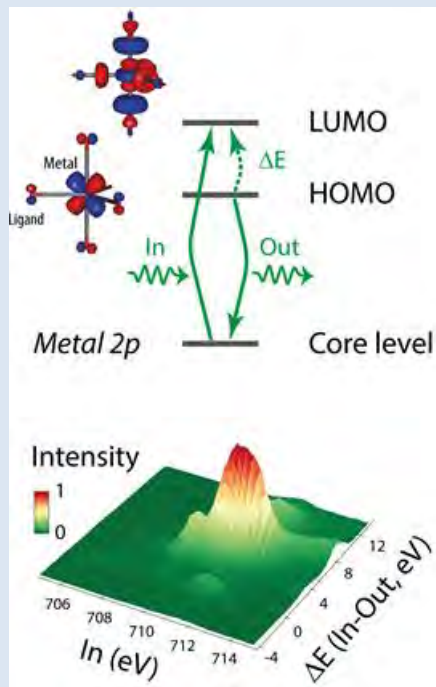

RIXS (spontaneous Raman) process: An incident photon promotes a core electron into a low-lying unoccupied level (LUMO) of the metal center of interest. The outgoing photon, corresponding to a valence level (HOMO) to core transition, is recorded with high spectral resolution and the corresponding RIXS map (ΔE vs. incident phonon energy) combined with quantum chemical calculations provides a detailed mechanistic picture of frontier-orbital

events critical to chemical bond formation and dissociation. While efficient, robust catalysts based on rare 4*d* and 5*d* transition metals have been demonstrated, we require a much more detailed understanding of how these work if we hope to achieve similar effectiveness with earth-abundant 3*d* metals. Nature exploits 3*d* metals for related enzyme function, which begs the question: *How can we learn from Nature to design ligand structures and create appropriate dynamic behavior in 3d–based complexes?*

The ability to interrogate the ultrafast evolution of electronic and nuclear structure with atomic resolution and specificity makes ultrafast X-ray spectroscopy and scattering indispensable for characterizing the complex electronic and nuclear rearrangements central to photocatalysis. While studies to date have focused on time-resolved X-ray absorption spectroscopy, LCLS-II will enable the full implementation of time-resolved resonant X-ray Raman spectroscopy (resonant inelastic X-ray Raman scattering, RIXS). RIXS uniquely provides information on both *occupied* and *unoccupied* valence states probed from core levels to achieve chemical specificity (see RIXS sidebar). RIXS is further sensitive to correlated multi-particle valence states. As a photon-in/photon-out technique, RIXS is particularly well-suited to *in-situ* studies. A complete time-resolved series of 2D RIXS maps (energy loss vs. incident photon energy tuned though an absorption edge) will reveal the evolution of the charge and spin density. Coupling such information with systematic changes in the electronic ground state intra- and inter-molecular structure, LCLS-II will assist the development of design principles for photocatalytic systems.

Understanding how to control the sub-picosecond non-Born-Oppenheimer dynamics of electronic excited states (see Section 2.1) that dictate stable charge separation necessitates measuring the time dependent evolution of electron and spin density, and how these changes couple to changes in nuclear structure. The transition metal based Ru-Co donor-bridge-acceptor complex (shown in Figure 21) illustrates these ideas that impact the performance of a diverse range of molecules and materials. In this model photo-catalyst, metal-to-ligand-charge transfer (MLCT) excitations of the coordinated Ru cation efficiently harvest visible light. This initiates a series of ultrafast changes in electronic and nuclear structure including: electron transfer, solvation between the distinct ligands coordinating the Ru and Co cations, and conversion of Co from low-spin Co(III) to high-spin Co(II). In principle, the oxidized Ru(III) site and the reduced Co(II) site can catalyze oxidation and reduction reactions. While the processes that follow photoexcitation have been identified, the sequence of events remains unclear, and we lack effective design rules for how to manipulate these processes through intra- and inter-molecular modifications.

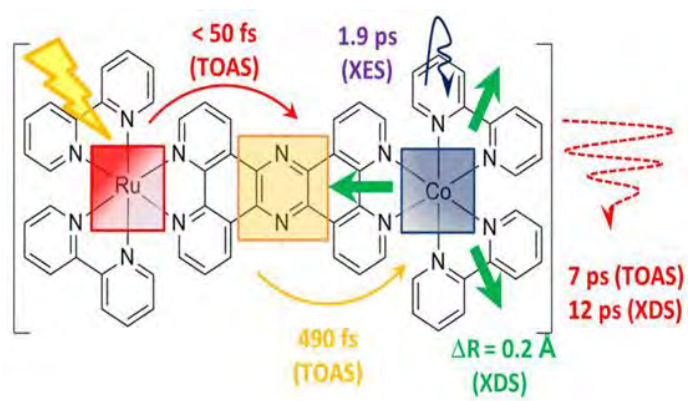

Figure 21. Non-equilibrium electron-transfer across the photoexcited (^{1}RuII=^{1}CoIII) model photo-catalyst. The schematic summarizes the fundamental timescales, as obtained from transient optical absorption spectroscopy (TOAS), X-ray emission spectroscopy (XES) and X-ray diffuse scattering (XDS).[2]

The ultrafast changes in charge, spin, and inner coordination shell structure that govern ultrafast charge separation also influence catalytic function. Another important class of molecular complexes can be utilized to investigate catalytic reactions initiated by photo-induced electron transfer, spin transitions, and ligand dissociation. The study of ligand dissociation and solute-solvent complexation demonstrated in $Fe(CO)_5$ (see sidebar) represents an example of this class of experiment. For these investigations, ultrafast optical excitation promptly generates reactive metastable catalysts. This synchronizes the reactions and will enable catalytic mechanisms to be characterized with atomic resolution and specificity.

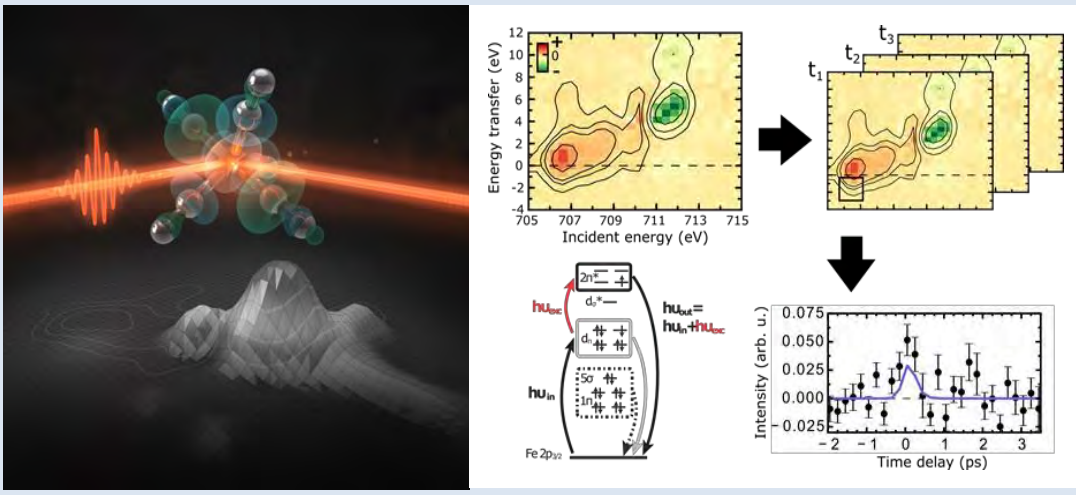

Demonstration of Time-resolved RIXS Studies of Photo-dissociation of $Fe(CO)_5$ at LCLS[3]

Converting the energy of an absorbed photon into a stable electrochemical potential through electronic excited state charge separation and transport is of central importance to making solar fuels. The mechanistic understanding of these processes in well-defined model systems guides the design of integrated functioning systems. Ultrafast optical pump and X-ray probe methods provide both the temporal resolution and atomic scale sensitivity required to disentangle coupling of transient electronic structure and nuclear dynamics. Time-resolved soft X-ray spectroscopy is a powerful tool to map the frontier-orbital interactions in molecular excited states with atom specificity. Recently this has been demonstrated at the LCLS where RIXS with femtosecond time resolution combined with quantum chemical calculations have provided for the first time a detailed mechanistic picture of frontier-orbital changes that drive excited-state dynamics.[3] These studies of large structural changes on model molecular systems at high concentrations (~1 M) demonstrate the potential of time-resolved RIXS to correlate orbital symmetry with spin multiplicity and reactivity in short-lived reaction intermediates. With the dramatic increase in average brightness at LCLS-II, high-resolution RIXS with femtosecond resolution will be used to map how frontier orbital energies drive charge separation and transfer in complex functioning systems.

LCLS-II studies of performance bottlenecks in integrated photocatalytic systems: The complex interdependence of energy, charge, and mass transport in photocatalytic systems present numerous challenges to system characterization. Identifying the performance limitations of integrated photocatalytic systems is an important step beyond the study of isolated model and natural photosynthetic systems. It contributes critically to the development of cost-effective solar fuels device based on abundant materials. A major scientific and technology gap is the durability of the components, and all-inorganic materials such as metal oxides are a promising approach to address this. However, metal oxides presently lack the facile tuning of the electrochemical potentials of light absorbers and catalysts that is needed to maximize energy conversion efficiency. In addition, a variety of charge trapping and deleterious reactions degrade the quantum efficiency of metal-oxide based photocatalytic devices. Here, molecularly defined all-inorganic units may provide a viable path to robustness and tunable electronic properties.

Addressing such a complex and multifaceted problem will require a diverse range of experimental, synthetic, and theoretical methods. While LCLS-II will not fully address all these problems, it will

provide critical new information. The ZrOCo(II) complex (Figure 22) is a model system that highlights the critical challenges that must be addressed that will benefit significantly from the unique capabilities of LCLS-II. This all-inorganic heterobinuclear unit coupled to a silica substrate has recently been shown to achieve photoinduced splitting of CO_2 to free CO and formate.[4] This system exploits an optical metal-to-metal charge transfer (MMCT) excitation to oxidize water and reduce CO_2. While this photosynthetic system requires a catalytic cluster made from costly iridium oxide, closing the photosynthetic cycle in one integrated and precisely defined system presents an excellent opportunity to identify the transient rate-limiting and efficiency-limiting steps of a complete photosynthetic system.[4]

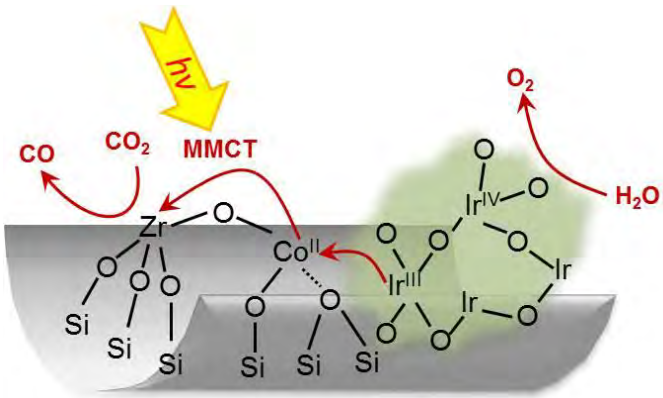

Figure 22. Heterobinuclear ZrOCo unit (light absorber and charge separator) coupled to Iridium oxide nanocluster catalyst for water oxidation. The unit reduces carbon dioxide by using electrons generated by catalytic water oxidation.[4]

LCLS-II will provide essential capabilities for identifying charge transport and catalytic bottlenecks for maximizing quantum efficiencies of such artificial photosynthetic assemblies via high resolution time-resolved X-ray spectroscopy. For example, the quantum efficiency for transfer of the charge from the Co center to the metal oxide nanocluster catalyst for driving water oxidation is determined by the competition with back electron transfer to the ZrOCo unit upon light absorption, which itself is dictated by the yield of ultrafast intersystem crossing (spin flip) of the initially excited ZrOCo state. Knowledge of the local structural changes of the excited metal centers on the ultrafast time scale will guide synthetic improvements for maximizing the intersystem-crossing path, inhibiting back-electron-transfer, and enhancing charge transport yields to the catalyst. Strong parallels are expected between dynamic phenomena occurring in the cobalt molecular complex shown in Figure 21 and the solid state cobalt oxide shown in Figure 22. Similar X-ray spectroscopy and scattering methods will be applicable to both systems. Ultrafast soft and hard X-ray spectroscopy of the photo-excited ZrOCo unit will reveal electronic and nuclear structural reorganization processes that could be exploited for enhancing intersystem crossing yields, while simultaneous probing of Co donor (Co L_3-edge at 778 eV) and surface Ir centers (Ir M_5-edge at 2.05 keV) will provide insight into elementary steps that result in the conversion of a transferred charge to catalytic transformation on the cluster surface. Developments in high resolution soft X-ray resonance Raman scattering also present the opportunity to characterize the vibrational structure of catalysts with charge and spin state specificity.

Example: Water oxidation on a Cobalt Oxide Nanoparticle Catalyst

A key characteristic of all reactions essential for fuel generation from sunlight (i.e. the reduction of protons to H_2, of CO_2 to liquid hydrocarbon, and the oxidation of H_2O to O_2) is that two or more charges are required for completing each of the reactions. In order to design catalysts that approach this criterion as closely as possible, the step-by-step mechanism of the catalytic cycle needs to be unraveled, which includes the atomic/molecular structure, and the energetics and kinetics of each intermediate formed upon sequential arrival of the transferred charges. LCLS-II will provide a real-time spectroscopic view of catalytic cycles for fuel generation. This new knowledge will lead improvements in the efficiency of existing photo-catalysts, and guidelines for the design of new photo-catalysts.

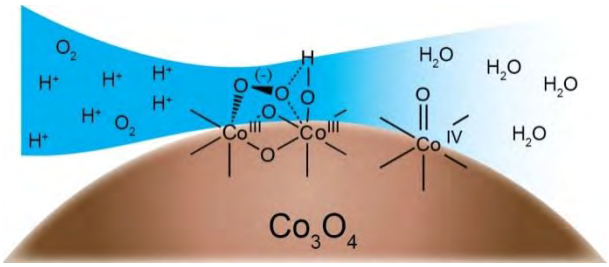

Figure 23. Visible light sensitized water oxidation at Co_3O_4 nanocatalyst surface. Two surface intermediates are detected: surface superoxide (three-electron oxidation intermediate), and oxo Co^{IV} site (one-electron oxidation intermediate). The temporal behavior of the intermediates reveal that they belong to different catalytic sites.[5]

Very recently the first direct temporally-resolved observation of surface intermediates of water oxidation was reported from an artificial first-row metal-oxide catalyst, namely Co_3O_4 in the form of single crystal nanoparticles.[5] Time-resolved vibrational spectroscopy revealed the formation of an oxo Co^{IV} intermediate and a superoxide surface intermediate (Figure 23). While vibrational spectroscopy provides limited structural details of the surface functionalities during the catalytic cycle, X-ray spectroscopy is able to provide element-specific information on the dynamic changes of the electronic structure and coordination environment of the active metal centers during the catalytic cycle. The multi-metal probing capability of LCLS-II on time scales from femtosecond to msec will allow detection of the dynamic structural changes of active surface metal centers. Specifically, it will address questions of how charges transferred to Earth abundant metal oxides induce catalytic change on the particle surface, and how transferred charges advance the catalytic activity through multiple sequential steps. Uncovering how specific elementary steps on the catalyst surface are driven by transferred charges will provide essential information for guiding catalyst design improvements for performance and durability.

2.2.2 Tracking heterogeneous chemistry in real time under working conditions

Heterogeneous catalysis is central to the transformation of many chemicals on which modern society depends, from petroleum, to industrial chemicals, to pharmaceuticals and fine products. It plays a decisive role in many geochemical and atmospheric processes – providing environmental protection by removing unwanted and often toxic byproducts, and enabling new selective chemistries such as the electrochemical and photochemical conversion of non-fossil fuelstock (such as CO_2) to liquid fuels.

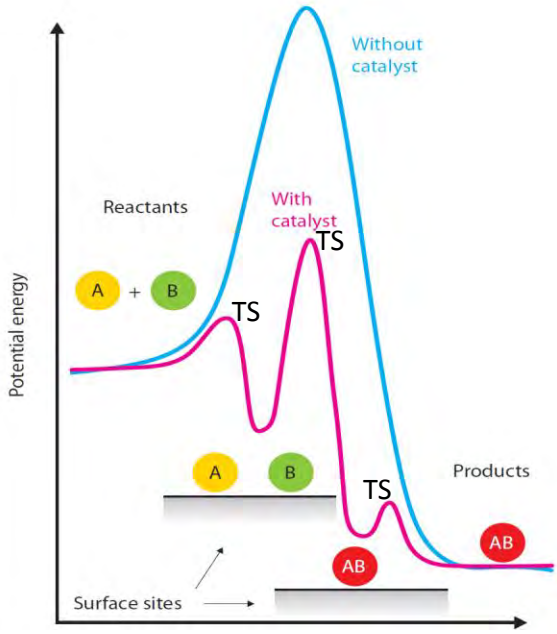

Figure 24. Schematic reaction energy diagram of the transformation of reactants (A and B) to final product (AB) along with the gas-phase barrier. Catalyzed reaction is directed along a path of various intermediate transition states (TS). The chemical transformation between each step requires energy sufficient to overcome the activation barrier between the steps. The catalyst lowers the activation barrier between the intermediate reaction steps, which accelerates the reaction and directs it towards the desired products.

Catalysis through heterogeneous chemistry accelerates and directs reactions by reducing the energy barrier between reactant and desired products. This is accomplished by introducing a series of intermediate (lower-energy) chemical transformation steps at the interface of the catalyst as illustrated in Figure 24. Key for selective and efficient catalysis are the short-lived "transition states" which define the chemical transformation from one intermediate to the next. Therefore, understanding the atomic and electronic structure of molecules, and their evolution through the elusive transition states, are critical to developing a predictive understanding for design of new catalysts.

LCLS has enabled the study of simple model catalytic reactions on relevant length- and time-scales,[6] and recent X-ray spectroscopy results report the first observation of a surface transition state.[7] These groundbreaking studies on ideal systems, prepared at high-concentrations, on a single crystal in a vacuum environment, demonstrate the potential for X-ray free electron lasers to provide a full understanding of chemical reactions on surfaces, in which the dynamics of making and breaking bonds are visualized in terms of the individual atomic and molecular motions and electronic transformations.

LCLSII will offer energy tunability spanning the soft, tender and hard X-ray range to provide element selectivity through resonant excitation, high repetition rate (high average brightness) for increased sensitivity, and resolution near the Fourier transform limit in energy and time. (see Experimental Approaches and Impact of LCLS-II at the end of Section 2.2). These properties all provide critical opportunities for studying chemistry at surfaces and interfaces. The diverse application of LCLS-II to interfacial chemistry will provide detailed information to benchmark theoretical models and lead to a fundamental understanding of surface catalytic reactions, directed design of better catalysts, and

ultimately control of catalytic reactions on a microscopic level. In this section, we discuss three important areas of heterogeneous chemistry where LCLS-II will have significant scientific impact:

- Chemical transformations on model surface systems
- Charge transfer at electrochemical interfaces
- Catalyst support assemblies

Chemical transformation on model surface system

Catalytically active species on surfaces are extremely difficult to characterize because of their high intrinsic reactivity and short lifetimes. Thus, despite theoretical predictions of various active intermediates, they have never been experimentally characterized. While hydrogenation and oxidation reactions of molecular resources are relevant for a large number of catalytic processes, significant knowledge gaps prevent us from fully exploiting and optimizing these processes based on prediction and directed design. An illustrative example is the Haber-Bosch reaction – a process discovered in 1908 for transforming N_2 into NH_3 (ammonia) for chemical fertilizer – but similar knowledge gaps impede the development of other catalysts, e.g. for the capture of CO_2 from the atmosphere for sequestration or transformation into useful fuels.

Today, roughly 1/3 of Earth's population is sustained by agriculture enabled by the Haber-Bosch reaction, often referred to as the most important invention of the 20th century.[8] Industrial ammonia production inherently involves hydrogen production via steam or dry reforming of methane as an important sub-process, and consumes approximately 20% of the total energy used in industry. Although increased production of ammonia is needed for food security in developing countries, there is also a pressing need to lower carbon emissions and reduce our energy footprint. The Fe-based catalyst for the Haber-Bosch reaction was discovered empirically through an Edisonian (trial and error) approach. Understanding the overall ammonia production process at the atomic-level aims to identify parameters that control reactivity and selectivity, to enable the directed design of catalysts that require less energy.

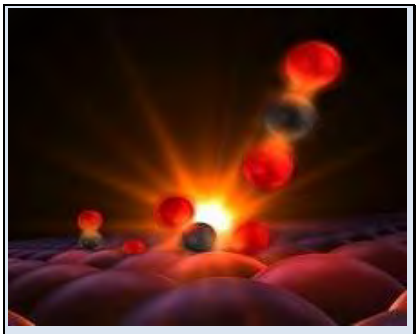

Capturing a Transition State
LCLS experiments capture the moment when atoms form a bond.[7] The reactants are a carbon monoxide molecule, made of a carbon atom (black) and an oxygen atom (red), and a single atom of oxygen, just to the right of it. They are attached to the surface of a ruthenium catalyst, which facilitates the reaction by holding them in proximity. When excited by an optical laser pulse, the reactants vibrate and bump into each other, and the carbon atom forms a transitional bond with the lone oxygen. The resulting carbon dioxide molecule detaches and desorbs, upper right.

The dissociation of the N_2 bond is the rate-limiting step in ammonia production, and the ability to break it is strongly influenced by the surface structure of the catalyst. Theoretical calculations combined with adsorption experiments have shown that N_2 dissociates primarily at under-coordinated sites on the catalyst surface (e.g. steps and kinks in the atomic structure) and is initiated from an up-right orientation of the N_2 molecule (as illustrated in Figure 25).[9]

LCLS-II studies of model surface systems for chemical transformation will exploit the combination of energy tunability, high average brightness, and energy/time resolution. In particular, advanced time-resolved X-ray emission, X-ray absorption, and photoelectron spectroscopy will be employed to follow the initial activation process, reveal details about the sub-processes involved (initial adsorption, presence/absence of a precursor state, bond activation), and characterize the role of the surface structure. In

addition to the Haber-Bosch reaction, the initial activation limits the rate, with a high activation energy barrier to the full decomposition reactions of methane and water, while subsequent steps are responsible for the selectivity towards desired products. The intermediate species involved are predicted to have very short lifetimes once produced. The unique capabilities of LCLS-II will enable the study of short-lived intermediates, and their branching into various competing channels, to fully characterize chemical transformations during catalytic processes. Fundamental insight provided by LCLS-II will be invaluable for guiding deliberate changes in the surface composition, reactant mixture, or reaction conditions, to enhance catalytic activity. Kinetic data will be correlated with structural properties and dynamics, deepening our understanding of the structure-activity relationships in catalysis.

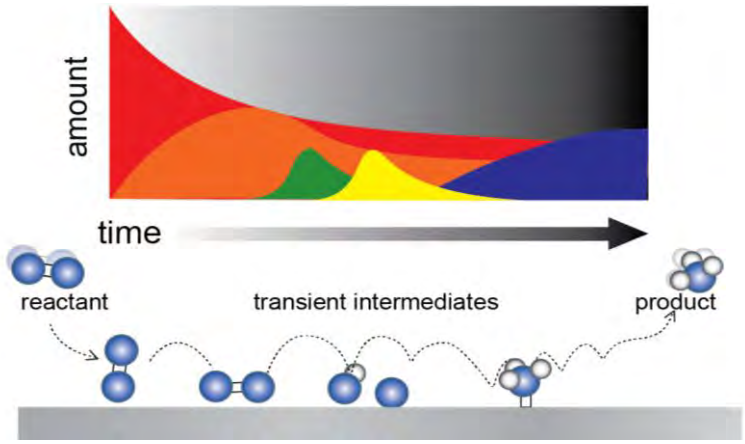

Figure 25. Elementary steps in a catalytic reaction involving molecular nitrogen and hydrogen initiated by an ultrafast temperature jump. LCLS-II will follow the concentration of reactants, various intermediates and products (color-coded) – in real time and under operating conditions.

Charge and Ion Transfer at Solid-Liquid Interfaces

Chemical reactions at solid-liquid interfaces can range from acid-base (hydrolysis) and surface complexation or adsorption reactions, to ligand exchange and electron or ion transfer reactions, to dissolution of solids, as well as their nucleation and growth when the solvent is water. For example, the compositions of surface waters, including the oceans, ground waters, and subsurface brines, are the result of mineral-aqueous solution interface reactions in which ions are released from solid surfaces into solution during chemical weathering or are removed from solution via sorption reactions on solid surfaces. The complexity of chemistry at the liquid-solid interface, as visualized in Figure 26, involves absorption/desorption, diffusion, solvation/desolvation, and the interaction between solvated and absorbed species with the dynamical surface geometric and electric structure.

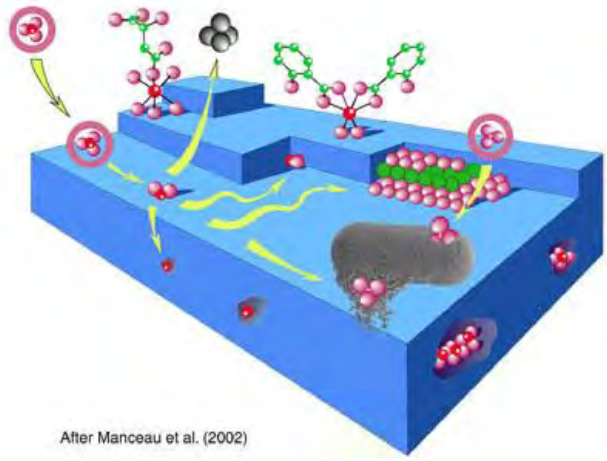

Figure 26. Processes of adsorbate molecules and atoms at mineral-water interface: physisorption, chemisorption, detachment, absorption or inclusion, occlusion, attachment, hetero-nucleation, and organo-mineral complexation (from ref. 10).

Relevant processes span a wide range of time scales, from the slow initial reorganization of nuclear and solvent coordinates, to the establishment of the transition point configurations, and the subsequent fast electron transfer between the electrode and the reactant molecules/ions. For example, cations and anions in aqueous solutions can exchange water molecules at rates ranging from ~10^{-6} sec^{-1} (about one day), which would be typical of the exchange of water molecules for hexaquo Cr^{3+} ions in aqueous solutions, to ~10^{10} sec^{-1} (about one nanosecond), which would be typical of ligand exchange reactions of Pb^{2+} or Li^{+} ions in aqueous solution.[12]

Heterogeneous chemistry at the liquid-solid interface plays a central role in emerging catalytic processes though electrochemistry. In transforming CO_2 to fuels, and nitrogen to ammonia, electrochemical reactions transfer protons from solvated liquid to adsorbed intermediates on the catalytic solid material. In spite of the importance of charge transfer processes in electrochemistry, these solid-electrolyte interfaces remain poorly understood at a fundamental level.

The structure of the liquid-solid interface has been intensively studied for over one hundred years. Our current understanding is based largely on the electrical double layer model, which was developed empirically in mid-19th to mid-20th century[13-17] (Figure 27), in which one plate is the metal surface, and the other plate is built up by solvated ions from the electrolyte. The ions in the Stern layer shield the charge of the surface, and are temporally bound to the electrode surface and immobile compared to the ions in the bulk. There are two different types of ions in the Stern layer. One has a complete solvation shell and is held in place by purely electrostatic forces in the outer Helmholtz layer. The other has only a partial solvation shell and undergoes direct chemical bonding with the solid surface, in the inner Helmholtz layer.

The structure of the electrochemical double layer is altered by the presence of an external voltage. The electric field in the layer influences the transition-state energy of the electrochemical reaction as reactant ions, molecules and electrode surfaces undergo solvation and desolvation to reach the transition point. The electrode surface, in contact with the electrochemical double layer, also undergoes solvation and desolvation processes. Once the nuclear coordinates have reached the transition point of an electrochemical reaction (Figure 28), electrochemical reaction theory assumes adiabatic electron-transfer between the electrode and the reactant molecules or ions. The rate of electron transfer at the transition point (the exchange current) determines the

Electrochemical double layer

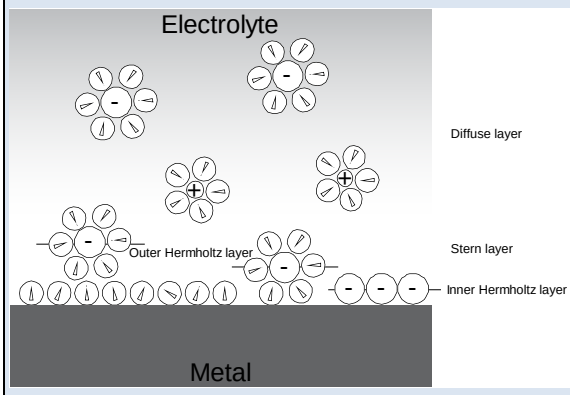

Figure 27. From ref. 11

Circles with charges denote the ions in the electrolyte. Circles with an arrow represent the polar solvent molecules.

At liquid-solid interfaces, a solvent molecule may adsorb at the surface altering the electron density distribution. Ions near the electrode surface cause an accumulation of counter charge on the surface to neutralize the charge on the electrolyte solution side. As a result, a layer consisting of surface charges and counter ions is formed at the interface: the electrical double layer.

The ions in the electrical double layer are immobile compared to the ions in the bulk. Whereas ions in the electrical double layer with complete solvation shell are held in place by purely electrostatic forces, ions with incomplete solvation shells can bond chemically to the surface.

LCLS-II capabilities (high repetition rate, greater coherence, broad tuning range) are essential new tools that will allow us to gain a fundamental understanding of interfacial behavior and the effects of structural, compositional, and temporal heterogeneities on the properties of natural and engineered solids.

electrochemical catalytic activity.

High repetition rate (moderate peak power with high average brightness) from LCLS-II will be invaluable for tracking charge and ion transfer during reactions – using advanced techniques such as time-resolved ambient-pressure photoemission and transient standing-wave techniques (see Section 2.2 Experimental Approaches and Impact of LCLS-II). Energy tunability enables resonant excitation for all constitutes in the solid-liquid interface (ions, solvent molecules, the solid surface and adsorbates) which will advance the characterization of molecular configurations and oxidation states in electrochemical reactions. Energy and time resolution near the Fourier transform limit will enable resonant X-ray Raman scattering measurements capable of identify proton transfer through molecular vibrations with site selectivity.

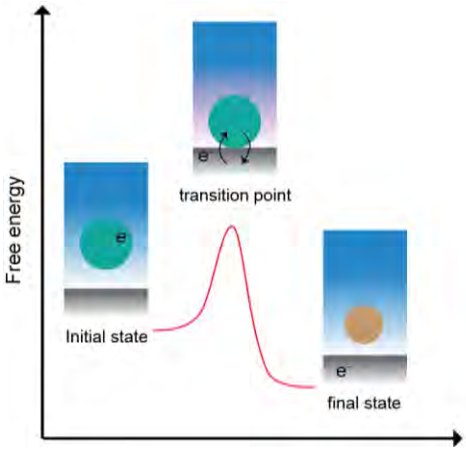

Figure 28. Free energy profiles of interfacial electron transfer process

LCLS-II studies of Catalyst Support Assemblies

The combination of synthetic control over nanostructured catalytic systems and the unique capabilities of LCLS-II will significantly advance our understanding of interface sites and putative highly-reactive short-lived species, pointing the way to produce much more active and selective heterogeneous catalysts for a variety of reactions. Among the most important pieces of information to describe catalytic properties are the atomic structural arrangement of catalytic nanoparticles, and the electronic properties of the surface – *while they are functioning*.

Nanoparticle-based catalysts most often consist of nanoparticles that are immobilized on oxide substrates to provide a large surface area. Exploring the material response as a function of environmental parameter space is exceptionally important to understand how the catalytic nanoparticles function. The stability of the as-synthesized nanoparticle is not guaranteed under reactive conditions, and changes in structure and chemical composition of catalysts are often mediated by environmental parameters including: temperature, gas pressure, or electrochemical potential.[18-24] As the structure and chemical composition deviate in a non-equilibrium fashion under reactive conditions, the catalytic properties fluctuate significantly over time. Non-equilibrium sintering dynamics on the mesoscale are responsible for structural and compositional transformations of nanoparticles on the support. Time-resolved examination under reactive conditions is essential to advance our understanding of these processes.

In addition to the surface of active nanoparticles, the interface region between the support and the active nanoparticle (illustrated in Figure 29) exhibit unique catalytic properties. There are several reports which associate the interface region with the active sites, and with the overall catalytic activity of the material, through distinct mechanisms. For example, different reactants can be activated on different surface sites and subsequently meet and combine at the interface region. Importantly, reactants can also be activated *exactly at in the interface region*, since relevant chemistry occurs at the interface that does not occur on

either of the two materials in isolation. One striking example is the supported Au catalysts used in oxidation reactions and water-gas shift-reactions. Au particles less than 5 nm in size become active for reactions such as CO oxidation, but only when they are on a support material. The importance of the Au/support interface in oxygen and water activation has been recognized, with researchers proposing Au-O-O-S (S=support) and Au-O-O-H chemical intermediates[25, 26] as illustrated in Figure 29.

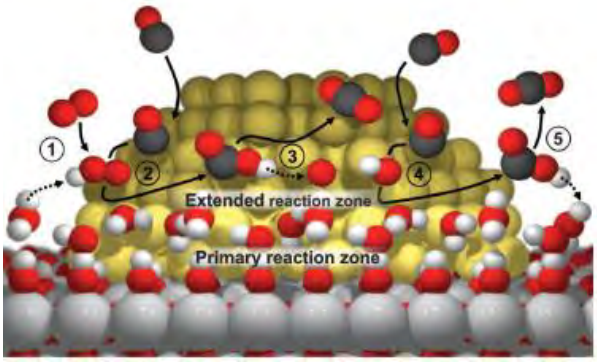

Figure 29. Catalytic CO oxidation on titania-supported Au catalyst (from ref. 26).

X-ray energy tunability will enable tracking the electronic structure changes in transition metals, post-transition metals, and C, N, O elements in supports, particles and adsorbed molecules using advanced techniques such as time-resolved ambient-pressure photoemission. Sensitivity provided by high repetition rate will be essential to probe the low concentrations of active catalytic sites (e.g. on the surface of nanoparticles or at the interface between a nanoparticle and the support). The combination energy and time resolution will allow probing non-equilibrium dynamics of nanoparticles under reactive conditions, at chemical resonances, via X-ray Photon Correlation Spectroscopy (XPCS, see Section 2.4). Mapping of chemical transformations across time scales, from femtoseconds to milliseconds, will provide an invaluable picture of these interfaces in action. LCLS-II will allow us to uncover how the charge migrates between support materials, particle surfaces, and adsorbed molecules while reactants are being converted – important information to advance our ability to predict and optimize reactivity in catalyst support assemblies.

Experimental Approaches & Impact of LCLS-II

The transformative science opportunities in the areas of catalysis, photo-catalysis, and environmental chemistry rely on a suite of time-resolved techniques that are element-specific, and sensitive to the dynamics of both local chemical structure/bonding and nuclear structure. Low concentrations and rare transient events require high sensitivity (high average flux), with moderate peak intensity (to avoid disruption of the chemistry being probed). An essential requirement is an ability to probe systems *in-situ*, and under operating conditions, which is often in condensed or liquid phases.

Pump and Probe methods for Catalytic Reactions

LCLS-II offers a unique possibility to study chemical reaction in heterogeneous systems in real-time. Time resolved spectroscopy at LCLS-II employs a pump-probe, with excitation pulses in the UV, visible, IR or THz region, and ultrafast X-ray probe pulses from LCLS-II.

Thermally-driven reactions may be triggered via a transient temperature jump. A range of thermal excitations play important roles in surface chemical reactions including: phonons (substrate lattice vibration); and frustrated vibrational, translational, and rotational motion of molecular adsorbates. When chemical bonds break/form during a reaction, these low energy vibrations in the THz regime are thermally excited and mediate the nuclear motion along the reaction coordinate.

In heterogeneous systems, thermally-driven catalytic reactions are triggered either directly or indirectly by the heat generated through coupling of hot electrons and holes to phonons. Femtosecond near-IR laser pulses are currently used to initiate surface reactions, and the time evolution is then probed using X-ray pulses. Though the absorption cross section of surface layer is small, femtosecond near-IR pulses produce highly excited hot electrons and holes at the surface which couple to the adsorbate excitations within the first picosecond. Since excitations of phonons and frustrated vibrational motion are in the THz regime, an intense ultrashort THz pulse can also be a suitable source to initiate a temperature-jump.

In addition, temperature jump techniques can be used to induce a change in the distribution of ionic species at the interface between an electrode and electrolyte materials. By selecting a laser wavelength which is transparent to the electrolyte or electrode material, a temperature gradient can be generated across the interface. The resulting temperature gradient induces a concentration gradient of components in the electrolyte (known as the Soret effect[27]), which will create a transient electrochemical perturbation at the interface for time-resolved X-ray studies (e.g. of ion exchange).

Photon-in/Photon-out X-ray Absorption and Resonant Inelastic X-ray Scattering

Resonant inelastic X-ray scattering (RIXS) will be a powerful tool for meeting the above challenges, and the capabilities of LCLS-II offer a major advance for RIXS spectroscopy beyond anything available today. RIXS is a spontaneous X-ray Raman process that uniquely provides information on both occupied and unoccupied valence states, probed from 1*s* (e.g. C, O, N) and *2p* (e.g. Co, Mn, Fe, Ir) core levels to achieve chemical specificity. RIXS is further sensitive to correlated multi-particle valence states. As a photon-in/photon-out technique, RIXS is particularly well-suited to *in-situ* and *operando* studies. A complete 2D RIXS map (energy loss vs. incident photon energy tuned though an absorption edge) is rich in scientific information, and LCLS-II will provide sequences of 2D RIXS maps over the entire time-course of a reaction (from femtoseconds to msec). X-ray emission spectroscopy (XES or non-resonant RIXS) is a related technique, providing 1D information on the partially occupied density of states, and X-ray absorption spectroscopy (XAS) reveals the unoccupied density of states. Both XES and XAS spectra are contained within a 2D RIXS map.

Unique capabilities for time-resolved RIXS provided by LCLS-II include:

Photon energy tunability through absorption edges of light elements (C, N, O) and 3*d* and 4*d* transition metals, pertaining the unique ability of tunable X-rays to provide selectivity through resonant excitation.

High repetition rate/high average brightness. Time-resolved RIXS at LCLS is severely limited by the low repetition rate, requiring ~1 day of integration for a single RIXS map from a high concentration (~1M) sample. High average brightness is essential to generate a complete time-series of maps in functional systems (~1mM concentrations).

Time and energy resolution near the Fourier transform limit is essential to resolve XANES features that are unique signatures of oxidation states and chemical intermediates (200meV), and for resolving ultrafast dynamics such as intersystem crossings and charge transfer (10fs).

The combination of Fourier transform limited resolution (<50 meV) and extremely high average brightness provides the opportunity to perform resonance Raman scattering measurements capable of resolving low frequency molecular vibrations with site selectivity. LCLS-II will be able to investigate both the steady state and non-equilibrium structure of reactants and intermediates bound to metal sites with spin and charge state selectivity. Since such experiments need not be focused on ultrafast time resolution to be state-of-the-art, they would broaden the scientific reach of LCLS-II significantly since they present significant potential value in both heterogeneous and metalloenzyme catalysis (as discussed in Section 2.6).

The combination of Fourier-transform-limited resolution and extremely high average brightness could prove to be the most critical beneficiary of non-linear X-ray spectroscopic methods. While still in the early stages of development, these methods have the potential to provide the same information as spontaneous RIXS measurements with greater efficiency and a much smaller instrument. Beyond spontaneous X-ray Raman, stimulated X-ray Raman scattering (SXRS) as discussed in Section 3.1 provides information on coherent charge flow and energy relaxation on fundamental (attosecond to femtosecond) time scales. This is also a promising approach for enhancing weak spontaneous X-ray Raman signals (e.g. from low-Z elements) and projecting the signal of interest to a 1D detector.

X-ray Photoelectron Spectroscopy (XPS) and Ambient Pressure XPS Dynamics of Electrochemical Interfaces

XPS probes the energy distribution of molecular orbitals with very high resolution and sensitivity to the local chemical state. Time-resolved XPS identifies chemical states in short-lived reaction intermediates (Figure 30). LCLS-II will provide unprecedented average brightness, which will enable science beyond simple model systems and highly concentrated samples that are accessible today. In recent years, we have seen a rapid development of ambient pressure XPS where measurements can be conducted at pressures around 1 torr and above,[28-35] and this has proven to be a powerful tool for probing electrochemical interfaces.[29, 33, 36, 37] Detailed understanding of catalytic reactions on surfaces requires simultaneous observation of the electronic transformations and the rearrangement of the atoms, in particular under catalytically relevant conditions of elevated pressure and temperature. LCLS-II will provide the key attributes to uncover these processes in real time.

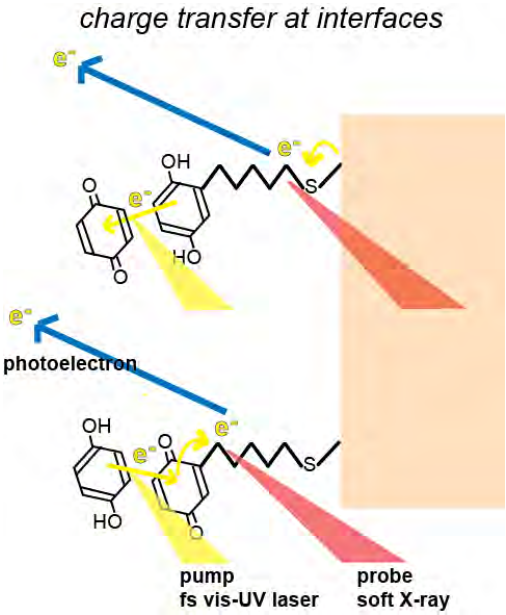

Figure 30. Chemical shift measurements provide high chemical specificity for both molecules on the surface and the substrate. XPS with differential pumping will allow for pressures in the few torr range which can be extended to even higher pressures using photon energies in the few keV range (generating high kinetic-energy photoelectrons with a substantial longer mean free path).

High repetition rate/high average brightness will significantly increase the number of X-ray interaction events with the system under study. The information content of current XPS measurements at LCLS is significantly limited by the low repetition rate. High repetition rate is critical to achieve reasonable count rates via time-of-flight spectroscopy by distributing the X-ray power over many pulses in order to mitigate space-charge effects.

Time and energy resolution near the Fourier transform limit (100 fs ⇔ 20 meV) from seeded X-ray FELs at LCLS-II will enable high energy-resolution and/or high time-resolution XPS, pushing to the sub-femtosecond limit for the fastest electronic events, and meV energy resolution for slower nuclear dynamics.

Photon energy tunability is critical to adjust the probing depth of XPS, varying the mean free path of photoelectrons from the surface, subsurface, and bulk. This will enable studies of gas/solid, liquid/solid and gas/liquid interfaces. It has also been recently demonstrated that tailoring the X-ray intensity into a standing-wave (SW) and then scanning the SW through the sample provides unprecedented resolution of species at the solid/liquid interface.[38, 39] Recently, ambient-pressure photoemission spectroscopy (APXPS) has been developed at synchrotron sources as powerful tool for *in-situ* investigation of electrochemical interfaces.[29, 33, 36, 37] Key attributes include simultaneous and quantitative characterization of the local elemental composition, chemical state, and electrical potentials, which allows for a direct correlation between the chemical state and the electrical properties of the interface (see ref. 40 and Figure 30). When combined with more traditional electrochemical characterization techniques such as voltammetry, a much more complete picture of the bulk and surface properties under operating conditions can be achieved.

There are two recent developments in APXPS that have made it even more powerful for catalysis and interfacial chemistry applications. First, APXPS has recently been extended from studies of only the gas-solid interface to studies of the liquid-solid interface using "tender" X-rays in the 3-5 keV regime. At these energies, photoelectrons can escape through an ultrathin liquid film (or meniscus) that is in equilibrium with an operating electrochemical cell.[37] Second, it has also been recently demonstrated that tailoring the X-ray intensity into a standing-wave (SW) and then scanning the SW through the sample provides unprecedented resolution of species at the solid/liquid interface.[38, 39] With APXPS techniques at LCLS-II, both the composition of interfacial species (EDL, SEI, intermediates...) and the *dynamics* of interfacial phenomena can be studied with great spatial resolution under electrostatic polarization for the first time.

References

1. B. K. Teo, *EXAFS: Basic principles and data analysis* (Springer-Verlag, Berlin, 1986).
2. S. E. Canton, K. S. Kjær, G. Vankó, T. B. van Driel, S.-i. Adachi, A. Bordage, et al., "Visualizing the non-equilibrium dynamics of photoinduced intramolecular electron transfer with femtosecond X-ray pulses," Nat Commun **6**, 6359 (2015).
3. P. Wernet, K. Kunnus, I. Josefsson, I. Rajkovic, W. Quevedo, M. Beye, et al., "Orbital-specific mapping of the ligand exchange dynamics of $Fe(CO)_5$ in solution," Nature **520**, 78 (2015).
4. W. Kim, G. Yuan, B. A. McClure, and H. Frei, "Light Induced Carbon Dioxide Reduction by Water at Binuclear $ZrOCo^{II}$ Unit Coupled to Ir Oxide Nanocluster Catalyst," Journal of the American Chemical Society **136**, 11034 (2014).
5. M. Zhang, M. de Respinis, and H. Frei, "Time-resolved observations of water oxidation intermediates on a cobalt oxide nanoparticle catalyst," Nat Chem **6**, 362 (2014).
6. M. Dell'Angela, T. Anniyev, M. Beye, R. Coffee, A. Föhlisch, J. Gladh, et al., "Real-Time Observation of Surface Bond Breaking with an X-ray Laser," Science **339**, 1302 (2013).
7. H. Öström, H. Öberg, H. Xin, J. LaRue, M. Beye, M. Dell'Angela, et al., "Probing the transition state region in catalytic CO oxidation on Ru," Science **347**, 978 (2015).
8. V. Smil, "Detonator of the population explosion," Nature **400**, 415 (1999).
9. S. Dahl, A. Logadottir, R. C. Egeberg, J. H. Larsen, I. Chorkendorff, E. Törnqvist, et al., "Role of Steps in N_2 Activation on Ru(0001)," Physical Review Letters **83**, 1814 (1999).
10. A. Manceau, M. A. Marcus, and N. Tamura, "Quantitative speciation of heavy metals in soils and sediments by synchrotron X-ray techniques," in *Applications of Synchrotron Radiation in Low-Temperature Geochemistry and Environmental Science*, P. Fenter, M. Rivers, N. C. Sturchio, and S. Sutton, eds. (Reviews in Mineralogy and Geochemistry, Mineralogical Society of America, Washington, D.C., 2002), pp. 341.
11. P. Strasser, and H. Ogasawara, "Chapter 6 - Surface electrochemistry," in *Chemical Bonding at Surfaces and Interfaces*, A. N. G. M. P. K. Nørskov, ed. (Elsevier, Amsterdam, 2008), pp. 397.
12. L. L. Pesterfield, "Ions in Solution—Basic Principles of Chemical Interaction, 2nd Edition (Burgess, John)," Journal of Chemical Education **78**, 456 (2001).

13. H. Helmholtz, "Ueber einige Gesetze der Vertheilung elektrischer Ströme in körperlichen Leitern mit Anwendung auf die thierisch-elektrischen Versuche," Annalen der Physik **165**, 211 (1853).
14. M. Gouy, "Sur la constitution de la charge électrique à la surface d'un électrolyte," J. Phys. Theor. Appl. **9**, 457 (1910).
15. D. L. Chapman, "LI. A contribution to the theory of electrocapillarity," Philosophical Magazine Series 6 **25**, 475 (1913).
16. O. Stern, "Zur theorie der elektrolytischen doppelschist," Zur theorie der elektrolytischen doppelschist **30**, 508 (1924).
17. D. C. Grahame, "The Electrical Double Layer and the Theory of Electrocapillarity," Chemical Reviews **41**, 441 (1947).
18. J. A. Dumesic, H. Topsøe, and M. Boudart, "Surface, catalytic and magnetic properties of small iron particles: III. Nitrogen induced surface reconstruction," Journal of Catalysis **37**, 513 (1975).
19. N.-Y. Topsøe, and H. Topsøe, "On the nature of surface structural changes in Cu/ZnO methanol synthesis catalysts," Topics in Catalysis **8**, 267 (1999).
20. T. W. Hansen, J. B. Wagner, P. L. Hansen, S. Dahl, H. Topsøe, and C. J. H. Jacobsen, "Atomic-Resolution in Situ Transmission Electron Microscopy of a Promoter of a Heterogeneous Catalyst," Science **294**, 1508 (2001).
21. P. L. Hansen, J. B. Wagner, S. Helveg, J. R. Rostrup-Nielsen, B. S. Clausen, and H. Topsøe, "Atom-Resolved Imaging of Dynamic Shape Changes in Supported Copper Nanocrystals," Science **295**, 2053 (2002).
22. Y. Nishihata, J. Mizuki, T. Akao, H. Tanaka, M. Uenishi, M. Kimura, et al., "Self-regeneration of a Pd-perovskite catalyst for automotive emissions control," Nature **418**, 164 (2002).
23. H. Tanaka, M. Uenishi, M. Taniguchi, I. Tan, K. Narita, M. Kimura, et al., "The intelligent catalyst having the self-regenerative function of Pd, Rh and Pt for automotive emissions control," Catalysis Today **117**, 321 (2006).
24. P. Nolte, A. Stierle, N. Y. Jin-Phillipp, N. Kasper, T. U. Schulli, and H. Dosch, "Shape Changes of Supported Rh Nanoparticles During Oxidation and Reduction Cycles," Science **321**, 1654 (2008).
25. I. X. Green, W. Tang, M. Neurock, and J. T. Yates, "Spectroscopic Observation of Dual Catalytic Sites During Oxidation of CO on a Au/TiO2 Catalyst," Science **333**, 736 (2011).
26. J. Saavedra, H. A. Doan, C. J. Pursell, L. C. Grabow, and B. D. Chandler, "The critical role of water at the gold-titania interface in catalytic CO oxidation," Science **345**, 1599 (2014).
27. C. Soret, Arch. Sci. Phys. Nat **2**, 48 (1879).
28. D. E. Starr, H. Bluhm, Z. Liu, A. Knop-Gericke, and M. Hävecker, "Application of Ambient Pressure X-ray Photoelectron Spectroscopy for the In-situ Investigation of Catalytically Relevant Processes," in *In-situ Characterization of Heterogeneous Catalysts*, J. A. Rodriguez, J. C. Hanson, and P. J. Chupas, eds. (John Wiley & Sons, Inc., NY, 2013), pp. 315.
29. M. Salmeron, and R. Schlögl, "Ambient pressure photoelectron spectroscopy: A new tool for surface science and nanotechnology," Surface Science Reports **63**, 169 (2008).
30. A. Knop-Gericke, E. Kleimenov, M. Hävecker, R. Blume, D. Teschner, S. Zafeiratos, et al., "High-pressure X-ray photoelectron spectroscopy: a tool to investigate heterogeneous catalytic processes,," in *Advances in Catalysis*, B. C. Gates, and H. Knözinger, eds. (Academic Press, Burlington, 2009), pp. 213.
31. H. Bluhm, "Photoelectron spectroscopy of surfaces under humid conditions," J. Electron Spectrosc. Relat. Phenom. **177**, 71 (2010).
32. J. Schnadt, J. Knudsen, J. N. Andersen, H. Siegbahn, A. Pietzsch, F. Hennies, et al., "The new ambient-pressure X-ray photoelectron spectroscopy instrument at MAX-lab," Journal of Synchrotron Radiation **19**, 701 (2012).
33. D. E. Starr, Z. Liu, M. Havecker, A. Knop-Gericke, and H. Bluhm, "Investigation of solid/vapor interfaces using ambient pressure X-ray photoelectron spectroscopy," Chemical Society Reviews **42**, 5833 (2013).
34. A. Shavorskiy, and H. Bluhm, "Ambient pressure X-ray photoelectron spectroscopy," in *Handbook of Heterogeneous Catalysts for Clean Technology – Design, Analysis and Application*, K. Wilson, and A. Lee, eds. (Wiley-VCH, Weinheim, Germany, 2013).
35. S. Kaya, H. Ogasawara, L.-Å. Näslund, J.-O. Forsell, H. S. Casalongue, D. J. Miller, et al., "Ambient-pressure photoelectron spectroscopy for heterogeneous catalysis and electrochemistry," Catalysis Today **205**, 101 (2013).

36. E. J. Crumlin, H. Bluhm, and Z. Liu, "In situ investigation of electrochemical devices using ambient pressure photoelectron spectroscopy," Journal of Electron Spectroscopy and Related Phenomena **190A**, 84 (2013).
37. S. Axnanda, E. J. Crumlin, B. Mao, S. Rani, R. Chang, P. G. Karlsson, et al., "Using "Tender" X-ray Ambient Pressure X-Ray Photoelectron Spectroscopy as A Direct Probe of Solid-Liquid Interface," Sci. Rep. **5**, 9788 (2015).
38. S. Nemšák, A. Shavorskiy, O. Karslioglu, I. Zegkinoglou, A. Rattanachata, C. S. Conlon, et al., "Concentration and chemical-state profiles at heterogeneous interfaces with sub-nm accuracy from standing-wave ambient-pressure photoemission," Nat Commun **5**, 5441 (2014).
39. O. Karslioglu, S. Nemsak, I. Zegkinoglou, A. Shavorskiy, M. Hartl, F. Salmassi, et al., "Aqueous Solution/Metal Interfaces Investigated in operando by Photoelectron Spectroscopy," Faraday Discussions, in press (2015).
40. C. Zhang, M. E. Grass, A. H. McDaniel, S. C. DeCaluwe, F. E. Gabaly, Z. Liu, et al., "Measuring fundamental properties in operating solid oxide electrochemical cells by using in situ X-ray photoelectron spectroscopy," Nat Mater **9**, 944 (2010).

2.3 Quantum Materials

2.3.1 Understanding and controlling emergent phenomena in materials with interacting degrees of freedom

Synopsis

"Quantum materials" refers broadly to solids that are not adequately described by single-electron band models and the related theories that provided the foundational basis for the semiconductor revolution of the 20th century. Quantum materials are promising materials for the 21st century — materials with powerful "emergent" properties such as high-temperature superconductivity, colossal magnetoresistivity, and topologically protected phases. Such properties are referred to as "emergent" because they cannot be understood or predicted based on a reductionist approach that considers only the constituent particles — individual atoms, electrons and their orbitals. Rather, we must also account for the strong coupling between these particles at the quantum level, and this extra complexity pushes the limits of our understanding. This knowledge gap prevents us from fully harnessing the emergent properties of quantum materials in order to address the technology applications that are at the frontier of modern electronics: from quantum information processing to superconducting electrical grids to nano-device engineering. A better understanding and control of the materials themselves is essential to developing their potential for these applications.

LCLS-II X-ray lasers will provide qualitatively new experimental capabilities for observing the energetically-fragile many-electron dynamics of quantum materials. The high repetition rate and high average spectral brightness of LCLS-II will enable photon-hungry spectroscopies such as Resonant Inelastic X-ray Scattering (RIXS) to finally achieve the energy and momentum resolution required to characterize the correlated states for effective comparison with theoretical predictions. Ultrafast time resolution applied with RIXS and advanced photoemission techniques will enable the observation of correlated states in the bulk (and in low-dimensional interfaces) as they develop and respond to specific excitations of the material. Importantly, the high repetition rate will make it practical to investigate these fragile states with moderate pulse energies (while maintaining high signal rate) in order to avoid disrupting the states being measured.

Direct probes of charge correlations and their dynamics have long been recognized as a critical capability gap of modern materials science. Bridging this gap requires the capabilities of LCLS-II and will propel the ability to use quantum materials in technology areas ranging from efficient energy transport to low-power/high-speed information processing and high-density information storage.

Introduction

A hallmark of quantum materials is the significant role played by quantum mechanics in determining the exotic properties that these compounds typically exhibit. These solids are not adequately described by the single-electron band models and related theories that provided the basis for the semiconductor revolution of the 20th century. Their properties are often termed "emergent" because they cannot be directly predicted by simple consideration of the constituent particles: individual atoms, electrons, their orbitals, and spins. Rather the strong coupling of these particles leads to exotic quantum phases and important properties such as unconventional high-temperature superconductivity, colossal magnetoresistivity, ferroelectricity, and topologically protected phases – properties that we wish to harness and control for myriad technology applications.

Furthermore, the delicate interplay between these electronic phases in quantum materials often gives rise to competition (phase separation) and heterogeneity – including nanoscale ordering or texture of charge, spin and orbitals – that are intimately related to the material properties. These phases exhibit temporal and spatial fluctuations over many time and length scales (see Section 2.4), and are very sensitive to

manipulation through chemical composition, charge doping, or external stimuli such as electro-magnetic fields.[1]

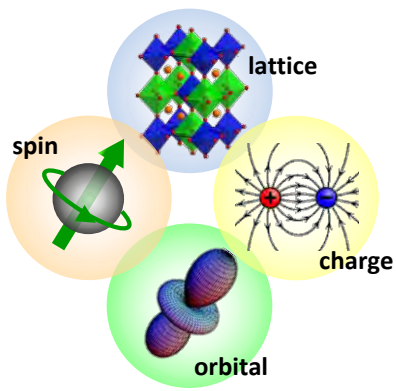

Figure 31: Strongly coupled spin, orbital, lattice, and charge degrees of freedom gives rise to rich phenomena in quantum materials.

The scientific richness of quantum materials and the major knowledge gaps in the field are illustrated in Figure 32 in terms of the strength of the interactions between the lowest electronic states with other degrees of freedom, and the strength of the spin-orbit coupling. Conventional metals — band insulators and semiconductors that are the mainstay of modern technology — are materials in the weak-coupling region. Here, the paradigm of Fermi-liquid theory and the conventional weak-coupling phase transition formalism satisfactorily explain the material properties. Quantum materials, however, reside outside this weak-coupling region, and understanding their rich electronic behavior requires new concepts beyond the conventional paradigms, and new experimental approaches that provide direct insight to collective modes in the strong-coupling regime.

Strongly-correlated electron systems represent one important frontier where the interaction strength is strong but spin-orbit (SO) coupling is negligible in determining the low-energy electronic states. The *3d* transition metal oxides, such as the high temperature (high-T_c) superconducting cuprates, are representative strongly correlated electron systems in this regime (see for example ref. 1). The fundamental model for understanding an interacting electron system in terms of the charged collective modes dates back to the 1950s treatment by Pines and Nozieres. They described the low-energy fermions as Landau qausiparticles and identified the elementary collective excitation as the well-known plasmon. The former are observed, for example, as a peak in the one-particle spectral function, $A(\boldsymbol{k},\omega)$, and the latter as a peak in the two-particle, dynamic structure factor, $S(\boldsymbol{q},\omega)$.

Remarkably, while the study of quasiparticles in quantum materials is now well advanced, we are still lacking an effective means to directly probe and study the collective modes. Because the ground states of quantum materials arise from a subtle balance among competing interactions, the relevant collective modes appear at modest energy, typically 1 to 100 meV (see Figure 38), where modern X-ray sources and scattering spectrometers lack the required combination of photon flux and energy resolution. The absence of a means to measure ground-state collective modes – *the essential observable of an interacting electron system* – represents an enormous gap in our understanding of quantum materials. It is in this area that LCLS-II will offer transformative capabilities – for both characterizing ground-state collective modes, and for following their response to tailored external stimuli.

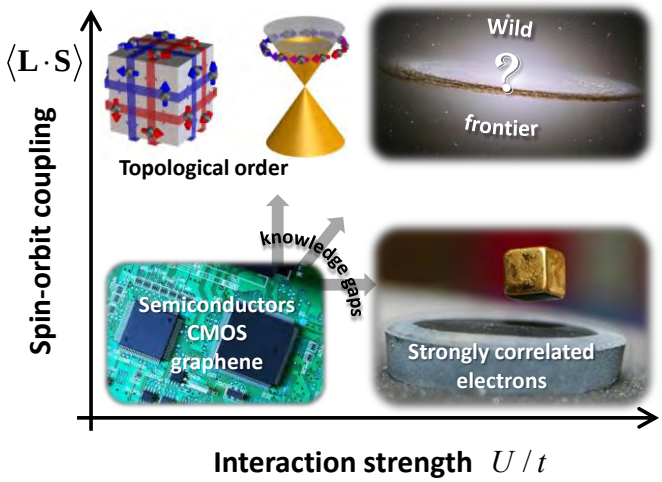

Figure 32: Classification of materials via spin-orbital coupling and interaction strength between low energy electronic states with other degrees of freedom, such as electron-phonon coupling, magnetic interaction, and other correlation effects.

Materials in the strong spin-orbit coupling limit have recently drawn much attention in the materials science community. The resulting effects of topological order and quantum geometry[2, 3] have been extensively explored in topological insulators and transition metal dichalcogenides. Here conventional band structure models provide an incomplete description of the charge and spin behaviors because they fail to capture the quantum geometry of the electronic wavefunctions, as embodied in the "Berry curvature" in momentum space – which is now understood to be at the heart of electronic phenomena both ancient (electric polarization) and modern (topological insulators and magneto-electricity). Berry curvature in real space describes the motion of electrons through a background of skyrmions (particle-like texture of spins, as discussed in Section 2.4).

Until recently, the role of spin-orbit coupling as an origin of new phenomena in strongly correlated materials has been largely overlooked. In this "wild frontier" (illustrated in Figure 32), there is now significant interest in searching for topological order in materials with strong interactions.[4] For example, electron correlation can result in frustrated magnetic order and high-T_c superconductivity, while strong SO coupling can create a novel electronic structure that is topologically protected by quantum-geometrical constraints, leading to a tantalizing prospect of topologically protected superconductivity. In this region, exemplified by heavy Fermion systems with *4f* valence electrons, both material synthesis and experimental characterization are largely exploratory but there is tremendous promise for discovering entirely new phenomena.

Revealing the fundamental origins of important emergent properties and ultimately controlling these quantum phases remain paramount open questions in the quantum materials field. While strongly correlated materials have been most intensely studied over the last few decades, the mechanism of high temperature superconductivity exhibited in cuprates and iron pnictides remains a puzzle. Novel theories and new experimental tools are required to make breakthroughs in these outstanding areas.

Notably, due to the rapid development of techniques, new approaches to tune interactions in quantum materials have been demonstrated. One is to facilitate interface engineering of quantum material heterostructures[5, 6] by material synthesis with atomic precision via molecular beam epitaxy (MBE) and Pulsed Laser Deposition (PLD). Surprising emergent phenomena have been discovered at these interfaces. Another intriguing approach is to drive the system out of equilibrium via tailored ultrafast photo-excitation or coherent vibrational excitation. Photo-induced superconductivity[7] and vibrationally-drive phase transitions[8] have been demonstrated in some quantum materials. In both approaches, the underlying microscopic picture of the observed phenomena is still lacking and highly debated. Progress in understanding these phenomena will provide new perspectives on quantum materials research, but requires the development of novel experimental tools well suited to characterizing the properties of

quantum materials and heterostructures, both in and out of equilibrium − unique opportunities brought by LCLS-II.

Unconventional "bulk" superconductors:

The most representative problem in quantum materials research is probably high-temperature superconductivity (HTSC), which is not only the honing stone for new theories and experimental techniques but also promises crucial applications in energy and electronic devices. Despite huge efforts, outstanding questions remain:

What are the microscopic interactions leading to HTSC?

What is the role of competing phases, fluctuations and heterogeneity (e.g. charge and spin order)?

How can we control these interactions and ultimately increase T_c?

As spin, charge, orbital and lattice excitations are fingerprints of this collective emergence, it is crucial to obtain a complete "genomic map" of collective low-energy excitations resulting from relevant degrees of freedom that define the physical properties of materials.

To date, momentum-resolved spectroscopies, such as angle-resolved photoemission spectroscopy (ARPES) and inelastic neutron scattering (INS), have revealed much information about single particle spectral functions and magnetic excitations in HTSC materials. However, information about the collective charge excitations and orbital excitations in energy-momentum space is still lacking. Recently, momentum-resolved resonant inelastic X-ray scattering (RIXS) has emerged as a powerful tool to characterize elementary excitations associated with lattice, spin, charge, and orbital degrees of freedom[9] (e.g., Figure 33). However, the full impact of this photon-hungry approach has been limited by the spectral brightness available from present X-ray sources lacking longitudinal coherence. High resolution RIXS exploiting seeded X-ray lasers at LCLS-II can reveal elementary excitations with energy scales comparable to the superconducting gap, pseudogap, and related low-energy phenomena, providing crucial information to characterize the complete bosonic spectrum that couples to electrons. Importantly, using time-resolved RIXS at LCLS-II, it is possible to track the evolution of elementary excitations in the time domain following tailored perturbations near equilibrium. This approach disentangles correlated phenomena based on characteristic time scales in response to either optical excitation (photo-doping and charge-transfer) or vibrational excitations (phonon coupling).

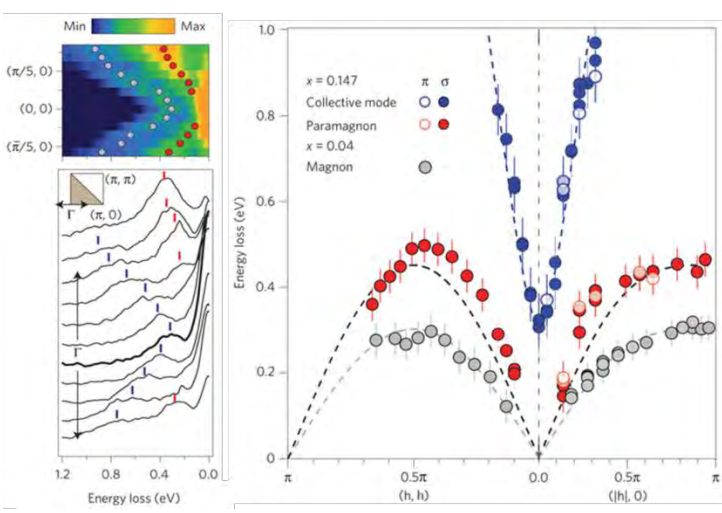

Figure 33: (Upper left) RIXS intensity map in energy-momentum space near the zone center of electron-doped superconducting cuprates $Nd_{1.85}Ce_{0.15}CuO_4$. The spectra were plotted in the low panel. (Right) Momentum-energy dispersion of magnon, para-magnon, and collective modes in electron-doped cuprates, with doping level of 4% and 15%, from ref. 10. High resolution RIXS could reveal new excitations at energy scales comparable to superconducting gap. In addition, time-resolved RIXS can reveal the relation between these collective excitations from different degrees of freedom.

In HTSC materials, applied magnetic fields provide important insight into the role of spin ordering, competing phases, and putative quantum critical phenomena. For example, transport measurements at high magnetic fields have revealed reconstructed Fermi surface[11] and the existence of two quantum critical points[12] inside the superconducting dome in the temperature-doping phase diagram. Crucial information about the microscopic degrees of freedom could be obtained, if X-ray scattering and RIXS can be performed at magnetic fields comparable to those used in these transport measurements. The ultra-bright X-ray FEL pulses with the tunable time structure make it possible to perform X-ray scattering/spectroscopy with a high-field-pulsed magnet. Furthermore, the role of competing phases in HTSC may also be closely related to the electronic inhomogeneity discovered via scanning tunneling microscopy (STM).[13] While STM spectra provides direct real-space information about static inhomogeneity, the varied energy/momentum space electronic structure in different regions (and the way in which it fluctuates) is beyond the capabilities of current tools. LCLS-II will provide the first access to such phenomena via time-of-flight, 3D imaging nano-ARPES, and via X-ray photon correlation spectroscopy (XPCS, as discussed in Section 2.4).

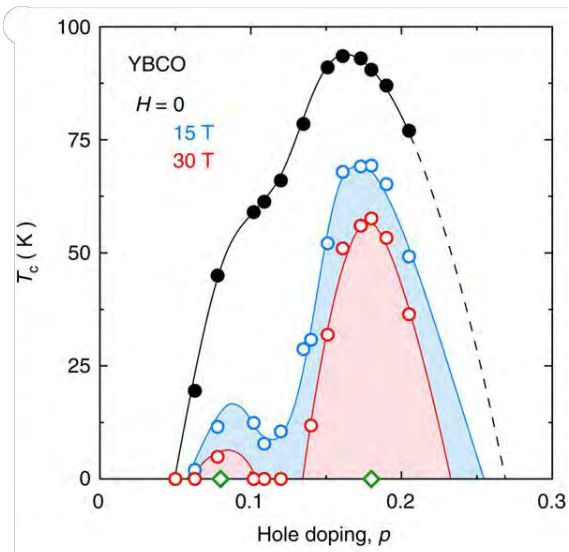

Figure 34: Two quantum critical points under the SC dome in cuprates revealed by transport measurements under high magnetic fields, from ref. 12. Important microscopic pictures can be obtained if X-ray scattering and RIXS can be performed at high field pulsed magnet, which could be achieved at LCLS-II.

Notably, the approaches outlined in this section are not only limited to the studies of HTSC, but are generally applicable to the investigation of similar electronic texture phenomena that are ubiquitous in quantum materials.

Emergent properties at the interface of quantum materials heterostructure

In addition to bulk quantum materials, rich emergent phenomena also occur at the interfaces of heterostructures consisting of distinct quantum materials. A well-known example is the interface of the $LaAlO_3/SrTiO_3$ heterostructure, at which exotic magnetic phases, superconductivity, and two dimensional electron gas with high mobility are discovered.[14-16] As another example, it was recently discovered that the T_C of interfacial superconductivity in monolayer FeSe grown on $SrTiO_3$ (FeSe/STO) can be as high as 100 K.[17-21] — significantly higher than T_C of bulk FeSe (8K). Yet another example: the monolayer transition metal dichalcogenides, such as MoS_2 and WSe_2,[22-24] have been shown to be direct band-gap semiconductors rather than indirect band-gap, as in the bulk form, which may allow for valley-dependent carrier spin polarization – a basis of valleytronic applications. Presumably, these exciting emergent phenomena occur because of strain, orbital reconstruction, and quantum confinement effects at the interface between constituent quantum materials.[5, 6] However, direct experimental probes that can reveal information about microscopic behavior of the underlying degrees of freedom is still lacking.

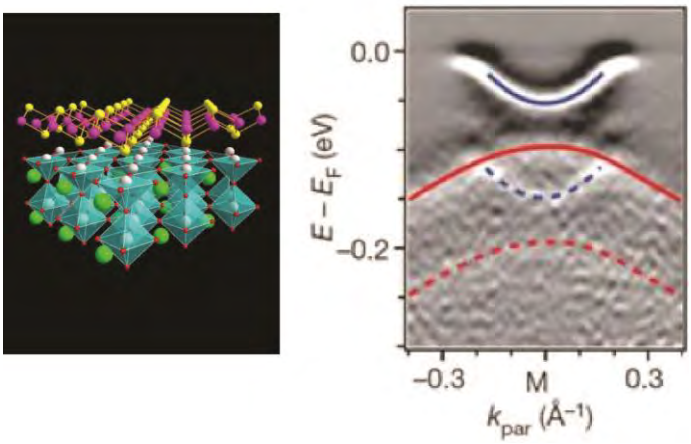

Figure 35: Electronic structure of monolayer FeSe/STO with bare bands (solid lines) and shake-off bands (dashed lines), from ref. 21. Using RIXS, one could further reveal the behavior of spin and phonons in this system.

Momentum-resolved RIXS can measure the elementary excitations of spin, charge, lattice and orbital degrees of freedom to characterize associated reconstruction in quantum materials heterostructures. For example, RIXS can directly map the phonon and magnetic excitations in FeSe/STO systems, providing critical new insight into the mechanism of the interfacial superconductivity. Note that the unprecedented high average photon flux in a narrow bandwidth available from LCLS-II (seeded operation at high repetition rate) provides the sensitivity needed to probe these monolayer systems. This capability similarly opens for study heterostructures with repetitive super-lattice layers. Importantly, element-specific information can be obtained by tuning the incident photon energy to the absorption edges of the elements of interest (in specific bonding geometries), thereby providing crucial information to clarify the role of individual building blocks.

An exciting opportunity is to manipulate quantum heterostructure via tailored near-equilibrium excitation.[25, 26] Structural distortions, such as the tilting of octahedrons in a transition metal oxide heterostructure, often couple to specific optical phonon modes. Selective coherent excitation of these modes may be used to create transient structural distortions as a means of manipulating the electronic properties to reveal new emergent phenomena and metastable phases. The recent development of standing-wave soft and hard X-ray ARPES from such heterostructures provides detailed information on interface properties, including momentum resolution.[27, 28] Powerful new tools, such as time-resolved RIXS and time-resolved hard X-ray ARPES at LCLS-II, will provide the first characterization of the time evolution of the underlying bosonic and fermionic excitations in quantum materials heterostructures driven out of equilibrium by tailored excitations.

Transient fields and time-domain disentanglement of couplings

A promising new approach to controlling quantum phases and emergent properties is to exploit coherent light-matter interactions. Especially important is the ability to drive a material directly on the low energy scales at which fundamental excitations are found, e.g. phonons, plasmons, magnons or other collective modes. While many conventional probes have studied the behavior of these excitations as quasi-static parameters have been tuned (e.g. as the materials is driven through a phase transition), their nonlinear response has not been studied in detail. It is possible to use ultrafast pulses spanning the visible-to-THz regimes to induce coherent collective excitations[29-31] and/or to temporally alter the strongly intertwined degrees of freedom to create new states that are inaccessible in thermal equilibrium.[7] These novel photo-induced phenomena are ultimately related to the mechanisms of emergent phenomena in equilibrium. Traditionally, optical pulses are used for pump-probe experiments. The availability of intense ultrafast mid-IR/THz source now allows for tailored pumping and for spectroscopic probing. For example, experiments have demonstrated vibrationally-driven insulator-metal transitions,[8] SDW transition,[32] and even HTSC in cuprates.[7] Most recently, signatures of photo-induced HTSC at 200K were reported on K-

doped C_{60},[33] indicating an entirely new route to achieve HTSC. Our understanding of these transient phenomena is still developing, but the evidence for coherent manipulation of emergent phenomena is tantalizing.

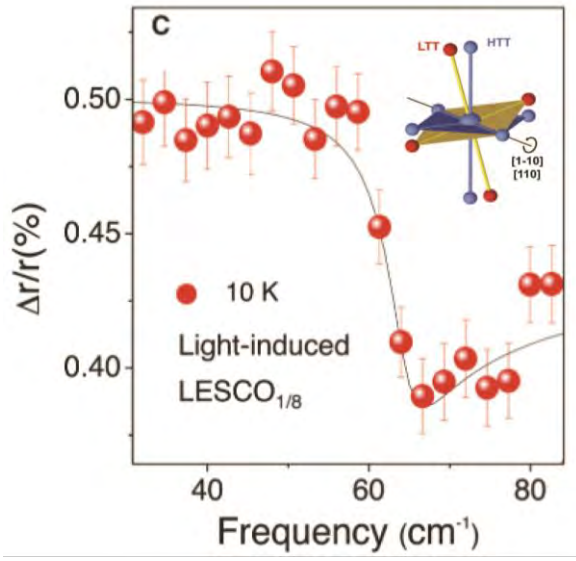

Figure 36: Photo-induced superconductivity in a charge stripe-ordered cuprate, Eu-doped $La_{1.875}Sr_{0.125}CuO_4$, from ref. 7. Using time-resolved RIXS, the time evolution of magnetic excitations, phonons, and the charge stripe order can be revealed simultaneously.

To date, time-resolved mid-IR spectroscopy provides information about the charge channel (e.g. optical conductivity and interlayer Josephson plasma resonance), but microscopic information of the underlying degrees of freedom and their coupling is still lacking. Crucial pieces of information can be provided by time- and momentum-resolved RIXS at LCLS-II. For example, in the case of photo-induced HTSC in cuprates (Figure 36), time-resolved RIXS at Cu *L*-edges can measure the time-evolution of magnetic excitations and phonons in energy-momentum space, providing a more complete microscopic picture about this photo-induced HTSC. Furthermore, the time-evolution of charge stripe order, a co-existing state in superconducting cuprates, and its associated excitations can be simultaneously monitored. This will shed a new light on the hotly debated issue concerning the role of charge order in HTSC. This approach is applicable to many other outstanding problems in cuprates, such as the relation of recently discovered collective modes near the zone center and the role of magnetic fluctuations in the electron-doped cuprates (Figure 33).

High field studies of quantum magnetism

The application of high magnetic fields is a crucial tool in studies of quantum magnetism and correlated electron systems. In high-temperature cuprate superconductors, the upper critical fields are typically greater than 60 Tesla. Hence, pulsed fields with X-rays would open the door to studying normal state excitations at low temperatures in the cleanest systems. In quantum magnets, applying magnetic fields allows for the exploration of competing ground states in the extended phase diagram. For example, one of the most interesting states of magnetism is the quantum spin liquid. In a quantum spin liquid the spins are strongly interacting and entangled yet still remain disordered at very low temperatures. This state plays a central role in many theories of high-T_C superconductivity in the cuprates, and may find use as topologically protected qubits for quantum information processing. Currently, only a handful of candidate materials are known which may realize this state. A central challenge in this field is to completely characterize the exotic spin-excitation spectrum to identify the type of spin liquid state that is realized. Soft X-ray RIXS, with a few tens of meV resolution, is a powerful probe of this information, particularly suitable for the small crystals that are presently available.

A unique capability at LCLS II will be elastic and inelastic X-ray magnetic scattering studies of samples under applied (transient) large magnetic fields (greater than 60 T). As an example, the quantum spin liquid material herbertsmithite [34] (an S=1/2 kagome lattice antiferromagnet) has a ground state that is predicted to enter various magnetization-plateau configurations with increasing applied field.[35] Unfortunately, current field strengths available at neutron scattering facilities are too low to reach these exotic states. Resonant X-ray scattering in a pulsed field is a powerful new approach to explore this new physics. Interesting plateau states at one ninth or one third of the saturated moment require fields of more than 60 T in herbertsmithite. The ability to measure the spin arrangement and excitations in the plateau states will provide definitive evidence of novel behavior in these quantum magnets. Furthermore, many other quantum magnetic materials have ground states which do not exhibit long-range order. Hence, it is impossible to determine the Hamiltonian parameters via measurement of the spin-wave dispersion.

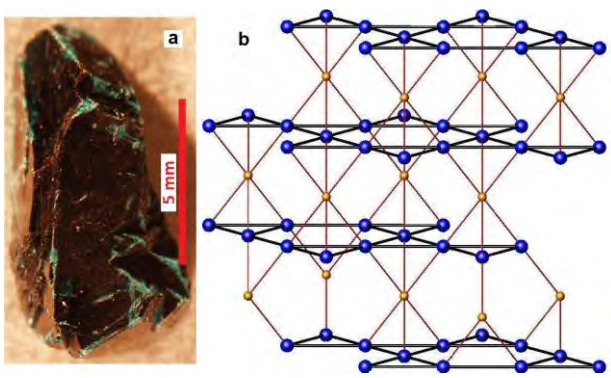

Figure 37: A quantum spin liquid material: herbertsmithite $ZnCu_3(OD)_6Cl_2$. (a) A high quality single crystal resulting from hydrothermal growth (b) Crystal structure with Cu^{2+} ions (large blue spheres) and Zn^{2+} ions (small brown spheres) displayed.

For X-ray scattering experiments, the figure of merit is the number of photons available during the peak magnetic field. For a typical few msec-field pulse, there is a time window of less than 1 msec for the measurement, during which the LCLS-II X-ray free electron laser can deliver more than 10^{12} photons to the sample, a 10,000-time gain compared with synchrotron sources applied to such experiments. Thus the combination of LCLS-II X-ray pulses with large saturating magnetic fields will allow for the determination of spin Hamiltonians in fully polarized states. This fundamental information cannot be directly obtained by other means.

Experimental approaches & impact of LCLS-II

With the advent of LCLS-II (seeded X-ray FEL with high repetition rate and tunable pulses near the Fourier-transform limit of energy

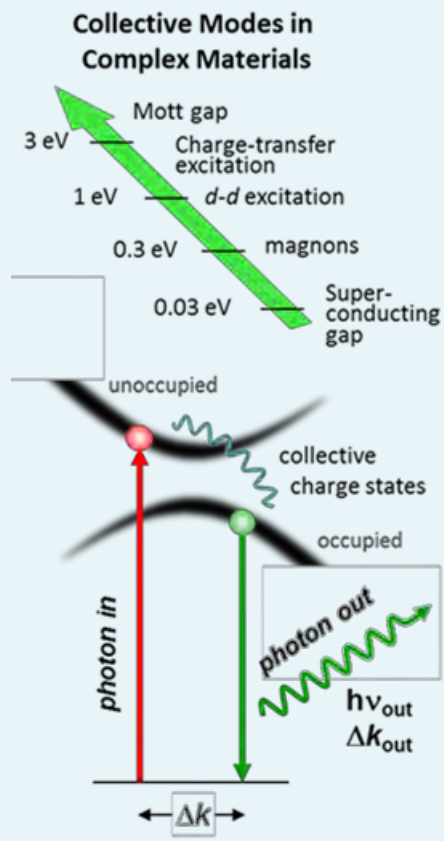

Momentum-resolved Resonant Inelastic X-ray Scattering (***q***-RIXS)

- Bulk sensitive
- Element-specific (L-edge, or K-edge)
  - Transition-metals (Fe, Cu, Mn, Ti, Ir etc.)
  - Oxygen, Arsenic
- Energy resolution (~20 meV)
- Momentum resolution
- Time resolution (20 meV⇔100 fs)
- Monolayer/interface sensitivity
- Applied fields (magnetic, electric)

Current limitations:

- Photon flux in narrow bandwidth (coherent X-ray source ⇒ laser)

and time resolution), a new "golden age" of spectroscopy is dawning with unprecedented opportunities for studies of quantum materials at nano- to microscopic length scales and femtosecond time scales. These capabilities are critical for deciphering how charge, spin, orbital and lattice degrees of freedom interact to produce emergent phenomena and exotic states of matter. There can be little doubt that we are at the threshold of a transition from observing to controlling matter at a much deeper level than has ever been possible. Advanced spectroscopic techniques will play a pivotal role in detailed explorations of electronic, geometric, and excited state properties of ordered and defected crystals, surfaces, interfaces, and complex nano-scale assemblies of atoms and molecules, and in the way in which this physics evolves with temperature, pressure, magnetic/electric fields, and other external control parameters.

Opportunities for Resonant Inelastic X-ray Scattering at LCLS-II

Resonant inelastic X-ray scattering (RIXS) has emerged as a powerful tool to measure elementary excitations of charge, spin, lattice and the orbitals, which bear unique fingerprints of the underlying electronic states. RIXS, a photon-in/photon-out spectroscopy, records the energy and momentum-transfer of light, which can be used to extract the energy-momentum dispersion of elementary excitations.[9] Currently, the state-of-the-art RIXS instrument allows us to investigate excitations with an energy resolution of ~ 120 meV (resolving power $E/\Delta E \sim 8{,}000$), which has revealed a number of collective excitations in energy-momentum space, such as the dispersions of magnons,[36] paramagnons,[37] triplons,[38] two-spinons,[39] phonons,[40] and orbitons,[39] to name a few (see also Figure 38). Soon, the "next-generation" RIXS instruments with a resolving power greater than 30,000 will become available to investigate collective excitations with energies comparable to the characteristic energy scales near the Fermi level (<50 meV) — e.g., the superconducting gap and pseudogap in high-T_c cuprate superconductors.

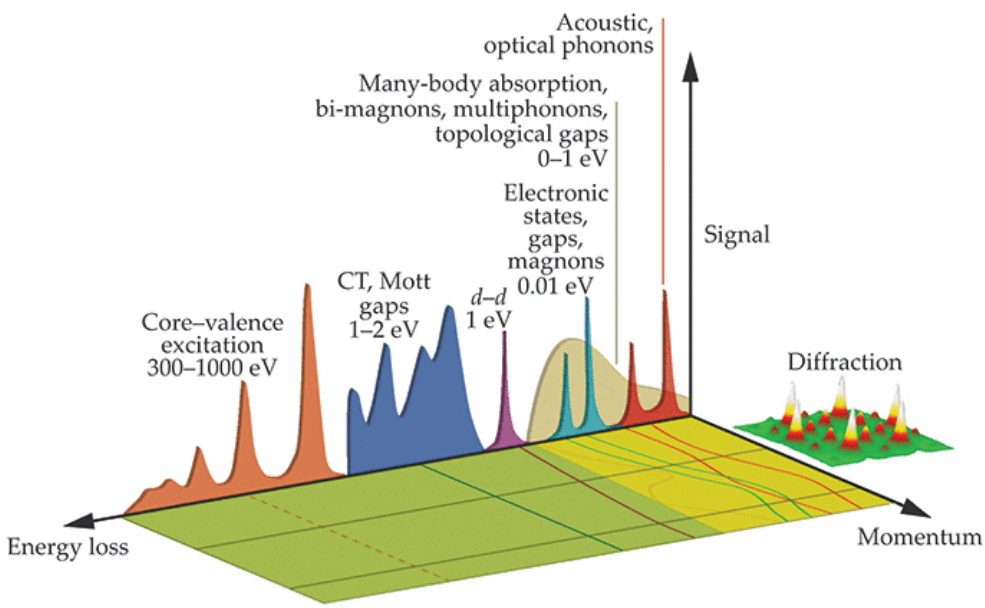

Figure 38: Collective excitations that can be characterized by RIXS – including excitations within *d*-orbital manifolds (*d*-*d*) and charge-transfer excitations (CT). Higher resolution is essential to reveal excitations with energy scales comparable to that of superconducting gap and pseudogap (courtesy of Y. Zhu, BNL)

A unique aspect of such a RIXS instrument enabled by LCLS-II is the capability of performing time-resolved measurements with high energy resolution (e.g., 100 fs ⇔ 18 meV) to study the dynamics of photo-induced non-equilibrium states. This is a major advance beyond the successful time-resolved resonant X-ray scattering program presently at LCLS. Upon photo excitation, as schematically shown in

Figure 32, one can readily probe the temporal evolution of elementary excitations, including magnons and phonons. As an example of the scientific impact, this information is essential to understanding the recently discovered photo-induced high-temperature superconductivity.[7] We further emphasize that element-specific, momentum-dependent information of these elementary excitations provided by RIXS is inaccessible by table-top time-resolved spectroscopy. Furthermore, sufficient energy resolution will reveal the collective modes arising from the symmetry-broken state induced by a tailored excitation pulse. The energy-momentum dispersion and the time scales of the collective modes are fingerprint signatures of the new photo-induced state.

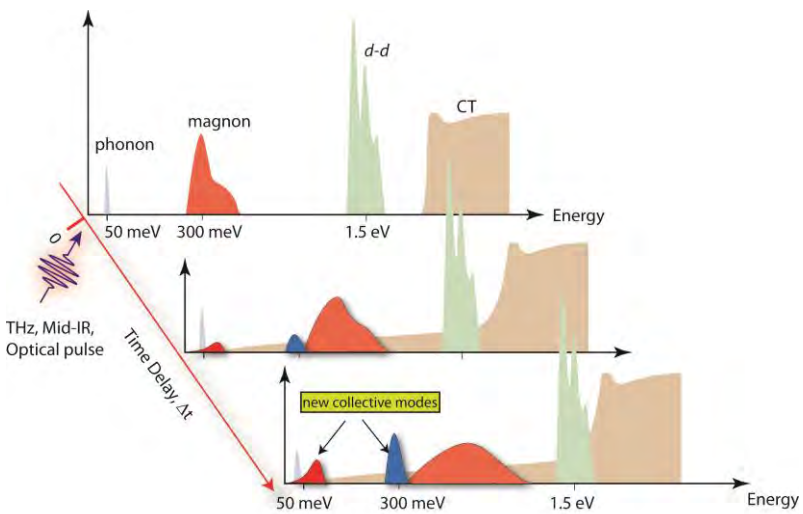

Figure 39 RIXS instrument at LCLS-II with energy and temporal resolution at the Fourier-transform limit ($\Delta E \Delta t$=1.8 eV•fs) will track the evolution of the elementary excitations in transient non-equilibrium states. New collective modes associated with new symmetry-broken states new state may also be discovered.

Another potential of an RIXS instrument at LCLS-II is the possibility of performing ultrahigh resolution RIXS measurements that are beyond the capabilities of synchrotron X-ray sources. This is simply because the high-repetition rate and the narrow bandwidth of a seeded X-ray FEL at LCLS-II can deliver orders of magnitude higher photo flux in a narrow bandwidth (e.g. 10 meV) than any synchrotron light source. Thus, an ultrahigh resolution RIXS instrument with a resolving power on the order of 100,000 is conceivable at LCLS-II, while the flux available at this resolving power from synchrotron light sources is marginal.

Since RIXS requires tuning the photon energy of X-ray to meet element-specific absorption edges, instruments optimized at different X-ray spectra are required to cover a wide range of quantum materials. For example, soft X-ray RIXS (250 eV to 2000 eV) is ideal to study strongly correlated *3d* transition metal oxides (via *3d* TM L-edges and oxygen K-edge), *4f* rare earth compounds (via metal *M*-edge and oxygen K-edge) and *5d* transition metal compounds (oxygen K-edge). Hard X-ray RIXS (greater than 10 keV) is ideally suited to study *5d* transition metal compounds, such as iridium oxides (TM L-edge). "Tender" X-ray RIXS (2 to 5 KeV) is suitable for studying compounds containing *4d* transition metal elements, which are much less explored due to challenges of building a high-resolution monochromator in this spectral range.

To maximize the scientific impact, the specifications of a RIXS instrument at LCLS-II in the first year of operation (2019) need to be at least comparable to those of state-of-the-art RIXS instruments worldwide at that time. Our survey indicates that the specifications for next-generation machines are quite consistent: resolving power of more than 30,000 with an option of polarization analysis. Thus, the recommended resolving power of the soft X-ray RIXS instrument at LCLS-II should be at least 30,000.

Note that it is important to allow full hemi-circle swing for the spectrometer in order to maximize the flexibility of experimental scattering geometry. As an example, the RIXS instrument at European XFEL

is designed to perform high-resolution RIXS, time-resolved RIXS, and stimulated RIXS (or two-wave mixing experiments alike). Therefore, the instrument is designed to cover both backscattering (for conventional and time-resolved RIXS experiments, $2\theta = 60° - 150°$), and forward scattering geometries (for stimulated RIXS experiments, $2\theta = 0° - 20°$). Thus, it is important to ensure that a RIXS instrument at LCLS-II has sufficient space for a full hemi-circle angular range. It is also essential to have control over the incident X-ray polarization. In addition, analysis of the polarization of the X-rays scattered from the sample is very informative; thus, it is important to ensure that the design of the spectrometer is compatible with polarimeters.

Since collective mode dynamics are a unique aspect of RIXS at LCLS-II, it is important to have a variety of tailored excitation sources available for the pump-probe studies. These should include conventional ultrafast optical, mid-IR, and THz sources. The integration of these lasers needs to be considered even at the stage of conceptual design for the instruments.

Opportunities for Photoemission-Based Methods at LCLS-II

ARPES is a powerful tool for analyzing electronic structures with high energy and momentum resolution and has played a crucial role in the study of correlated materials, particularly high-T_c superconductors. The exceptional beam parameters of LCLS-II present unique opportunities to implement sophisticated photoemission spectroscopy (PES) based methods that will open new areas of research. Enabling capabilities for all these ideas are the ultrafast and ultra-bright X-ray pulses with a remarkably high repetition rate of less than 1 MHz, which is crucial to overcoming space charge limits in PES. Photon energies in the soft and hard X-ray regime have thus far been used rarely in PES, and LCLS-II will enable numerous cutting-edge PES experiments on important material families. While first-generation time-resolved hard X-ray experiments have been demonstrated at very low repetition rates, it is noteworthy that none of the approaches below has ever fully realized for state-of-the-art material science studies with femtosecond time-resolution and spin-resolution, due to the lack of a suitable light source. The supreme time-resolution of LCLS-II coupled with high repetition rate and photon flux will permit a new classes of time-resolved PES experiments to be conducted:

X-ray Angle-Resolved Photoemission Spectroscopy (X-ARPES) has been severely impeded by the drastic reduction of the PES cross-section at photon energies in the X-ray range. The ultra-bright beams of LCLS-II lift this limitation completely while providing direct access to the additional information of femtosecond electron dynamics in pump-probe experiments. These characteristics permit developing fundamentally new capabilities that compliment conventional ARPES experiments in the VUV spectral range. Complications due to the finite momentum of the X-ray photons and phonon effects have already been mastered.[41-43]

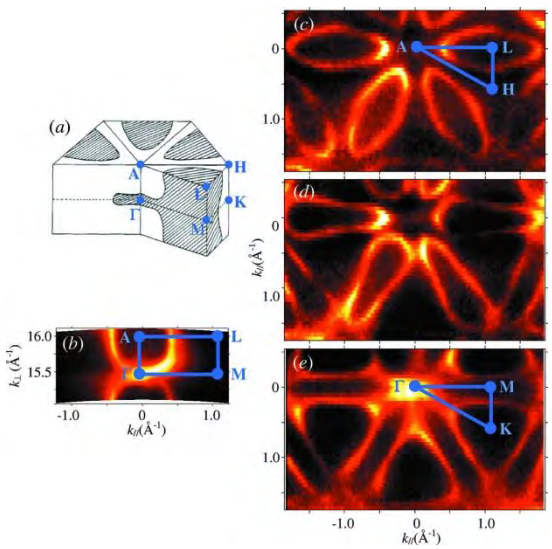

Figure 40: Three dimensional band mapping in VSe_2 via soft X-ray ARPES, from ref. 41.

The large kinetic energy of the photoemitted electrons results in a longer mean free path which provides more bulk sensitivity and enables the study of buried interfaces and heterostructures.[44] A prominent example is the superconducting two-dimensional electron gas in LAO/STO.[45]

The increased mean free path of the photoelectrons leads to a well-defined electron momentum $k_\perp$ perpendicular to the surface and a superior $k_\parallel$ resolution compared to VUV-based ARPES. Moreover, at energies of several 100eV, the final states become free-electron-like, which allows accurate mapping of 3D band structures. This approach is beneficial for all 3D materials, and in particular unconventional "bulk" superconductors.

PES matrix element effects often complicate the analysis of conventional ARPES data. For X-ARPES, the matrix elements are essentially those of free atoms. This not only simplifies the data analysis significantly but also enables ARPES experiments that exploit the chemical selectivity of the X-rays — e.g., when studying impurity-related band structures.

Spin-Resolved ARPES (S-ARPES) profits from all of the above capabilities, in particular because the reduced efficiency of S-ARPES detectors requires high photon flux. Moreover, the pulsed timing structure of the LCLS-II will enable the use of novel spin-resolving spectrometers utilizing time-of-flight techniques for energy analysis. S-ARPES will grant full access to the spin- and electronic structure of novel materials and interfaces such as LAO/STO, where the spin degree of freedom is known to interact with charge, lattice, and orbital degrees of freedom.[46] Other fascinating materials to be studied include superconductors with unconventional pairing symmetries (e.g., *p*-wave pairing in $SrRuO_4$), manganites characterized by strongly correlated magnetic phases,[47] and a range of magnetic materials as discussed in Section 2.3.2.

Standing-wave ARPES (SW-ARPES) takes advantage of the shorter X-ray wavelengths that permit Bragg reflection from periodic heterostructures or single-crystal/epitaxial samples to generate standing waves that can be scanned through the sample layers. SW-ARPES at LCLS-II provides unique information on interface composition and properties, and on interface-specific electron dynamics, including momentum resolution.[27, 28]

Nano-ARPES (N-ARPES) is another PES-based method requiring high photon flux due the difficulty of X-ray focusing to nanometer-length scales. Many correlated materials such as cuprates have been known to exhibit fluctuations of fundamental material properties on nanometer length and ps time scales (see Section 2.4).[13, 48, 49] Yet to date, remarkably few experiments have tackled this crucial problem due to the

lack of suitable light sources and efficient detection schemes that provide nanometer spatial and femtosecond time resolution. The development of a new class of time-of-flight 3D imaging analyzer[50, 51] facilitates N-ARPES with less than10 nm spatial resolution and less than 10 meV energy resolution while achieving a remarkable efficiency with a throughput more than 1,000 times more than that of N-ARPES with conventional dispersive electron analyzers. Note that this approach does not rely on nanometer focusing of the X-rays, but rather nanometer-resolution imaging of the photoelectrons. The combination of a super-bright, high repetition rate, ultrafast X-ray light source with highly efficient detection schemes will enable fundamentally new N-ARPES experiments at LCLS-II, which have the potential to transform our understanding of correlated materials in general.

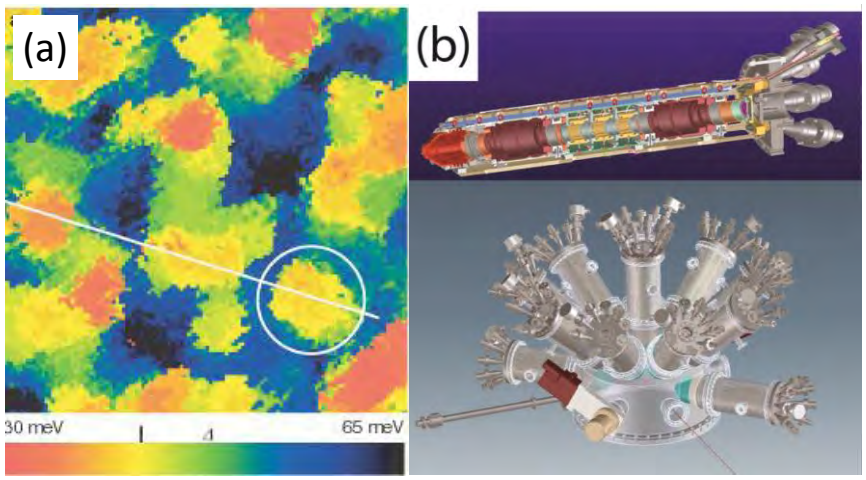

Figure 41: (a) Fluctuating order parameter in high T_c Superconductor Bi2212 (~15×15 nm), from ref. 13. (b, upper) Time-of- flight 3D imaging analyzer can image ARPES spectra with a spatial resolution better than 10 nm with high efficiency. (lower) It is possible to equip several time-of-flight analyzers in one chamber to increase data acquisition efficiency and perform time-resolved, nano-, and spin-resolved ARPES simultaneously.

Pulsed magnet at LCLS-II

Recent X-ray and neutron scattering experiments in high magnet fields have received a lot of attention for their relevance in understanding quantum materials. A state of the art DC magnet designed for scattering can reach field strengths up to ~20 T. Moreover, it is recognized that pulsed magnets are an economic yet highly-effective approach for reaching field strengths beyond 50 T. For a typical pulsed field of a few msec duration, the time window for X-ray scattering measurements is less than 1 msec, during which the LCLS X-ray free electron laser can deliver more than 10^{12} photons to the sample, a 10,000-time gain compared with synchrotron sources applied to such experiments. This makes it feasible for the first time to detect weaker order parameters in correlated materials, such as the charge density wave (CDW) phenomena in high T_c superconductors.

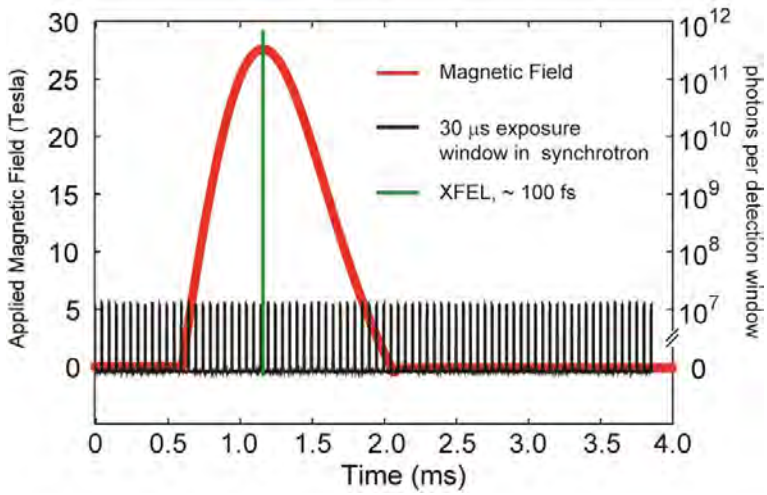

Figure 42: Applied magnetic field as a function of time. The black spikes are the gated 30 μs detection window used in beam line 6ID-B of APS. The green spike is an illustration of an X-ray FEL pulse with 10^{12} photons on the sample at the maximal magnetic field. Alternatively, at 1 MHz repetition rate, LCLS-II provides ~10^{13} photons within a 100 μs detection window.

This is further elaborated in Figure 42. According to the current pulsed magnet technology, the magnetic field pulse lasts for approximately 1.5 msec within which the magnetic field strength varies as a function of time. The conventional approach at a synchrotron facility is to gate the detector with a detection window of 30 microseconds (black spikes in Figure 42). Unfortunately, however, data collection window occurs at different magnetic field strengths. Furthermore, each detection window effectively allows only ~10^8 photons on the sample, which is insufficient to detect any weak features. In general, a forbidden reflection in quantum materials, such as charge and spin orders in *3d* transition metal oxides, is often approximately seven orders of magnitude weaker than their structural Bragg reflection. For these reasons, the synchrotron X-ray sources are not well matched for science requiring pulsed magnetic fields.

Combining X-ray FEL capabilities with a pulsed magnet can be game-changing. With proper synchronization between the FEL and the pulsed magnet, many photons (~ 10^{12} photons) can be deposited on the sample within the FEL pulse duration (~ 100 fs), or ~10^{13} photons within a 100 μs burst, at the maximum magnetic field (green line in Figure 42). For the first time it will be possible to discern weak features in scattering experiments and to fully characterize samples via X-ray spectroscopy.

While such experiments are already feasible at LCLS-I, the potential increase of the highest available photon energy to 25 keV significantly expands the momentum transfer range accessible through the limited opening of the magnet. This is a dramatic increase in measurement flexibility on one hand, and on the other it allows the design of split-pair coils to reach even higher fields. In addition, the high repetition rate of LCLS-II will make it possible to decrease the peak power (and thereby avoid disruption of the electronic structure of the sample, see Appendix 1) while still having sufficient integrated flux within the pulsed magnetic field.

References

1. E. Dagotto, "Complexity in strongly correlated electronic systems," Science **309**, 257 (2005).
2. X.-L. Qi, and S.-C. Zhang, "Topological insulators and superconductors," Reviews of Modern Physics **83**, 1057 (2011).
3. M. Z. Hasan, and C. L. Kane, "Colloquium: Topological insulators," Reviews of Modern Physics **82**, 3045 (2010).
4. E. S. Reich, "Hopes surface for exotic insulator," Nature **492**, 165 (2012).
5. E. Dagotto, "When Oxides Meet Face to Face," Science **318**, 1076 (2007).
6. J. Chakhalian, A. J. Millis, and J. Rondinelli, "Whither the oxide interface," Nat Mater **11**, 92 (2012).
7. D. Fausti, R. I. Tobey, N. Dean, S. Kaiser, A. Dienst, M. C. Hoffmann, et al., "Light-Induced Superconductivity in a Stripe-Ordered Cuprate," Science **331**, 189 (2011).

8. M. Rini, R. Tobey, N. Dean, J. Itatani, Y. Tomioka, Y. Tokura, et al., "Control of the electronic phase of a manganite by mode-selective vibrational excitation," Nature **449**, 72 (2007).
9. L. J. P. Ament, M. van Veenendaal, T. P. Devereaux, J. P. Hill, and J. van den Brink, "Resonant inelastic x-ray scattering studies of elementary excitations," Reviews of Modern Physics **83**, 705 (2011).
10. W. S. Lee, J. J. Lee, E. A. Nowadnick, S. Gerber, W. Tabis, S. W. Huang, et al., "Asymmetry of collective excitations in electron- and hole-doped cuprate superconductors," Nat Phys **10**, 883 (2014).
11. S. E. Sebastian, N. Harrison, F. F. Balakirev, M. M. Altarawneh, P. A. Goddard, R. Liang, et al., "Normal-state nodal electronic structure in underdoped high-T_c copper oxides," Nature **511**, 61 (2014).
12. G. Grissonnanche, O. Cyr-Choinière, F. Laliberté, S. René de Cotret, A. Juneau-Fecteau, S. Dufour-Beauséjour, et al., "Direct measurement of the upper critical field in cuprate superconductors," Nat Commun **5**, 3280 (2014).
13. K. M. Lang, V. Madhavan, J. E. Hoffman, E. W. Hudson, H. Eisaki, S. Uchida, et al., "Imaging the granular structure of high-T_c superconductivity in underdoped $Bi_2Sr_2CaCu_2O_{8+\delta}$," Nature **415**, 412 (2002).
14. A. Ohtomo, and H. Y. Hwang, "A high-mobility electron gas at the LaAlO3/SrTiO3 heterointerface," Nature **427**, 423 (2004).
15. S. Okamoto, and A. J. Millis, "Electronic reconstruction at an interface between a Mott insulator and a band insulator," Nature **428**, 630 (2004).
16. J. S. Lee, Y. W. Xie, H. K. Sato, C. Bell, Y. Hikita, H. Y. Hwang, et al., "Titanium d_{xy} ferromagnetism at the $LaAlO_3/SrTiO_3$ interface," Nat Mater **12**, 703 (2013).
17. Q.-Y. Wang, Z. Li, W.-H. Zhang, Z.-C. Zhang, J.-S. Zhang, W. Li, et al., "Interface-Induced High-Temperature Superconductivity in Single Unit-Cell FeSe Films on $SrTiO_3$," Chinese Physics Letters **29**, 037402 (2012).
18. D. Liu, W. Zhang, D. Mou, J. He, Y.-B. Ou, Q.-Y. Wang, et al., "Electronic origin of high-temperature superconductivity in single-layer FeSe superconductor," Nat Commun **3**, 931 (2012).
19. S. He, J. He, W. Zhang, L. Zhao, D. Liu, X. Liu, et al., "Phase diagram and electronic indication of high-temperature superconductivity at 65 K in single-layer FeSe films," Nat Mater **12**, 605 (2013).
20. S. Tan, Y. Zhang, M. Xia, Z. Ye, F. Chen, X. Xie, et al., "Interface-induced superconductivity and strain-dependent spin density waves in $FeSe/SrTiO_3$ thin films," Nat Mater **12**, 634 (2013).
21. J. J. Lee, F. T. Schmitt, R. G. Moore, S. Johnston, Y. T. Cui, W. Li, et al., "Interfacial mode coupling as the origin of the enhancement of T_c in FeSe films on $SrTiO_3$," Nature **515**, 245 (2014).
22. K. F. Mak, C. Lee, J. Hone, J. Shan, and T. F. Heinz, "Atomically Thin MoS_2: A New Direct-Gap Semiconductor," Phys. Rev. Lett. **105**, 136805 (2010).
23. W. J. Yu, Z. Li, H. Zhou, Y. Chen, Y. Wang, Y. Huang, et al., "Vertically stacked multi-heterostructures of layered materials for logic transistors and complementary inverters," Nat Mater **12**, 246 (2013).
24. Y. Zhang, T.-R. Chang, B. Zhou, Y.-T. Cui, H. Yan, Z. Liu, et al., "Direct observation of the transition from indirect to direct bandgap in atomically thin epitaxial $MoSe_2$," Nat Nano **9**, 111 (2014).
25. A. D. Caviglia, R. Scherwitzl, P. Popovich, W. Hu, H. Bromberger, R. Singla, et al., "Ultrafast Strain Engineering in Complex Oxide Heterostructures," Phys. Rev. Lett. **108**, 136801 (2012).
26. A. D. Caviglia, M. Först, R. Scherwitzl, V. Khanna, H. Bromberger, R. Mankowsky, et al., "Photoinduced melting of magnetic order in the correlated electron insulator $NdNiO_3$," Phys. Rev. B **88**, 220401 (2013).
27. A. X. Gray, C. Papp, B. Balke, S. H. Yang, M. Huijben, E. Rotenberg, et al., "Interface properties of magnetic tunnel junction $La_{0.7}Sr_{0.3}MnO_3/SrTiO_3$ superlattices studied by standing-wave excited photoemission spectroscopy," Phys. Rev. B **82**, 205116 (2010).
28. A. X. Gray, J. Minár, L. Plucinski, M. Huijben, A. Bostwick, E. Rotenberg, et al., "Momentum-resolved electronic structure at a buried interface from soft X-ray standing-wave angle-resolved photoemission," EPL (Europhysics Letters) **104**, 17004 (2013).
29. A. Laubereau, and W. Kaiser, "Vibrational dynamics of liquids and solids investigated by picosecond light pulses," Reviews of Modern Physics **50**, 607 (1978).
30. F. Schmitt, P. S. Kirchmann, U. Bovensiepen, R. G. Moore, L. Rettig, M. Krenz, et al., "Transient electronic structure and melting of a charge density wave in TbTe3," Science **321**, 1649 (2008).
31. J. P. Hinton, J. D. Koralek, Y. M. Lu, A. Vishwanath, J. Orenstein, D. A. Bonn, et al., "New collective mode in $YBa_2Cu_3O_{6+x}$ observed by time-domain reflectometry," Phys. Rev. B **88** (2013).

32. K. W. Kim, A. Pashkin, H. Schäfer, M. Beyer, M. Porer, T. Wolf, et al., "Ultrafast transient generation of spin-density-wave order in the normal state of $BaFe_2As_2$ driven by coherent lattice vibrations," Nat Mater **11**, 497 (2012).
33. A. Cavalleri, "Nonlinear phononics and ultrafast control at complex interfaces," in *APS March meeting* (2015), p. 00001.
34. T.-H. Han, J. S. Helton, S. Chu, D. G. Nocera, J. A. Rodriguez-Rivera, C. Broholm, et al., "Fractionalized excitations in the spin-liquid state of a kagome-lattice antiferromagnet," Nature **492**, 406 (2012).
35. S. Nishimoto, N. Shibata, and C. Hotta, "Controlling frustrated liquids and solids with an applied field in a kagome Heisenberg antiferromagnet," Nat Commun **4**, 2287 (2013).
36. M. Guarise, B. Dalla Piazza, M. Moretti Sala, G. Ghiringhelli, L. Braicovich, H. Berger, et al., "Measurement of Magnetic Excitations in the Two-Dimensional Antiferromagnetic $Sr_2CuO_2Cl_2$ Insulator Using Resonant X-Ray Scattering: Evidence for Extended Interactions," Phys. Rev. Lett. **105**, 157006 (2010).
37. M. Le Tacon, G. Ghiringhelli, J. Chaloupka, M. M. Sala, V. Hinkov, M. W. Haverkort, et al., "Intense paramagnon excitations in a large family of high-temperature superconductors," Nat Phys **7**, 725 (2011).
38. J. Schlappa, T. Schmitt, F. Vernay, V. N. Strocov, V. Ilakovac, B. Thielemann, et al., "Collective Magnetic Excitations in the Spin Ladder $Sr_{14}Cu_{24}O_{41}$ Measured Using High-Resolution Resonant Inelastic X-Ray Scattering," Phys. Rev. Lett. **103**, 047401 (2009).
39. J. Schlappa, K. Wohlfeld, K. J. Zhou, M. Mourigal, M. W. Haverkort, V. N. Strocov, et al., "Spin-orbital separation in the quasi-one-dimensional Mott insulator Sr_2CuO_3," Nature **485**, 82 (2012).
40. W. S. Lee, S. Johnston, B. Moritz, J. Lee, M. Yi, K. J. Zhou, et al., "Role of Lattice Coupling in Establishing Electronic and Magnetic Properties in Quasi-One-Dimensional Cuprates," Phys. Rev. Lett. **110**, 265502 (2013).
41. V. N. Strocov, X. Wang, M. Shi, M. Kobayashi, J. Krempasky, C. Hess, et al., "Soft-X-ray ARPES facility at the ADRESS beamline of the SLS: concepts, technical realisation and scientific applications," Journal of Synchrotron Radiation **21**, 32 (2014).
42. A. X. Gray, J. Minár, S. Ueda, P. R. Stone, Y. Yamashita, J. Fujii, et al., "Bulk electronic structure of the dilute magnetic semiconductor $Ga_{1-x}Mn_xAs$ through hard X-ray angle-resolved photoemission," Nat Mater **11**, 957 (2012).
43. A. X. Gray, C. Papp, S. Ueda, B. Balke, Y. Yamashita, L. Plucinski, et al., "Probing bulk electronic structure with hard X-ray angle-resolved photoemission," Nat Mater **10**, 759 (2011).
44. C. S. Fadley, "Looking Deeper: Angle-Resolved Photoemission with Soft and Hard X-rays," Synchrotron Radiation News **25**, 26 (2012).
45. N. Reyren, S. Thiel, A. D. Caviglia, L. F. Kourkoutis, G. Hammerl, C. Richter, et al., "Superconducting Interfaces Between Insulating Oxides," Science **317**, 1196 (2007).
46. P. D. C. King, S. McKeown Walker, A. Tamai, A. de la Torre, T. Eknapakul, P. Buaphet, et al., "Quasiparticle dynamics and spin–orbital texture of the $SrTiO_3$ two-dimensional electron gas," Nat Commun **5**, 3414 (2014).
47. C. D. Ling, J. E. Millburn, J. F. Mitchell, D. N. Argyriou, J. Linton, and H. N. Bordallo, "Interplay of spin and orbital ordering in the layered colossal magnetoresistance manganite $La_{2-2x}Sr_{1+2x}Mn_2O_7$ (0.5~x~1.0)," Phys. Rev. B **62**, 15096 (2000).
48. D. H. Torchinsky, F. Mahmood, A. T. Bollinger, I. Božović, and N. Gedik, "Fluctuating charge-density waves in a cuprate superconductor," Nat Mater **12**, 387 (2013).
49. M. Fäth, S. Freisem, A. A. Menovsky, Y. Tomioka, J. Aarts, and J. A. Mydosh, "Spatially Inhomogeneous Metal-Insulator Transition in Doped Manganites," Science **285**, 1540 (1999).
50. A. S. Tremsin, G. V. Lebedev, O. H. W. Siegmund, J. V. Vallerga, J. S. Hull, J. B. McPhate, et al., "High spatial and temporal resolution photon/electron counting detector for synchrotron radiation research," Nuclear Instruments and Methods in Physics Research Section A: Accelerators, Spectrometers, Detectors and Associated Equipment **580**, 853 (2007).
51. G. Lebedev, A. Tremsin, O. Siegmund, Y. Chen, Z. X. Shen, and Z. Hussain, "Complete momentum and energy resolved TOF electron spectrometer for time-resolved photoemission spectroscopy," Nucl. Instrum. Meth. A **582**, 168 (2007).

2.3.2 Understanding and controlling nonequilibrium spin states at fundamental length and time scales

Synopsis

Science and our understanding of nature are founded on the principles of conservation of energy and momentum, both linear and angular. Their impact on our understanding of matter in states very far from equilibrium is particularly important considering that a theoretical description of such states is still in its infancy, but it is now within experimental reach through ultrafast and intense laser excitation processes (see Figure 43). While energy and linear momentum conservation are often employed to help understand ultrafast phenomena ranging from catalysis to photosynthesis, it is the conservation of angular momentum which is most important for understanding ultrafast magnetism, which is relevant to information technology. Femtosecond X-ray pulses, specifically circularly polarized ones, provide the ideal tools to observe the ultrafast and nanoscale flow of angular momentum between electrons, spins and lattice atoms. LCLS II will enable groundbreaking experiments that will influence the way we think about non-equilibrium states in magnetic solids and help us design new ways to store and process *information.*

Introduction

Magnetism in novel nanoscale materials is a key ingredient in modern information technology. Moore's Law predicting an exponential increase in data storage density and processing speed requires that the bits in magnetic hard drives and power-efficient transistors in our mobile phones and computers approach dimensions of only tens of nanometers. In order to continue along the path of Moore's Law and achieve the needed gains in density and speed of data storage and processing, it is necessary to overcome fundamental scientific and technological limits. As current information densities on hard disk drives are already heading towards the Tbit/in^2 threshold we need to find out if we can store and process *Tbit densities at THz speeds*.

Exploring the speed and size limit for manipulation of electrons and spins is not only technologically relevant, but it also constitutes a grand challenge for modern science. We need to understand the behavior of novel nanoscale magnetic materials — far from equilibrium — and find out how to control the magnetic interactions via energy and angular momentum flow between electronic, spin and lattice degrees of freedom. LCLS II will enable unique insights that could lead to all-optical control of emerging novel transient magnetic states with altered exchange interaction (Section 2.3.2.1). The utilization of the spin-orbit interaction is of central importance for charge-spin current conversion in novel spintronics applications and LCLS II will provide novel high-precision spectroscopic tools to understand and control the underlying elementary spin scattering processes (Section 2.3.2.2). Section 2.3.2.3 explores how ultrafast snapshot imaging can capture the inherent stochastic motion of topological spin textures driven by spin currents. Finally, Section 2.3.2.4 describes the fascinating opportunities for capturing the complex interplay of spin and electronic order parameters in multiferroic heterostructures.

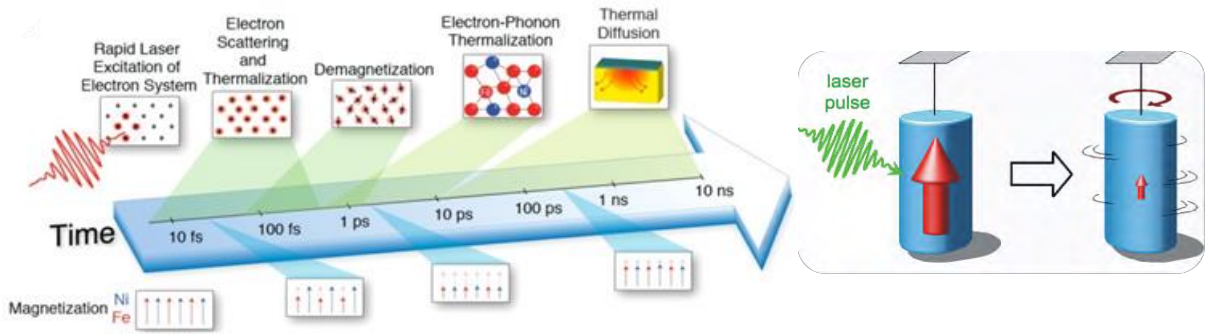

Figure 43. Left: illustration of the laser-heating-induced flow of energy from electrons to spins and ultimately to the lattice. This is accompanied by angular momentum exchange between different magnetic sub-systems (from ref. 1). Right: schematic view of how spin-lattice coupling could conserve angular momentum. LCLS II will allow the first direct corroboration of this process.

2.3.2.1 Emergence of magnetic order at ultimate length and timescales

The unexpected observation of all-optical magnetic switching (AOS) has opened the way for a radically new approach to manipulating the magnetization of a sample using ultrafast and non-thermal effects of circularly polarized femtosecond laser pulses as the external stimulus. Discovered originally in transition metal–rare earth alloys[2] exhibiting a peculiar lattice structure, all-optical switching was recently confirmed in artificial heterostructures[3] and even ferromagnets,[4] which indicates that AOS is a rather ubiquitous phenomenon. However, a comprehensive microscopic understanding of the switching process, which could guide further exploitation of AOS, is still in its infancy. Using femtosecond x-ray pulses, which enable the detection of magnetization dynamics with element specificity, revealed the emergence of a transient, non-equilibrium ferromagnetic state promoting the magnetic switching of intermittently antiparallel oriented spins.[5] Such an all-optical switching scheme can be used to write nanoscale, topologically protected magnetic structures [6] that can be viewed as magnetic bits in future data storage devices (see Figure 44) operating at much higher speed and much reduced energy consumption. To fully harness this potential, several key questions for fundamental science need to be answered, as they will have significant impact on a technological exploitation of AOS.

What is the origin and proper theoretical description of the highly non-equilibrium state following optical excitation?

This state is commonly described by phenomenologically assigning an electron temperature that is out of equilibrium with the lattice. It is currently debated, however, to what degree spin angular momentum can be transferred to the lattice (see Figure 43). Another theoretical approach to explain this non-equilibrium state involves the so-called superdiffusive spin currents that can transport spin angular momentum across nanometer distances.[7, 8]

How is angular momentum conserved on the femtosecond timescale?

In 1915 Einstein and de Haas experimentally demonstrated the equivalence of spin and lattice angular momentum and their conversion into each other [9]. However, the ultrafast analog of the Einstein-de Haas effect has eluded experimental corroboration so far (see Figure 43). This is at the heart of an ongoing debate about the mechanism of angular momentum conservation during the far-from-equilibrium excitation of a ferromagnet by a femtosecond optical laser pulse, even after almost two decades of research.[10]

Ultimately, the quenched spin angular momentum, as observed with femtosecond laser or soft X-ray pulses,[10, 11] has to be transferred to the lattice. However, the current inability to directly observe lattice angular momentum has fueled an ongoing debate about the underlying mechanism and even the mere existence of an ultrafast spin-lattice angular momentum transfer. Ultimately, it points to an inherent inadequacy of current theoretical models of magnetic order.[12]

The high-repetition rate will make LCLS II very sensitive to scattering from non-equilibrium phonons.[13] In magnetic solids first theoretical predictions point to a circular polarization of phonon modes via interaction with the magnetic valence shell.[14] Being able to observe a phonon polarization buildup on ultrafast timescales will have significant impact on our understanding of non-equilibrium magnetism.

What are the channels for ultrafast angular momentum transfer between magnetic sub-lattices?

All-optical switching in transition-metal/rare-earth alloys requires an intermittent antiferromagnetic alignment of the elemental magnetic constituents. This may also be important for magnetic heterostructures,[3] although it has not been observed yet. Understanding the ultrafast spin transfer processes and the possible changes in the magnetic exchange coupling with the sample far from equilibrium will enable us to predict the use of more commonly accessible magnetic materials for future applications.

How do topological magnetic structures (e.g. skyrmions) form?

Although topologically protected magnetic structures have been successfully generated via nano-focused femtosecond optical laser pulses,[6] their formation process and control of their topological nature remain controversial. Magnetic data storage applications demand not only skyrmion structures operating at ambient conditions but also shrinking of the skyrmion size (see Figure 44) by at least an order of magnitude compared to what can be done today.

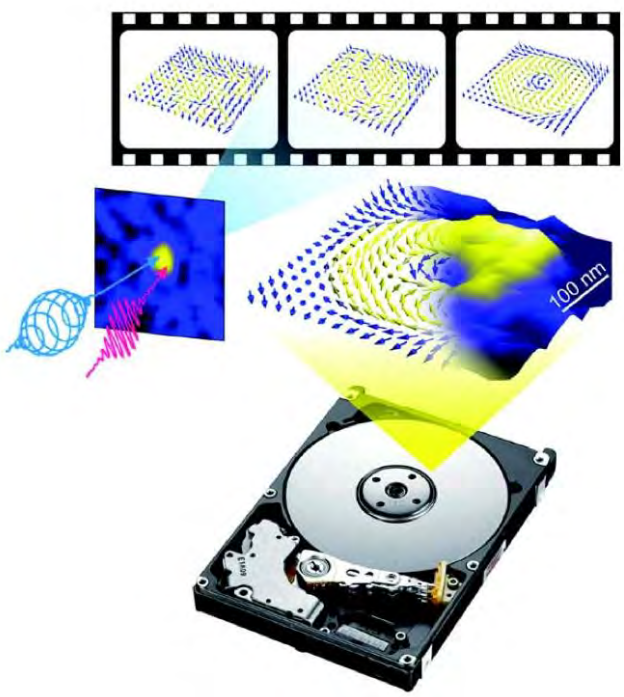

Figure 44: Exploring the future of magnetic data storage. Topologically protected magnetic structures (skyrmions) have recently been written into CoFeTb alloy films, as shown by the scanning optical near field image reproduced from ref. 6. Their formation process following excitation with nano-focused optical femtosecond laser pulses remain so far accessible only to simulations reproduced in the individual frames. A real time femtosecond X-ray movie will become feasible using magnetic X-ray holography with polarized soft X-rays from LCLS-II.

2.3.2.2 Spintronics at THz frequencies

Most practical implementations of actual spintronic devices are metal-based and the spin current used to store and process information is also accompanied by dissipative charge transport. Despite their technological relevance, the direct imaging of either spin currents or accumulations in these structures has only recently been achieved[15]. Additionally, the concept of pure spin currents, which are not accompanied by a net charge current, has recently received increased attention.[16] From a fundamental point of view these pure spin currents provide direct insight into spin-dependent physics and are completely undisturbed by charge transport[17, 18]. For technological applications, they offer significant potential advantages, such as reduced power dissipation, absence of Oersted stray fields, and decoupling of spin and charge noise.

Pure spin currents can be generated through non-local electrical injection, optical injection, spin pumping from a precessing ferromagnet, and via the spin Hall effect (SHE).[19] For example, little is understood about the origins of the SHE in transition metals, such as Pt and Ta. Such effects show great promise for next-generation, non-volatile memory technologies that are currently of great interest throughout the semiconductor industry [20]. While the SHE at low frequencies (<1 MHz) has been studied extensively, it is only recently that measurements have been made at microwave frequencies.[21] These data already indicate that the usual phenomenological description for SHE does not fully encompass the rich physics of the SHE, nor other related spin-orbit coupling effects (e.g., the Dzyaloshinskii-Moriya effect, interfacial spin-orbit torques, the Rashba-effect).

Detailed insight could be obtained if we could study the influence of spin-orbit coupling on spin transport at the time-scale of the elastic scattering process that results in the dc phenomenology (i.e. tens of femtoseconds). One method by which this could be done is to use ultrafast generation of ballistic spin currents via optically driven demagnetization of a ferromagnetic film[7, 22] resulting in large spin currents equivalent to a current density of 10^{10} A cm^{-2} if using a 100 percent spin-polarized charge current. If such a spin current remains ballistic upon propagation from Ni into an adjacent Pt layer, we expect that the SHE should generate a ballistic charge current (see Figure 45). Indeed, it is claimed that this mechanism is the origin of THz emission in Fe/Au and Fe/Ru bilayers pumped with femtosecond optical pulses.[23] The high repetition rates at LCLS II provides the ability to directly probe the momentum and spin states of the excited electrons at the buried ferromagnet/Pt interfaces via spin-polarized ARPES. High kinetic electron energy will make this technique sensitive to buried interfaces (Figure 45). To arrive at a fundamental understanding and potential technological exploitation, the following urgent questions need to be answered:

What is the relevant time-scale for the injected ballistic current decay in Pt?

Is the decay process long enough to permit the observation of coherent spin-orbit coupled states in Pt that should result in an oscillatory response at the frequency of the coupling?

Is the resultant charge current spin-polarized, or is it purely a depolarized charge current?

Figure 45: Probing the spin-Hall effect in real-time. Superdiffusive spin current generated by laser excitation in a ferromagnet (e.g., Ni) injects spins into a Pt layer, where both momentum- and spatial-resolved spectroscopies can detect the electronic motion in the presence of strong spin-orbit coupling.

In addition, X-ray imaging with element-specific magnetic contrast through X-ray circular dichroism is a very promising approach. The achievable spatial resolution is comparable or better than even the shortest spin diffusion lengths encountered in most metals. High-precision X-ray investigations of spin accumulations in metals[15] will become possible at LCLS II. They will result in a significantly more detailed understanding of spin-dependent scattering and accumulation effects. This is important since the impact of spin currents goes far beyond the spintronics paradigm. Spin currents can be observed in insulators[24] and can be coupled to heat transport[25], thereby offering a wide variety of novel opportunities for energy conversion at the nanoscale.

2.3.2.3 Spin textures and topologically-protected order

Finite size effects, which are dominant on nanometer length scales, play an important role in magnetization processes. For example, the magnetization reversal in a ferromagnetic nanowire is much more complex than predicted from analytical theory.[26] Point singularities, such as Bloch points (see Figure 46), which are topological defects in the vector field of magnetization causing the exchange energy to diverge, have to be taken into account. So far, these models are exclusively supported by micro-magnetic simulations, but not yet verified experimentally.

It is particularly important to understand the interaction of such spin textures with a driving spin current. In STT-MRAM devices to operate efficiently, it is necessary to understand switching rates, which also determines the error-rate in real devices. It has been found that the actual energy barrier for switching seems to be lower than theoretically predicted, indicative of a lack in microscopic understanding of the switching process. Current models suggest that in small circular magnetic elements with perpendicular anisotropy, the switching nucleates through a Suhl-like instability leading to edge domains.[27] These processes are highly stochastic and therefore the high repetition rate of LCLS-II will enable to accumulate a statistically significant amount of data to elucidate the degree of deterministic behavior.

X-ray imaging experiments at LCLS-II providing nanometer spatial and femtosecond time resolution will be able to answer the following questions:

How does the divergence of exchange energy impact the local spin texture on a fast time scale.

Are nanoscale magnetic processes deterministic?

Can one control the degree of stochastic behavior specifically in view of energy efficient future devices?

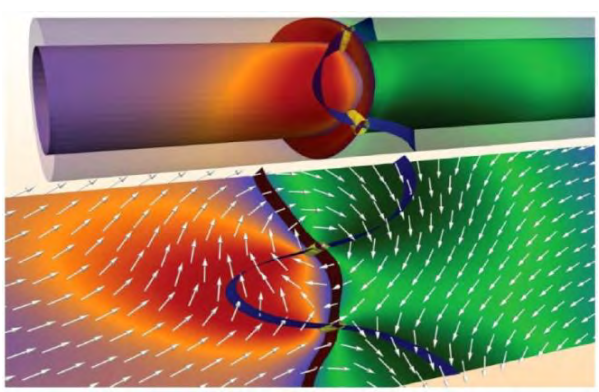

Figure 46: Simulated vortex domain-wall propagation in a ferromagnetic cylinder showing the spin configuration around the Bloch point in its core. Reproduced from ref. 28.

2.3.2.4 Disentangling/controlling coupled degrees of freedom in multiferroic materials

Multiferroics, materials or heterostructures in which anti- and ferromagnetic, ferroelectric and ferroelastic order parameters coexist promise novel functionalities and the possibility of manipulating the magnetic order by an electric field through switching of the electric polarization.[29] This is appealing for applications as it enables information to be efficiently written into magnetic bits without the need for dissipative currents. The search for multiferroic materials and suitable control mechanism has since become a very active research field[30] in which the direct imaging of ferroelectric and magnetic order parameters play important roles.[31]

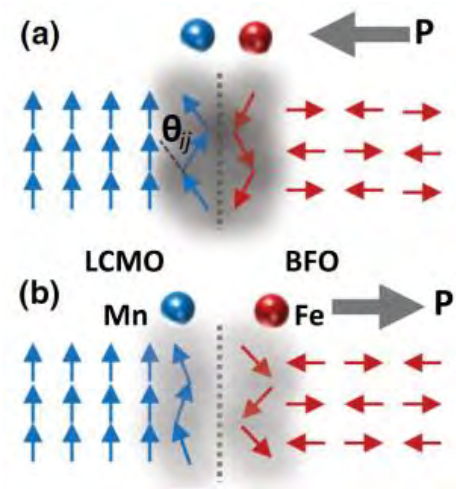

Figure 47. Illustration of the importance of interfacial coupling between ferroelectric (BFO) and ferromagnetic (LCMO) order. Reproduced from ref. 32. X-rays form LCLS II will enable the disentangling of the coupled order parameters via element specific determination of interface spin order as well as stress propagation through the layers.

Time-domain measurements are promising new tools to disentangle the strongly coupled spin, charge, orbital and lattice degrees of freedom whose delicate interplay results in nanoscale spatial inhomogeneity and a complex response to dynamic stimuli in these materials.[33, 34] The ability to probe the time-resolved evolution and coupling of the spin and electric polarization on fundamental time and length scales is essential to understanding and controlling the functionality of these materials (see Figure 47). Time-resolved X-ray magnetic dichroism spectroscopies, diffraction and imaging hold a great promise in this regard, especially when combined with tailored excitation for THz to optical frequencies as those being pioneered at LCLS.[35] LCLS II offers the unique prospect of moving the investigation of complex heterostructures towards nanoscale imaging in real space.

Experimental approaches and the impact of LCLS-II

Spin-resolved photoemission and X-ray magnetic circular dichroism spectroscopy

LCLS II will provide unbiased spectroscopic access to the transient states that emerge when the system is driven far from equilibrium and ultimately control the switching process. Figure 48 illustrates the complementarity of angle resolved photoemission spectroscopy (ARPES) and X-ray absorption spectroscopy (XAS). Time-resolved ARPES at soft and tender X-ray energies, exploits the greater electron escape depth to access buried interfaces, and standing-wave techniques further enhance depth resolution.[36, 37] Spin-resolved detection of transient spin populations will be enabled for the first time. The MHz repetition rate of LCLS II will be essential to avoid space charge limitations inherent in ARPES with short pulse sources (see also section 2.3.1). Spin detection will also allow an unprecedented momentum-resolved view of transient spin populations and spin currents (see Figure 45).

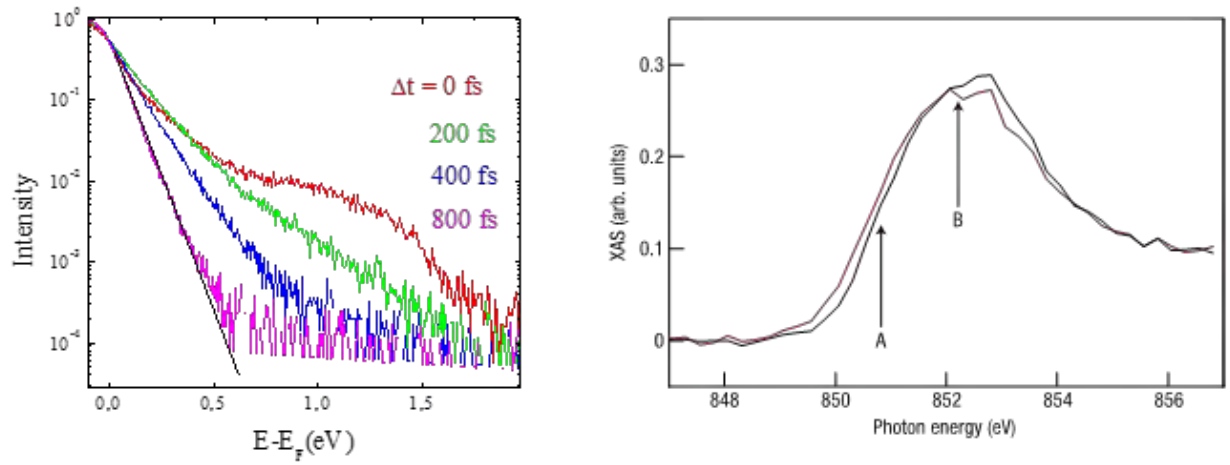

Figure 48. Angle-resolved photoemission spectroscopy (ARPES) and X-ray absorption spectroscopy (XAS) are known to provide unbiased access to equilibrium electronic structure below and above the Fermi level, respectively. Following femtosecond laser excitation, the transient non-equilibrium population of electrons above the Fermi level is accessible to time-resolved ARPES (left panel)[38], whereas XAS monitors the appearance of holes below Fermi (arrow A in the right panel). LCLS II will enable high-precision measurements of transient electronic states using both spectroscopies in the time domain.

XAS and the use of polarized X-rays, X-ray magnetic linear and circular dichroism (XMLD and XMCD) are directly connected to the evolving orbital and spin magnetic moments in anti- and ferromagnets, respectively. The high-stability and high repetition rate of LCLS II will allow us to measure XAS, XMCD and XMLD with unprecedented sensitivity (dynamic range of 10^{-4} and lower[15]), bringing the detection of subtle transient spin states and spin transport effects described in Sections 2.2.2 within reach. This capability will enable us to probe the third transition metal L-edges and rare earth M-edges in the soft X-ray regions as well as relevant 4*d* (Pd) and 5*d* (Pt) edges in the tender X-ray region.

X-ray imaging of transient spin order

Seeded, polarized, femtosecond soft X-ray pulses at high-repetition-rate from LCLS-II will be instrumental to access to the nanometer length scale – via resonant scattering[8] for repetitive processes, or via single-shot imaging for non-periodic processes.[39] We note that the science described above requires extracting the imaginary part of the X-ray optical constants across the relevant absorption edges from coherent scattering measurements. This can then be used to reconstruct quantities such as XAS, XMCD and XMLD with nanometer spatial resolution. This has not been possible so far at LCLS, and further technique development will be required to turn this into a standard tool for LCLS II. The use of X-ray holography methods,[40] in which both phase and amplitude information is encoded by a reference wave, seems best suited to achieve this goal. However, other imaging techniques such as phase retrieval and full field imaging using Fresnel zone plates[41] also need to be explored. An advantage of zone-plate full-field microscopy is that it directly produces real-space images with a larger field of view than X-ray holography. The challenge with X-ray holography is to develop appropriate X-ray masks that allow a high throughput of samples, whereas the zone-plate microscopes require new illumination schemes to slightly reduce the coherence to avoid speckle patterns in the image. With regard to spatial resolution, X-ray holography relies on further reduction of the reference hole on the mask and zone-plate full-field microscopes rely on a further development of their imaging optical elements.

The high repetition rate of LCLS-II will also enable the accumulation of statistically significant datasets to address the scientifically and technologically relevant problem of deterministic behavior on the nanoscale. While 50-to-100 nm spatial resolution has been achieved at LCLS, the dramatically increased

flux at LCLS II through the use of optimized helical undulators will allow single-shot snapshots of magnetic skyrmion formation on the <10 nm-length scale. The pulse duration can be adjusted to avoid electronic damage during the X-ray pulses.[39] In addition, the imaging of deterministic processes will benefit directly from the accumulative data acquisition with the high LCLS II repetition rate, and a spatial resolution down to the few nanometer level is envisioned.

Towards coherent diffraction imaging of interface order

Heterostructures, as described in Section 2.3.2.4 and the emergent phenomena at interfaces described in Section 2.3.1, require spectroscopic access to interfaces and depth-resolved electronic and magnetic structure. Resonant X-ray reflectivity and coherent diffractive imaging seem the techniques of choice here. In general, the interfaces are thin, chemically heterogeneous, and have a complex electron density profile, which makes them harder to study. The ultrafast dynamics will be measured as a function of wavevector change. By selecting wavevectors that are characteristic of the interfacial length scale, it will be possible to identify spectral signatures unique to the interface. To image transport across interfaces we need single-shot imaging at 5 to 10 kHz repetition rate. While some of the existing experimental techniques could be adapted, new techniques need to be developed. Particularly, holography in reflection geometry could be an important tool to image interfaces at the ultrafast time scales.

References

1. S. Mathias, C. La-O-Vorakiat, P. Grychtol, P. Granitzka, E. Turgut, J. M. Shaw, et al., "Probing the timescale of the exchange interaction in a ferromagnetic alloy," Proceedings of the National Academy of Sciences **109**, 4792 (2012).
2. C. D. Stanciu, F. Hansteen, A. V. Kimel, A. Kirilyuk, A. Tsukamoto, A. Itoh, et al., "All-Optical Magnetic Recording with Circularly Polarized Light," Phys. Rev. Lett. **99**, 047601 (2007).
3. S. Mangin, M. Gottwald, C. H. Lambert, D. Steil, V. Uhlíř, L. Pang, et al., "Engineered materials for all-optical helicity-dependent magnetic switching," Nat Mater **13**, 286 (2014).
4. C. H. Lambert, S. Mangin, B. S. D. C. S. Varaprasad, Y. K. Takahashi, M. Hehn, M. Cinchetti, et al., "All-optical control of ferromagnetic thin films and nanostructures," Science **345**, 1337 (2014).
5. I. Radu, K. Vahaplar, C. Stamm, T. Kachel, N. Pontius, H. A. Durr, et al., "Transient ferromagnetic-like state mediating ultrafast reversal of antiferromagnetically coupled spins," Nature **472**, 205 (2011).
6. M. Finazzi, M. Savoini, A. R. Khorsand, A. Tsukamoto, A. Itoh, L. Duo, et al., "Laser-Induced Magnetic Nanostructures with Tunable Topological Properties," Phys. Rev. Lett. **110**, 177205 (2013).
7. D. Rudolf, C. La-O-Vorakiat, M. Battiato, R. Adam, J. M. Shaw, E. Turgut, et al., "Ultrafast magnetization enhancement in metallic multilayers driven by superdiffusive spin current," Nat Commun **3**, 1037 (2012).
8. C. E. Graves, A. H. Reid, T. Wang, B. Wu, S. de Jong, K. Vahaplar, et al., "Nanoscale spin reversal by non-local angular momentum transfer following ultrafast laser excitation in ferrimagnetic GdFeCo," Nat Mater **12**, 293 (2013).
9. A. Einstein, "Experimenteller Nachweis der Ampèreschen Molekularströme," Naturwissenschaften **3**, 237 (1915).
10. E. Beaurepaire, J.-C. Merle, A. Daunois, and J.-Y. Bigot, "Ultrafast Spin Dynamics in Ferromagnetic Nickel," Phys. Rev. Lett. **76**, 4250 (1996).
11. C. Stamm, T. Kachel, N. Pontius, R. Mitzner, T. Quast, K. Holldack, et al., "Femtosecond modification of electron localization and transfer of angular momentum in nickel," Nat Mater **6**, 740 (2007).
12. A. J. Schellekens, and B. Koopmans, "Comparing Ultrafast Demagnetization Rates Between Competing Models for Finite Temperature Magnetism," Phys. Rev. Lett. **110**, 217204 (2013).
13. M. Trigo, M. Fuchs, J. Chen, M. P. Jiang, M. Cammarata, S. Fahy, et al., "Fourier-transform inelastic X-ray scattering from time- and momentum-dependent phonon-phonon correlations," Nat Phys **9**, 790 (2013).
14. L. Zhang, and Q. Niu, "Angular Momentum of Phonons and the Einstein-de Haas Effect," Phys. Rev. Lett. **112**, 085503 (2014).

15. R. Kukreja, S. Bonetti, Z. Chen, D. Backes, Y. Acremann, J. Katine, et al., "X-Ray Detection of Transient Spin Accumulation on Cu atoms near a Co/Cu Interface," arXiv:1503.07275 (2015).
16. C. Chappert, and J.-V. Kim, "Metal spintronics: Electronics free of charge," Nat Phys **4**, 837 (2008).
17. G. Mihajlovic, J. E. Pearson, M. A. Garcia, S. D. Bader, and A. Hoffmann, "Negative Nonlocal Resistance in Mesoscopic Gold Hall Bars: Absence of the Giant Spin Hall Effect," Phys. Rev. Lett. **103**, 166601 (2009).
18. O. Mosendz, J. E. Pearson, F. Y. Fradin, G. E. W. Bauer, S. D. Bader, and A. Hoffmann, "Quantifying Spin Hall Angles from Spin Pumping: Experiments and Theory," Phys. Rev. Lett. **104**, 046601 (2010).
19. A. Hoffmann, "Pure spin-currents," physica status solidi (c) **4**, 4236 (2007).
20. S. Yuasa, A. Fukushima, K. Yakushiji, T. Nozaki, M. Konoto, H. Maehara, et al., "Future prospects of MRAM technologies," in *Electron Devices Meeting (IEDM), 2013 IEEE International*(2013), pp. 3.1.1.
21. M. Weiler, J. M. Shaw, H. T. Nembach, and T. J. Silva, "Phase-Sensitive Detection of Spin Pumping via the ac Inverse Spin Hall Effect," Phys. Rev. Lett. **113**, 157204 (2014).
22. A. Melnikov, I. Razdolski, T. O. Wehling, E. T. Papaioannou, V. Roddatis, P. Fumagalli, et al., "Ultrafast Transport of Laser-Excited Spin-Polarized Carriers in Au/Fe/MgO(001)," Phys. Rev. Lett. **107**, 076601 (2011).
23. KampfrathT, BattiatoM, MaldonadoP, EilersG, NotzoldJ, MahrleinS, et al., "Terahertz spin current pulses controlled by magnetic heterostructures," Nat Nano **8**, 256 (2013).
24. Y. Kajiwara, K. Harii, S. Takahashi, J. Ohe, K. Uchida, M. Mizuguchi, et al., "Transmission of electrical signals by spin-wave interconversion in a magnetic insulator," Nature **464**, 262 (2010).
25. K. Uchida, S. Takahashi, K. Harii, J. Ieda, W. Koshibae, K. Ando, et al., "Observation of the spin Seebeck effect," Nature **455**, 778 (2008).
26. A. S. Arrott, B. Heinrich, and A. Aharoni, "Point singularities and magnetization reversal in ideally soft ferromagnetic cylinders," Magnetics, IEEE Transactions on **15**, 1228 (1979).
27. K. Munira, and P. B. Visscher, "Calculation of energy-barrier lowering by incoherent switching in STT-MRAM," arXiv:1410.7361 (2014).
28. C. Andreas, A. Kakay, and R. Hertel, "Multiscale and multimodel simulation of Bloch-point dynamics," Phys. Rev. B **89**, 134403 (2014).
29. N. A. Spaldin, and M. Fiebig, "The Renaissance of Magnetoelectric Multiferroics," Science **309**, 391 (2005).
30. S. H. Baek, H. W. Jang, C. M. Folkman, Y. L. Li, B. Winchester, J. X. Zhang, et al., "Ferroelastic switching for nanoscale non-volatile magnetoelectric devices," Nat Mater **9**, 309 (2010).
31. T. Zhao, A. Scholl, F. Zavaliche, K. Lee, M. Barry, A. Doran, et al., "Electrical control of antiferromagnetic domains in multiferroic $BiFeO_3$ films at room temperature," Nat Mater **5**, 823 (2006).
32. Y. M. Sheu, S. A. Trugman, L. Yan, J. Qi, Q. X. Jia, A. J. Taylor, et al., "Polaronic Transport Induced by Competing Interfacial Magnetic Order in a $La_{0.7}Ca_{0.3}MnO_3/BiFeO_3$ Heterostructure," Physical Review X **4**, 021001 (2014).
33. Y. M. Sheu, S. A. Trugman, L. Yan, Q. X. Jia, A. J. Taylor, and R. P. Prasankumar, "Using ultrashort optical pulses to couple ferroelectric and ferromagnetic order in an oxide heterostructure," Nat Commun **5** (2014).
34. H. Wen, P. Chen, M. P. Cosgriff, D. A. Walko, J. H. Lee, C. Adamo, et al., "Electronic Origin of Ultrafast Photoinduced Strain in $BiFeO_3$," Phys. Rev. Lett. **110**, 037601 (2013).
35. T. Kubacka, J. A. Johnson, M. C. Hoffmann, C. Vicario, S. de Jong, P. Beaud, et al., "Large-Amplitude Spin Dynamics Driven by a THz Pulse in Resonance with an Electromagnon," Science **343**, 1333 (2014).
36. A. X. Gray, C. Papp, B. Balke, S. H. Yang, M. Huijben, E. Rotenberg, et al., "Interface properties of magnetic tunnel junction $La_{0.7}Sr_{0.3}MnO_3/SrTiO_3$ superlattices studied by standing-wave excited photoemission spectroscopy," Phys. Rev. B **82**, 205116 (2010).
37. A. X. Gray, J. Minár, L. Plucinski, M. Huijben, A. Bostwick, E. Rotenberg, et al., "Momentum-resolved electronic structure at a buried interface from soft X-ray standing-wave angle-resolved photoemission," EPL (Europhysics Letters) **104**, 17004 (2013).
38. H. S. Rhie, H. A. Dürr, and W. Eberhardt, "Femtosecond Electron and Spin Dynamics in N/W(110) Films," Physical Review Letters **90**, 247201 (2003).
39. T. Wang, D. Zhu, B. Wu, C. Graves, S. Schaffert, T. Rander, et al., "Femtosecond Single-Shot Imaging of Nanoscale Ferromagnetic Order in Co/Pd Multilayers Using Resonant X-Ray Holography," Phys. Rev. Lett. **108**, 267403 (2012).

40. S. Eisebitt, J. Luning, W. F. Schlotter, M. Lorgen, O. Hellwig, W. Eberhardt, et al., "Lensless imaging of magnetic nanostructures by X-ray spectro-holography," Nature **432**, 885 (2004).
41. P. Fischer, D.-H. Kim, W. Chao, J. A. Liddle, E. H. Anderson, and D. T. Attwood, "Soft X-ray microscopy of nanomagnetism," Materials Today **9**, 26 (2006).

2.4 Nanoscale Heterogeneity, Fluctuations and Dynamics of Functional Materials

Synopsis

Dynamic heterogeneity at the nanoscale is ubiquitous in functional materials and processes, ranging from protein librations that are essential to biological function, to super-paramagnetic fluctuations that limit the density of information that can be stored on a hard drive. An important characteristic of such processes is that they connect thermally-driven ultrafast events on the nanoscale with kinetic phenomena and properties on the macro scale. This connection has been intensely studied for many decades and in many different contexts, since it governs the emergence of complex material properties from simple microscopic interactions.

LCLS-II will revolutionize our ability to probe dynamic nanoscale electronic-, chemical-, and structural-heterogeneity by providing access to very broad ranges of time and length scales, in combination with incisive resonant X-ray contrast mechanisms. The high average coherent power from LCLS-II will enable acquisition of correlation spectroscopy scattering snapshots that will characterize heterogeneity and fluctuations over longer time scales such as chemical kinetics, diffusion, reactive flow in porous media, and material systems where fast events cross over to domain wall or microphase boundary motion.

LCLS-II coherent X-ray laser pulses and programmable time structure will enable two-pulse "probe-probe" correlation spectroscopy/scattering measurements of spontaneous processes on ultrafast time scales. For example, thermally-driven fluctuations of electronic structure, polaron motion, and topological spin states in transition metal oxides will be characterized on relevant nanometer length scales and fundamental time scales for the first time. These approaches will be further applicable to emergent heterogeneity and fluctuations associated with non-equilibrium processes and matter in transient extreme environments. Spontaneous nucleation processes occurring on picosecond and sub-picosecond time-scales in extreme states of matter often determine the evolution of new phases.

Complementing the X-ray 'probe-probe' capabilities, coherent THz excitation provides a means to impulsively trigger thermal events by localization of energy in specific vibrational modes. In the near-equilibrium regime, these excitations relate directly to spontaneous thermal excitations. Excitation far from equilibrium can induce phase transitions and the formation of metastable phases that are not thermally accessible. Ultrafast hard X-ray scattering probes will be indispensable for characterizing these driven phase transitions. In summary, ultrafast X-ray tools provided by LCLS-II will provide a qualitative advance in our understanding of dynamic heterogeneity across a broad range of functional nanomaterials.

2.4.1 Spontaneous Fluctuations and Nanoscale Heterogeneity

Introduction

A variety of nanostructured systems exhibit dynamical heterogeneity driven either thermally or by adiabatic variation of external fields, including molecular switches,[1, 2] polymer melts,[3] colloidal suspensions,[4] magnetic domains (as discussed in Section 2.3.1),[5-14] single-center fluorophores,[15, 16] biopolymers,[17-20] and charge and orbital domains in complex oxides (as discussed in Section 2.3.2).[21-24] An important challenge in studying such systems is the need to probe a very broad range of temporal and spatial scales (1/kT~100 fs). In complex materials, spontaneous fluctuations of electron and spin ordering will start to dominate at nanometer length scales, and may provide an inherent lower size limit for devices. Relevant modes in protein folding and function, for example, span from molecular-scale vibrations at THz frequencies to macromolecular-scale librations on the scale of 1 Hz.

Coupled to the question of dynamics is the issue of heterogeneity, in both space and time. Correlations between dynamics and heterogeneity can profoundly affect the properties of functional materials.[25] For example, in magnetic recording technologies it is well known that as the bit size is decreased, fluctuations begin to dominate and will ultimately limit the stability of the system.[26] Dynamic heterogeneity is often associated with fast or ultrafast intermittent nanoscale events that spawn statistically self-similar spatial and/or temporal structures. Power law dependencies and the absence of characteristic length and time scales are of central importance in understanding the emerging macroscopic properties, though this connection is rarely understood in detail.

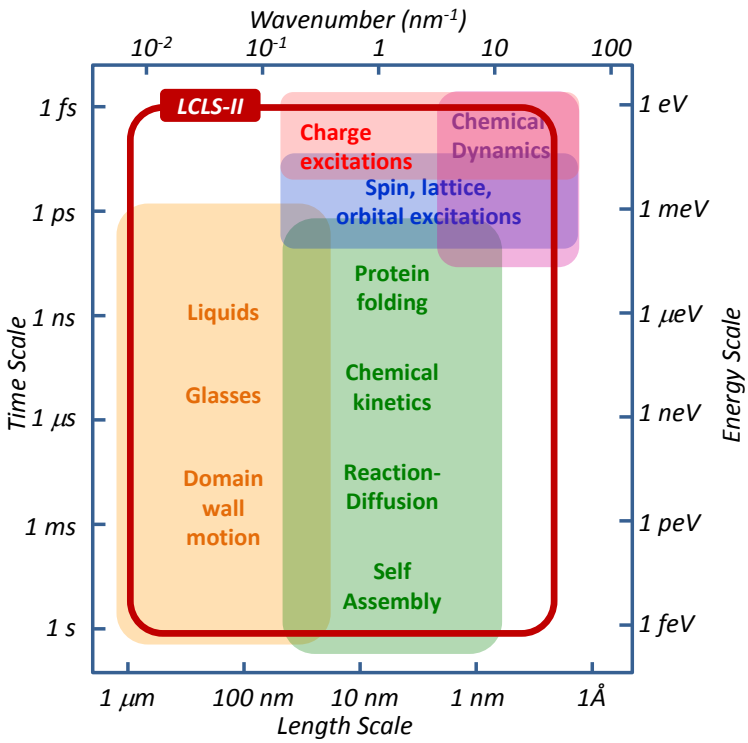

Figure 49. Time and length scales of spontaneous dynamics associate with various materials and chemical processes. X-ray photon correlation spectroscopy operates in a key area not accessible by other techniques. LCLS-II will open up new frontiers in correlation spectroscopy by characterizing materials over a broad range of length and time scales. Note that time resolution scales as the square of the average brightness, and LCLS-II will be ~1,000 brighter than any soft X-ray storage ring.

X-ray photon correlation spectroscopy (XPCS) is one powerful approach for characterizing spontaneous fluctuations and nanoscale heterogeneity is X-ray photon correlation spectroscopy (XPCS). This X-ray analogue of dynamic light scattering measures the dynamics structure factor S(***q***,t) – the two-point correlation function that describes density correlations and their evolution – with element/chemical specificity and sub-nm resolution provided by X-rays. The details of this approach and the anticipated impact of LCLS-II are discussed in further detail at the end of Section 2.4.1 (Experimental approaches and the impact of LCLS-II).

Spontaneous Fluctuations and Heterogeneity in Electronic Structure: Driven Functionality in Complex Oxides:

Hallmarks of strongly correlated systems are competing spin, charge, orbital and lattice degrees of freedom, which result in spontaneous emergence of nanoscale inhomogeneities in the electronic structure.[27-32] Examples include smectic (stripe) phases and phase coexistence observed in spin- and charge-density wave materials, underdoped high-T_c superconductors and colossal magnetoresistive (CMR) transition-metal oxides, emergence of metallic domains during Metal-Insulator transition etc. (see Figure 50).

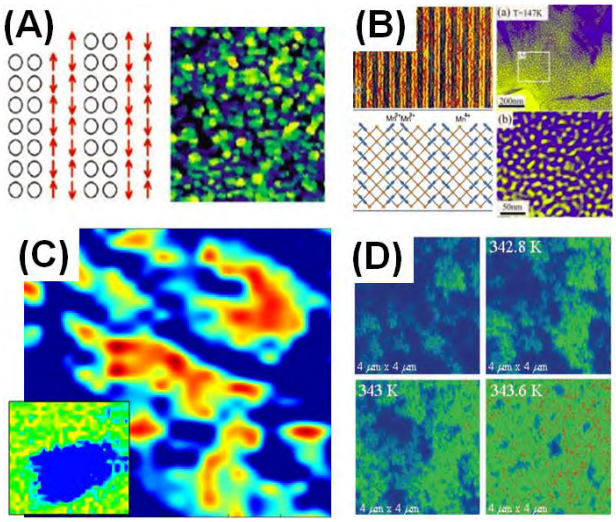

Figure 50: Examples of nanoscale inhomogeneities in a variety of strongly correlated systems: (A) Scanning Tunneling Spectroscopy of the inhomogeneous distribution of superconducting energy-gap and stripe (or checkerboard) patterns in underdoped high-T_c superconductors;[27,33,34] (B) Phase separation in colossal magnetoresistive (CMR) manganites;[28,34,35] (C) Charge-Density Wave[32] and Spin-Density Wave (inset)[36] domains in Chromium; (D) Coexistence of Conducting and Insulating domains in VO_2 at the onset of the Metal-Insulator Transition.[37]

The inhomogeneous domains in correlated oxides, such as Mott insulators, CMR manganites, superconductors and other materials typically occur as a result of strong correlations and competition between different electronic (ordered) phases. However, it is not yet clear to what extent nanoscale phase separation and fluctuating order parameters are determined primarily by intrinsic electronic effects, or if crystalline imperfections such as lattice strain, defects, or inhomogeneous distribution of dopants influence the formation of textured patterns. XPCS studies of fluctuations in correlated electron systems performed at LCLS-II would provide us with invaluable insight into how electronic correlations emerge and what role the disorder plays in their formation.

The ways in which spin-order, charge-order, orbital-order and lattice-order parameters can be accessed with X-ray diffraction are shown schematically in Figure 51. Panel (A) shows an example of real-space and reciprocal (momentum) space manifestations of the incommensurate antiferromagnetic spin density and charge density waves in elemental chromium.[36] By varying the X-ray scattering geometry (and polarization) one can tune to various charge density or spin density wave satellite scattering peaks, as well as the Bragg peaks originating from the crystalline lattice, allowing for independent access to relevant lattice, charge and spin order parameters. Panel (B) shows a similar example of charge, magnetic, orbital and lattice ordering in a mixed valence magnetoresistive manganite, in this case $Pr_x(Ca_ySr_{1-y})_{1-x}MnO_3$ (PCSMO).[38]

Additional examples of fluctuating order parameters that will be studied with XPCS enabled by LCLS-II include fluctuations of charge-ordered stripes in high-Tc superconductors and strongly correlated oxides, fluctuations of orbital domains, antiferromagnetic and spin-density wave domain walls, skyrmion dynamics, ferromagnetic, ferroelectric domain wall dynamics, etc. An important example of a long-standing question in this area is the role of fluctuating stripes (comprised of charge, spin and/or orbital order) and electronic heterogeneity in determining the properties of unconventional superconductors. Fluctuating order appears to dominate in the pseudogap regime of cuprate superconductors. This non-superconducting regime exhibits many properties that mirror those of the superconducting phase, and may provide a route toward higher T_C. However, the physics of this regime and its relation to the adjacent superconducting phase remain poorly understood.

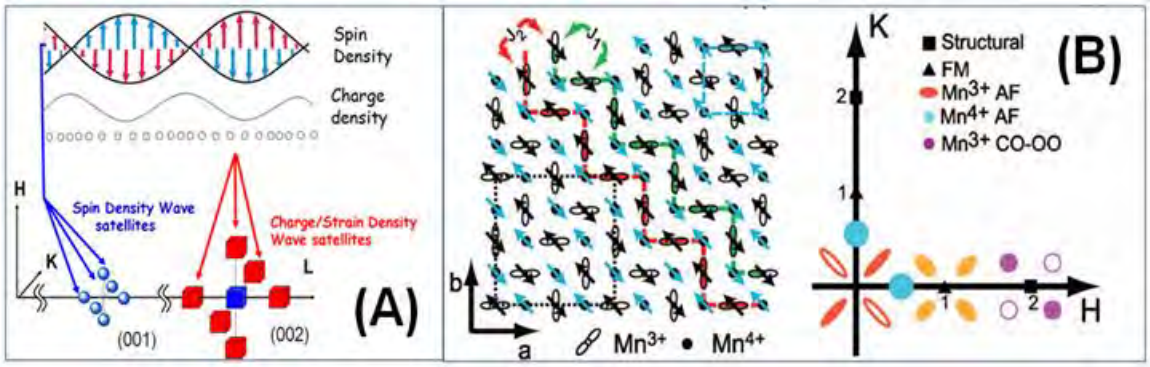

Figure 51: Representation of Charge-, Spin- and Orbital- order parameters as satellites in reciprocal space: (A) Charge Density Wave and Spin Density Wave in Chromium. Adopted from ref. 32; (B) Ferromagnetic (FM), Antiferromagnetic (AFM), Charge-Ordered (CO) and Orbital-Ordered (OO) phases in the nearly half-doped perovskite manganites in the pseudo-cubic phase.[38]

It should be noted that many of the competing order parameters in correlated electronic materials, such as spin, orbital and charge ordering, are best studied using resonant X-ray scattering techniques. Of particular importance are the soft X-ray (L-edges) of transition metals (500eV-800eV), M-edges of rare earth elements (1 keV-1.5 keV) and M edges of the actinides (2 keV-5 keV). In this regime, LCLS-II will have unique capabilities for providing ultrafast X-rays with high average brightness.

An Example: Fluctuation-mediated topological spin texture:

Topologically protected novel phases in condensed matter systems are currently a research topic of tremendous interest due both to the unique physics and to their potential in device applications. Skyrmions are a topological phase of spins that originates from thermal fluctuations and are manifest in magnetic materials as a hexagonal lattice of spin vortices. The concept of skyrmions originates with the work of T. Skyrme who proposed a topologically stable (soliton) solution to wave-like excitations in a continuum field (in the context of interacting pions). In magnetic materials, the skyrmion spin vortices are particle-like excitations existing in a background field of ferromagnetic order, and have recently been identified by neutron scattering and Lorentz transmission electron microscopy in chiral magnetic systems.

Various mechanisms contribute simultaneously to the emergence of skyrmions in magnetic systems, including: long-ranged magnetic dipolar interactions, Dzyaloshinskii–Moriya (DM) interaction, frustrated exchange interaction, and thermal fluctuations. The emergent skyrmion magnetic field is robust to perturbations that do not alter the topology of the spin texture. The topological nature protects the skyrmion against defects, and they can be made to move with 100,000 times lower current density (e.g. compared to domain walls) without destroying the spin texture. These transport properties and robust character make magnetic skyrmions appealing as potential spintronic memory bits.

Skyrmions were first discovered in the magnetic system MnSi[39] a helical antiferromagnet with an ordering temperature of 30 K. Application of a modest magnetic field creates a conical phase, and at still higher field the system becomes ferromagnetic. At a temperature slightly below T_c there exist a phase called "A-phase," which is identified as the skyrmion phase. Apart from MnSi, soft X-ray scattering has recently been applied to characterize skyrmions in a multiferroic system.[40] The existence of skyrmions in an insulating multiferroic is of particular interest since it now provides a way to control the skyrmions with an electric field.

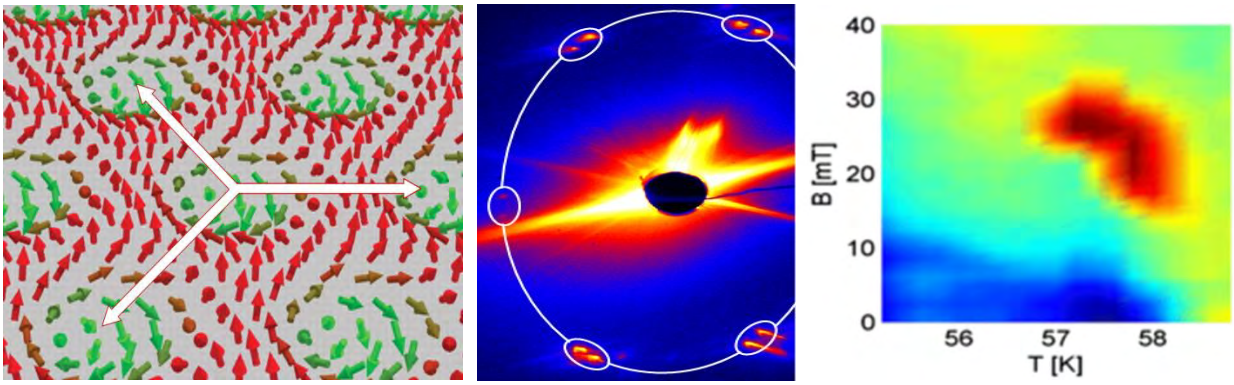

Figure 52: Left shows skyrmion spin texture.[39] Skyrmions form a hexagonal lattice in a plane that is perpendicular to the applied field direction. Middle: Resonant soft X-ray scattering from skyrmions in Cu_2OSeO_3.[40] Six distinct scattering peaks reflect the 3Q nature of the ordering. Right: Phase diagram of Cu_2OSeO_3 with the skyrmion phase indicated in red.[40]

Similar to skyrmions, fluctuations play an important role in surface and 2D magnetic systems as discussed in Section 2.3.2. They have a profound effect on the spin reorientation phase transition. Significant stochastic effects are predicted for point singularities, such as Bloch points, which are topological defects in the vector field of magnetization causing the exchange energy to diverge. Domain wall fluctuations are believed to be the origin of 1/f noise in magnetic devices, so it is of interest to study these in real time. To date there have been almost no studies of spin dynamics using coherent X-rays. Using coherent X-ray beams at the L- or M-edges of rare earth metals, such as Dy or Ho, which possess antiferromagnetic spiral structures at low temperatures at accessible values of wave-vector transfer, it will be possible to carry out studies of spin fluctuations by observing the temporal evolution of speckle intensity in the neighborhood of the magnetic satellite peaks. Of particular interest is the direct observation and characterization of critical fluctuations near magnetic phase transitions, including quantum phase transitions. The signal from spin textures are generally weak, and high repetition rate based light sources such as LCLS-II will be ideal to study the spontaneous nanoscale fluctuations in these magnetic systems.

Spontaneous Fluctuations and Heterogeneity in Chemistry

Multi-phase chemical processes, diffusion, and transport are central to a broad range of energy and environmental challenges, from heterogeneous catalysis (as discussed in Section 2.2), to carbon sequestration, to energy storage and conversion systems, to sub-surface environmental chemistry. These are fundamentally stochastic processes dominated by chemical heterogeneity and fluctuations of the local chemical structure and environment. Characterizing and controlling the chemical mechanisms and kinetic pathways that span many orders of length scales and time scales is a grand challenge where LCLS-II capabilities will have a qualitative impact.

An Example: Site-specific chemical kinetics in advanced energy conversion processes:

Understanding and controlling reactive chemical flow through porous media is central to both environmental issues and technology applications. Porous materials increasingly support novel application in catalysis, chemical separation, and energy conversion processes, and they provide an ideal platform to study chemical dynamics in confined geometries.[41-43] A long-standing challenge is to synthesize open crystals with pore apertures of a size suitable for the inclusion of large organic, inorganic, and biological molecules. A promising new class of materials are the metal-organic frameworks (MOFs), which are compounds consisting of metal ions coordinated to organic molecules to form three-dimensional porous structures.[41] MOFs have broad applications in industry, and are among the most

exciting developments in nanotechnology in the past decade. One important potential application of MOFs with suitable chemical structure and power size is the capture of atmospheric CO_2.

Very recent advances in nanoscale synthesis have produced networks with pore sizes that can be varied and properties that can be controlled by functionalization. For example, in the MOF-74 material, pore sizes are varied from 14 to 98 Å by systematically expanding the oligo-phenylene moiety lengths from one unit to 11.[44] Similarly, meso-porous silica and carbon with large apertures (whose sizes can be varied up to 100 nm) have been created through suitable chemical synthesis.

Studies related to CO_2 capture applications indicate local structure and symmetry variations are induced in both the lattice and electronic structure due to gas adsorption. There is significant scientific debate about the role of kinetic correlations due to gas adsorption on the nanosecond-to-picosecond time scales and the nanometer-to-micrometer length scales. However there is a large knowledge gap, and a lack of experimental tools for direct measurement on these time and length scales. XPCS measurements of correlated temporal, spatial, and chemical information can provide critical experimental results that may lead to fine-tuning of MOF structures and pore functionalization for the development of "smart nano-porous materials" for use in a broad range of applications in catalysis, separation and energy conversion.

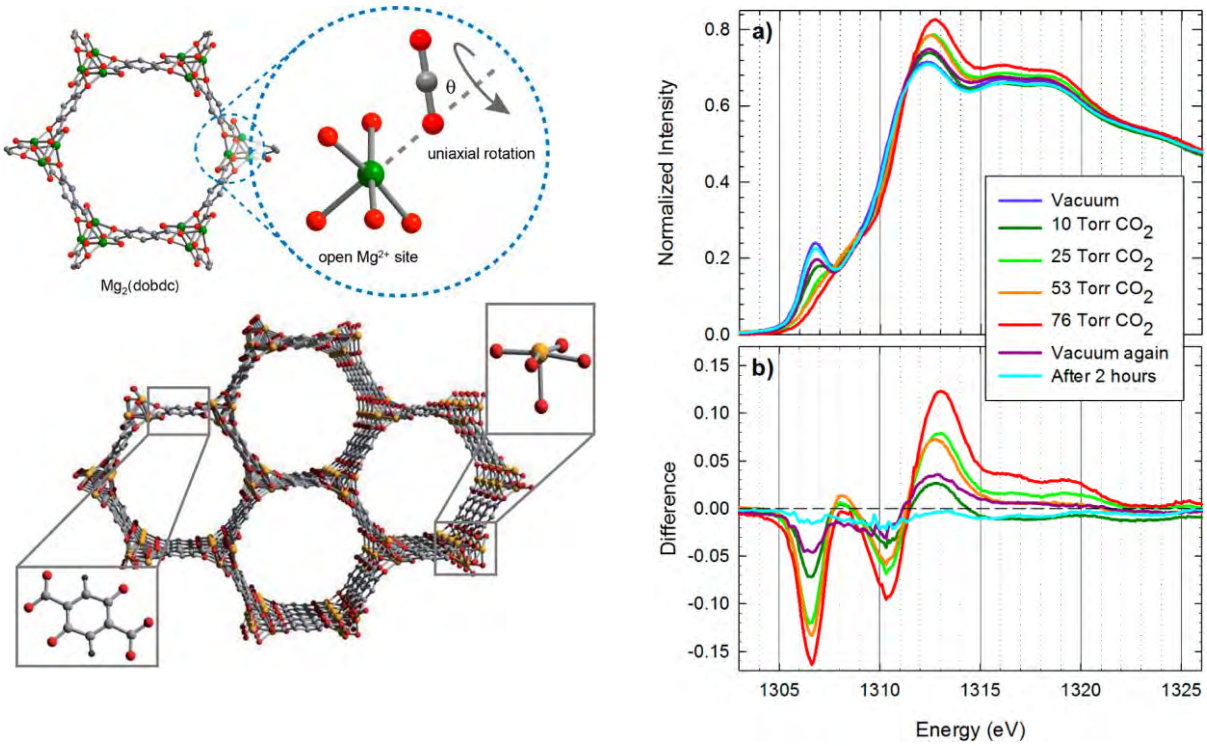

Figure 53: Left: Organic gas flows into a MOF structure.[45] Chemical reaction inside the pores can be used to convert organic molecules into fuel. The transition metal cation in the MOF has one dangling bond facing into the pores. These are the reaction sites where the gas molecules get attached. Mg XANES spectra indicates that the prominent pre-edge feature gets suppressed as CO_2 is dosed into the system.[46]

For example, M_2(dobdc), (M = transition metal) is a well-studied MOF with a structure consisting of one dimensional metal oxide chains that are connected to dobdc4- ligands giving rise to a hexagonal array of channels of 11 Å that are oriented along the c-axis.[45] The metal ions have open coordination sites facing the pores, and these are likely binding sites for gas adsorption. During the CO_2 adsorption process in the *low pressure regime* MOFs based on different metal cations show remarkable differences in CO_2

adsorption properties. However, the differentiated functionality becomes negligible at higher loading pressure, most likely due to the isostructural nature of the frameworks. Around 1 bar pressure, the adsorption capacity of the Mg, Ni, Fe, and Co frameworks are ≈1.1 CO_2 per metal(II) site, indicating that these materials are already approaching the saturation capacity of the primary adsorption site. DFT calculations show binding enthalpies, -ΔH, ranging from 27.1 to 40.9 kJ mol^{-1} at 0.167 CO_2 per M^{2+}. It is conceivable that orbitals and electronic structure also plays a role.

X-ray absorption studies on Mg-MOF-74 show changes in the pre-edge features associated with changes in *s-p* hybridization at the open sites of the metal cation initiated by CO_2 adsorption.[46] The XANES spectra at the Mg edge (Figure 53) exhibit a distinct pre-edge peak that is a spectral fingerprint of the activated Mg-MOF-74sample. This pre-edge feature is suppressed and blue-shifted when CO_2 gas is introduced (see Fig. 4). Additional spectral signatures include an increase in intensity and slight blue shift of the strongest main edge feature. These features evolve progressively as a function of gas pressure. One possible reason is the breaking of local symmetry around the metal ion and mixing of *p* character into the predominantly metal s character. [13]

Carbon NMR studies revealed details of the rotational dynamics of CO_2 molecules.[47] A strong interaction exists between CO_2 and the metal cation. The NMR data reveals that motional freedom of CO_2 is arrested. The CO_2 is not only spatially confined within the pores, rather, a fixed uniaxial rotation of the CO_2 with most likely geometric center of the rotation axis along the Mg–O(CO_2) vector takes place. The correlation time and temperature dependence of the rotational motion has also been studied and follows an Arrhenius model.

Important open questions remain about the nature of the chemical processes occurring along the pore surface (primarily interacting with the metal site) and/or through the pore opening (interacting with surface bound gas). It is these dynamic processes, for which we lack direct experimental probes, that determine the rate and efficiency of gas separation or storage in the porous materials. The porous materials exhibit multiple length scales that can be accessed via Bragg scattering in the soft X-ray range. Tuning to resonant scattering at specific spectral features accesses different chemical kinetic and dynamic processes such as the oxidation changes in Co sites as organic gas flows through the system. There must be a charge transfer between the metal ion and the ligands. There are diffusive processes due to the gas flow. The soft X-ray capabilities at the LCLS-II will enable the first XPCS studies of chemical dynamics in porous materials in resonance with either the metal ion absorption edge (e.g. Co L_3-edge for MOF Co2(dobdc)) or absorption edges of reacting species, at nanometer spatial resolution. Such chemically-specific length scale dependent reaction-diffusion information will give unprecedented insight into the fundamental interaction between a confined metal cation in a pore and flowing organic molecules.

Experimental approaches and the impact of LCLS-II

X-ray Photon Correlation Spectroscopy (XPCS)

The capabilities of LCLS-II offer a qualitative advance for X-ray photon correlation spectroscopy as a direct probe of temporal fluctuations and correlations.[32, 48-54] In the soft X-ray range, XPCS scattering methods can provide correlation information with nano- to mesoscale spatial resolution, and chemical specificity via X-ray resonances. Scattering with coherent X-rays produces a speckle pattern that is an instantaneous spatial Fourier representation of the illuminated structure. Two speckle patterns from a sample with exactly the same morphology are identical, i.e. fully correlated with each other at all values of momentum transfer ***q***. For an evolving system the speckle pattern changes from one time snap-shot to the next, often in a time and ***q***-dependent fashion.

XPCS probes these spontaneous material dynamics through the intermediate scattering function S(q,t), which is the Fourier transform of the dynamical structure factor S(***q***,ω) as discussed in Section 2.3.1. Thus, by measuring S(***q***,t) over a wide range of time and ***q***, it is possible to obtain a dispersion curve that characterizes the dynamics. In this sense, XPCS is a complimentary method to RIXS and hence can serve as bridge to close the time (energy) regions that are not easily accessible by RIXS. At present, even at a diffraction limited light source, XPCS cannot access sub μs time scales. LCLSII will enable studies of spontaneous fluctuations from μs (or longer) to fundamental femtosecond time scales, and will open up whole new areas of science (as illustrated in Figure 49).

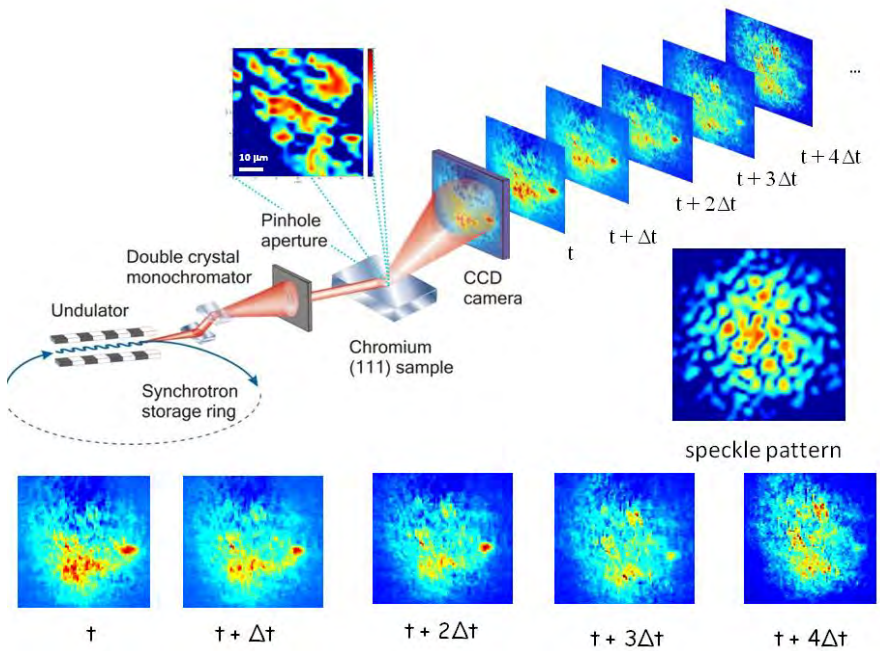

Figure 54: A series of ultrafast diffraction snapshots. For a static system, the speckle pattern on the detector remains same meaning individual snapshots are correlated. For a dynamical system, the speckle pattern will change, and measuring the time constant for the de-correlation gives us information about the intermediate scattering function S(***q***,t), which is the Fourier transform of the dynamical structure factor S(***q***,ω).

Correlations between a series of two-dimensional speckle patterns is represented by the autocorrelation function $g_2(Q, t)$, calculated for each pixel of an area detector and averaged over the pixels within the same range of wavevector transfer Q:

$$g_2(\vec{Q},t) = 1 + A[S(\vec{Q},t)/S(\vec{Q})]^2 = \frac{\left\langle I(\vec{Q},t\ )I(\vec{Q},t\ +\tau)\right\rangle_\tau}{\left\langle I(\vec{Q},\tau\ )\right\rangle_\tau^2} \qquad \text{Eq. (1)}$$

where, I(τ) and I (t+τ) are the intensities in a given pixel for frames taken at times τ and τ+t respectively, and averaging is carried out over all τ, while keeping time t constant. Resulting $g_2(t)$ functions calculated for each individual pixel are then averaged for the particular region of interest of the CCD. The decay of the autocorrelation function $g_2(Q,t)$ as a function of time-difference between speckle frames t and the wave vector Q reveals important information about spatial (Q-dependence) and temporal (t-dependence) behavior of the system. As expressed in the Eq.(1) $g_2(Q,t)$ is related to the normalized intermediate scattering function (ISF) described above. XPCS relies on average coherent flux, and capabilities at present synchrotron sources are severely limited due to the low coherent X-ray flux available. The average brightness of LCLS-II will exceed these sources by perhaps as much as ~10,000 times, and will

be a game-changer for XPCS studies of fluctuations and heterogeneity across a broad range of materials and chemical systems.

Techniques now under development at LCLS will provide the foundation for major advances in XPCS research in the next few years.[55, 56] These techniques, combined with the very high repetition rate of LCLS-II X-ray lasers will open for study entirely new time regimes of dynamic nanoscale heterogeneity that are not accessible with present synchrotron or low repetition-rate X-ray FEL sources.

XPCS capabilities at present sources are severely limited due to the low coherent X-ray flux available, and the subtlety of the underlying physics (and associated X-ray contrast mechanisms). The signal-to-noise ratio of XPCS experiments scales as:

$$S/N_{XPCS} \sim t^{1/2} B \sigma_{X\text{-}ray} \qquad \text{Eq. (2)}$$

where B is the average brightness of the source, $\sigma_{X\text{-}ray}$ is the scattering cross-section per volume and t is the sampling (integration) time. Thus, the shortest accessible time interval (measurable correlation time) scales as $1/B^2$. Enhanced brightness from diffraction-limited storage rings is anticipated to extend the accessibly time-regime to ~1 μs in the soft X-ray range (see Figure 1). Accessing nanosecond time scales that are relevant for functional devices will require a fully-coherent, high-repetition rate source. Reaching the fundamental time scales of vibrational dynamics, charge-transfer, and charge correlation will require an ultrafast X-ray laser in combination with two-pulse probing as described below to establish the correlation time of the speckle pattern. High repetition rate is indispensable to insure that the flux per pulse remains within tolerable limits while maintaining the high average flux.

XPCS Time series – 10 nsec to many second time scale dynamics:

The "sequential mode" follows the protocol described above: a temporal autocorrelation function $g_2(\boldsymbol{q},t)$ is produced from a timed sequence of speckle patterns, as shown in Figure 54. The presently accessible temporal range in this approach is limited by the repetition rate of present X-ray FEL's. In the SASE mode, LCLS-II will operate initially at 100 kHz (with an upgrade path to 1 MHz), dramatically expanding the range of experiments that can be performed. The high LCLS-II repetition rate will make experiments on systems with very low scattering contrast possible in both the sequential and the split pulse modes discussed below. The high LCLS-II repetition rate will also open for study the important time regime between ~100 ns and ~30 msec. This will not be easily probed at other facilities because delay lines longer than ~100 ns become unmanageable in the split and delay approach. Also, the minimum time scale accessible in the sequential XPCS approach is determined by the source repetition rate.

XPCS Split pulse delay line – sub picosecond to nanosecond dynamics:

The ultrafast "two-pulse" mode [55, 56] for XPCS relies on superimposed pairs of speckle patterns collected with time-delayed X-ray pulses. The decay in speckle fringe visibility is driven by thermally mediated decorrelation between the two pulses and can be related to $g_2(\boldsymbol{q},t)$. This approach will probe ultrafast, thermally driven dynamics for the first time, with a time resolution limited only by the X-ray delay. An example of such an experiment at LCLS-II is the dynamic formation of magnetic domains from a paramagnetic state. As the system passes through the Neel temperature, the spins start to order and fluctuate in the form of 'spin droplets'. The spin fluctuation is very fast, but as the temperature is further lowered the domains start to form in order to minimize the energy. The split pulse mode will allow the temporal and spatial dependence of these spin droplets to be measured.

Sample damage and modification at 4th generation light sources:

Sample damage/modification due to the intense FEL pulses are significant issues that have been extensively considered, and are discussed briefly in Appendix 1. These issues are particularly relevant in the split pulse approach, where the first X-ray pulse in a pair cannot disrupt the phenomena being measured by the second pulse. The capability to use moderate peak-power pulses, while maintaining high average power via high-repetition rate will be essential. The shorter absorption length will make the problem more serious since the pulse energy will be deposited in a smaller volume. However, this decreased extinction length is partially compensated by the lower energy per photon. It is becoming increasing clear that one gets the best contrast in diffractive imaging experiments by using a wavelength that is closer to the desired resolution and not arbitrarily short wavelengths to avoid radiation damage. The importance of limiting sample damage or disruption of the states being measured means that the number of photons/pulse that can be effectively used will be comparable at all FEL facilities. The higher LCLS-II repetition rate – up to 10,000 times higher than LCLS - will make experiments on systems with very low scattering contrast possible, in both the sequential and the split pulse modes.

2.4.2 Materials Dynamics, Energy Transport, and Phase Transitions at the Nanoscale

Introduction

The sustainability of modern society depends on our means to convert and utilize energy efficiently with minimal environmental impact. Solutions to these problems require an ability to understand, design and control the physical processes of materials that underlie energy conversion, dissipation and storage and transport at the level of the fundamental constituents. Novel, coherent X-ray sources that can access the ultrafast timescales of these processes with atomic-scale resolution and element specificity will transform our understanding of these processes and lead to the development of novel materials with new functionality. These opportunities arise from the unprecedented combination of high-repetition rate, polarization control and multiple-color, multiple ultrashort pulses with high flux and coherence provided by an X-ray FEL.

In particular, the high-repetition rate of LCLS-II at the 3rd harmonic will open up new possibilities for studying processes near equilibrium involving small lattice displacements. Additionally, the extension to 25 keV at 120 Hz and the associated higher accessible momentum transfers will open up the application of pair distribution function (PDF) approaches in the time domain. Examples of problems where the LCLS-II will have a transformative impact within materials science are: (i) the mechanisms for emergent behavior in correlated materials, (ii) understanding the dynamics of energy transport, conversion and dissipation in nanoscale materials for novel applications, (iii) understanding and controlling phase transitions and dynamical fluctuations at the nanoscale, (iv) ultrafast dynamics of non-trivial atomic correlations in non-periodic systems such as glasses and soft matter, and (v) the role that inhomogeneity plays in determining the tunable properties of advanced materials.

Energy conversion, transport, & phase transitions at the nanoscale

The problem of heat conduction at nanoscale dimensions[57, 58] is of wide fundamental interest and sets stringent physical limits to the size of semiconductor devices. Understanding and controlling heat flow at this scale will provide novel technological solutions to our increasing energy demands. In particular, a fundamental understanding of how heat flows at the nanoscale will enable technologies to manipulate the flow of heat with artificial nanostructures. Applications range from improving the energy efficiency and performance of microelectronic, thermoelectric, and optoelectronics devices, to phase change memory devices[59] to heated nanoparticles for medical therapies.[60]

As the characteristic size of a nanostructure decreases, we reach a regime where the dimensions of the devices are comparable to the phonon mean free path, and thus phonons propagate ballistically across structures. This crossover between diffusive and ballistic transport means Fourier's law of conduction breaks down and heat flow does not follow the diffusion equation. Here, the wave nature of the phonons determines most of the transport properties.[61, 62] Thus, interfaces become extremely important at the nanoscale. Novel opportunities are associated for example with understanding of thermoelectric properties and phonon transport within two-dimensional materials or two-dimensional heterostructures.[63]

In spite of advances in theory and simulations, progress is limited by the lack of experimental probes at the relevant time- and length-scales. In general, time-domain spectroscopy can probe the dynamics of heat transport. However, all methods based on light scattering probe only small momentum transfers near $\boldsymbol{q}$=0 (where $\boldsymbol{q}$ is the phonon wavevector), and thus are ineffective to probe the heat-carrying, short-wavelength phonons that have THz frequencies. Conversely, atomic-scale scattering techniques which are effective under thermal equilibrium conditions, such as inelastic X-ray and neutron scattering, lack the temporal resolution to probe the nonequilibrium dynamics intrinsic to this problem.

LCLS-II presents new opportunities to fill the gap in experimental probes of nanoscale energy transport. Hard-X-ray pump-probe can compete with inelastic neutron scattering (INS) at probing phonon dispersions[64] with the unique advantage of also accessing non-equilibrium dynamics and transient states as illustrated in Figure 55. First experiments have demonstrated the feasibility of such measurements and these pave the way for a new momentum- and time-resolved technique for measuring, microscopically, the phonon anharmonicity and contribution to the thermal conductivity. The future capabilities of LCLS-II will be revolutionary: currently, these experiments are limited primarily by source fluctuations rather than the number of photons per pulse. The high repetition rate of the LCLS-II at its harmonics will not only increase the data quality by orders of magnitude but will allow *in-situ* studies on weakly scattering structures that are too small for the current capabilities, such as artificial nanostructures and devices.

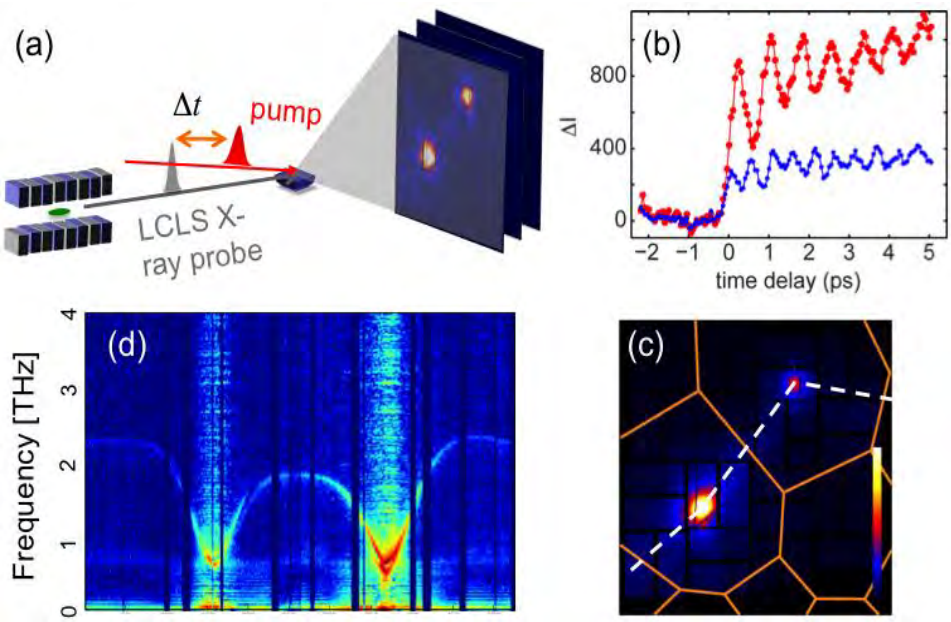

Figure 55. Summary of time-domain phonon spectroscopy, from ref. 64. (a) phonons are probed by X-ray diffuse scattering with an area detector after ultrafast excitation. (b) the diffuse scattering intensity, ΔI(t) for different momentum transfers (pixels) oscillates with the corresponding phonon frequency. (c) equilibrium diffuse scattering image from Ge(110) with 10 keV photons, orange lines are Brillouin zone boundaries. (d) phonon dispersion along the dashed line in (c) obtained from the Fourier transform of ΔI(t).

The study of energy transport processes are intrinsically coupled to an understanding of the phase diagram of materials; for example, materials tuned near a phase boundary exhibit novel or tunable thermoelectric properties.[65-67] From a broader perspective, the functionality of materials and devices is determined in part by the ways in which external perturbations such as stress, strain, electric and magnetic fields modify this phase diagram.[68, 69] At the nanoscale, very little is known about the morphological shape changes and crystallographic changes associated with nonequilibrium phase transitions. This is in part due to the ultrafast nature of these processes, associated with sound-speed-limited transformations over length-scales of nanometers. Recently LCLS has enabled first snapshots of these processes[70, 71] but these studies are additionally hindered by the fact that the relevant scattering patterns span a broad range of reciprocal space such that even large-amplitude structural or morphological changes lead to small transient effects in scattering patterns.[72]

Example: atomic-scale structural fluctuations

Consider the case of nanocrystals engineered for solid-state lighting applications. It is known that ultrasmall semiconductor nanocrystals emit broadband light at their smallest sizes but the mechanisms underlying these processes are not understood. Figure 56 shows the broadband emission for a 2 nm diameter CdSe nanocrystal spanning the visible spectrum, along with scanning transmission electron microscope snapshots taken seconds apart which indicate dynamic fluctuations of the nanocrystal structure, blurred out by the temporal resolution of the imaging technique.[73] Similar pair distribution function (PDF) analyses from X-ray scattering[74] extending out to high Q show blurring of the local structure, associated with temporal averaging. It is thought that these dynamic structural fluctuations give rise to fluctuations in the electronic band structure and thus the broad-band emission, but prior studies have not been able to resolve these processes directly, and the time-scales for these processes are unknown. XPCS-based approaches at LCLS-II, coupled with high Q-scattering PDF-based approaches to resolve the local structure, will enable measurement of these intrinsic dynamics across a range of time-scales spanning microseconds to picoseconds and enable a fundamental understanding of this technologically-relevant process.

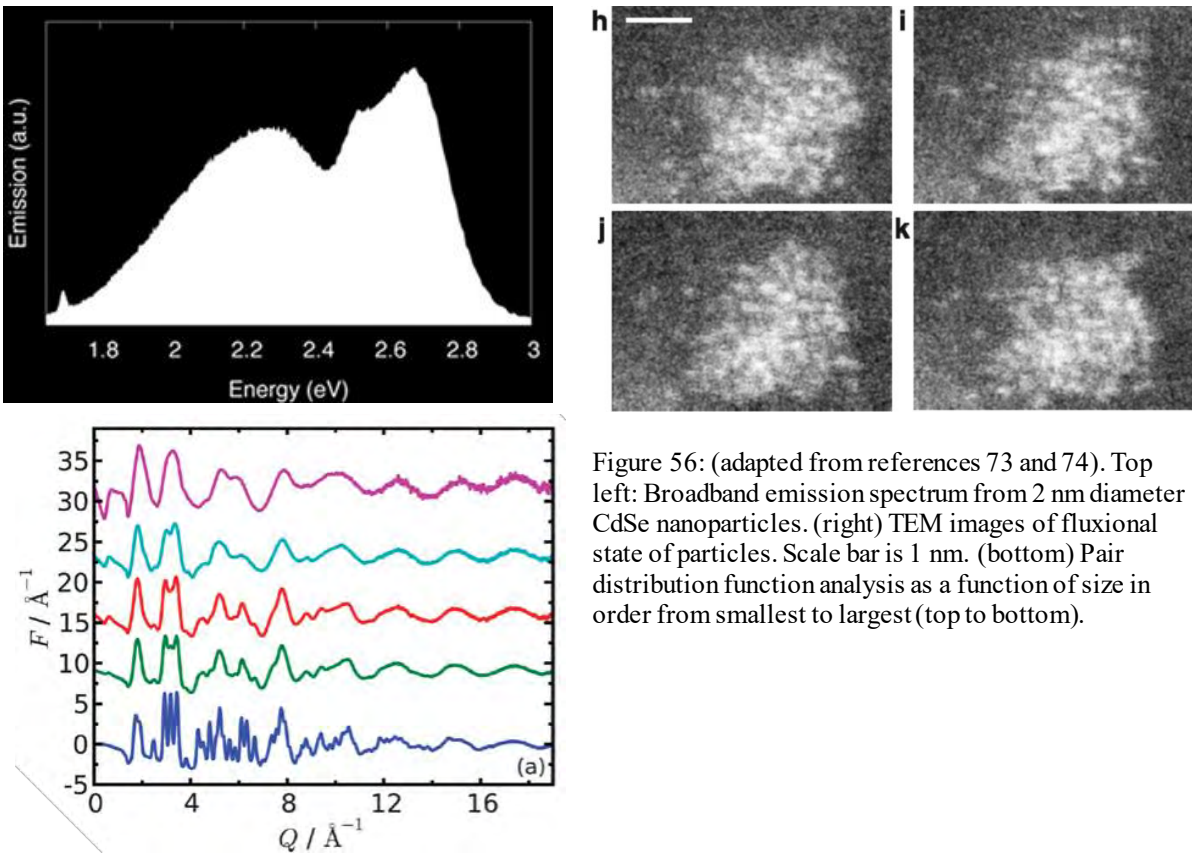

Figure 56: (adapted from references 73 and 74). Top left: Broadband emission spectrum from 2 nm diameter CdSe nanoparticles. (right) TEM images of fluxional state of particles. Scale bar is 1 nm. (bottom) Pair distribution function analysis as a function of size in order from smallest to largest (top to bottom).

Example: beyond ideal materials

From a general perspective, materials functionality is often determined by the defects and imperfections that represent deviations from ideal crystalline or periodic structures. Phase-change materials exploit the sensitivity of the electrical and optical properties to the underlying crystalline or amorphous atomic structures that can be accessed,[75] and the efficiency of solar cells are determined by recombination processes at defect states or surfaces or by the sensitivity of transport properties to disorder, structural degrees of freedom, and conformations on atomic, nanoscale, and mesoscopic length-scales.[76] High

repetition rate scattering capabilities of LCLS-II will enable studies of these local strains and polaronic distortions, and these will be coupled with spectroscopic studies with elemental specificity probing these defect states and the associated short range order within solids. For example, recent synthetic work has led to the creation of two-dimensional hybrid perovskites that emit broadband white light upon UV excitation. [77, 78] These materials are promising as next generation phosphors for solid-state lighting (SSL) devices.[79] In preliminary work, mechanistic studies suggest that the observed emission arises from excited electrons/holes trapped through strong coupling to a deformable lattice (Figure 57). Such transient defect states and associated electron-phonon coupling constants can be indirectly probed using ultrafast optical probes[80] but direct information about the local polaronic-like strains surrounding trapped electrons or bound excitons has never been measured. The lifetime of these states are typically of order nanoseconds in duration with sub-picosecond formation times, depending on the dimensionality of the system. LCLS-II enables direct and element-specific measurements of these local distortions, both through XANES measurements at relevant absorption edges (e.g. Br L-edge for emitters based on $PbBr_4$) and through XPCS and diffuse X-ray scattering studies following above-gap femtosecond excitation. Although electron-phonon coupling is very strong in these materials, favoring the formation of self-trapped-excitons, these correspond to localized lattice distortions and require high-repetition-rate high signal-to-noise measurements in order to study these processes under technologically-relevant conditions.

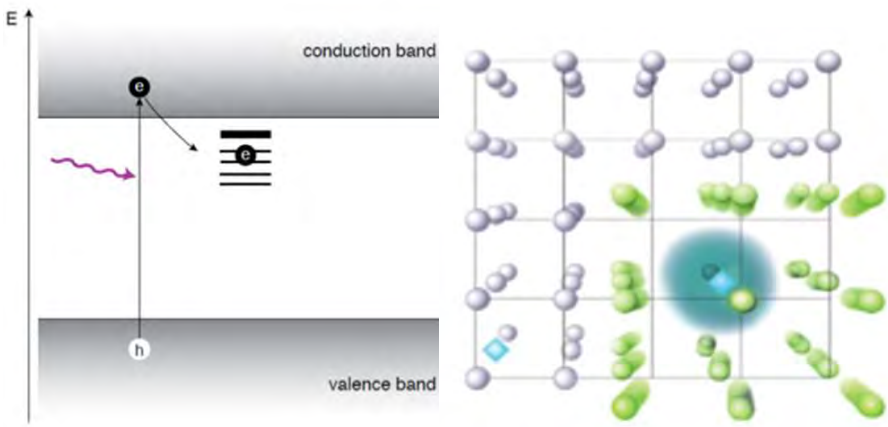

Figure 57: Schematic of light-induced defect state and associated lattice distortions giving rise to novel optoelectronic properties. LCLS-II enables first measurements of the associated ultrafast dynamical processes and visualization of the atomic structure and localized strain associated with these polaronic distortions.

Example: phase-change materials

Extensions of the approaches discussed above will involve optical pump followed by multiple pulse X-ray probing of the non-equilibrium dynamics occurring within nanoscale materials and the fluctuations which occur as a nanocrystal or nanoscale heterostructure transforms between structural phases. From a general perspective, when an energy barrier separates two structural phases, the switching response will be statistical in nature and involve nanoscale nucleation processes and associated fluctuations. Thus optical triggers may drive large amplitude temperature jumps or modulate the free energy surfaces separating structural configurations and XPCS-based approaches can be applied to capture the dynamical processes which ensue. This approach is broadly applicable to materials in extreme conditions as discussed in Section 2.5.

Consider as an example, recent studies which have shown that short pulse laser excitation provides a new means of fabricating thin film solar cells in an economic and scalable manner.[81] This approach enables

separation of an epitaxially-grown III-V material like GaAs from a substrate in a rapid and efficient manner by selective and localized deposition of energy within a buried layer, serving as an alternative to existing etching-based approaches. This procedure provides a new means for transferring high-quality single-crystal III-V films to flexible polymer substrates, but the atomic-scale mechanisms underlying the liftoff process are still largely unknown and unexplored at this time.

From a fundamental perspective, there is no atomic-level understanding of the structural processes and nanoscale nucleation events that occur when a buried single-crystal layer is selectively superheated on short time scales. How does the structure of the buried, coherently strained layer evolve as it is superheated above its melting point in a confined geometry, without a free surface to nucleate the liquid phase? Answering these questions will not only provide useful insight for the optimization of our laser liftoff process, but may also dramatically expand our understanding of some of the most fundamental concepts in materials science.

LCLS-II will enable new approaches to visualizing the first steps in these processes. Single shot X-ray scattering measurements with X-ray energies of 25 keV will allow for selective probing of the buried layer through selective monitoring of Bragg peaks, resolving the transition from crystalline to superheated liquid as reflected in the X-ray diffuse scattering pattern.[82] In the sub-threshold regime, these measurements may be carried out at high rep-rate working at the third harmonic of the superconducting RF source, probing the associated acoustic stress and strain dynamics that likely play a role in the lift-off process itself.

One may also envision combined X-ray scattering approaches with element-specific near-edge spectroscopic techniques (e.g. at the In L-edge, 3.7 keV, associated with an InGaAs absorbing buried layer) in order to probe changes in local order and electronic structure during the lift-off process. Together these approaches will enable fundamental studies of this phenomenon with the potential to lead directly to technological applications for thin film solar cell technologies. Fig. 6 shows first principles simulations of the dynamic lift-off processes and associated nucleation events following laser excitation of a surface.[82] LCLS-II will enable direct experimental probes connecting to this theoretical work.

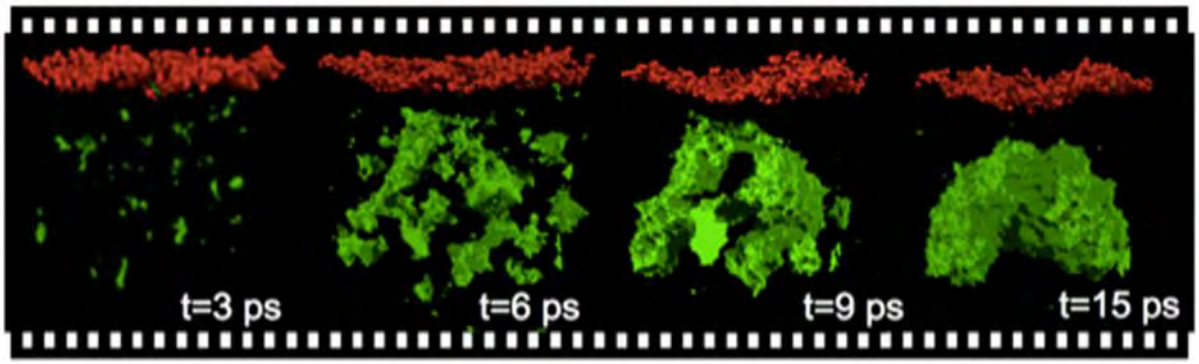

Figure 58: Adapted from reference 82, showing snapshots of the near-surface region of a silicon surface at various times after excitation and the spontaneous development of nanoscale voids (in green) below the surface (in red)

Example: fluctuations and field-induced processes in ferroelectrics

Ferroelectric materials comprise non-centrosymmetric unit cells with a permanent electric dipole moment switchable by an external electric field, with strong coupling between polarization, strain, and electronic/charge degrees of freedom. Their response to external strains, stresses or electric fields are

often enhanced at phase boundaries e.g. between the ferroelectric and paraelectric phases[83] and they play an important role as potential multifunctional devices for next generation non-volatile memory in which information is encoded in the polarization state of the material. The dynamics of how the ferroelectric polarization changes underlie this functionality, but these processes, and the time-scales on which they occur, are not understood.[84-89]

A window into these processes can be obtained through the use of single-cycle terahertz fields which act as an optical bias – turning on and off on hundreds of femtosecond time-scales. Recent studies using LCLS X-ray pulses to probe ultrafast THz electric-field driven processes in perovskite $BaTiO_3$ nanoscale thin films have shown transient structure factor modulations at the 1% level, associated with large-amplitude volume-preserving distortions of the unit cell and modulations of the ferroelectric polarization. However, these studies are limited by the range of accessible Bragg reflections, and by the signal to noise at LCLS. Extensions to higher energy (25 keV) using PDF approaches and to higher repetition rate (e.g. 5 keV, ~1 MHz, resonant at the Ti K-edge) as enabled by LCLS-II, would provide the first direct visualizations of these local atomic-scale motions.

With respect to THz-driven excitations, an additional benefit of higher-rep-rate, lower peak power operating modes as enabled by LCLS II is the ability to focus X-ray beams within nanoscale electrode structures without damaging the materials by the X-ray pulses. The structures in turn enable large amplitude field-enhancements and the ability to reach THz fields at the >10 MV/cm level. Because these fields are on for only a single optical cycle, breakdown processes are less important than in the DC limit allowing for application of larger fields strengths. Similar efforts can be applied to a broad range of problems associated with phase-change materials. Here, field-induced threshold switching leads to the formation of an amorphous on-state and reversible switching between amorphous and crystalline phases. These processes as above involve statistical processes associated with the complex free energy surfaces that define glassy states of matter, and THz-pump / XPCS probe experiments would enable direct visualization of these processes and the fundamental speed limits that underlie them.

Experimental Approaches and Impact of LCLS-II

Current approaches for dynamic studies of atomic structure – including time-resolved diffuse scattering, PDF, and SAX/WAX – will benefit substantially from the extension of LCLS-II to 25 keV. This will enable higher resolution (higher scattering $\boldsymbol{q}$), and will provide penetration capabilities to probe bulk phenomena in high-Z materials.

Current time-resolved X-ray scattering approaches utilizing 120 Hz in the 3-8 keV range will benefit from the higher repetition rate and substantially higher average flux up to 5 keV. This will improve the measurement statistics for experiments that are presently limited by intensity fluctuations of the source. For scattering studies at photon energies above 5 keV, harmonics from LCLS-II may provide some benefit. The average 3rd harmonic flux from LCLS-II at 300 kHz may be comparable to (or as much as ten times higher) than the fundamental flux from LCLS. In this regime, the higher repetition rate may also provide a decisive advantage for signal averaging and sensitivity for some experiments.

References

1. F. Liu, M. Bao, H.-J. Kim, K. L. Wang, C. Li, X. Liu, et al., "Giant random telegraph signals in the carbon nanotubes as a single defect probe," Appl. Phys. Lett. **86**, 163102 (2005).
2. S. Chang, J. He, L. Lin, P. Zhang, F. Liang, M. Young, et al., "Tunnel conductance of Watson–Crick nucleoside–base pairs from telegraph noise," Nanotechnology **20**, 185102 (2009).
3. E. V. Russell, and N. E. Israeloff, "Direct observation of molecular cooperativity near the glass transition," Nature **408**, 695 (2000).

4. E. R. Weeks, J. C. Crocker, A. C. Levitt, A. Schofield, and D. A. Weitz, "Three-Dimensional Direct Imaging of Structural Relaxation Near the Colloidal Glass Transition," Science **287**, 627 (2000).
5. D.-H. Kim, and S.-C. Shin, "Intermittency of Barkhausen avalanche in Co nanothin films " J. Appl. Phys. **95**, 6971 (2004).
6. O. Narayan, "Self-Similar Barkhausen Noise in Magnetic Domain Wall Motion," Physical Review Letters **77**, 3855 (1996).
7. P. J. Cote, and L. V. Meisel, "Self-organized criticality and the Barkhausen effect," Phys. Rev. Lett. **67**, 1334 (1991).
8. G. Durin, and S. Zapperi, "Scaling exponents for Barkhausen avalanches in polycrystalline and amorphous ferromagnets," Phys. Rev. Lett. **84**, 4705 (2000).
9. O. Perkovic, K. Dahmen, and J. P. Sethna, "Avalanches, Barkhausen noise, and plain old criticality," Phys. Rev. Lett. **75**, 4528 (1995).
10. E. Puppin, "Statistical properties of Barkhausen noise in thin Fe films," Phys. Rev. Lett. **84**, 5415 (2000).
11. D. Spasojevic, S. Bukvic, S. Milosevic, and H. E. Stanley, "Barkhausen noise: elementary signals, power laws, and scaling relations," Phys. Rev. E **54**, 2531 (1996).
12. J. S. Urbach, R. C. Madison, and J. T. Markert, "Interface depinning, self-organized criticality, and the Barkhausen effect," Phys. Rev. Lett. **75**, 276 (1995).
13. A. Vazquez, and O. Sotolongo-Costa, "Dynamics of a Domain Wall in Soft-Magnetic Materials: Barkhausen Effect and Relation with Sandpile Models," Phys. Rev. Lett. **84**, 1316 (2000).
14. S. Zapperi, P. Cizeau, G. Durin, and H. E. Stanley, "Dynamics of a ferromagnetic domain wall: Avalanches, depinning transition, and the Barkhausen effect," Phys. Rev. B **58**, 6353 (1998).
15. R. Verberk, A. M. van Oijen, and M. Orrit, "Simple model for the power-law blinking of single semiconductor nanocrystals," Physical Review B **66**, 233202 (2002).
16. A. Issac, C. von Borczyskowski, and F. Cichos, "Correlation between photoluminescence intermittency of CdSe quantum dots and self-trapped states in dielectric media," Physical Review B **71**, 161302 (2005).
17. H. P. Lu, L. Xun, and X. S. Xie, "Single-Molecule Enzymatic Dynamics," Science **282**, 1877 (1998).
18. A. S. Deniz, S. Mukhopadhyay, and E. A. Lemke, "Single-molecule biophysics: at the interface of biology, physics and chemistry," J. Roy. Soc. Interface **6**, 15 (2007).
19. M. K. Prakash, and R. A. Marcus, "An interpretation of fluctuations in enzyme catalysis rate, spectral diffusion, and radiative component of lifetimes in terms of electric field fluctuations," PNAS **104**, 15982 (2010).
20. S.-J. Chen, "RNA Folding: Conformational Statistics, Folding Kinetics, and Ion Electrostatics," Annual Review of Biophysics **37**, 197 (2008).
21. G. B. Alers, A. P. Ramirez, and S. Jin, "1/f resistance noise in the large magnetoresistance manganites," Appl. Phys. Lett. **68**, 3644 (1996).
22. H. T. Hardner, M. B. Weissman, M. Jaime, R. E. Treece, P. C. Dorsey, J. S. Horwitz, et al., "Non-Gaussian noise in a colossal magnetoresistive film," J. Appl. Phys. **81**, 272 (1997).
23. V. Podzorov, C. H. Chen, M. E. Gershenson, and S.-W. Cheong, "Mesoscopic, non-equilibrium fluctuations in inhomogeneous electronic states in manganites," Europhys. Lett. **55**, 411 (2001).
24. B. Raquet, A. Anane, S. Wirth, P. Xiong, and S. von Molnár, "Noise Probe of the Dynamic Phase Separation in $La_{2/3}Ca_{1/3}MnO_3$," Phys. Rev. Lett. **84**, 4485 (2000).
25. V. Skumryev, S. Stoyanov, Y. Zhang, G. Hadjipanayis, D. Givord, and J. Nogues, "Beating the superparamagnetic limit with exchange bias," Nature **423**, 850 (2003).
26. R. Pecora, ed. *Dynamic Light Scattering* (Plenum Press, New York, 1985).
27. E. Dagotto, "Complexity in Strongly Correlated Electronic Systems," Science **309**, 257 (2005).
28. M. Uehara, S. Mori, C. H. Chen, and S. W. Cheong, "Percolative phase separation underlies colossal magnetoresistance in mixed-valent manganites," Nature **399**, 560 (1999).
29. J. Lee, K. Fujita, K. McElroy, J. A. Slezak, M. Wang, Y. Aiura, et al., "Interplay of electron–lattice interactions and superconductivity in Bi2Sr2CaCu2O8+d," Nature **442**, 546 (2006).
30. K. K. Gomes, A. N. Pasupathy, A. Pushp, S. Ono, Y. Ando, and A. Yazdani, "Visualizing pair formation on the atomic scale in the high-Tc superconductor $Bi_2Sr_2CaCu_2O_{8+\delta}$," Nature **447**, 569 (2007).
31. M. Vershinin, S. Misra, S. Ono, Y. Abe, Y. Ando, and A. Yazdani, "Local Ordering in the Pseudogap State of the High-Tc superconductor $Bi_2Sr_2CaCu_2O_{8+\delta}$," Science **303**, 1995 (2004).

32. O. G. Shpyrko, E. D. Isaacs, J. M. Logan, Y. J. Feng, G. Aeppli, R. Jaramillo, et al., "Direct measurement of antiferromagnetic domain fluctuations," Nature **447**, 68 (2007).
33. T. Hanaguri, C. Lupien, Y. Kohsaka, D. H. Lee, M. Azuma, M. Takano, et al., "A 'checkerboard' electronic crystal state in lightly hole-doped Ca2-xNaxCuO2Cl2," Nature **430**, 1001 (2004).
34. M. Dierolf, O. Bunk, S. R. Kynde, P. Thibault, I. Johnson, A. Menzel, et al., "Ptychography & lensless X-ray imaging," Europhysics News **39**, 22 (2008).
35. S. Mori, C. H. Chen, and S. W. Cheong, "Pairing of charge-ordered stripes in (La,Ca)MnO3," Nature **392**, 473 (1998).
36. P. G. Evans, E. D. Isaacs, G. Aeppli, Z. Cai, and B. Lai, "X-ray Microdiffraction Images of Antiferromagnetic Domain Evolution in Chromium," Science **295**, 1042 (2002).
37. M. M. Qazilbash, M. Brehm, B. G. Chae, P. C. Ho, G. O. Andreev, B. J. Kim, et al., "Mott transition in VO2 revealed by infrared spectroscopy and nano-imaging," Science **318**, 1750 (2007).
38. F. Ye, J. A. Fernandez-Baca, P. Dai, J. W. Lynn, H. Kawano-Furukawa, H. Yoshizawa, et al., "Electronically smecticlike liquid-crystal phase in a nearly half-doped manganite," Phys. Rev. B **72**, 212404 (2005).
39. S. Mühlbauer, B. Binz, F. Jonietz, C. Pfleiderer, A. Rosch, A. Neubauer, et al., "Skyrmion Lattice in a Chiral Magnet," Science **323**, 915 (2009).
40. M. C. Langner, S. Roy, S. K. Mishra, J. C. T. Lee, X. W. Shi, M. A. Hossain, et al., "Coupled Skyrmion Sublattices in Cu_2OSeO_3," Phys. Rev. Lett. **112**, 167202 (2014).
41. U. Mueller, M. Schubert, F. Teich, H. Puetter, K. Schierle-Arndt, and J. Pastre, "Metal-organic frameworks-prospective industrial applications," Journal of Materials Chemistry **16**, 626 (2006).
42. H. Furukawa, K. E. Cordova, M. O'Keeffe, and O. M. Yaghi, "The Chemistry and Applications of Metal-Organic Frameworks," Science **341** (2013).
43. D. Farrusseng, ed. *Metal-Organic Frameworks: Applications from Catalysis to Gas Storage* (Wiley-VCH Verlag GmbH & Co. KGaA, 2011).
44. H. Deng, S. Grunder, K. E. Cordova, C. Valente, H. Furukawa, M. Hmadeh, et al., "Large-Pore Apertures in a Series of Metal-Organic Frameworks," Science **336**, 1018 (2012).
45. W. L. Queen, M. R. Hudson, E. D. Bloch, J. A. Mason, M. I. Gonzalez, J. S. Lee, et al., "Comprehensive study of carbon dioxide adsorption in the metal-organic frameworks M_2(dobdc) (M = Mg, Mn, Fe, Co, Ni, Cu, Zn)," Chemical Science **5**, 4569 (2014).
46. W. S. Drisdell, R. Poloni, T. M. McDonald, J. R. Long, B. Smit, J. B. Neaton, et al., "Probing Adsorption Interactions in Metal–Organic Frameworks using X-ray Spectroscopy," Journal of the American Chemical Society **135**, 18183 (2013).
47. X. Kong, E. Scott, W. Ding, J. A. Mason, J. R. Long, and J. A. Reimer, "CO_2 Dynamics in a Metal–Organic Framework with Open Metal Sites," Journal of the American Chemical Society **134**, 14341 (2012).
48. M. Sutton, "A review of x-ray intensity fluctuation spectroscopy," C.R. Physique **9**, 657 (2007).
49. G. Grübel, and F. Zontone, "Correlation spectroscopy with coherent X-rays," J. Alloys and Compounds **362**, 3 (2004).
50. P. Livet, "Diffraction with a coherent X-ray beam: dynamics and imaging," Acta Cryst. A **A63**, 87 (2007).
51. S. B. Dierker, R. Pindak, R. M. Fleming, I. K. Robinson, and L. Berman, "X-Ray Photon Correlation Spectroscopy Study of Brownian Motion of Gold Colloids in Glycerol," Phys. Rev. Lett. **75**, 449 (1995).
52. S. G. J. Mochrie, A. M. Mayes, A. R. Sandy, M. Sutton, S. Brauer, G. B. Stephenson, et al., "Dynamics of Block Copolymer Micelles Revealed by X-Ray Intensity Fluctuation Spectroscopy," Phys. Rev. Lett. **78**, 1275 (1997).
53. S. W. Chen, H. Guo, K. A. Seu, K. Dumesnil, S. Roy, and S. K. Sinha, "Jamming Behavior of Domains in a Spiral Antiferromagnetic System," Phys. Rev. Lett. **110**, 217201 (2013).
54. E. Dagotto, *Nanoscale phase separation and colossal magnetoresistance : the physics of manganites and related compounds* (Springer, Berlin ; New York, 2003).
55. G. Grübel, G. B. Stephenson, C. Gutt, H. Sinn, and T. Tschentscher, " XPCS at the European X-ray free electron laser facility," Nucl. Instrum. Methods B **262**, 357 (2007).
56. C. Gutt, L.-M. Stadler, A. Duri, T. Autenrieth, O. Leupold, Y. Chushkin, et al., "Measuring temporal speckle correlations at ultrafast x-ray sources," Opt. Express **17**, 55 (2009).
57. D. G. Cahill, W. K. Ford, K. E. Goodson, G. D. Mahan, A. Majumdar, H. J. Maris, et al., "Nanoscale thermal transport," Journal of Applied Physics **93**, 793 (2003).
58. D. G. Cahill, P. V. Braun, G. Chen, D. R. Clarke, S. Fan, K. E. Goodson, et al., "Nanoscale thermal transport. II. 2003-2012," Applied Physics Reviews **1**, 011305 (2014).

59. F. Xiong, A. D. Liao, D. Estrada, and E. Pop, "Low-power switching of phase-change materials with carbon nanotube electrodes," Science **332**, 568 (2011).
60. J. L. Carvalho-de-Souza, J. S. Treger, B. Dang, S. B. H. Kent, D. R. Pepperberg, and F. Bezanilla, "Photosensitivity of Neurons Enabled by Cell- Targeted Gold Nanoparticles," Neuron, 1 (2015).
61. M. N. Luckyanova, J. Garg, K. Esfarjani, A. Jandl, M. T. Bulsara, A. J. Schmidt, et al., "Coherent Phonon Heat Conduction in Superlattices," Science **338**, 936 (2012).
62. A. M. Marconnet, M. Asheghi, and K. E. Goodson, "From the Casimir Limit to Phononic Crystals: 20 Years of Phonon Transport Studies Using Silicon-on-Insulator Technology," Journal of Heat Transfer **135**, 061601 (2013).
63. E. Pop, V. Varshney, and A. K. Roy, "Thermal properties of graphene: Fundamentals and applications," MRS Bulletin **37**, 1273 (2012).
64. M. Trigo, M. Fuchs, J. Chen, M. P. Jiang, M. Cammarata, S. Fahy, et al., "Fourier-transform inelastic X-ray scattering from time-and momentum-dependent phonon-phonon correlations," Nature Physics **9**, 790 (2013).
65. G. J. Snyder, and E. S. Toberer, "Complex thermoelectric materials," Nature Materials **7**, 105 (2008).
66. S. Kastbjerg, N. Bindzus, M. Søndergaard, S. Johnsen, N. Lock, M. Christensen, et al., "Direct Evidence of Cation Disorder in Thermoelectric Lead Chalcogenides PbTe and PbS," Advanced Functional Materials **23**, 5477 (2013).
67. C. Xiao, J. Xu, K. Li, J. Feng, J. Yang, and Y. Xie, "Superionic Phase Transition in Silver Chalcogenide Nanocrystals Realizing Optimized Thermoelectric Performance," J. Am. Chem. Soc **134**, 4287 (2012).
68. J. Li, Z. Shan, and E. Ma, "Elastic strain engineering for unprecedented materials properties," MRS Bulletin **39**, 108 (2014).
69. J. S. Brockman, L. Gao, B. Hughes, C. T. Rettner, M. G. Samant, K. P. Roche, et al., "Subnanosecond incubation times forelectric-field-induced metallization of acorrelated electron oxide," 1 (2014).
70. E. Szilagyi, J. S. Wittenberg, T. A. Miller, K. Lutker, F. Quirin, H. Lemke, et al., "Visualization of nanocrystal breathing modes at extreme strains," Nature Communications **6**, 1 (2015).
71. J. N. Clark, L. Beitra, G. Xiong, A. Higginbotham, D. M. Fritz, H. T. Lemke, et al., "Ultrafast Three-Dimensional Imaging of Lattice Dynamics in Individual Gold Nanocrystals," Science **341**, 56 (2013).
72. J. S. Wittenberg, T. A. Miller, E. Szilagyi, K. Lutker, F. Quirin, W. Lu, et al., "Real-Time Visualization of Nanocrystal Solid\textendashSolid Transformation Pathways," Nano Lett **14**, 1995 (2014).
73. T. J. Pennycook, J. R. McBride, S. J. Rosenthal, S. J. Pennycook, and S. T. Pantelides, "Dynamic Fluctuations in Ultrasmall Nanocrystals Induce White Light Emission," Nano Letters **12**, 3038 (2012).
74. X. Yang, A. S. Masadeh, J. R. McBride, E. S. Bozin, S. J. Rosenthal, and S. J. L. Billinge, "Confirmation of disordered structure of ultrasmall CdSe nanoparticles from X-ray atomic pair distribution function analysis," Physical Chemistry Chemical Physics **15**, 8480 (2013).
75. S. Raoux, "Phase Change Materials," Materials Research **39**, 25 (2009).
76. R. Noriega, J. Rivnay, K. Vandewal, F. P. V. Koch, N. Stingelin, P. Smith, et al., "A general relationship between disorder, aggregation and charge transport in conjugated polymers," Nat Mater **12**, 1038 (2013).
77. E. R. Dohner, E. T. Hoke, and H. I. Karunadasa, "Self-Assembly of Broadband White-Light Emitters," J. Am. Chem. Soc **136**, 1718 (2014).
78. S. Brittman, G. W. P. Adhyaksa, and E. C. Garnett, "The expanding world of hybrid perovskites: materials properties and emerging applications," MRS Communications, 1 (2015).
79. C. Wehrenfennig, M. Liu, H. J. Snaith, M. B. Johnston, and L. M. Herz, "Homogeneous Emission Line Broadening in the Organo Lead Halide Perovskite $CH_3NH_3PbI_{3-x}Cl_x$," The Journal of Physical Chemistry Letters **5**, 1300 (2014).
80. X. Wu, M. T. Trinh, D. Niesner, H. Zhu, Z. Norman, J. S. Owen, et al., "Trap States in Lead Iodide Perovskites," Journal of the American Chemical Society **137**, 2089 (2015).
81. G. J. Hayes, and B. M. Clemens, "Laser liftoff of gallium arsenide thin films," MRS Communications (2015).
82. A. M. Lindenberg, S. Engemann, K. Gaffney, K. Sokolowski-Tinten, J. Larsson, P. Hillyard, et al., "X-Ray Diffuse Scattering Measurements of Nucleation Dynamics at Femtosecond Resolution," Physical Review Letters **100**, 135502 (2008).
83. D. Kan, V. Anbusathaiah, and I. Takeuchi, "Chemical Substitution-Induced Ferroelectric Polarization Rotation in $BiFeO_3$," Advanced Materials **23**, 1765 (2011).

84. C. Korff Schmising, M. Bargheer, M. Kiel, N. Zhavoronkov, M. Woerner, T. Elsaesser, et al., "Coupled Ultrafast Lattice and Polarization Dynamics in Ferroelectric Nanolayers," Physical Review Letters **98** (2007).
85. D. Daranciang, M. Highland, H. Wen, S. Young, N. Brandt, H. Hwang, et al., "Ultrafast Photovoltaic Response in Ferroelectric Nanolayers," Physical Review Letters **108**, 087601 (2012).
86. J. Li, B. Nagaraj, H. Liang, W. Cao, C. H. Lee, and R. Ramesh, "Ultrafast polarization switching in thin-film ferroelectrics," Applied Physics Letters **84**, 1174 (2004).
87. H. Wen, P. Chen, M. P. Cosgriff, D. A. Walko, J. H. Lee, C. Adamo, et al., "Electronic Origin of Ultrafast Photoinduced Strain in $BiFeO_3$," Physical review letters **110**, 037601 (2013).
88. P. Chen, R. J. Sichel-Tissot, J. Young Jo, R. T. Smith, S.-H. Baek, W. Saenrang, et al., "Nonlinearity in the high-electric-field piezoelectricity of epitaxial $BiFeO_3$ on $SrTiO_3$," Applied Physics Letters **100**, 062906 (2012).
89. T. Qi, Y.-H. Shin, K.-L. Yeh, K. Nelson, and A. Rappe, "Collective Coherent Control: Synchronization of Polarization in Ferroelectric $PbTiO_3$ by Shaped THz Fields," Physical Review Letters **102**, 247603 (2009).

2.5 Matter in Extreme Environments

Synopsis

The majority of the visible Universe is in an extreme state of matter. The material conditions often involve high pressures, high temperatures, high densities, and combinations thereof. The investigation of these conditions is of fundamental importance to making new discoveries in fusion research and to developing high-energy particle and X-ray beams for applications in radiography and material science. The results of laboratory experiments have broad impact to our fundamental understanding of planets and have the potential to demonstrate the physics mechanism that will explain the origin of cosmic rays.

The capabilities of LCLS-II will allow unprecedented explorations in this area of research, allowing ultrafast probing with high-energy X-ray photons. These capabilities enable experiments that produce short-lived states of extreme matter by high-power laser beam irradiation of solid or liquid targets. Powerful and penetrating X-ray beams will need to provide large numbers of photons at high-peak brightness in single shots. LCLS-II will visualize the dynamic evolution of the structure and determine the physical properties with spectrally resolved X-ray scattering, imaging and diffraction. The new range of X-ray photon energies extending to 25 keV will determine material strength and compression and phase transitions, and will uncover the transformation into new high-pressure material phases.

A comprehensive understanding of the physical properties of extreme matter and the time scales for reaching equilibrium will ultimately provide the foundations for fusion in the laboratory and future applications for energy and energetic radiation sources.

Introduction

Matter in extreme conditions is central to scientific research aimed at demonstrating fusion as a future energy source, to developing radiation sources with unique properties, and to many processes in astrophysics. Fusion research aims to produce plasmas with temperatures and densities at which heavy isotopes of hydrogen fuse to alpha particles and neutrons producing 17.6 MeV energy per fusion reaction. This process powers the sun makes possible all life on Earth. The present worldwide effort generally pursues two complementary efforts where the hot dense plasma is confined by magnetic fields or by inertia and heated to fusion temperatures in the range of 5 to 50 keV (1 eV = 11,605 K). The understanding of the physical properties of fusion plasmas and the material and target conditions involved in producing and confining the plasmas are of critical importance to the successful demonstration of fusion and its future development as an energy source. The recent development of ultrahigh-power short-pulse lasers has allowed approaching relevant conditions for short times and has further initiated new research in high-energy particle and X-ray beams for producing and interrogating matter in extreme conditions. These lasers are now at the threshold of producing some of the most extreme conditions with energy densities previously only observed in astrophysical events.

Key to these research efforts is the application of computer simulations that rely on equation of state data and physics models describing the microscopic formation of thermodynamic equilibrium and hydrodynamic instabilities. The combination of high-power lasers with bright X-ray pulses will allow critical experimental tests of modeling and will challenge our understanding and ability to predict the behavior of extreme matter states. Figure 59 shows a schematic of matter in extreme conditions studies with LCLS-II. High-energy X-ray pulses are required to penetrate through dense plasmas and to provide *in situ* measurements of the conditions. The X-ray beam must provide sufficiently large numbers of photons in femtosecond pulses to allow scattering experiments in a single shot during the short-lived state of matter. Focusing the beam to small areas will allow for unprecedented studies of matter at high energy density and will resolve previously unexplored energy and particle transport properties. Novel

combinations of soft and hard X-ray beams and the combination of multiple X-ray pulses with multiple X-ray energies at femtosecond to nanosecond delays will open up previously unthinkable pump-probe capabilities for resolving the evolution of extreme matter states towards or away from equilibrium.

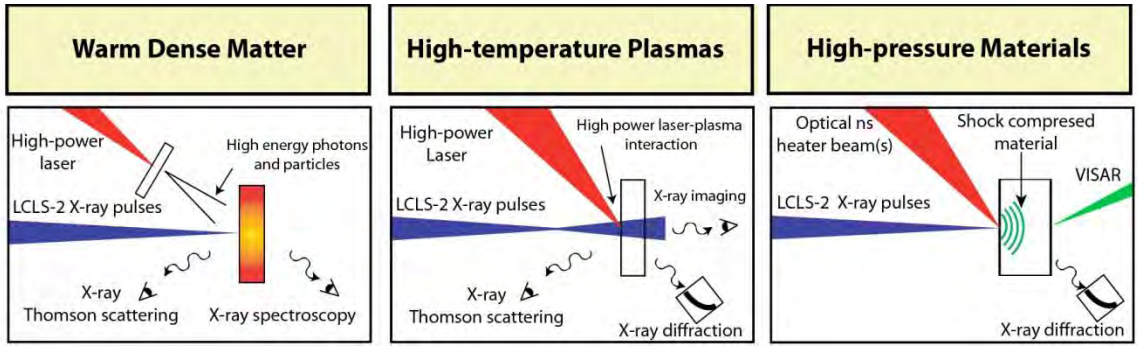

Figure 59: Examples of investigation of matter in extreme conditions with LCLS-II.

2.5.1 Warm and Hot Dense Matter: Laboratory Astrophysics

X-ray scattering investigations

The LCLS-II X-ray capabilities will greatly enhance the opportunity for discovery. Present experiments performed at the LCLS MEC instrument have demonstrated novel *in situ* measurements of the electron temperature, pressure and density by simultaneous high-resolution angularly and spectrally resolved X-ray scattering from shock-compressed aluminum in the warm dense regime [1]. The experiments combine a record peak brightness seeded X-ray beam to spectrally resolve plasmons for density and temperature measurements [2]. With the higher photon energies available at LCLS-II, the structure of mid- and high-Z materials can be visualized as they compress and undergo phase transitions to dense charged-particle systems that are dominated by strong correlations and quantum effects. This complex state, known as warm dense matter, exists in planetary interiors and many laboratory experiments, such as during high-power laser interactions with solids or the compression phase of inertial confinement fusion implosions. The high peak brightness X-rays at the LCLS are required to resolve ionic interactions at atomic (Ångstrom) scale lengths and to determine their physical properties. Measurements on aluminum have characterized the compressed lattice and resolved the transition to warm dense matter, demonstrating that short-range repulsion between ions must be accounted for to obtain accurate structure factor and equation of state data.

The measurements at LCLS have been performed on aluminum where the X-ray energy was matched to the absorption length. These explorations of warm dense matter will greatly benefit from LCLS-II, with higher X-ray energies allowing the study of denser material and higher-Z elements, and with multiple X-ray pulses facilitating investigations of dynamics. In addition, they will also benefit from future developments in lasers and targets.

At high pressures beyond the range shown in Figure 60, LCLS-II will lead the discovery of the transformation into new materials. Examples are the BC-8 in diamond and metallic hydrogen. Especially interesting is the effect of ionization on the equation of state that is predicted at high pressures above 10 Mbar. In addition, LCLS-II will further allow the study of liquid-liquid phase transitions and plasma phase transitions. For this purpose, the unique properties of the X-ray laser provide plasmon spectra [2] that yield the temperature and density with unprecedented precision at micrometer-scale resolution in dynamic compression experiments.

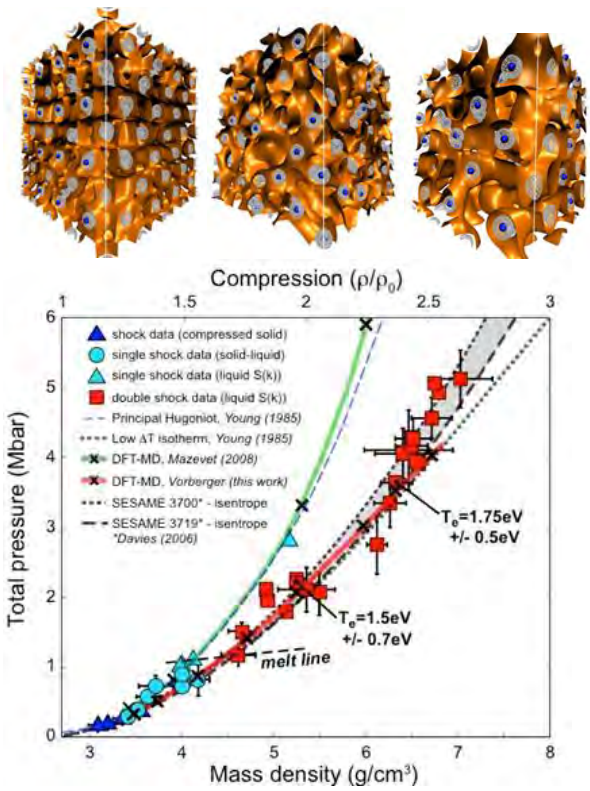

Figure 60: (top) DFT-MD simulations of the structural evolution from solid-state aluminum to WDM transition (left-right); (bottom) X-ray scattering measurements of pressure vs density data for compressed aluminum.[1]

Plasma spectroscopy investigations

The X-ray capabilities of the LCLS have proven to be very well suited both to creating dense plasmas via X-ray isochoric heating and to probing their properties via a range of spectroscopic and scattering techniques. In particular, inner-shell X-ray emission spectroscopy has proven to be an exceptional diagnostic tool, allowing access to the full electronic structure of ions in dense plasmas on inertially confined time scales. The LCLS-II project has the potential to significantly advance our understanding of the fundamental properties of these extreme yet very important systems in several ways. By providing a larger range of X-ray wavelengths it will be possible to investigate a broader range of plasma conditions and different materials and to improve diagnostics. Higher photon energies will equally be beneficial for heating higher Z materials and creating larger samples of extreme states of matter, which in turn are considerably easier to probe.

To date, experiments have reported the isochoric creation of micron-sized silver plasmas in the warm-dense matter regime[3] as well as aluminum plasmas at solid density and temperatures of up to 200 eV,[4] conditions well within the regime of hot-dense matter. The capability to create well-defined plasmas in such extreme conditions has then allowed for the direct measurement of continuum lowering of ions embedding in the plasma[5] and for the detailed investigation of electron impact collisional ionization rates in a dense system.[6] Both these results have shown discrepancies between the experimental measurements and the models commonly used in the plasma community to describe these effects, illustrating the key importance of accurate experimental investigations to guide future developments in the field.

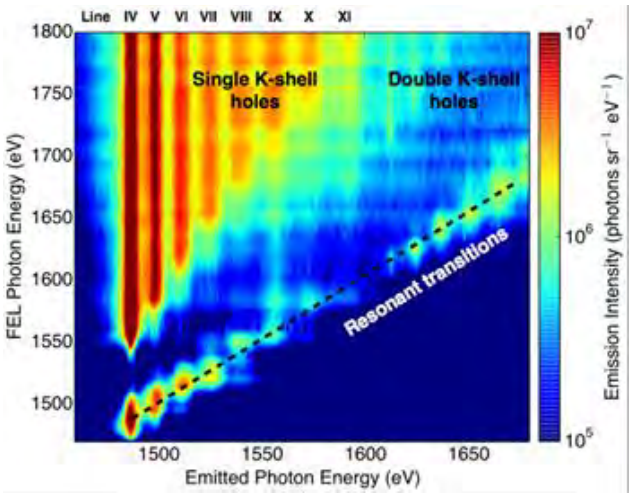

Figure 61: Spectrally resolved K_α of Al.[4]

A key new diagnostic technique enabled by the LCLS beam that has recently been developed is X-ray-driven, Kα emission spectroscopy. As described in refs. 4, 7 by pumping a hot-dense plasma with intense, narrow-bandwidth X-rays, the electronic structure of ions immersed in a strongly coupled plasma can be investigated on ultra-short timescales via spectroscopy of the radiative K-shell recombination process. This emission is driven by the FEL pulse, since the intense X-ray beam is the only significant generator of K-shell core holes, making the technique very different from normal X-ray (self) emission spectroscopy (XES). In fact, the method has several similarities with X-ray absorption spectroscopy (XAS) measurements, since the bandwidth of the X-ray pulse (~0.4 percent) will only be absorbed if a 1s electron can be either excited to some higher-lying bound state or ionized. However, unlike XAS, which for a single photon energy yields only a transmitted intensity, here the absorption process gives rise to inner-shell radiative recombination in the plasma, providing an entire emission spectrum. While the integrated photon yield of this spectrum is, of course, directly related to the absorbed energy fraction via the radiation transport function, the full spectrum carries much more detailed information. This measurement is therefore unique, and by scanning the X-ray photon energies across the various ion energy levels, maps the full electronic structure of all the ions present in the dense plasma, providing an exceptionally rich diagnostic for investigating both plasma structure and dynamics.[5, 6]

This research is currently ongoing and in many aspects still in its nascent stages. But the plasma conditions achievable on the LCLS, ranging from warm-dense systems to the hot-dense plasmas described above, are exceptionally well suited to contribute to a range of fields that depend on a good understanding of fundamental plasma properties and dynamics, such as planetary physics, astrophysics, laser-plasma interactions, and inertial confinement fusion.

High-resolution emission, absorption and scattering measurements

The combination of powerful optical lasers and the bright, high-energy LCLS-II beam provides enormous opportunities to study warm and hot dense matter. High-resolution spectroscopy enables the measurements of the fine detail of electronic configurations in extreme states of matter, providing rigorous tests of theoretical models. High resolution ($\lambda/\Delta\lambda > 2000$) is important for distinguishing fine features in emission, absorption and scattering spectra, which can reveal information about the density, temperature, charge state distribution, and effects of strong coupling in the samples.

A bright continuum back-lighter enables spectroscopic absorption and XAFS measurements for warm, dense samples prepared by irradiation with the LCLS XFEL samples. Absorption spectroscopy is a

powerful diagnostic tool for warm dense matter, which has too little self-emission for direct emission spectroscopy and is opaque to standard optical probes.

An example of a high-impact measurement that would be enabled with high-resolution absorption spectroscopy and bright continuum backlighting is the confirmation of recent monochromatic opacity measurements in ~10x-expanded iron at 200 eV. At slightly lower densities and higher temperatures, many state-of-the-art opacity models can match measured data.[8] But at more extreme conditions, more relevant to the solar photosphere, none of the existing models predict the extreme broadening and persistently intense bound-free opacity observed in the recent experiments.[9]

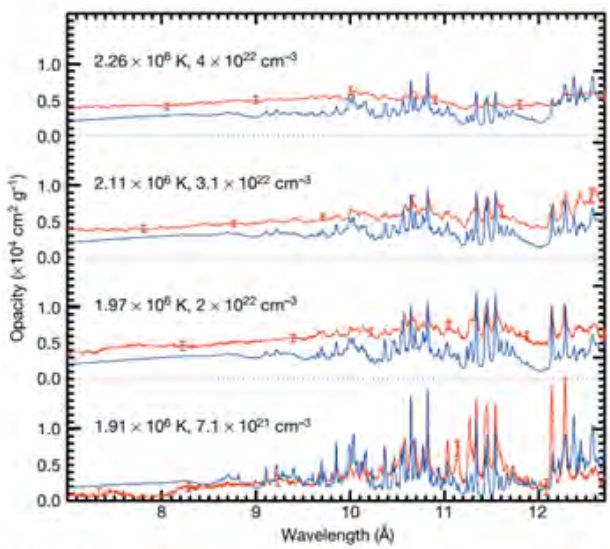

Figure 62: Measured iron opacity spectra at four T_e/n_e values compared with calculations.[9]

L-shell photoexcitation by the LCLS-II X-ray FEL incident on a thin Fe foil would result in a large population of energetic Auger electrons, which would rapidly thermalize, heating the sample to several hundred eV. Using the short-pulse optical laser to generate a bright, short-lived continuum (betatron) backlighter could produce an extremely valuable measurement for the astrophysical, plasma and atomic physics communities. High resolution L- or K-shell spectroscopy coupled with the higher LCLS-II X-ray FEL energies could be used to probe the intriguingly lattice-dependent effects of emission from higher-Z samples. With a bright continuum backlighter, information-rich measurements of XANES and XAFS can also be made.

But the X-ray FEL itself is also a valuable probe. In seeded mode and coupled to high-resolution spectrometers, it can provide measurements of X-ray Thomson scattering with unparalleled precision. While such measurements have been done for years on cold samples at other advanced light sources, providing a critical test bed for condensed matter theory, the optical lasers at LCLS-II can be used to bring samples into the complex warm dense matter regime. This could enable measurements of sharp bound-free features (Figure 63 from ref. 10) and even direct measurements of binding energies (thus also direct measurements of continuum lowering). Higher photon energies will enable investigation of complex valence features of high-Z materials.

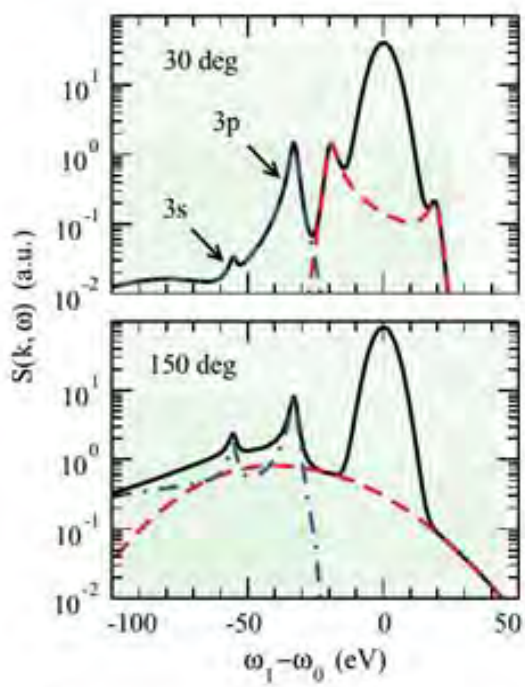

Figure 63: Dynamic structure factor S(k, ω) for scattering of a 2960 eV photon from metallic density Ti at T_e=10 eV.[10]

Finally, LCLS-II may provide new data to help validate transport theory for materials in extreme environments. Transport models depend on both ionic and electronic structure, which can both, in principle, be measured by angle- and energy-dependent scattering of an X-ray FEL probe beam. Like opacities, transport quantities are an essential input for radiation-hydrodynamics simulations, but there are large uncertainties in the calculations and a pressing need for detailed, benchmark data.

Isochoric Compton heating by ultra-intense X-rays

The physical properties of hydrogen, the most abundant chemical element in the observable universe, at the extreme conditions characteristic of astrophysical objects remain largely unexplored. For some of the most violent physical phenomena in the cosmos, including supernovae, gamma ray bursts, and black hole accretion disks, matter endures extremely intense X-ray radiation. Compton scattering is the primary interaction between these high-energy X-rays and hydrogen, which results in the characteristic transfer of energy from the photons to the recoil electrons. At high enough intensities, the energy deposition from the Compton scattering may overcome the radiative cooling leading to a net heating.

The Compton heating of dense hydrogen can be studied with the 25 keV LCLS-II beam at a nm-focus. A liquid hydrogen target may be combined with the 25 keV LCLS-II beam to maximize the Compton scattering cross section. At spot sizes of 10 to 100 nm, the average dose per atom is of order 10 to 100 eV. The temperature can be diagnosed by observing non-collective X-ray scattering and time-resolved optical emission. At ~1 X-ray photon/atom, nonlinear effects may also be seen such as enhanced absorption from multi-photon scattering. Two-color operation enables the study of electron-ion equilibration. The investigation of Compton heating can provide new insights into the equation of state of dense hydrogen over a wide parameter space with implications for theoretical models of the structure of astrophysical objects.

Precise, warm dense matter states for stopping power measurements

Understanding interactions of ion beams with warm dense matter (WDM) at temperatures of 1eV<T<100eV is fundamental to various fields of research, including condensed matter and high energy density physics in astrophysical and fusion plasmas. In particular, ion energy deposition in the WDM

regime is of great importance for fusion science as it affects energy balance in burning plasmas. Various models of ion transport in hot[11] and warm[12] dense plasmas have been developed, but they lack rigorous experimental validation.

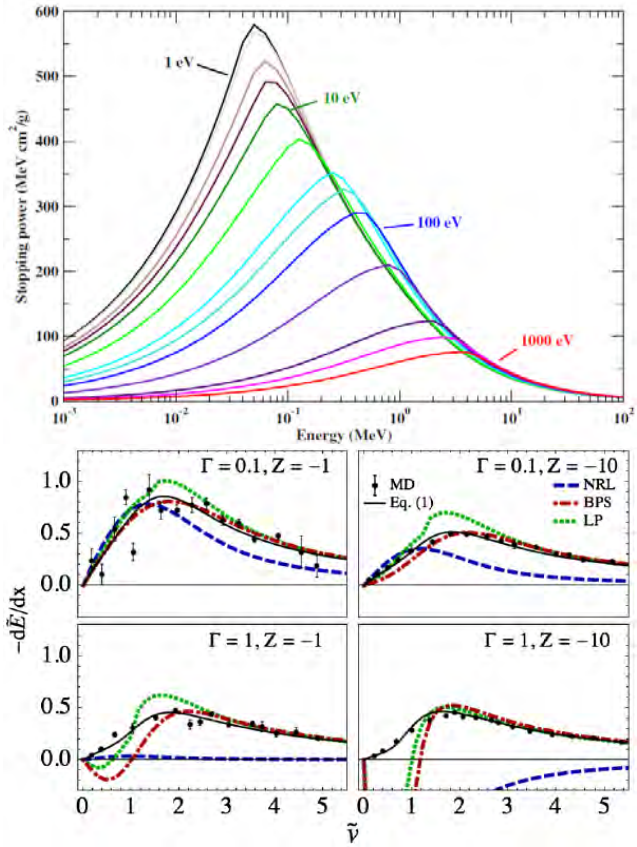

Figure 64: Proton stopping power in WDM is expected to be very sensitive to temperature,[12] but models fail to agree for all temperature and energy regimes;[13] benchmarking is needed.

Attempts to make these important measurements at purely optical laser facilities have proven challenging due to the requirement of producing both a macroscopic, uniform WDM sample and a reliable proton source. The LCLS-II hard X-ray beam will enable the creation of larger uniform WDM samples than those created at any facility to date. Combined with the capability of a high-intensity optical laser, measurements will finally be practical over a large range of proton and ion energies.

Uniform WDM samples are difficult to create with existing methods. LCLS-II at 20 keV photon energy could heat Al in tens of femtoseconds to WDM as thick as 1.1 mm, enough to stop 14 MeV protons. This large stopping range will allow high accuracy stopping power measurements. WDM samples of various temperatures can be created by adjusting the LCLS-II beam energy. The ultrahigh photon energy of LCLS-II will increase the range of materials that can be studied to mid-Z materials approaching Ag.

LCLS-II in high-energy configuration could produce large volume, uniform WDM, which can be precisely characterized using inelastic X-ray Thomson Scattering (XRTS), a robust, proven technique [14] for measuring n_e, T_e, and n_i. A high intensity short pulse laser will create proton and carbon probe beams[15] with controllable, sharp, maximum cutoff energy. The protons are originated from the hydrocarbon contaminant present at the solid laser target rear surface and preferentially accelerated (due to its large charge-to-mass ratio) by the target normal sheath field set up by the escaping relativistic electrons produced from the high intensity laser solid interaction. Protons made this way have been focused to smaller than 100 μm FWHM.[16] The light ions, such as carbon, present in the contaminant will also be accelerated to high energy (MeV/nucleon). Their stopping powers can be measured via continuous spectral measurements using a Thomson Parabola (TP) ion spectrometer. The proposed ultrahigh photon

energy of LCLS-II is particularly appealing, enabling these challenging, critical stopping power measurements.

High intensity laser interactions and relativistic plasmas

Recently laser-plasma interaction experiments at relativistic intensities (exceeding 10^{18} Wcm^{-2} for lasers of wavelength $\lambda = 800$ nm) have attracted significant interest due to potentially important applications as sources of energetic particles and radiation. The current generation of high-power lasers can already achieve peak intensities in excess of 10^{21} Wcm^{-2} using 30-1000 fs pulses with high pulse energy ($\gg$1 J). When such lasers interact with matter, they rapidly ionize the material and accelerate electrons to relativistic energies in a single optical cycle within the focal volume, generating a relativistic plasma environment in the presence of strong electromagnetic fields. Such plasmas are of fundamental interest for their own sake as well as for being a ready source of energetic radiation.

As sources of high-energy charged particle and photon beams, laser based techniques may be useful for a wide range of future applications. These include ion beam acceleration, coherent X-ray generation and the production of attosecond light pulses. In particular, laser wakefield acceleration (LWFA) has been a very successful technique for accelerating electrons to energies in excess of 1 GeV. In terms of energy gain, early claims of accelerating gradients greater than 100 GeV/m have now been experimentally confirmed, with maximum reported beam energies greater than 4 GeV.[17] Such relativistic beams of electrons and the radiation generated by these beams may be used in conjunction with the capabilities of LCLS-II to enable a range of novel experiments.

In laser wakefield acceleration, a high power pulse of optical radiation generates a plasma wave with relativistic phase velocity through its ponderomotive force. The electric field of this plasma wave can be used to accelerate the electrons that remain in phase with it over long distances. Since the plasma fields are not restricted by material breakdown limits, acceleration gradients orders of magnitude higher can be sustained relative to those in RF cavities. Hence, a plasma-based accelerator can be extremely compact. In practice, the generation of electrons by laser wakefield acceleration involves loosely focusing a laser pulse into a gas plume at near atmospheric densities. The (usually) helium gas is rapidly ionized by the leading edge of the laser pulse to form a plasma. Electrons are then spontaneously injected into the electric field structure from the background plasma. An ultra-relativistic electron beam with high current (~10kA), ultrashort duration (<10 fs) and high energy (> few GeV) can be generated in this way. In addition to being a source of relativistic electrons, betatron oscillations of the electrons in the fields of the plasma waves created by laser have been shown to result in bright, broadband sources of femtosecond duration X-rays.[18]

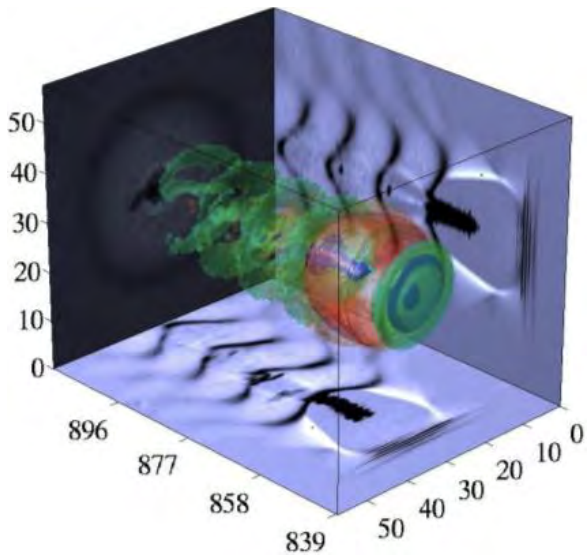

Figure 65: Laser wakefield accelerator: Isocontours of longitudinal current density from an OSIRIS 2.0 simulation in a moving window showing stable wakefield formation, electron trapping and acceleration.[19]

In extremely intense focused light, a new plasma regime will also manifest itself – one that has similarities to extreme environments, such as those found in pulsar magnetospheres.[20] This happens because electrons are accelerated to very relativistic energies directly by the laser fields. In the rest frame of the electrons, the field strength may be Lorentz boosted to reach the critical field strength of quantum electrodynamics (QED).[21] This implies that effects such as radiation friction and pair production greatly modify plasma dynamics leading to fundamentally new behavior. The many-body QED theory that describes this physics is presently not well understood.

In conjunction with LCLS-II, direct laser-matter interactions or laser driven sources of electrons, photons, and ion beams, open up a wealth of possible QED-plasma, high-energy density, warm dense matter and atomic physics experiments. The femtosecond duration of the laser-driven electron beams in combination with the few-femtosecond, bright LCLS-II X-ray pulses will allow ultrafast X-ray pump-electron-beam probe or electron-beam pump-X-ray probe experiments. Such experiments can exploit the relativistic boost to the X-ray fields in the e-beam frame to explore strong field QED or enable e-beam probing of the magnetic fields under conditions similar to those of the atmosphere of a neutron star.

Observing the Formation of Local Thermodynamic Equilibrium

The dynamics of electronic relaxation is a matter of primary concern in the study of warm dense matter. In experiments with nanosecond or slower heating, the electron distribution is assumed to be in local thermodynamic equilibrium, but with the use of ultrafast photon sources to generate hot matter, this assumption become invalid, as the formation of an electronic equilibrium can be on the same time scale as the photon source. Moreover, fusion research is limited by the poor understanding of the various mechanisms carrying away energy; an understanding of the separate pathways will aid in the pursuit of sustainable fusion power. Despite the fundamental importance of electron energy equilibration, there has been no direct observation of the formation of an electronic local thermodynamic equilibrium from a well-defined initial energetic state. LCLS-II can provide unique capabilities allowing this for the first time.

LCLS-II could be used to create and probe such a process; non-equilibrium excited dense matter can be formed with an intense X-ray pulse, and the evolution of the electron energy distribution can be tracked by the Thomson scattering of a second X-ray pulse. An X-ray pump can create a well-defined initial non-equilibrium state. X-rays heat solid-density targets by one-photon photoionization allowing for volumetric energy absorption.[4, 22] Upon creation of non-equilibrium WDM, the electrons will eventually reach local equilibrium, with simulations suggesting timescales of 10-1000 fs.[23, 24] Figure 66 shows

calculated electron energy distributions of liquid hydrogen following irradiation by an EUV pulse.[22] During this process, the electron energy distribution can be tracked by an X-ray probe using Thomson scattering. The technique has the advantages that the X-rays will be well above the plasma frequency and can probe the entire volume of the excited matter, and the spectral response can be a sensitive probe for relatively small fractions of energetic electrons.[25] The two-color X-ray pump-probe technique could finally yield quantitative results on the formation of a local thermodynamic equilibrium in warm dense matter.

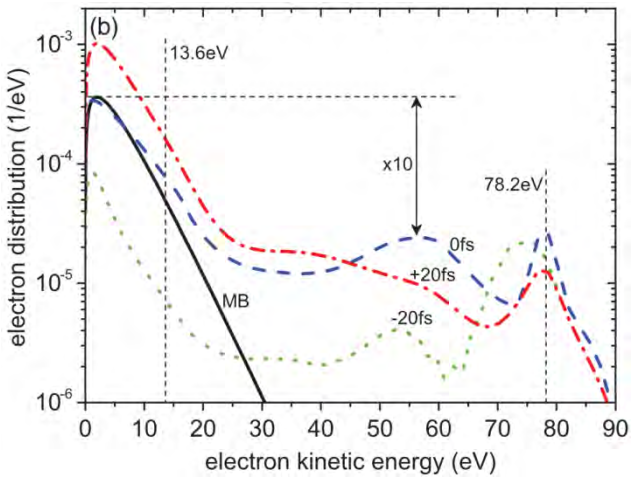

Figure 66: Predicted equilibration of electron energy in liquid hydrogen irradiated with 91.8 eV photons. Hydrogen atom photoionization (78.2 eV) and ionization potential (13.6 eV) energies are shown for comparison. Throughout the duration of a ~40 fs pulse, the electron energy distribution has a fraction populated near the photoionization energy, which relaxes to a broad energetic tail. Adapted from Ref. 22.

2.5.2 Dynamic compression, shock and impact physics

Shock and Quasi-Isentropic Compression of Matter

The femtosecond X-ray capabilities of the LCLS, combined with high-power optical-laser technology, have proven to be very well suited to the study of solid-state matter under high pressure. Whilst the creation of high-pressure states of matter via the application of pressure produced by laser-ablation is by no means new, LCLS and LCLS-II have the capacity to transform the field owing to several key characteristics. Firstly, the few femtosecond x-ray pulse is shorter than the period of the most energetic phonon in the system, resulting in a diffraction pattern that has no motional blurring. Secondly, the brightness of the beam is such that x-ray spots of just a few tens of microns (for small grained samples) can be used to generate diffraction patterns. This in turn means that relatively small optical laser spots can be used for shock compression (of order down to 100-microns or less), which in turn leads to relatively high irradiances (and thus pressures) for very modest optical laser energies. Finally, with tailored optical laser pulse-shaping and 'smart' target design, ramp compression experiments should also be capable of being performed keeping the material close to an isentropic, and hence potentially solid even at very high pressures (the high entropy caused by a shock results in melting of metals at pressures typically between 150 and 300-GPa).[26] Such isentropic compression experiments have been proven on pure optical-laser platforms.[27]

Some key themes are beginning to emerge from research at LCLS – those being the study of materials under shock compression, mechanisms of deformation, melt, recrystallization, and polymorphic phase transformations. Further, as noted above, isentropic compression allows the investigation of high-pressure off-Hugoniot (cooler) states, which in turn are of direct relevance to the conditions found within and towards the center of the giant planets that exist within our own solar system and beyond.

In principle, the major benefit of LCLS-II will be the more than two-fold increase in photon energy. The current maximum energy of LCLS severely limits true structure determination, owing to the small volume

of reciprocal space that can be interrogated. To date, most of the materials studied at MEC have been relatively simple – and in many cases single elements. In this situation, the few reciprocal lattice vectors present within the Ewald sphere are, at least in many cases, sufficient for adequate structure determination – or at least confirming consistency with a presumed structural model. For example, under ambient conditions many metals have a lattice spacing of order 3.6- 4.0 Angstroms, which, with a FEL photon energy of 1.5 Angstroms, allows in *fcc* materials Miller indices to be recorded up to the reciprocal lattice vector of (331). Note however, that under shock compression, the lattice parameter can decrease by of order $2^{1/3}$, restricting the number of reciprocal lattice vectors in the Ewald sphere even further. This is totally insufficient for more complicated structures and minerals, where the sometimes subtle relative position of multiple elements within the unit cell needs to be determined. This can even be the case for quite simple elements, if the phases are closely related (e.g. the β-Sn and Imma phase in Si). In this sense the increased capability that LCLS-II would afford (by stint of the higher X-ray photon energy of 25 keV) should be thought of as an increase in the volume of reciprocal space that can be probed by close to an order of magnitude.

This increase in reciprocal space landscape will also give rise to the opportunity to better determine the equation of state of the crystals studied. In particular, the temperature of matter under compression is notoriously difficult to measure. However, diffraction affords the means to measure this quantity via the Debye-Waller effect – i.e. the reduction in the integrated intensity of the diffraction with increasing reciprocal lattice vector. For example, even at a temperature of 4 times the Debye temperature (T_D) of 371K, the (400) reflection of Ge is only reduced to of order 80% of the room temperature intensity, whereas (444) would be reduced to 50%, providing far higher accuracy in a T/T_D measurement.[28]

The higher photon energy of LCLS-II will also improve signal to noise: as the optical laser intensity is increased, this will lead to an increase in the energy of the x-rays emitted from the laser-produced plasma that provides the ablation pressure - this will be the case particularly for high-intensity quasi-isentropic compression. It is certainly the case that using higher photon energies to diffract from the sample allows considerably greater shielding on the detectors from the laser-produced-plasma radiation.

The two-color capability of LCLS-II could also give rise to a whole new class of experiments - for example fluorescence spectroscopy on certain shocked or ramp-compressed samples – where the hard x-ray beam would be used to determine lattice parameter, whilst the beam up to 5 keV could be used to generate L or K (for low Z) holes, and the resultant characteristic L or K shell emission lines, which in turn could provide information on the position and shape of the bands within the compressed sample. There are further advantages to being able to use the two colors of LCLS-II simultaneously - e.g. the beam at up to 5 keV, alongside that at 25 keV. This could aid in particular in the study of compression to off-Hugoniot states, by using the 5 keV beam, a few tens of picoseconds before optical shock compression, to heat a target to a well-defined temperature before compression and diagnose via diffraction by the 25 keV beam.

Structure factor measurements in high-pressure liquids

Transitions between solid and liquid phases are ubiquitous under conditions of high pressure and high temperature. Under strong enough shock loading, most materials will melt. Studies of the transitions between liquid and solid states are fundamental to many geophysical processes, including high velocity meteor impacts and the Earth's molten iron core. Studies of these transitions are also relevant for material processing, such as additive manufacturing that employs sintering or rapid solidification of metals.

In addition to solid-liquid transitions, liquid-liquid transitions are of significant interest. Under static high pressure and high temperature conditions, a liquid-liquid transition has been shown in Ce.[29] Under dynamic loading conditions, a liquid-liquid transition has also been observed in $MgSiO_3$,[30] which has important implications for terrestrial planetary mantles.

Solid-liquid and liquid-liquid transitions can best be studied under conditions in which the materials structure factor can be measured. The structure factor can be determined from measuring the X-ray diffraction over a large Q range. Some of the difficulties of making these measurements on dynamically compressed samples using currently available capabilities include the limited X-ray flux from synchrotrons, the geometric restrictions arising from the configuration of laser-produced X-ray backlighter sources at high energy laser facilities, and the limited photon energy that is currently available at LCLS. LCLS-II will provide an essential increase in X-ray photon energy, up to 25 keV, which is critical for enabling structure factor measurements in dynamically compressed liquids.

In studying transitions between liquid and solid phases, it would be highly advantageous to concurrently measure small angle X-ray scattering (SAXS). The SAXS measurements would provide data relating to the diffracting domain size during these transitions, a quantity that would be especially interesting during additive manufacturing processes and during re-solidification from liquid states. The current limitation of the LCLS maximum photon energy and the maximum distance to the detector limits the Q-range for SAXS. The increase in photon energy for LCLS-II is beneficial for SAXS.

Geophysics and planetary sciences

There are numerous scientific problems in geophysics and planetary sciences to which we could apply the unique capabilities of MEC, including the Earth's mantle and core evolution (i.e., silicate-oxide-iron interactions at extreme conditions) and exoplanet and icy satellite constitution. A case study is highlighted here, which is relevant to geophysics and planetary sciences involving water. Water, H_2O, critical for life and ubiquitous in biology, is one of the most abundant molecules in the solar system. High P-T phases of water, including the superionic state, is thought to be a major constituent phase of icy gas giants (i.e., Neptune, Uranus) and extrasolar planets (icy "super-Earths").[31] Convection of superionic water is thought to be the source of the magnetosphere – a necessary and critical component for life. But the material structure of this superionic state remains elusive. Understanding the state and structure of water at the conditions of planetary interiors will allow us to better understand the constitution and evolution of icy planets and the formation of our solar system and other planetary systems. Direct evidence of the existence of this phase has not yet been established. Technologies currently available at LCLS are poised to be competitive with other shock wave facilities. But to accomplish the feat of observing the structure of the superionic phase, introducing the capabilities possible with the construction of LCLS-II would be an important and necessary step forward.

The Matter in Extreme Conditions (MEC) Instrument at LCLS allows experiments to reach high pressure (P) and temperature (T) with laser-driven shock waves and the capability of taking snapshots during a dynamic process with the ultrafast X-rays of the LCLS X-ray FEL. This capability allows researchers to capture the dynamics of phase transformations step by step. By varying the drive laser pulse energy and temporal profile, the P and T conditions of the material are tunable and permit simultaneous ultrafast X-ray probing techniques (e.g., diffraction, phase contrast imaging, spectroscopy) that move well beyond the temporal and spatial resolution of traditional/current static compression (diamond-anvil cells) and dynamic compression technologies. To date, X-ray diffraction data of superionic water collected during shock compression does not exists. The precision of the diffraction can be enhanced by making unique use of an extended energy range (i.e., out to 25 keV). With this energy range we could better determine the precise structure by observing more peaks from the high-pressure phase.

Furthermore, investigating other high-pressure phases besides crystalline ice, such as high density amorphous phases, is only possible with smaller wavelength (higher energy) X-rays. Critical to resolving the structure factor of amorphous phase is the extension of the Q-range to include observation of both the first and second sharp diffraction peaks from a disordered material. This is impossible with existing LCLS capabilities. Understanding the coordinating and long-range order of high density amorphous phases would only be possible with LCLS-II.

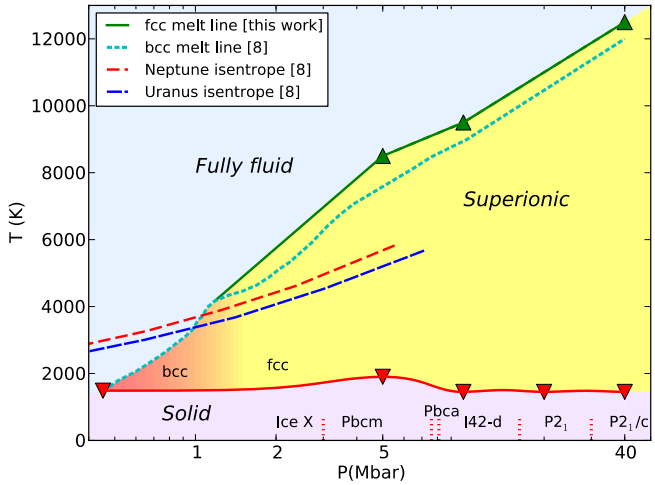

Figure 67: Phase diagram of water showing the superionic regime.[32]

Resolving the equation of state controversy of deuterium at high pressures

Hydrogen, the simplest element in the universe, has a surprisingly complex phase diagram. Owing to fundamental questions about the structure and core stability of gas giants in our solar system,[33-35] hydrogen's high-pressure properties have been the subject of intense study over the past two decades. The recently launched of NASA Juno mission is expected to provide detailed new data on hydrogen gas giants when it arrives in July 2016. Of critical importance is the equation of state of deuterium — one of the most contested and important science questions in the high-pressure community. A precise determination will affect our understanding of the formation and evolution of the solar system and will further affect our ability to achieve inertial confinement fusion in the laboratory.

Numerous experiments using laser drivers and z-pinches have provided equation-of-state data that show significant uncertainties for pressures above 50 GPa (e.g., refs. 1, 36). What these studies have in common is the use of velocity interferometry (i.e. VISAR) to measure shock and particle velocities to infer pressure and compression. Using the unique high X-ray brightness properties of LCLS-II, we have the unique capability to complement VISAR measurements with high-precision X-ray scattering measurements that provide densities from first principles [1]. Here, the high photons per pulse make it possible to obtain data in a single shot during the short lived state of highly compressed hydrogen. In addition, seeded X-ray beams provide a narrow bandwidth for resolving the plasmon scattering spectrum.

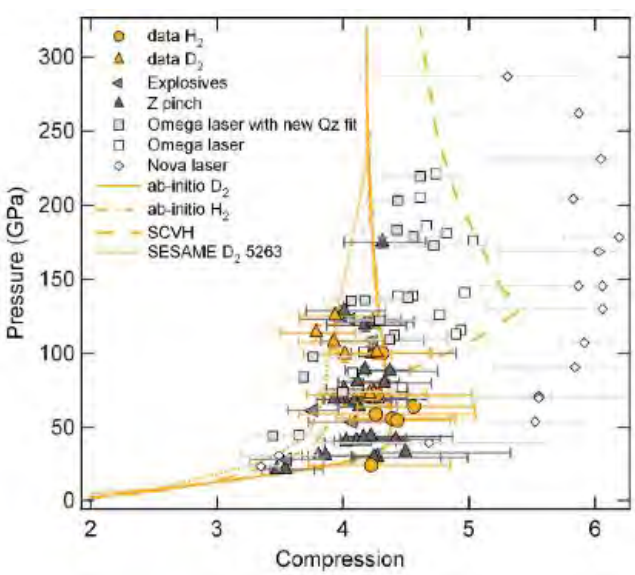

Figure 68: Phase diagram of hydrogen and deuterium showing the equation of state versus compression along the shock Hugoniot.[37]

Experimental approaches and the impact of LCLS-II

Several topics in this section, including the equation of state of deuterium and the formation of superionic water, address phenomena that require pressures above 100 GPa. Therefore, the ability to generate high pressure shock conditions will be essential. The current LCLS MEC ns optical laser requires the use of a very small drive area (50 to 100 μm) to generate such high pressures. The use of a small drive area also results in non-uniaxial stress conditions in the sample due to edge release waves, thereby limiting the time duration over which measurements can be made for well-defined sample conditions. Upgrading the long-pulse laser system energy to provide at least 100 J in 10 ns would permit the study of specimens in well-known thermodynamic conditions and would compress a significant volume that can be probed by both by X-rays and VISAR.

An upgrade of the LCLS's existing high intensity, short pulse laser capability is required for several types of investigations. An increased power would provide an intense (betatron) continuum X-ray source for high-resolution spectroscopy. For protons, the short pulse laser at the LCLS MEC instrument has already demonstrated generation of MeV proton beams with laser energy of only 1 J (25 TW). However, a high-energy PW-class laser would allow greater flexibility to the proton probe, e.g. allowing selection of discrete ($\Delta E \sim eV$) ion probing energies. Higher laser powers would benefit all laser-matter interaction studies.

The possibility of using two X-ray beams from separate FELs is an exciting element of LCLS-II. This capability would allow, for the first time, the use of isochoric X-ray heating together with key X-ray diagnostics (spectroscopy, scattering, diffraction) in an independent way. Experiments which aim to use one X-ray pulse to both generate and diagnose a system have to deal with the fact that the two are invariably coupled and act on the same ultra-short time scales. Decoupling the two would provide a range of new opportunities and, in particular, would allow for much more tailored and accurate diagnostics. For example, in the plasma spectroscopy work shown above the probing of the atomic states dictates the FEL photon energy. This wavelength must then also be used to heat the plasma, which will often not be a good choice, especially for higher Z materials. Furthermore, two FEL pulses would allow time-resolved studies to be performed in which the full range of mature X-ray diagnostics could finally be used on well-defined plasma samples created via X-ray isochoric heating. This would be a boon for investigations concerning plasma dynamics and transport properties, but would find applications elsewhere as well.

References

1. L. B. Fletcher, H. J. Lee, DöppnerT, GaltierE, NaglerB, HeimannP, et al., "Ultrabright X-ray laser scattering for dynamic warm dense matter physics," Nat Photon **9**, 274 (2015).
2. L. B. Fletcher, E. Galtier, P. Heimann, H. J. Lee, B. Nagler, J. Welch, et al., "Plasmon measurements with a seeded x-ray laser," Journal of Instrumentation **8**, C11014 (2013).
3. A. Lévy, P. Audebert, R. Shepherd, and e. al., Physics of Plasmas, in press (2015).
4. S. M. Vinko, O. Ciricosta, B. I. Cho, K. Engelhorn, H. K. Chung, C. R. D. Brown, et al., "Creation and diagnosis of a solid-density plasma with an X-ray free-electron laser," Nature **482**, 59 (2012).
5. O. Ciricosta, S. M. Vinko, H. K. Chung, B. I. Cho, C. R. D. Brown, T. Burian, et al., "Direct Measurements of the Ionization Potential Depression in a Dense Plasma," Phys Rev Lett **109** (2012).
6. S. M. Vinko, O. Ciricosta, T. R. Preston, and e. al., Nature Communications **6**, 6397 (2015).
7. B. I. Cho, K. Engelhorn, S. M. Vinko, H. K. Chung, O. Ciricosta, D. S. Rackstraw, et al., "Resonant K alpha Spectroscopy of Solid-Density Aluminum Plasmas," Phys Rev Lett **109** (2012).
8. J. E. Bailey, G. A. Rochau, C. A. Iglesias, J. Abdallah, J. J. MacFarlane, I. Golovkin, et al., "Iron-plasma transmission measurements at temperatures above 150 eV," Phys Rev Lett **99** (2007).
9. J. E. Bailey, T. Nagayama, G. P. Loisel, G. A. Rochau, C. Blancard, J. Colgan, et al., "A higher-than-predicted measurement of iron opacity at solar interior temperatures," Nature **517**, 56 (2015).

10. W. R. Johnson, J. Nilsen, and K. T. Cheng, "Thomson scattering in the average-atom approximation," Phys Rev E **86** (2012).
11. C. K. Li, and R. D. Petrasso, "Charged-Particle Stopping Powers in Inertial Confinement Fusion Plasmas," Phys Rev Lett **70**, 3059 (1993).
12. G. Faussurier, C. Blancard, P. Cosse, and P. Renaudin, "Equation of state, transport coefficients, and stopping power of dense plasmas from the average-atom model self-consistent approach for astrophysical and laboratory plasmas," Physics of Plasmas **17** (2010).
13. P. E. Grabowski, M. P. Surh, D. F. Richards, F. R. Graziani, and M. S. Murillo, "Molecular Dynamics Simulations of Classical Stopping Power," Phys Rev Lett **111** (2013).
14. S. H. Glenzer, O. L. Landen, P. Neumayer, R. W. Lee, K. Widmann, S. W. Pollaine, et al., "Observations of plasmons in warm dense matter," Phys Rev Lett **98** (2007).
15. J. Fuchs, P. Antici, E. D'Humieres, E. Lefebvre, M. Borghesi, E. Brambrink, et al., "Laser-driven proton scaling laws and new paths towards energy increase," Nat Phys **2**, 48 (2006).
16. T. Bartal, M. E. Foord, C. Bellei, M. H. Key, K. A. Flippo, S. A. Gaillard, et al., "Focusing of short-pulse high-intensity laser-accelerated proton beams," Nat Phys **8**, 139 (2012).
17. W. P. Leemans, B. Nagler, A. J. Gonsalves, C. Toth, K. Nakamura, C. G. R. Geddes, et al., "GeV electron beams from a centimetre-scale accelerator," Nat Phys **2**, 696 (2006).
18. A. Rousse, K. T. Phuoc, R. Shah, A. Pukhov, E. Lefebvre, V. Malka, et al., "Production of a keV x-ray beam from synchrotron radiation in relativistic laser-plasma interaction," Phys Rev Lett **93** (2004).
19. C. M. Huntington, A. G. R. Thomas, C. McGuffey, T. Matsuoka, V. Chvykov, G. Kalintchenko, et al., "Current Filamentation Instability in Laser Wakefield Accelerators," Phys Rev Lett **106** (2011).
20. Goldreic.P, and W. H. Julian, "Pulsar Electrodynamics," Astrophys J **157**, 869 (1969).
21. C. P. Ridgers, C. S. Brady, R. Duclous, J. G. Kirk, K. Bennett, T. D. Arber, et al., "Dense Electron-Positron Plasmas and Ultraintense gamma rays from Laser-Irradiated Solids," Phys Rev Lett **108** (2012).
22. R. R. Fäustlin, T. Bornath, T. Döppner, S. Düsterer, E. Förster, C. Fortmann, et al., "Observation of Ultrafast Nonequilibrium Collective Dynamics in Warm Dense Hydrogen," Phys Rev Lett **104**, 125002 (2010).
23. N. Medvedev, U. Zastrau, E. Förster, D. O. Gericke, and B. Rethfeld, "Short-Time Electron Dynamics in Aluminum Excited by Femtosecond Extreme Ultraviolet Radiation," Phys Rev Lett **107**, 165003 (2011).
24. S. P. Hau-Riege, "Nonequilibrium electron dynamics in materials driven by high-intensity x-ray pulses," Phys Rev E **87**, 053102 (2013).
25. D. A. Chapman, and D. O. Gericke, "Analysis of Thomson Scattering from Nonequilibrium Plasmas," Phys Rev Lett **107**, 165004 (2011).
26. A. Higginbotham, J. Hawreliak, E. M. Bringa, G. Kimminau, N. Park, E. Reed, et al., "Molecular dynamics simulations of ramp-compressed copper," Physical Review B **85**, 024112 (2012).
27. J. R. Rygg, J. H. Eggert, A. E. Lazicki, F. Coppari, J. A. Hawreliak, D. G. Hicks, et al., "Powder diffraction from solids in the terapascal regime," Review of Scientific Instruments **83**, 113904 (2012).
28. W. J. Murphy, A. Higginbotham, J. S. Wark, and N. Park, "Molecular dynamics simulations of the Debye-Waller effect in shocked copper," Physical Review B **78**, 014109 (2008).
29. A. Cadien, Q. Y. Hu, Y. Meng, Y. Q. Cheng, M. W. Chen, J. F. Shu, et al., "First-Order Liquid-Liquid Phase Transition in Cerium," Phys Rev Lett **110**, 125503 (2013).
30. D. K. Spaulding, R. S. McWilliams, R. Jeanloz, J. H. Eggert, P. M. Celliers, D. G. Hicks, et al., "Evidence for a Phase Transition in Silicate Melt at Extreme Pressure and Temperature Conditions," Phys Rev Lett **108**, 065701 (2012).
31. C. Cavazzoni, G. L. Chiarotti, S. Scandolo, E. Tosatti, M. Bernasconi, and M. Parrinello, "Superionic and metallic states of water and ammonia at giant planet conditions," Science **283**, 44 (1999).
32. H. F. Wilson, M. L. Wong, and B. Militzer, "Superionic to Superionic Phase Change in Water: Consequences for the Interiors of Uranus and Neptune," Phys Rev Lett **110** (2013).
33. T. Guillot, "Interiors of giant planets inside end outside the solar system," Science **286**, 72 (1999).
34. N. Nettelmann, B. Holst, A. Kietzmann, M. French, R. Redmer, and D. Blaschke, "Ab initio equation of state data for hydrogen, helium, and water and the internal structure of Jupiter," Astrophys J **683**, 1217 (2008).
35. G. W. Collins, L. B. Da Silva, P. Celliers, D. M. Gold, M. E. Foord, R. J. Wallace, et al., "Measurements of the equation of state of deuterium at the fluid insulator-metal transition," Science **281**, 1178 (1998).

36. M. D. Knudson, D. L. Hanson, J. E. Bailey, C. A. Hall, J. R. Asay, and W. W. Anderson, "Equation of state measurements in liquid deuterium to 70 GPa," Phys Rev Lett **87** (2001).
37. P. Loubeyre, S. Brygoo, J. Eggert, P. M. Celliers, D. K. Spaulding, J. R. Rygg, et al., "Extended data set for the equation of state of warm dense hydrogen isotopes," Physical Review B **86**, 144115 (2012).

2.6 Revealing Biological Function on Natural Length and Time Scales

Synopsis

Solving the most challenging problems at the frontiers of biology requires understanding biological function and dynamics through direct observations of complex heterogeneous systems – in operation, in their native environments, and over a wide range of time and spatial scales. Integrative approaches and sharper tools are essential, as no single structural method can provide a complete solution to this challenge. While current state-of-the art techniques for structural biology are quite powerful, they are nevertheless limited in several key respects, and this prevents our complete understanding of biological systems.

X-rays and electron beams provide the basis for the most incisive information about structural biology, but both have significant limitations due to radiation damage. The advent of ultrafast X-ray lasers has qualitatively changed this paradigm, and paved the way for damage-free determination of structure at high resolution via the "diffraction-before-destruction" concept applied to femtosecond macromolecular crystallography and scattering.[1]

Macromolecular crystallography has provided a torrent of information on protein structures over the past few decades.[2] However, many of the most important macromolecular complexes refuse to be crystallized, due primarily to their intrinsic structural dynamics and heterogeneity. Moreover, these intrinsic dynamics are central to the biological function of these important complexes, and we sorely lack adequate tools to directly probe and characterize these processes. Electron microscopy (and associated detectors) have advanced remarkably in the last several years, and can now image single macromolecules at better than 3 Angstrom resolution. However, it does not readily allow for time-resolved dynamics studies, and has limited ability to fully characterize heterogeneity as samples must be frozen. Synchrotron X-ray techniques in principle allow for time resolution down to ~100 ps, but applicability is limited due to the low available flux/pulse and the inter-related issues of repetition rate and sample damage (recovery, or replacement).

X-ray FELs offer a unique set of capabilities for circumventing these limitations as demonstrated by the results from LCLS over the first several years of operation. LCLS-II will build on this initial success, and open new areas of bioscience that will capitalize on the high repetition rate and expanded tuning range. For example, conformational dynamics of macromolecules and nano-machines, and extremely fast electronic excited-state dynamics in enzymes and charge-transfer complexes and single particle imaging of non-repetitive biological objects are just a few of many new classes of bioscience that will be enabled by the capabilities of LCLS-II. These capabilities will support new methods in crystallography, single particle imaging, fluctuation (correlation) X-ray scattering and spectroscopy, and novel instrumentation that will be essential in addressing these bioscience challenges.

Introduction

The unprecedented peak brightness from X-ray lasers has enabled the determination of high resolution structures and electronic states of biological systems before the onset of X-ray radiation damage. The so-called "diffraction–before-destruction" approach[1] has provided atomic-resolution structures of biologically and biomedically important classes of molecules such as GPCR membrane proteins,[3, 4] synaptic fusion complexes, and photosystem complexes[5, 6] – in some cases with higher resolution or with structural details more representative of the room temperature native state. Many protein complexes contain transition-metals at the active sites or as integral components of the structure. It is often these metals which are crucial to the unique functionalities of enzymes. These metal centers are much more susceptible to damage than the rest of protein molecules (e.g. oxidation effects). Here, X-ray FELs, and particularly LCLS-II offer unique capabilities – not only ultrafast pulses for crystallographic analyses of radiation damage-free structures, but also X-ray spectroscopic analyses of the dynamic electronic states of

the metal centers. The combination of crystallography and spectroscopy will be one of the keys to correlating structural dynamics and electronic states.

LCLS-II represents a great advance in technology and overall capabilities and will be a very powerful light source. The life science community will make great use of this new machine. However, it must be stated that in its initial implementation, LCLS-II does not represent a paradigm change for structural biology. High-resolution is critical for most studies and the limitations in achievable photon energy will limit the use of the full capabilities of LCLS-II for crystallography for example. A subset of the improved capabilities of LCLS-II will enable key new science, such as the increased photon energy available on the Cu-linac but full use of the higher repetition rate will be limited by the photon energy and the readout rate of detectors. One clear exception where the LCLS-II capabilities will be fully exploited is spectroscopic techniques where multiple pulses can be accumulated before a detector readout and access to low photon energies where the absorption edges of biologically relevant atoms can be probed will be extremely valuable.

The X-ray energy range of LCLS-II will also enable discrimination of metal ions from each other, from ligand moieties, or from oxygen atoms in water. For example, an important question in biological function is which kinds of atoms are present at the constricted passage of membrane channels or transporters that regulate transport across the cellular membrane. In these cases it is critically important to be able discriminate sodium cations from other possible metals. Having access to the absorption edges of these metals (sodium 1,072 eV, potassium 3,610 eV, chlorine 2,825 eV) can resolve this unequivocally. Full development of tools capable of utilizing the tender X-ray range (2-5 keV) will be central to the LCLS-II life science program.

Crystallography is the workhorse technique in structural biology with numerous synchrotron beamlines around the world dedicated to macromolecular structural studies. This has also been true at LCLS with femtosecond crystallography techniques being intensely developed in the first 6 years of operation and now producing important results.[7, 8] LCLS-II will complement and improve the capabilities of the LCLS complex in macromolecular crystallography. The higher photon energies, above 11.2 keV, generated by LCLS-II will provide increased resolution and access to the selenium edge for phasing. The increased repetition rate will be critical for dynamics studies by allowing fast data collection greatly increasing the number of time points collected or conformations that can be probed during an experiment, although in this case the photon energy at high repetition rates (<5 keV) will be a limiting factor.

While crystallography is an extremely powerful tool for elucidating atomic structures, many complex biological machines defy crystallization due to their intrinsic flexibility. Fluctuation scattering and single particle imaging can provide alternative paths towards understanding dynamics at low to medium resolution of non-crystalline samples. Single particle imaging (SPI) using LCLS continues to evolve towards higher resolution along the paths defined in LCLS SPI roadmap.[9] LCLS-II, along with X-ray optics and instrumentation development, will help fill the critical energy gap between 2 kV and 5 keV. The option of delivering the beam from the Cu linac to the soft X-ray undulator could also provide a higher energy per pulse (>5 mJ at 120 Hz) than is presently available from LCLS in this energy range (see Section 5).

Fluctuation scattering is an ensemble scattering approach that is enabled by the combination of ultrafast X-ray pulses and high repetition rate. It potentially provides ~100 times greater information content than conventional SAXS – sufficient for 3D reconstruction. It has emerged as a method bridging SPI and crystallography, and is potentially powerful for understanding dynamics and protein interactions in native environments.

Time resolved X-ray spectroscopy is an extremely powerful tool deciphering dynamics of electron transfer among critically important metalloenzyme membrane complexes such those found in photosynthesis, respiration, and nitrogen-cycles. The high repetition rate and extended X-ray energy range of LCLS-II will enable the application of these methods to important problems in biology. It will also open up new possibilities for hybrid approaches for characterizing biological function across multiple length and time scales. In combination, these X-ray based structural biology methods can help solve a number of fundamental questions in biology from femtoseconds to minutes and from atomic to cellular levels. It is also important to note that bio-computing (including advanced computation and data analysis methods) can provide theoretical foundations of the reaction mechanisms and can connect multi-scale phenomena.

2.6.1 Understanding the dynamics of biological complexes & molecular machines

Dynamics is the key to understanding the function of macromolecular complexes and machines which exhibit structural dynamics and plasticity at different time and length scales relevant to phenomena of interest. Initial response to photo activation is extremely fast, sub picosecond to nanosecond, with local energy absorption by the active site leading to ultrafast coordinated motion of the molecule, the protein quake.[10, 11] Subsequent rearrangements of protein sidechains are slower but more extensive, conferring distinctive signals to which cognate molecules respond. Enzyme reactions similarly span many decades of time.

Research tools for structural biology often dictate measurement conditions such as temperature, concentration, crystalline or solution environments. A notable example is modern synchrotron X-ray crystallography in which protein crystals are cryo-cooled to prolong the lifetime of protein crystals in the intense X-ray beam for data collection at the highest possible resolution. The crystalline conditions at low temperature "freeze" proteins in a subset of conformations that are not necessarily representative of the entire range of their dynamic structures.[12, 13] This calls for new methods which allow measurements on natural time scales and in physiological environments.

Recent crystallography experiments at LCLS, at room-temperature, have shown substantial structural dynamics of macromolecules.[3] Structural dynamics are particularly important for enzymes where high-resolution crystal structures at cryogenic temperature are unable to explain the fast enzyme kinetics observed in physiological conditions. For example, acetylcholine esterase (shown in Figure 69) has a catalytically active site deep inside the protein, accessible only through a very narrow channel, yet it has a reaction turnover rate of 50,000 times a second. This is normally impossible because of the 3.0 Å constriction in the channel through which substrates and reactants must pass. Therefore, there must be an internal breathing motion to facilitate this high reaction rate, but neither high resolution crystal structures nor solution scattering experiments to date have been able capture such a motion, or explain the dynamic function of this enzyme. Hence completely new structural dynamics methods will be required to follow structural dynamics in physiological conditions – either in response to direct triggering of the reaction (pump-probe) or have the capacity to capture rare transient events associated with spontaneous dynamics. LCLS-II will enable such studies using crystallography, time-resolved small and wide angle scattering, fluctuation scattering and single particle imaging as explained in the following sections.

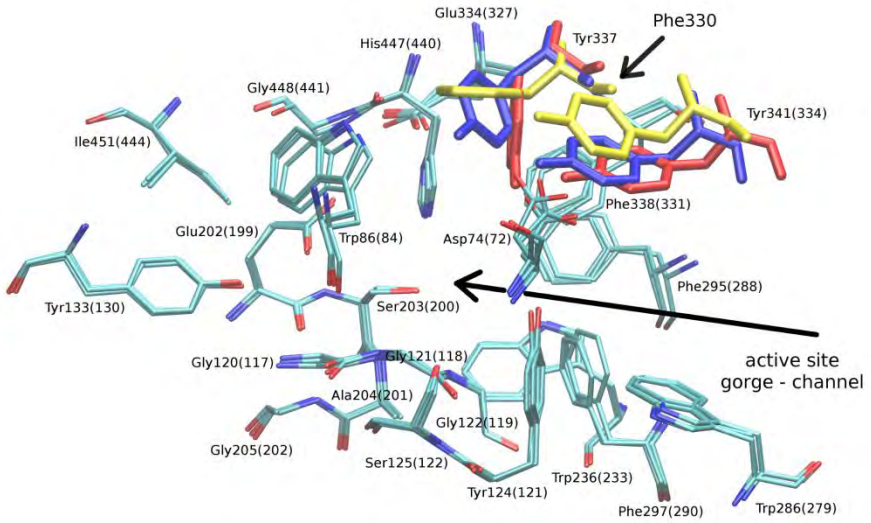

Figure 69. Acetylcholine esterase structure, detailed view of the active site (alignment from homo sapiens, mus musculus and torpedo californica).[14]

Structure & dynamics at high resolution – femtosecond crystallography

Resolution

Crystallography excels at revealing fine structural detail about the electron density in macromolecules. At LCLS and LCLS-II, the intense X-ray pulses uniquely enable measurements to be accomplished before damage can set in. This has made possible the study of crystals at room temperature and enabled the use of crystals typically smaller than usable at other X-ray sources. The study of membrane proteins and specifically GPCRs represents an important area illustrating the scientific impact of this capability.[3, 7, 8]

LCLS-II will further enable these studies by providing X-rays above 12.7 keV. The advantage is not only higher resolution (which can be definitive in many cases) but also access to Single-wavelength or Multi-wavelength Anomalous Dispersion phasing (SAD/MAD) at the selenium K-edge, techniques well-demonstrated and proven at synchrotron sources. In bio-molecules where metal centers are present, radiation damage at a synchrotron sources often limits the achievable resolution. Shorter wavelength ultrashort pulses of X-rays at LCLS-II will enable new high resolution discoveries in biological sciences. Moreover, the variable gap undulator system will allow rapid scanning of the photon energy, enabling faster data collection of MAD datasets.

Room-temperature

In addition to limiting radiation-induced damage and allowing data collection at room temperature, ultrafast X-ray pulses provide access to dynamics and can provide a path to observe multiple conformations which are central to biological function. Biomolecules in crystals are expected to be in a more native state at room temperature, and they are less likely to be "frozen" or trapped in specific conformations as the thermal energy allows access to more of the conformational landscape (within the constraints of the crystalline structure). Evidence is now mounting that most crystalline structures are comprised of multiple conformations which can be extracted from crystallographic data with proper modeling.[15]

Limitations in resolving the conformations of dynamic proteins impede the design and engineering of potential drugs or novel macromolecules with unique functions. The lack of dynamic knowledge also limits our understanding of the effects of disease and drug resistance mutations. Current protein structure models lack precise information on active sites that catalyze novel reactions. Drug resistance mutations at distant sites can increase the dynamics at an active site but the mechanisms are unknown. Room-temperature studies can reveal cryptic drug pockets and advance our understanding of how mutations alter

protein function in diseases. Room-temperature studies at LCLS-II with high-throughput, combined with modeling will provide unique access to conformational as well as potentially dynamical information. The increased repetition rate here will provide access to rare conformations and enable sufficient statistics to be obtained to properly extract the natural dynamic information from the data.

Dynamics

A frontier goal for many structural biologists is to determine crystal structures of as many steps as possible around a proposed reaction cycle, including reactive intermediates – often metastable, higher-energy states that are difficult to study by traditional crystallographic methods.[16, 17] Macromolecular crystals are typically ~50% solvent, with water-filled channels traversing the crystal lattice. The average enzyme turnover takes 60 msec and the fastest rates are just below 1 μs.[18-20] Small molecule substrates like O_2 or sucrose diffuse via Brownian motion in water with rates that range from 2–0.5 μm2/msec. Furthermore, many substrates and enzymes exhibit electrostatic complementarity to yield binding steps that may be much faster than random diffusion. Therefore, most enzyme microcrystals (~1 μm per side) will equilibrate with their substrate many times faster than their overall reaction cycle. Thus, time-resolved crystallographic analysis is potentially applicable to most enzyme reactions. Moreover, because of the complexity of catalysis and the uncertainty in interpreting electron density maps, time-resolved serial crystallography methods will benefit from correlations with complementary spectroscopic and kinetic methods (as discussed in Section 2.6.3).

Beyond the increased resolution afforded by high-energy X-rays, the high repetition rate provided by LCLS-II offers a unique opportunity for higher throughput studies for generating larger data sets in a shorter time, with more time points measured during the dynamic process. This represents a revolutionary new capability for the study of dynamics in biomolecules as current experiments at LCLS can only collect a few sample points of a complete time sequence. The need for many indexed diffraction patterns leads to significant data collection time for each time point, and the repetition rate of LCLS-II will break this bottleneck.

For most time-resolved crystallography studies, slow, viscous sample delivery media will not be adequate and a more efficient method to use fast flowing samples will be enabled by LCLS-II. Viscous jets typically flow too slowly to allow a well-defined laser illumination for example, with laser illumination covering a sample volume that takes many LCLS pulses to flow through the interaction region. This prevents the study of irreversible reactions entirely with such slow jets. The LCLS-II high repetition rate will allow fast jets suitable for time-resolved studies to be used efficiently without too much wasted sample.

Direct pumping of photoactive sites by laser illumination is not the only method to initiate dynamics and a host of important studies can be driven by other stimuli, such as laser Raman pumping of water to create fast temperature jumps as well as rapid mixing and diffusion. In the latter case, the ability to rapidly mix reagents to obtain a high temporal resolution will rely on low viscosity samples, making fast-flowing water-based jets the only option. This is where the increased repetition rate of LCLS-II will again provide unique capabilities for studying many time points of a triggered reaction and allow exploration of multiple conformations and the identification of rare events.

Some limitations are obvious and realized with the high repetition rate LCLS-II limited to 5 keV at the fundamental energy. Crystallography typically desires higher resolution and there is a clear desire for extending the energy range of the high repetition rate LCLS-II to as high as possible as soon as possible. However, some important scientific questions can be answered at lower photon energies. For example, the undocking of ferredoxin from photosystem I triggered by absorption of a visible light photon is not known even at low resolution and the high repetition rate LCLS-II might allow to better understand this system even using the lower energy X-rays. In the longer term, an increase in achievable photon energy at

high repetition rate would be of great benefit to characterize rare events and small conformational changes at the highest resolution.

Native Phasing

Another important capability of LCLS-II is high-repetition rate pulses in the 2-5 keV range, where absorption edges of many biologically relevant elements exist. For example, phasing close to the sulfur edge could provide a robust technique to phase many novel proteins at low resolution without the need for modifications or the use of other elements. Recent developments at the Diamond Light Source are demonstrating the power of sulfur phasing at low photon energies.[21] Phasing at low resolution could be sufficient to allow inference of the phases to high resolution, thus providing a two-step approach to solving novel structures at high resolution. Phasing requires very high data quality and using an X-ray FEL beam this so-far has meant high data redundancy to average all the fluctuating parameters in the measurement. Very large data sets have been required[22] and the higher repetition rate, combined with faster detectors will make phasing as a routine technique more realistic. Of additional importance is elemental discrimination for low-Z elements such as Na or Mg using anomalous scattering. In order to make full use of these capabilities, investment are likely required in instrumentation and detectors aimed at optimal use of the tender X-ray range. Specialized detectors such as the one developed specifically for sulfur phasing at the Diamond Light Source may be necessary for LCLS-II.

LCLS-II will be capable of producing high-quality pulses with two distinct colors. This will open the door to multiple new possibilities. It will allow MAD phasing data to be collected with the two different wavelengths provided in a single pulse on the same crystal. This will allow much better scaling between the two-colors and should greatly reduce the time for collection of a MAD dataset. Combined with the increased repetition rate of LCLS-II and the likely improved capabilities for two-color generation compared to LCLS, this could provide a routine method for phasing novel structures. Access to two-color pulses around the selenium K-edge will also provide new phasing capabilities.

Novel Techniques

Another potential use of two-color LCLS-II pulses could enable novel time-resolved techniques that would again provide higher quality data with intrinsic scaling between the dark and light-activated states. In a technique called probe-pump-probe, delaying the two-colors would allow a time point before and after light activation to be measured, with a laser pump pulse coming between the two X-ray pulses of different colors. It should be possible to index each of the two crystal lattices on the same diffraction patterns independently and separate the first probe signal from the second probe. Again such a technique could open the door to many time-resolved applications and combined with the high repetition rate of LCLS-II, allow many more time points to be collected for any given experiment, making molecular movies a much more immediate reality.

Finally, the continued trend of use of hybrid techniques will be critical to LCLS, with simultaneous use of protein crystallography and spectroscopy techniques to obtain complementary information on single shots, allowing better characterization of unique and rare events as well as a more complete understanding of dynamics in molecular movies. The example of photosystem II remains an excellent use of LCLS-II with short lived states requiring light activation in a highly-radiation sensitive molecule. The ability to characterize the electronic state of the manganese cluster via X-ray emission spectroscopy simultaneously with collecting crystal diffraction, at much higher repetition rates will allow movies with suitable time steps to be generated with LCLS-II.

Bridging the Gap between Single-Particle Imaging and Macromolecular Crystallography

Macromolecular crystallography provides an in-depth view of structures at an atomic level. Single particle X-ray scattering methods on the other hand will provide likely lower resolution structural

information of macromolecules in solution or in the gas phase. Although these two methods are complementary in nature, these two techniques alone do not span the full dynamic range of length scales of interest to biology. Medium-scale domain movements as observed in membrane protein dynamics, viral-capsid maturation or in the molecular machinery associated with DNA repair and protein synthesis are essential to the understanding fundamental biology, but are not well captured by crystallography or single particle diffraction.

In order to obtain a full imaging coverage of the complete spatial dynamic range of length scales of interest to biology, additional techniques are required to bridge the gap. Traditionally, small and wide angle X-ray scattering (SAXS/WAXS) has fulfilled this niche, capturing large and medium scale motions in protein.[23] The FEL-based extension of this method, named fluctuation X-ray scattering (FXS) or correlated X-ray scattering (CXS) as discussed in the Section 2.6.2, enriches traditional SAXS/WAXS data by providing experimental access to intensity correlations that are directly related to molecular structure. Using iterative or model based phasing routines, one can obtain high-quality 3D representations of the electron density of the model under investigation. If a ground state or partial model is available, existing real-space modeling techniques can be used to interpret the derived electron density.

The high repetition rate of the LCLS-II will allow rapid acquisition of high-quality scattering data from ensemble of molecules. The additional information that can be obtained from these experiments is highlighted in Figure 70 where a shape reconstruction from synthetic SAXS/WAXS data is compared to one obtained from synthetic intensity correlation data. As can be seen in Figure 70, the level of recoverable detail from the intensity correlation data is far greater than what is retrieved from the SAXS/WAXS data.[24]

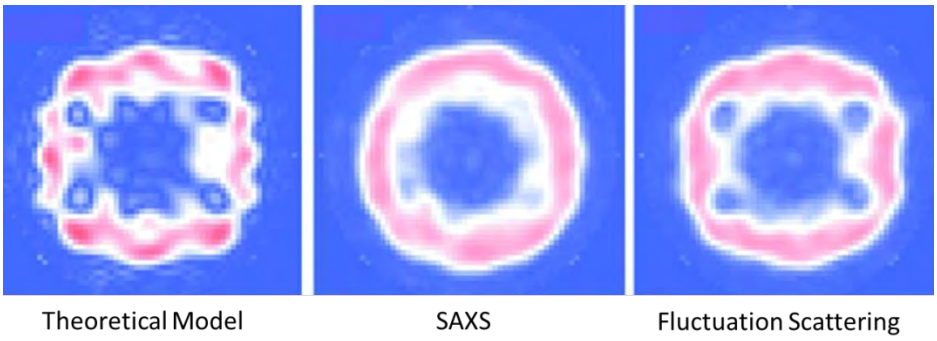

Figure 70. The added value of FXS data as compared to SAXS data is demonstrated on synthetic STMV data.[24] A density section of the STMV reference model is shown on the left. The scale bar is 10nm. Ab initio models generated from SAXS (middle) data show significantly fewer details as compared to those obtained from FXS data (right). This increase in recoverable detail will provide new biological insights from macromolecules in solution that cannot be obtained via traditional scattering methods.

Molecular movies via single-particle imaging

One of the original grand visions for X-ray FELs is the ability to image non-crystalline and non-reproducible structures with single femtosecond X-ray pulses. The underlying concept is that the X-ray pulses from FEL sources are so intense that the imaging process outruns the X-ray induced sample damage, while also having enough photons in the incident pulse to produce a measurable and interpretable diffraction pattern in a single shot.[1] Initial single particle imaging experiments at LCLS have produced single-shot coherent diffraction images of viruses [25], bacteriophages [26], organelles [27], and cyanobacteria [28] to name a few. First data sets have been assembled into three dimensional images.[29] In

addition to biological systems, single shot diffractive imaging has been used to study the morphology of aerosols [30], power density dependent damage processes in atomic clusters [31], and superfluid quantum systems.[32]

Important opportunities for single particle imaging in biology include the investigation of proteins that do not crystalize as well as determining the energy landscapes of nanomachines. The unique advantages of imaging with intense X-ray pulses are the possibility to image the specimen at physiological temperatures in their native environment and to follow their dynamics from the shortest timescales of bond-breaking to long timescales of large conformational changes.

The optimum conditions for single shot particle imaging are subject of much debate, and active research.[9] Biological samples are typically only weak scatterers, leading to low signal-to-noise ratios in the collected data. Sample heterogeneity complicates the assembly of complete data sets, and of course in many complexes, the heterogeneity is of significant relevance for biological function. Sample injection techniques need to be refined for the delivery of high-concentration beams of pristine particles. In order to address these scientific and technical challenges, LCLS has developed a roadmap towards single particle imaging with 3 Å resolution[9] and launched the Single Particle Imaging initiative, consisting of 100 scientists from 20 institutions spanning 8 countries. The initiative covers all aspects of SPI, from ultrafast X-ray induced damage processes to sample delivery and algorithm development.

LCLS-II has the potential to uniquely benefit single particle imaging for the investigation of biological function. Extrapolating today's knowledge, there is evidence suggesting that the optimum region for single particle imaging is in the tender X-ray range between 2 keV and 6 keV, which may represent the best compromise between scattering cross-section and resolution (see Figure 71). With the possibility of delivering the Cu-linac electron beam to the soft X-ray undulator of LCLS-II comes the opportunity for high pulse intensities in this regime that could allow recording single shot snapshots of biological specimen with high contrast and nanometer resolution. Conversely, using the high repetition rate of LCLS big data sets of low contrast data under controlled conditions can be recorded with XFELs for the first time that can then be assembled into energy landscapes. Both aspects are explained in more detail below.

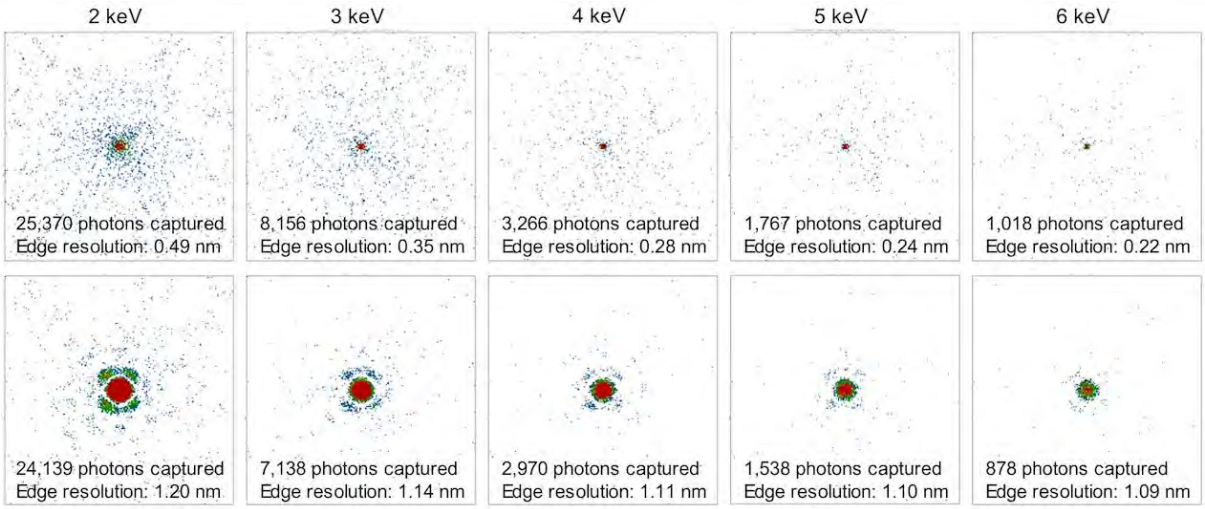

Figure 71. Expected diffraction signal from a macromolecule (Rubisco, MW: 550,000)[33] at LCLS-II in a 1 μm focus. The figure shows the number of scattered photons on the entire detector surface (top row) and on the central part of the detector (bottom) as a function of photon energy. Pulse energy: 2 mJ (10 mJ with 20% beam line transmission), top-hat focus profile at 1 μm focus. A smaller focus would further enhance the signal.

High-intensity single-shot X-ray imaging in the tender X-ray regime

A full three-dimensional reconstruction of single particles requires reproducible samples exposed to the X-ray beam one-by-one in different orientations.[1, 29, 34-36] Each of the conformers may be present in a number of different conformational sub-states. How reproducible is a "reproducible object" and how well can we distinguish between similar and dissimilar structures will affect the resolution in the reconstructed image.[37]

Imaging one particle at a time has the potential of separating conformational states and thus to image the entire ensemble of structures of a protein.[38] This provides a fingerprint of structural dynamics. Each X-ray shot is a unique structure measurement and the exposures can be sorted to explore differences, first at a coarse-grained level, and then at increasingly higher levels of resolution and complexity as permitted from the measurement. A prerequisite for sorting different structural states is the ability to capture enough information in each exposure. One has to be able to tell if two shots originate from the same conformer or from two different conformers. Achieving this requires the highest possible information content per shot, and this in turn requires very intense pulses.

One of the grand challenges in structural sciences is to determine experimentally the conformational phase-space of large macromolecules. Without the ability to separate different structural states, incoherent addition of dissimilar structures will lower the overall resolution of a 3D reconstruction. Grouping dynamic structures into unique structural sub-states opens a path to solving them separately at higher resolution.

The results will provide an experimental survey of the conformational phase space of macromolecules, and will offer comparison with molecular dynamics (MD) simulations. There are strong synergies between MD and single particle imaging, the former capable of simulating dynamics of small systems at time scales reaching about a millisecond, while X-ray FEL imaging can easily be extended to much longer time scales. The snapshots captured by an X-ray FEL pulse can be compared with MD simulations and should be able to reveal which conformations sampled by the simulation are present in the experiment, what is their relative ratio, offering a direct way to validate MD simulations. If successful, the techniques would truly augment each other to provide a combined structure that is reliable at both low resolution, high resolution, and in time.

Biological function, conformational movies, and energy landscapes from low contrast large data sets

Elucidating function is a paramount goal of structural biology. Biological function often involves important conformational changes. Determining the conformational spectra ("movies") of molecular machines and the energy landscapes traversed in the course of function represents an important new frontier in biology.[39] LCLS-II has the potential to provide unprecedented access to conformational movies and energy landscapes associated with biological function at physiological temperatures.

Extensive experience in cryogenic electron microscopy (cryo-EM) has established that it is possible to extract three-dimensional structure [40], conformational movies, and energy landscapes from experimental ultralow-signal snapshots of biological entities viewed in unknown orientations at unknown points in their work cycle (Figure 72).[41] Biological machines function under severe Brownian bombardment, and no single observation is fully reproducible. Reliable information necessitates averaging over homogeneous (i.e., sorted) ensembles. The richness of a conformational movie and the detail with which an energy landscape can be mapped depend critically on the number of available snapshots.[41]

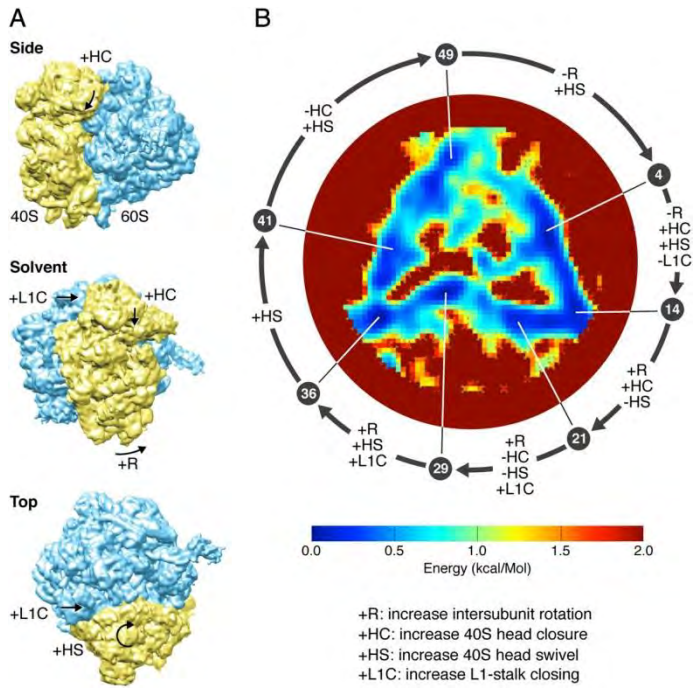

Figure 72. (A) Three views of a cryo-EM map of the 80S ribosome from yeast, with arrows indicating four key conformational changes associated with the elongation work cycle of the ribosome. (B) The energy landscape traversed by the ribosome. The color bar shows the energy scale. The roughly triangular minimum-free-energy trajectory is divided into 50 states. The arrows indicate the structural changes between seven selected states, each identified by its place in the sequence of 50 states.[41]

It is well established that detailed structural information can be recovered from snapshots with extremely low signal. Three-dimensional structure, conformational movies, and energy landscapes are now routinely extracted from image snapshots with signal-to-noise ratios as low as 0.06.[40-42] The same capability has been demonstrated for simulated [35, 36, 42, 43] and experimental diffraction snapshots containing as few as 10 diffracted photons per frame.[44] Current experimental diffraction snapshots of large viruses, in contrast, contain millions of scattered photons from the object of interest.[27] However, substantial shot-to-shot variations in extraneous factors –such as scattering from apertures and particle injectors, as well as difficult-to-control detector nonlinearities - severely degrade the available information. Developments in the source, optics and instrumentation to fully utilize LCLS-II have the potential to reduce such extraneous variations to levels small compared with the (conformational) signal from the object.

The enhanced repetition rate of LCLS-II, combined with improvements in shot-to-shot uniformity in the incident illumination and detector response, can be expected to revolutionize our ability to obtain molecular movies of biological machines at physiological temperatures, and the energy landscapes traversed in the course of biological function.

2.6.2 Dynamics, structure and function of biological assemblies in near-native environments

Synopsis

The relationship between the structure of macromolecular assemblies, how this structure changes upon external influences and its function of the entity plays a fundamental role in biology. Whereas protein crystallography is the technique of choice to determine interactions at an atomic level in and between macromolecules and its cofactors, in general the technique is limited to long-lived structural species that are able to form crystals. Techniques such as small and wide angle X-ray scattering (SAXS/WAXS) have been able to provide insight in the structure of macromolecules, unconstrained by a crystal lattice, but suffer from lack of information due to the inherent one-dimensional nature of such data. Fluctuation X-ray Scattering (FXS), also known as Correlated X-ray scattering (CXS) is an extension of these techniques that allows the extraction of significantly more information than possible using traditional scattering methods.

Fluctuation X-ray scattering from an ensemble of molecules in solution, using X-ray pulses from an FEL with exposures of <100 femtoseconds, result in diffraction patterns with a wealth of additional information in the form of speckle. Subsequent extraction of angular correlations of the scattering intensity results in a dataset with three-dimensional information content far exceeding what can be obtained with synchrotron solution scattering methods, and closer to what can be obtained from single particle studies. The capabilities of LCLS-II will allow these experiments to be performed in a routine fashion, such that the screening of a large number of ligands and metabolic analogues can be accomplished rapidly with minimal amount of sample. The application of fluctuation or correlated X-ray scattering in the study of time-dependent reactions is another crucial scientific opportunity provided by LCLS-II. These time-resolved experiments will allow one to visualize structural changes in membrane proteins and, when performed at higher energies, are capable to track detailed structural changes associated with ligand binding

Introduction

Structural information provides important insight into the understanding of matter. The link between structure and its properties can suggest new avenues for designed improvements of materials or nano particles. For samples without long-range order, such as solutions of biological macromolecules, disordered organic polymers or magnetic domains, as well as (partially) ordered materials, such as self-assembled block-copolymers, liquid crystals or assemblies of nanoparticles, structural information can efficiently be obtained using traditional small and wide angle X-ray scattering (SAXS/WAXS) techniques. The samples without long-range order typically display angular isotropic X-ray scattering patterns where the mean intensity as a function of scattering angle is directly related to the average shape and local organization of the material investigated.

The isotropic nature of these SAXS/WAXS diffraction patterns is a result of orientational averaging of the scattering species due to the fact that the X-ray exposure exceeds that of rotational diffusion. The advent of pulsed X-ray sources such as free-electron lasers allows one to reduce the exposure times below that of rotational diffusion such that the non-isotropic intensity fluctuations (or speckle) in the scattering pattern can be resolved. The first experimental demonstration of this technique, known as Fluctuation X-ray Scattering (FXS) or Correlated X-ray Scattering (CXS) was provided by Kam, Koch & Bordas on frozen Tobacco Mosaic Virus in the early days of synchrotron-based small-angle scattering.[45] Subsequently, fluctuation scattering has been used to detect hidden symmetries in colloids[46] and magnetic domains [47] as well as for structure determination of 2D particles.[48, 49] X-ray FEL-based fluctuation scattering data and structure determination has produced preliminary results from single inorganic nanoparticles [50, 51] and single polystyrene dumbbells.[52]

Information is extracted from the experimental speckle patterns by computing in-frame angular intensity correlations.[53] These angular intensity correlation curves, can be used for structure determination, either

via reciprocal-space techniques [54, 55] or via real space methods.[50] In earlier studies FXS has been presented as a method to overcome experimental and theoretical hurdles in single particle imaging, but recent developments indicate that the true potential of this technique comes to fruition when combined with known atomic models.[24, 51]

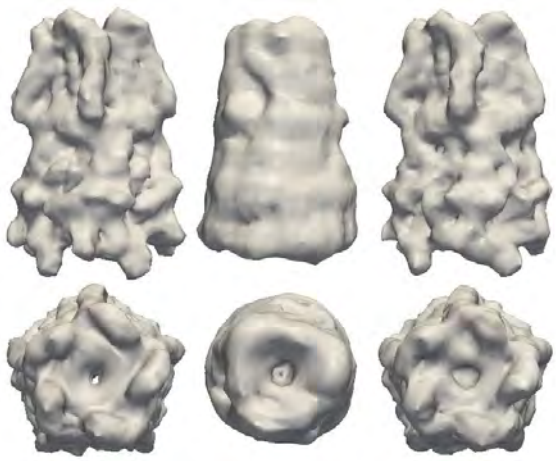

Figure 73. The reconstruction of a pentameric protein (left) from FXS/CXS data results in the absence of assumed symmetry (middle) and when enforcing 5-fold rotational symmetry (right) results in a 12Å and 7 Å reconstructions. Image taken from ref. 56.

The fluctuation or correlated scattering experiment requires the acquisition of a large number of femtosecond X-ray snapshot on a continuously renewed ensemble of molecules. The high repetition rate of the proposed LCLS-II would allow the rapid acquisition of this data, to the extent that multiple experiments can be done on the protein sample under different conditions or in a time-resolved fashion. Current state-of-the art FELs, like LCLS and SACLA have limited repetition rates that are insufficient to collect fluctuation scattering data of a protein sample bound to a variety of potential inhibitors. The maximum possible repetition rate of LCLS-II is likely to be set by the sample delivery system and detectors rather than by the machine itself. Current estimates suggest that a rep-rate of 10 kHz should be feasible, resulting in the ability to collect a half a million images within 10 minutes. The tender X-ray region (~2-5keV) accessible at high repetition rates at LCLS-II will allow data collection up to ***q***-values normally associated with standard SAXS experiments ($q<0.5A^{-1}$). Higher X-ray energies ~10 keV (either from the LCLS fundamental at 120 Hz or higher harmonics at high repetition rate from LCLS-II) will allow data to be collected in the WAXS region, up to ***q***-values of 2 $Å^{-1}$. These ***q*** -ranges will provide sufficient resolution for structural information of unknown samples.

Capabilities

As shown in Figure 73 (Section 2.6.2), the additional information obtained from the speckle patterns, provides access to higher order Fourier components of the molecular transform otherwise only accessible via crystallography or single particle diffraction methods. Although it is has been argued[57] that a general structure might not be uniquely determined by its fluctuation scattering data, it is unclear whether this non-uniqueness corresponds to small perturbations around a single solution, several clusters of solutions, or a continuum of solutions. It is furthermore unclear if prior knowledge, such as density histograms or symmetry can satisfactorily break remaining ambiguities, and likely depends on the complexity of the structure. As shown by Donatelli and coworkers,[56] *ab-initio* structure solution from FXS data is possible using iterative phasing methods, Figure 73. As shown earlier, shape reconstruction from SAXS data alone does not nearly provide as much detail as those obtained from FXS/CXS data,[24] ultimately allowing structural details to be obtained that can aid in the resolution of complex biological questions.

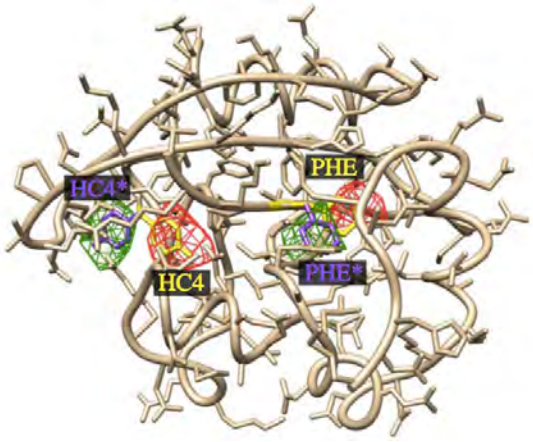

Figure 74. Difference maps obtained from synthetic data from a perturbed model, with knowledge of the structure of the ground state. Image from ref. 58.

In the case where data is collected from a known model that has been perturbed, FXS/CXS data can be used to calculate difference maps, highlighting local structural changes in a known model (Figure 74). Fluctuation X-ray scattering, like X-ray crystallography can thus provide an easy route to visualize electron differences induced by ligand binding, pH changes or upon photo-excitation. Unlike crystallography, the sample doesn't have to be in the crystalline state. Given the high-throughput nature of the experiment, allowing one to screen a large library of drug-like or metabolic compounds, this technique can provide a valuable asset in the development of drugs or the understanding of fundamental biological processes like membrane protein dynamics.[58]

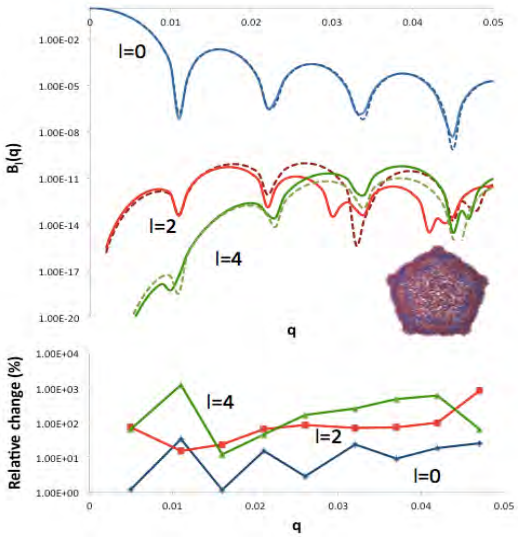

Figure 75. Simulated FXS data (top) for two states of HK97, Head-II (solid line) and intermediate IV (dotted line), indicates that FXS data (l=2,4) is more sensitive to small structural changes as compared to standard SAXS data (l=0) alone, as seen from the relative changes in FXS data (bottom).

Scientific Avenues

High throughput experiments on static samples

Solution scattering has provided the structural biology community with an understanding of the nature of structural changes and flexibility of macromolecular complexes in solution. Given the aforementioned drawbacks of SAXS/WAXS, the associated confidence intervals or uniqueness of structural models, the use of Fluctuation or Correlated X-ray scattering will radically improve upon this technique. The use of LCLS-II to provide scattering data in a high-throughput fashion, would allow rapid collection of structural information of proteins under a variety of conditions. It would, for example, allow the study of the maturation stages of the viral capsid of common viruses and provide essential insight in how to inhibit

or regulate this essential step in the life-cycle of most viral agents. Although this problem is currently analyzed using traditional solution scattering methods, the use of femtosecond exposure and availability of angular intensity correlation will provide order of magnitude in sensitivity to structural changes, as shown in Figure 74.

The current capabilities of LCLS and SACLA, in terms of rep rate and brightness, do not allow the collection of a large number of datasets within a reasonable time frame. When studying biological systems, the protein concentration, the effect of pH, ionic strength of the buffer, the presence of additives such as ligands are typically varied as to obtain the best possible data or gain specific insight. With the current repetition rates, a systematic study of all significant factors is not possible unless a large amount of beamtime is available. Collecting half a million shots per sample at LCLS requires a little over an hour to obtain a complete dataset. The proposed repetition rate of LCLS-II will cut this time down to a little under 10 minutes, assuming fast enough area detectors are developed, making it possible to optimize sample conditions and explore the parameter space to get the best possible and most relevant data.

Combinatorial ligand and metabolic cofactor screening

Macromolecules in the living cell do not work in a (metaphorical) vacuum, but interact with cofactors, metabolic products and other partners to perform their function. It is precisely these interactions and their interplay in larger systems that make biological processes complex and hard to decipher. High-throughput methods in small and wide angle scattering have allowed the elucidation of these interactions using conformational mapping techniques [59]. By performing a combinatorial ligand screen, monitored by SAXS/WAXS data, structural similarities between protein states bound to different ligands can be classified on the basis of their scattering patterns, providing a shape classification of the complexes that is linked to the function of the sample. In order to perform this experiment, a large number of complexes need to be studied to get a holistic view of the behavior of the protein subjected to a variety of ligands or metabolic compounds. The need for a large number of datasets to extract biological information requires a high rep-rate machine, such as LCLS-II. The combinatorial screening approach outlined above can be combined with the difference map capabilities showcased above. If the structure of the apo-protein is known, or if a good reconstruction is available, the autocorrelation data from these experiments can be used to generate difference maps resulting in three-dimensional views of the location of the ligands, possible binding modes and other structural changes.

Time resolved measurements at atomic resolution

Fluctuation X-ray Scattering offers the potential to measure structural details for biomolecules. If this can be done at atomic resolutions, then the data can provide constraints on the detailed conformation of a biomolecule such as an enzyme during the course of its trajectory in a functional reaction with a substrate. In order to achieve atomic resolution, scattering must be measured at large momentum transfer or angles, essentially the same as those used in biomolecular crystallography. For resolutions on the scale of 2 Å needed for modeling the interaction of small molecule drugs with biomolecules, the X-ray energy must be greater the 2 keV. This would require a detector covering all angles and for practical matters, an energy above 4 keV is highly desirable. Benefits exists with the high repetition rate increases of LCLS-II using the superconducting accelerator as well as from using the potential Cu linac beam in the SXR undulator for an increased pulse energy in the tender X-ray range. High resolution measurements could also make use of the higher photon energies available above 11 keV at low repetition rates.

Given the fact that the signal to noise in the final reduced data of these experiments scales with the square root of the number of images, and that the correlation signal scale inversely with the 8th power of the momentum transfer, the high repetition rate of the LCLS-II is required to allow the acquisition of millions of images within a reasonable time as to perform time resolved studies, following protein dynamics along the reaction coordinate.

2.6.3 Understanding the relationships between electronic structure & biological function

Enzymes enable living organism to perform thermodynamically highly demanding chemical transformations under ambient conditions and as close to the thermodynamic limit as possible. This is often achieved by breaking down of steps requiring a high redox potential/ high barrier into several sequential steps that each exhibit a lower barrier and by a fast stabilization of charge separated states due to electron transfer chains, generating stable charge separated states with minimal loss of stored energy content. In addition the enzymatic systems are often highly regulated in order to control the synthesis of desired products and avoid the release of toxic or wasteful side or alternate reaction products and have integrated self-repair capabilities. All these aspects are highly desired features for artificial catalysts but their targeted implementation is not well established. Therefore understanding enzymatic catalysis in natural systems can provide valuable insight for the optimization of catalytic processes that are of tremendous importance in many areas of society, e.g. in the chemical industry, for the energy sector or for the production of fertilizers.

By employing one or several metal ions in its catalytic site, enzymes can tailor their reactivity and achieve bond activation of substrates that is not possible using only "light" atoms as C, N, O, S and P. Such metal clusters play a key role in many of the most important energy conversion enzymatic reaction cycles, e.g. in respiration, photosynthesis, nitrogen fixation but also in many highly relevant health related processes (e.g. production of NO as a signaling molecule in NO synthase, deactivation of potentially harmful chemical species as in catalase, synthesis of nucleotides in ribonucleotide reductase). The structures of selected metal active sites from important enzymes are shown in Figure 76. These include the NiFe center in hydrogenase, an enzyme catalyzing the two electron reduction of protons into molecular hydrogen; the FeMo cofactor of nitrogenase, catalyzing the eight electron reaction of converting dinitrogen into ammonia; the water oxidizing complex of photosystem II, catalyzing the four electron oxidation of water into dioxygen and protons in photosynthesis; the FeCu center of cytochrome c oxidase, catalyzing the reverse reaction of reducing oxygen and protons to water in respiration.

For such metal-containing systems the geometric structure is a first but often not sufficient step to fully understand their function. Rather, the static picture of the structure of the catalytic site by itself does not explain the reactivity and specificity of the catalyst, key questions that have to be answered in order to extract working principles of such systems and transfer them into optimized synthetic systems. A molecular-level understanding of how transition-metal complexes catalyze reactions, and in particular of the role of short-lived and reactive intermediate states involved, will be critical for such optimization. The deep understanding necessary for this translation has to include information regarding the electronic structure of the active site and changes of it over the reaction cycle. Therefore a multi-dimensional structural approach will be necessary following not only the evolution of the atom dynamics by structural methods, as crystallography or solution scattering (see Sections 2.6.1 and 2.6.2), but also follow changes in the electron configuration and spin state in the individual atoms. Here X-ray spectroscopic methods with their specificity towards selected elements and chemical speciation can play a major role. The reactivity is dominated by the frontier orbitals and recent advances in the quantum-chemical treatment of large systems indicate that calculations of atom-specific frontier-orbital interactions will become feasible in the near future. Corresponding experimental approaches to provide similar information from biological systems under in-situ conditions are largely missing. Experiments at LCLS-II, utilizing the high repetition rate of intense fs X-ray pulses in the soft X-ray regime, can uniquely fill this gap.

Many of the spectroscopic approaches employed for studying catalytic reactions in smaller molecules, as described in Section 2.2 will eventually be transferable to biological systems, provided that the experimental conditions can be adapted to cope with the specific challenges connected to the study of biological systems, including lower concentrations of active sites, faster damage rates and higher intrinsic heterogeneity.

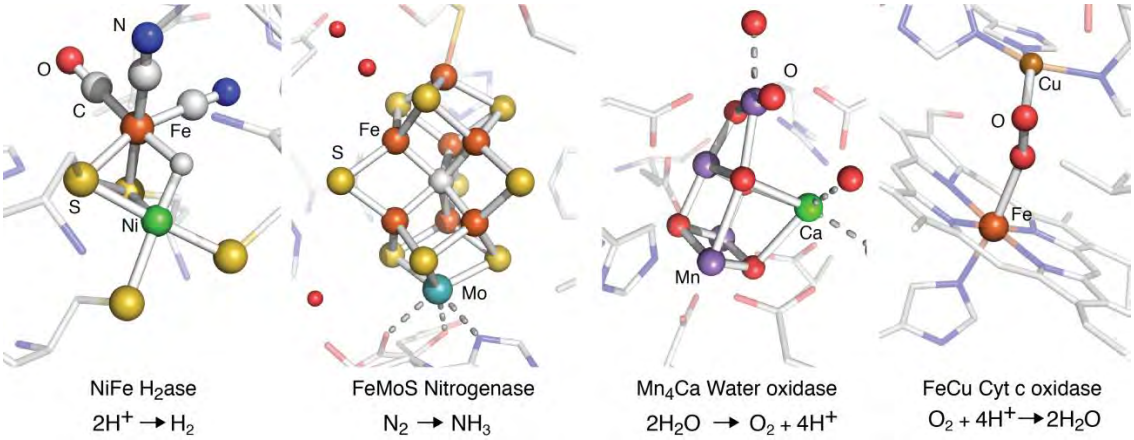

Figure 76: Structures of active sites of several metalloenzymes, showing the metal center and surrounding amino acids. Shown are (from left to right) the NiFe center of hydrogenase, the FeMo cofactor of nitrogenase, the Mn_4CaO_5 cluster of the water oxidase photosystem II and the heme$_A$ Cu_B center of cytochrome c oxidase.[60-63]

Biological systems are intrinsically dilute systems and the achievable metal concentrations for samples of metalloenzymes are often in the sub millimolar range. Thereby, any way to increase the signal that can be obtained from such systems by either increasing the flux, changing the spectroscopy method, or experimental setup is of extreme importance. In addition, redox active metal centers are intrinsically more prone to radiation-induced modifications during X-ray measurements compared to the protein scaffold itself [64, 65]. This circumstance often severely limits the radiation dose that can be applied at synchrotron sources even at cryogenic temperatures. Here the fs pulses of an X-ray FEL can be used to extract information before the X-ray-induced modification of the sample has taken place. The huge advantage of using X-ray FEL pulses instead of a synchrotron source is therefore often not only the increase in the time resolution achievable, but also the ultrafast nature of the probe that avoids the damage. This allows probing the same sample volume with orders of magnitude more photons compared to a synchrotron experiment without inducing damage within the time span of the probe pulse (few 10's of fs).

Initial experiments at X-ray FELs have already leveraged both of these advantages for spectroscopic studies of solution samples under ambient conditions[66-70] and first attempts of X-ray spectroscopy on metal enzymes were reported using the Mn K-edge emission from the Mn cluster of photosystem II at LCLS [6, 71]. While transition metal K-edge studies can provide important information regarding oxidation and spin state of a metal center, the L-edge region is more informative, as it can provide electronic structural information with significantly better resolution. The natural line widths at the L_2 and L_3 edges are about one-fourth of those at the K-edge (~0.3 eV for L-edge vs ~1.2 eV for K-edge), therefore more amenable to theoretical analysis. Furthermore, the soft X-ray signal will be more intense, since 2p → 3d transitions are allowed under dipole selection rules, while only $s \rightarrow p$ transitions are allowed at the K-edge and the greater sensitivity to the occupancy of the 3d orbitals provides a better indication of the oxidation states and symmetry of the complex involved.

In contrast to the field of material sciences, where metal L-edge spectroscopy of 3d transition metals has been used widely to provide important electronic structure information through X-ray absorption (XAS) and emission spectroscopy (XES), as well as 2p → 3d resonant inelastic X-ray scattering spectroscopy (RIXS), this region has not been exploited for biological samples. The current average flux available at X-ray FEL sources hinders the extension of such experiments to concentration regimes relevant for metalloenzymes. At LCLS, it is feasible to collect L-edge spectra of transition metals in metalloenzymes and such efforts are currently underway [69] but they are at the limit of the current possibilities. However, extending this approach beyond the L-edge spectra into two-dimensional electronic spectra by conducting

RIXS experiments is not possible in dilute systems. Such experiments would require several months of beam time, rendering them practically infeasible. Leveraging the greatly increased repetition rate of LCLS-II in the soft X-ray regime such experiments could be conducted within a few days. For example, L-edge RIXS on solutions with a metal concentration around several 100 mM is possible today at LCLS [70] and a 100x-1000x increase in repetition rate would enable similar experiments with biological samples that have metal concentrations in the mM range.

Extending the biological soft X-ray spectroscopy beyond the L-edge spectra into two dimensional electronic spectra by conducting RIXS experiments would allow obtaining a detailed picture of the electronic structure (electron localization/delocalization and spin states) in the studied system (see Figure 77a for a schematic representation of the process and detailed explanation of the technique in section 2.2.1) and probing the local chemistry at the catalytic site. This would allow understanding of the relationship between electronic structure and function of metalloproteins on an atomic and quantum-chemical level, leaving the classical "ball-and-stick" approach behind.

While increasing X-ray flux helps collecting RIXS data from dilute samples, a caution is necessary as there is possible electronic structural damage at very high doses. In the case of extreme doses (in the range of GGy), direct effects due to multiple ionizations are observed, e.g. RIXS on metal complexes in solution using fs pulses at LCLS showed new features due to the electronic damage at high dose with 2 mJ/pulse [70]. Also, SFX experiments on the Fe enzyme ferredoxin at the 100 nm focus at the CXI instrument indicated changes in the FeS clusters,[72] compared to low dose datasets, in agreement with simulations.[73] These results indicate that just increasing the brightness of individual pulses might not be a feasible strategy to increase the signal level from dilute systems, and the damage to the electronic structure under high fluence has to be studied carefully. On the contrary increasing the repetition rate while keeping the level of photons/pulse and replacing the sample fast enough to keep up with the repetition rate, will allow obtaining spectral information from dilute systems in drastically reduced time while circumventing potential electronic damage to the sample. This makes the capabilities of LCLS-II an ideal match for the experiments described here.

The next step would then be to integrate the two-dimensional X-ray spectroscopy with a pump-probe setup to trigger the studied reaction and follow the evolution of the RIXS plane over time. Here some of the possible phenomena, for example excited state dynamics, are ultrafast (see Figure 77b). In such cases the fs pulses of LCLS-II would serve a dual purpose, a) ultrafast probe to enable "probe-before-destruction" time measurements and b) studying ultrafast transient states in the sub-ps to ps time regime. But also for the study of transients in slower reactions that are important for the bond forming/breaking chemistry taking place in nearly all metal cluster catalyzed enzyme reactions (e.g. see Figure 77c for transition times in photosystem II), the ability to perform ambient condition 'undamaged' time resolved RIXS studies will add tremendous information about the evolution of the electron density over the reaction cycle. RIXS gives unique chemical resolution, and is expected to reveal the dynamically changing population of various electronic sub-species. Such measurements would complement approaches that probe structural dynamics, e.g. by crystallography or solution scattering in these processes. The combined information can be directly correlated with density functional calculations that describe the frontier orbitals and their change as a function of the reaction coordinate.

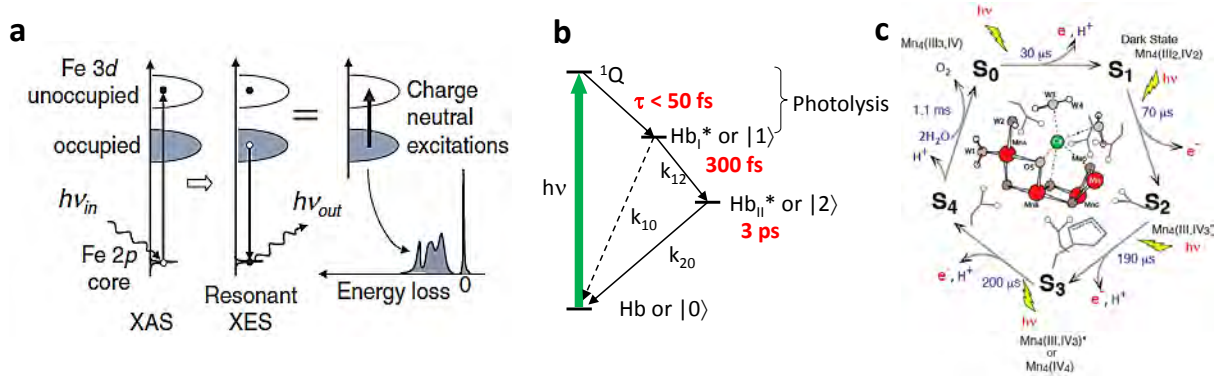

Figure 77: a) Scheme for 2*p*-3*d* RIXS process for the example of a Fe system. The energy loss (or energy transfer) spectrum is measured for a series of excitation energies ($h\nu_{in}$) across the metal absorption edge to obtain the two dimensional RIXS plane. B) Kinetic scheme for ultrafast decay processes occurring in a heme molecule after light excitation.[74] C) Catalytic scheme for the S-state transition in the Mn_4CaO_5 cluster of photosystem II with transition times ranging from 30 µs to 1.1 msec.

One prime example that could profit from L-edge spectroscopy at LCLS-II is the catalytic center of the membrane protein complex photosystem II that catalyzes the light driven oxidation of water in plants, algae and cyanobacteria. This molecular machine combines three functional units. The first one is a light collecting antenna domain populated with numerous chlorophyll and carotenoid co-factors that channels the absorbed light via excitation transfer to the second component, the reaction center. Here the primary charge separation takes place within picoseconds, and subsequent electron transfer steps spanning the width of the membrane stabilize this initial charge separated pair quickly. The stable primary donor cation then extracts in turn an electron from the third functional part of the complex, the catalytic site for water oxidation. The Mn_4CaO_5 cluster at this active site acts as a charge storage device and accumulates oxidation equivalents after each light induced charge separation in the reaction center of photosystem II. After accumulating four oxidation equivalents the cluster undergoes a reduction concomitant with the oxidation of the bound substrate waters and release of the formed dioxygen (c).

Tremendous progress has been made in the structural characterization of this catalytic center in its resting state, culminating in the recent high resolution structure based on diffraction images collected under non-damaging conditions using X-ray FEL pulses at SACLA.[75] But this static picture does not provide the necessary information to deduce the electronic configuration of the metals in the resting state and the flow of electrons within the catalytic center and the substrate during the reaction cycle. Many suggestions about possible reaction mechanisms have been put forward [76-78] but no experimental method so far has provided definitive evidence for deciding between them. First attempts have been made to monitor this reaction under physiological conditions with SFX and spectroscopy experiments at LCLS [5, 6, 71]. The necessary more detailed information about the electron flow could be obtained by spectroscopy at the Mn-L edge, especially Mn L-edge RIXS. Even the static RIXS measurement under ambient conditions is not possible with the current average fluence of LCLS. The high rep rate of LCLS-II would allow not only conducting such measurements in the resting state but beyond that to probe various delay times within the catalytic cycle within a reasonable measurement time. This approach would allow a molecular-level understanding of how this transition-metal complex catalyzes the formation of molecular oxygen, and in particular of the role and nature of short-lived and reactive intermediate states that cannot be trapped/monitored with other methods. This information will be critical for extracting design principles that can be used to optimize artificial water oxidation catalysts.

Many enzymatic reactions proceed in the µs to msec time scale making the repetition rate of 100 kHz to 1 MHz of LCLS-II an ideal match. One can envision using the resulting pulse spacing in the µs to 100 µs range to follow these processes in their natural time scale, similar to the probe-pump-probe approach

described for crystalline samples in section 2.6.1. In this approach the beam would be defocused to lower the dose significantly below the damage threshold and a train of pulses would be delivered to the same sample volume over the time window of interest, e.g. up to several millisecond and the detector would be read out for each single shot. After this pulse train the sample would be replaced and a new measurement started. The high repetition rate would here compensate for the lower signal/shot. Such an approach could be used for various techniques, e.g. X-ray emission, X-ray absorption and combined scattering and spectroscopy experiments.

Access to high repetition rates in the tender X-ray region enabled by LCLS-II, along with optics and instrumentation developments, would also allow to access transition metal absorption edges that are not available at LCLS. One example here is the Mo L-edge at 2.5 keV. Mo is part of the FeMo cofactor in nitrogenase and studying the evolution of the electronic structure of this cluster over the reaction cycle of nitrogen fixation from both the view of Fe and Mo would allow a deeper understanding of the mechanism of this highly important reaction. Such studies could also be combined with diffraction measurements at limited resolution (around 5Å).

The novel access to the tender X-ray region at LCLS would also enable XAS of P, S, and Ca, all of them playing important roles in many biological systems. The K-edge (at 4 keV) of Ca has a rich pre-edge structure that is very sensitive to the local structure of the binding site. One could follow time resolved changes in the Ca XAS to monitor changes in Ca ligation during an enzymatic reaction. Similarly, sulphur is often involved in metal ligation in active sites and following sulphur XAS (at around 2.47 keV) over a reaction cycle would elucidate the involvement of the sulphur ligands in the reaction mechanism. Here specificity against the large background of sulphur atoms present in the protein could be achieved by difference XANES, as the edge position and shape of sulphur changes over a wide energy range with change in the chemical speciation/oxidation state.

Extending the seeded beam capabilities it might be possible to probe two different elements at the same time, e.g. ligand K-edge and transition metal L-edge. One example here would be probing the oxygen K-edge and the Fe L-edge at the same time in oxygen activating Fe enzymes using two color X-ray emission spectroscopy.

A preferred method to obtain very high-resolution structural information about the first and second shell ligation of a specific center is EXAFS (extended X-ray absorption fine structure). EXAFS allows determination of bond distances to levels of <0.05 Å, an accuracy in general not achievable with macromolecular crystallography for biological systems. Pioneering work at LCLS has shown the feasibility to record transition metal K-edge XAS from model systems with concentrations in the 50 mM range. Lemke et al. exploited transient XANES to follow time-dependent changes in the local structure of a Fe center[67] and reasonable quality spectra where obtained within about 1 hour of measurement time. By using the 3rd harmonic of LCLS-II one could exploit the cw super conducting LINAC to obtain high repetition rate pulses in the hard X-ray regime necessary for reaching for example the Fe K-edge (7.11 keV) or alternatively use the fundamental of the Cu-LINAC at 120 Hz. Due to the high repetition rate, even considering the low yield of the 3rd harmonics (~ 0.5-1% of the fundamental), there would still be a substantial gain in sensitivity (from improved statistics at high rep rate) and achievable photons over time compared to the current LCLS capability. This would allow performing XANES and even EXAFS with biological samples in the mM concentration range within reasonable measurement times.

Experimental approaches & impact of LCLS-II

The envisioned time-resolved RIXS experiments on biomolecules are basically limited by the currently available photon flux. On the contrary the instrumentation available already should be sufficient for initial experiments with the high rep rate X-ray source and integrating detectors. For biological L-edge RIXS

spectroscopy the current resolution level of standard RIXS spectrometers is sufficient. Also, given a stable temporal overlap between optical pump and X-ray probe integration of many shots on a slow detector would be possible, allowing the use of the full repetition rate of the X-ray source with currently available detector technology. Sample replacement with current injector technologies[79, 80] is feasible and for example allows replacement of the sample by several 100 μm between individual shots at a repetition rate of 100 kHz. The energy range necessary for L-edge 2*p*-3*d* transition metal RIXS would be from several 100 eV to ~ 1 keV, depending on the L-edge position of the transition metal studied, ideally matching the proposed capabilities of LCLS-II.

References

1. R. Neutze, R. Wouts, D. van der Spoel, E. Weckert, and J. Hajdu, "Potential for biomolecular imaging with femtosecond X-ray pulses," Nature **406**, 752 (2000).
2. S. Steeb, and H. Warlimont, eds. *Rapidly Quenched Metals V* (Elsevier, Amsterdam, 1985).
3. W. Liu, D. Wacker, C. Gati, G. W. Han, D. James, D. J. Wang, et al., "Serial Femtosecond Crystallography of G Protein-Coupled Receptors," Science **342**, 1521 (2013).
4. U. Weierstall, D. James, C. Wang, T. A. White, D. J. Wang, W. Liu, et al., "Lipidic cubic phase injector facilitates membrane protein serial femtosecond crystallography," Nature Communications **5**, 3309 (2014).
5. C. Kupitz, S. Basu, I. Grotjohann, R. Fromme, N. A. Zatsepin, K. N. Rendek, et al., "Serial time-resolved crystallography of photosystem II using a femtosecond X-ray laser," Nature **513**, 261 (2014).
6. J. Kern, R. Tran, R. Alonso-Mori, S. Koroidov, N. Echols, J. Hattne, et al., "Taking snapshots of photosynthetic water oxidation using femtosecond X-ray diffraction and spectroscopy," Nat Commun **5**, 4371 (2014).
7. H. Zhang, H. Unal, C. Gati, Gye W. Han, W. Liu, Nadia A. Zatsepin, et al., "Structure of the Angiotensin Receptor Revealed by Serial Femtosecond Crystallography," Cell **161**, 833 (2015).
8. G. Fenalti, N. A. Zatsepin, C. Betti, P. Giguere, G. W. Han, A. Ishchenko, et al., "Structural basis for bifunctional peptide recognition at human δ-opioid receptor," Nat Struct Mol Biol **22**, 265 (2015).
9. A. Aquila, A. Barty, C. Bostedt, S. Boutet, G. Carini, D. dePonte, et al., "The linac coherent light source single particle imaging road map," Structural Dynamics **2**, 041701 (2015).
10. D. Arnlund, L. C. Johansson, C. Wickstrand, A. Barty, G. J. Williams, E. Malmerberg, et al., "Visualizing a protein quake with time-resolved X-ray scattering at a free-electron laser," Nat Meth **11**, 923 (2014).
11. M. Levantino, G. Schirò, H. T. Lemke, G. Cottone, J. M. Glownia, D. Zhu, et al., "Ultrafast myoglobin structural dynamics observed with an X-ray free-electron laser," Nat Commun **6**, 6772 (2015).
12. J. S. Fraser, H. van den Bedem, A. J. Samelson, P. T. Lang, J. M. Holton, N. Echols, et al., "Accessing protein conformational ensembles using room-temperature X-ray crystallography," Proceedings of the National Academy of Sciences **108**, 16247 (2011).
13. J. S. Fraser, M. W. Clarkson, S. C. Degnan, R. Erion, D. Kern, and T. Alber, "Hidden alternative structures of proline isomerase essential for catalysis," Nature **462**, 669 (2009).
14. J. F. Lutsko, D. Wolf, S. Yip, S. R. Phillpot, and T. Nguyen, "Molecular-dynamics method for the simulation of bulk-solid interfaces at high temperatures," Phys. Rev. B **38**, 11572 (1988).
15. J. M. Holton, S. Classen, K. A. Frankel, and J. A. Tainer, "The R-factor gap in macromolecular crystallography: an untapped potential for insights on accurate structures," Febs J **281**, 4046 (2014).
16. R. Neutze, and K. Moffat, "Time-resolved structural studies at synchrotrons and X-ray free electron lasers: opportunities and challenges," Current Opinion in Structural Biology **22**, 651 (2012).
17. D. Bourgeois, and M. Weik, "Kinetic protein crystallography: a tool to watch proteins in action," Crystallography Reviews **15**, 87 (2009).
18. C. Walsh, "Enabling the chemistry of life," Nature **409**, 226 (2001).
19. V. L. Schramm, "Enzymatic Transition States, Transition-State Analogs, Dynamics, Thermodynamics, and Lifetimes," Annual Review of Biochemistry **80**, 703 (2011).
20. V. L. Schramm, "Enzymatic transition states and transition state analogues," Current Opinion in Structural Biology **15**, 604 (2005).

21. K. El Omari, O. Iourin, J. Kadlec, R. Fearn, D. R. Hall, K. Harlos, et al., "Pushing the limits of sulfur SAD phasing: de novo structure solution of the N-terminal domain of the ectodomain of HCV E1," Acta Crystallographica Section D **70**, 2197 (2014).
22. T. R. M. Barends, L. Foucar, S. Botha, R. B. Doak, R. L. Shoeman, K. Nass, et al., "De novo protein crystal structure determination from X-ray free-electron laser data," Nature **505**, 244 (2014).
23. C. D. Putnam, M. Hammel, G. L. Hura, and J. A. Tainer, "X-ray solution scattering (SAXS) combined with crystallography and computation: defining accurate macromolecular structures, conformations and assemblies in solution," Quarterly Reviews of Biophysics **40**, 191 (2007).
24. E. Malmerberg, C. A. Kerfeld, and P. H. Zwart, "Operational properties of fluctuation X-ray scattering data," IUCrJ **2**, 309 (2015).
25. M. M. Seibert, T. Ekeberg, F. R. N. C. Maia, M. Svenda, J. Andreasson, O. Jonsson, et al., "Single mimivirus particles intercepted and imaged with an X-ray laser," Nature **470**, 78 (2011).
26. S. Kassemeyer, J. Steinbrener, L. Lomb, E. Hartmann, A. Aquila, A. Barty, et al., "Femtosecond free-electron laser x-ray diffraction data sets for algorithm development," Optics express **20**, 4149 (2012).
27. M. F. Hantke, D. Hasse, F. R. N. C. Maia, T. Ekeberg, K. John, M. Svenda, et al., "High-throughput imaging of heterogeneous cell organelles with an X-ray laser," Nature Photonics **8**, 943 (2014).
28. G. van der Schot, M. Svenda, F. R. N. C. Maia, M. Hantke, D. P. DePonte, M. M. Seibert, et al., "Imaging single cells in a beam of live cyanobacteria with an X-ray laser," Nat Commun **6**, 5704 (2015).
29. T. Ekeberg, M. Svenda, C. Abergel, F. R. N. C. Maia, V. Seltzer, J.-M. Claverie, et al., "Three-Dimensional Reconstruction of the Giant Mimivirus Particle with an X-Ray Free-Electron Laser," Physical Review Letters **114**, 098102 (2015).
30. N. D. Loh, C. Y. Hampton, A. V. Martin, D. Starodub, R. G. Sierra, A. Barty, et al., "Fractal morphology, imaging and mass spectrometry of single aerosol particles in flight," Nature **486**, 513 (2012).
31. H. Thomas, A. Helal, K. Hoffmann, N. Kandadai, J. Keto, J. Andreasson, et al., "Explosions of Xenon Clusters in Ultraintense Femtosecond X-Ray Pulses from the LCLS Free Electron Laser," Physical Review Letters **108**, 133401 (2012).
32. L. F. Gomez, K. R. Ferguson, J. P. Cryan, C. Bacellar, R. M. P. Tanyag, C. Jones, et al., "Shapes and vorticities of superfluid helium nanodroplets," Science **345**, 906 (2014).
33. T. C. Taylor, A. Backlund, K. Bjorhall, R. J. Spreitzer, and I. Andersson, "First Crystal Structure of Rubisco from a Green Alga,Chlamydomonas reinhardtii," Journal of Biological Chemistry **276**, 48159 (2001).
34. G. Huldt, A. Szőke, and J. Hajdu, "Diffraction imaging of single particles and biomolecules," Journal of Structural Biology **144**, 219 (2003).
35. N. T. Loh, and V. Elser, "Reconstruction algorithm for single-particle diffraction imaging experiments," Phys Rev E **80**, 026705 (2009).
36. P. Schwander, R. Fung, J. G. N. Phillips, and A. Ourmazd, "Mapping the conformations of biological assemblies," New J Phys **12**, 035007 (2010).
37. F. R. N. C. Maia, T. Ekeberg, N. Tîmneanu, D. van der Spoel, and J. Hajdu, "Structural variability and the incoherent addition of scattered intensities in single-particle diffraction," Physical Review E **80**, 031905 (2009).
38. T. Ekeberg, "Flash Diffractive Imaging in Three Dimensions," (Acta Universitatis Upsaliensis, 2012).
39. P. B. Moore, "How should we think about the ribosome?," Annual review of Biophysics **41**, 1 (2012).
40. J. Frank, *Three-Dimensional Electron Microscopy of Macromolecular Assemblies* (Oxford University Press, New York, 2006).
41. A. Dashti, P. Schwander, R. Langlois, R. Fung, W. Li, A. Hosseinizadeh, et al., "Trajectories of the ribosome as a Brownian nanomachine," Proceedings of the National Academy of Sciences of the United States of America **111**, 17492 (2014).
42. P. Schwander, R. Fung, and A. Ourmazd, "Conformations of macromolecules and their complexes from heterogeneous datasets," Phil. Trans. R. Soc. B **369**, 20130567 (2014).
43. R. Fung, V. Shneerson, D. K. Saldin, and A. Ourmazd, "Structure from fleeting illumination of faint spinning objects in flight," Nat Phys **5**, 64 (2009).
44. H. T. Philipp, K. Ayyer, M. W. Tate, V. Elser, and S. M. Gruner, "Solving structure with sparse, randomly-oriented x-ray data," Optics express **20**, 13129 (2012).

45. Z. Kam, M. H. Koch, and J. Bordas, "Fluctuation x-ray scattering from biological particles in frozen solution by using synchrotron radiation," Proceedings of the National Academy of Sciences of the United States of America **78**, 3559 (1981).
46. P. Wochner, C. Gutt, T. Autenrieth, T. Demmer, V. Bugaev, A. D. Ortiz, et al., "X-ray cross correlation analysis uncovers hidden local symmetries in disordered matter," Proceedings of the National Academy of Sciences of the United States of America **106**, 11511 (2009).
47. R. Su, K. A. Seu, D. Parks, J. J. Kan, E. E. Fullerton, S. Roy, et al., "Emergent rotational symmetries in disordered magnetic domain patterns," Phys Rev Lett **107**, 257204 (2011).
48. G. Chen, M. A. Modestino, B. K. Poon, A. Schirotzek, S. Marchesini, R. A. Segalman, et al., "Structure determination of Pt-coated Au dumbbells via fluctuation X-ray scattering," Journal of synchrotron radiation **19**, 695 (2012).
49. D. K. Saldin, V. L. Shneerson, D. Starodub, and J. C. Spence, "Reconstruction from a single diffraction pattern of azimuthally projected electron density of molecules aligned parallel to a single axis," Acta crystallographica. Section A, Foundations of crystallography **66**, 32 (2010).
50. H. Liu, B. K. Poon, D. K. Saldin, J. C. Spence, and P. H. Zwart, "Three-dimensional single-particle imaging using angular correlations from X-ray laser data," Acta crystallographica. Section A, Foundations of crystallography **69**, 365 (2013).
51. D. Mendez, T. J. Lane, J. Sung, J. Sellberg, C. Levard, H. Watkins, et al., "Observation of correlated X-ray scattering at atomic resolution," Philosophical transactions of the Royal Society of London. Series B, Biological sciences **369**, 20130315 (2014).
52. D. Starodub, A. Aquila, S. Bajt, M. Barthelmess, A. Barty, C. Bostedt, et al., "Single-particle structure determination by correlations of snapshot X-ray diffraction patterns," Nat Commun **3**, 1276 (2012).
53. Z. Kam, "Determination of Macromolecular Structure in Solution by Spatial Correlation of Scattering Fluctuations," Macromolecules **10**, 927 (1977).
54. D. K. Saldin, H. C. Poon, M. J. Bogan, S. Marchesini, D. A. Shapiro, R. A. Kirian, et al., "New light on disordered ensembles: ab initio structure determination of one particle from scattering fluctuations of many copies," Phys Rev Lett **106**, 115501 (2011).
55. D. K. Saldin, H. C. Poon, P. Schwander, M. Uddin, and M. Schmidt, "Reconstructing an icosahedral virus from single-particle diffraction experiments," Opt Express **19**, 17318 (2011).
56. Donatelli, Zwart, and Sethian, "Iterative phasing for fluctuation scattering data," PNAS, submitted (2015).
57. V. Elser, "Strategies for processing diffraction data from randomly oriented particles," Ultramicroscopy **111**, 788 (2011).
58. K. Pande, P. Schwander, M. Schmidt, and D. K. Saldin, "Deducing fast electron density changes in randomly orientated uncrystallized biomolecules in a pump-probe experiment," Philosophical transactions of the Royal Society of London. Series B, Biological sciences **369**, 20130332 (2014).
59. G. L. Hura, H. Budworth, K. N. Dyer, R. P. Rambo, M. Hammel, C. T. McMurray, et al., "Comprehensive macromolecular conformations mapped by quantitative SAXS analyses," Nature methods **10**, 453 (2013).
60. H. Ogata, K. Nishikawa, and W. Lubitz, "Hydrogens detected by subatomic resolution protein crystallography in a [NiFe] hydrogenase," Nature, 571 (2015).
61. T. Spatzal, M. Aksoyoglu, L. Zhang, S. L. Andrade, E. Schleicher, S. Weber, et al., "Evidence for interstitial carbon in nitrogenase FeMo cofactor," Science **334**, 940 (2011).
62. M. Suga, F. Akita, K. Hirata, G. Ueno, H. Murakami, Y. Nakajima, et al., "Native structure of photosystem II at 1.95 A resolution viewed by femtosecond X-ray pulses," Nature **517**, 99 (2015).
63. K. Hirata, K. Shinzawa-Itoh, N. Yano, S. Takemura, K. Kato, M. Hatanaka, et al., "Determination of damage-free crystal structure of an X-ray-sensitive protein using an XFEL," Nature methods **11**, 734 (2014).
64. J. Yano, J. Kern, K. D. Irrgang, M. J. Latimer, U. Bergmann, P. Glatzel, et al., "X-ray damage to the Mn_4Ca complex in single crystals of photosystem II: a case study for metalloprotein crystallography," Proceedings of the National Academy of Sciences of the United States of America **102**, 12047 (2005).
65. K. G. Sigfridsson, P. Chernev, N. Leidel, A. Popovic-Bijelic, A. Graslund, and M. Haumann, "Rapid X-ray photoreduction of dimetal-oxygen cofactors in ribonucleotide reductase," The Journal of biological chemistry **288**, 9648 (2013).

66. W. Zhang, R. Alonso-Mori, U. Bergmann, C. Bressler, M. Chollet, A. Galler, et al., "Tracking excited-state charge and spin dynamics in iron coordination complexes," Nature **509**, 345 (2014).
67. H. T. Lemke, C. Bressler, L. X. Chen, D. M. Fritz, K. J. Gaffney, A. Galler, et al., "Femtosecond X-ray absorption spectroscopy at a hard X-ray free electron laser: application to spin crossover dynamics," The journal of physical chemistry. A **117**, 735 (2013).
68. R. Alonso-Mori, J. Kern, R. J. Gildea, D. Sokaras, T. C. Weng, B. Lassalle-Kaiser, et al., "Energy-dispersive X-ray emission spectroscopy using an X-ray free-electron laser in a shot-by-shot mode," Proceedings of the National Academy of Sciences of the United States of America **109**, 19103 (2012).
69. R. Mitzner, J. Rehanek, J. Kern, S. Gul, J. Hattne, T. Taguchi, et al., "L-Edge X-ray absorption spectroscopy of dilute systems relevant to metalloproteins using an X-ray Free-Electron Laser," The journal of physical chemistry letters **4**, 3641 (2013).
70. P. Wernet, K. Kunnus, I. Josefsson, I. Rajkovic, W. Quevedo, M. Beye, et al., "Orbital-specific mapping of the ligand exchange dynamics of $Fe(CO)_5$ in solution," Nature (2015).
71. J. Kern, R. Alonso-Mori, R. Tran, J. Hattne, R. J. Gildea, N. Echols, et al., "Simultaneous femtosecond X-ray spectroscopy and diffraction of photosystem II at room temperature," Science **340**, 491 (2013).
72. K. Nass, L. Foucar, T. R. Barends, E. Hartmann, S. Botha, R. L. Shoeman, et al., "Indications of radiation damage in ferredoxin microcrystals using high-intensity X-FEL beams," Journal of synchrotron radiation **22**, 225 (2015).
73. H. N. Chapman, C. Caleman, and N. Timneanu, "Diffraction before destruction," Philosophical transactions of the Royal Society of London. Series B, Biological sciences **369**, 20130313 (2014).
74. S. Franzen, L. Kiger, C. Poyart, and J. L. Martin, "Heme photolysis occurs by ultrafast excited state metal-to-ring charge transfer," Biophys J. **80**, 2372 (2001).
75. M. Suga, F. Akita, K. Hirata, G. Ueno, H. Murakami, Y. Nakajima, et al., "Native structure of photosystem II at 1.95 Å resolution viewed by femtosecond X-ray pulses," Nature **517**, 99 (2015).
76. J. Yano, and V. Yachandra, "Mn4Ca cluster in photosynthesis: where and how water is oxidized to dioxygen," Chem Rev **114**, 4175 (2014).
77. N. Cox, M. Retegan, F. Neese, D. A. Pantazis, A. Boussac, and W. Lubitz, "Photosynthesis. Electronic structure of the oxygen-evolving complex in photosystem II prior to O-O bond formation," Science **345**, 804 (2014).
78. P. E. Siegbahn, "Water oxidation mechanism in photosystem II, including oxidations, proton release pathways, O-O bond formation and O2 release," Biochimica et biophysica acta **1827**, 1003 (2013).
79. M. J. Bogan, "X-ray free electron lasers motivate bioanalytical characterization of protein nanocrystals: serial femtosecond crystallography," Analytical chemistry **85**, 3464 (2013).
80. U. Weierstall, "Liquid sample delivery techniques for serial femtosecond crystallography," Philosophical transactions of the Royal Society of London. Series B, Biological sciences **369**, 20130337 (2014).

3.0 New Experimental Approaches

3.1 Multidimensional X-ray Spectroscopy

Over the past several decades, 2nd and 3rd generation synchrotron sources have enabled the development of a wide range of incisive *linear* probes of the electronic, atomic, and chemical structure of matter. Examples include X-ray emission spectroscopy, X-ray absorption spectroscopy, and inelastic X-ray scattering, to name just a few. As a MHz X-ray laser, the unique capabilities of LCLS-II will open the entirely new fields of *nonlinear* X-ray science and multi-dimensional X-ray spectroscopy.

In general, multi-dimensional X-ray spectroscopy incorporates time-ordered sequences of X-ray pulses to generate a signal that is a function of multiple time delays and/or photon energies. These are nonlinear coherent wave mixing techniques in which X-ray pulses are used as both a pump, to prepare specific near-equilibrium states of matter, and as a probe of these evolving states. Where there are numerous variations of these multidimensional methods, they share in common the attempt to view ***coherent evolution***, which ordinary linear spectroscopy can never see. These new tools rely on simultaneous combinations of: high peak power, high average power (high repetition rate), spatial coherence, temporal coherence, and tunability which is only available from a facility like LCLS-II.

Multi-Dimensional Spectroscopy: From NMR (radio waves) to Infrared to Visible to X-rays

Nuclear magnetic resonance (NMR), as an analogous technique, illustrates the tremendous potential impact of multi-dimensional X-ray spectroscopy. NMR incorporates sequences of radio-frequency (RF) pulses to generate a two-dimensional signal-map (based on the Fourier transform of the time intervals between pulses) that is a fingerprint of specific chemical structures, and their relationship within a molecular complex. Over the past decade, multi-dimensional spectroscopy (enabled by ultrafast laser sources) has been extended to the infrared[1-3] (to provide a fingerprint map of the coupling between different vibrational modes in a molecule) and to the visible regime[3-5] (to map the dynamic quantum coupling between electronic states). These techniques are invaluable for following quantum coherences and charge relaxation between electronic states in systems ranging from chlorophyll (responsible for light harvesting in photosynthesis) to excitonic states in semiconductors (for a review, see ref. 3).

Figure 78 illustrates a multi-dimensional electronic spectroscopy measurement of the bacteriochlorophyll photosynthetic reaction center[5]. This light-harvesting complex consists of seven coherently-coupled exciton states. The multi-dimensional spectroscopy map (Figure 78, lower right) shows the coupling between these exciton states – a snapshot of the coherent and incoherent transfer of charge population between the seven states at a delay of 1,000 fs delay following the initial excitation.

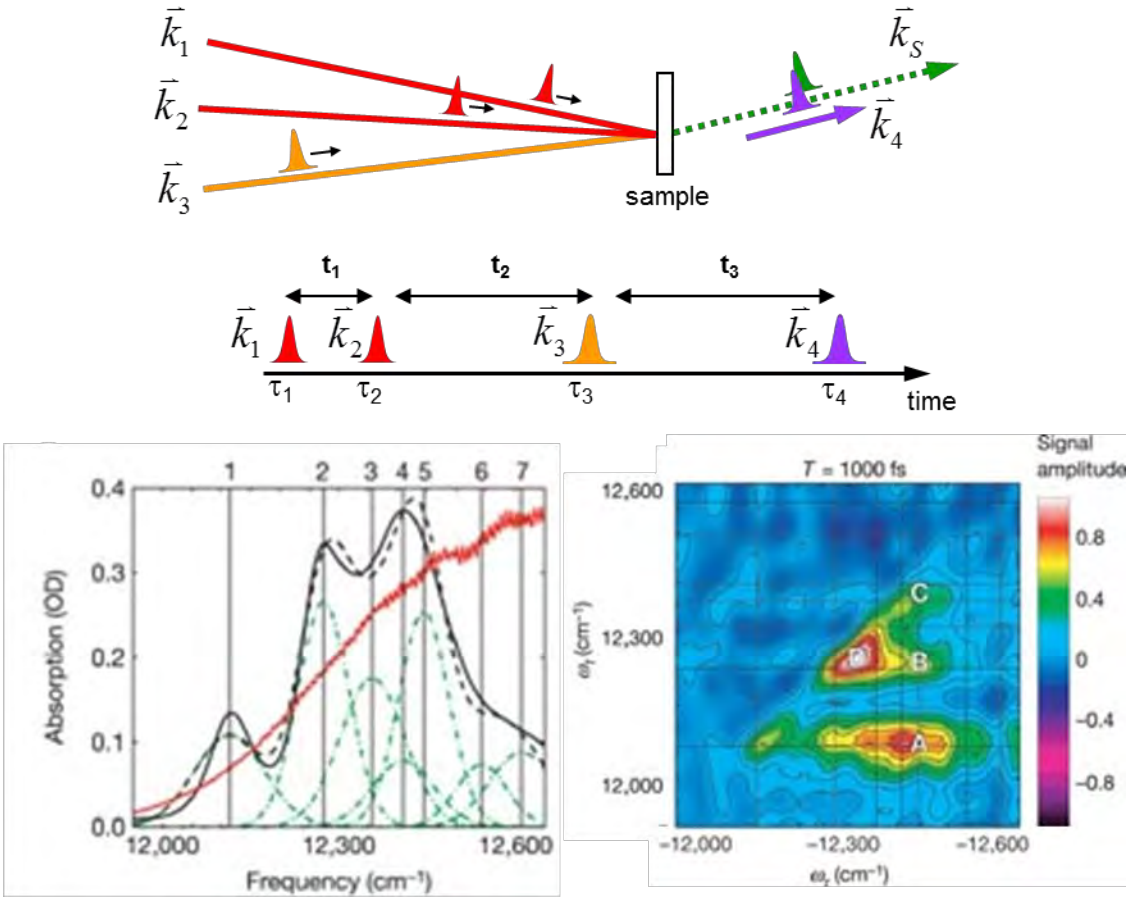

Figure 78. Top: Generalized schematic of multi-dimensional electronic spectroscopy using a four-wave mixing geometry with a three-pulse sequence (k_1, k_2, k_3). The signal of interest is the nonlinear polarization $P^{(3)}{}_S$ (k_S=-k_1+k_2+k_3) — shown here resolved in phase and amplitude via heterodyne detection with a local-oscillator field k_4. Bottom: 2D electronic spectra snapshot (at 1000 fs delay, t_{13}) of bacteriochlorophyll photosynthetic reaction center[5] which consists of seven coherently-coupled exciton states (lower right). The two (energy/frequency) axes of the 2D spectrogram are the Fourier variables corresponding to the delay t_{12}, and the delay between k_3 and E_{LO}.

X-ray Multi-Dimensional Spectroscopy

In the X-ray region, the tremendous promise of multi-dimensional spectroscopy lies in the capability to follow coherent charge flow and energy relaxation on fundamental (attosecond to femtosecond) time scales with access to the full range of valence states (unrestricted by dipole selection rules). Importantly, the element specificity provided by X-rays (tuned to core-level absorptions) will enable us for the first time to follow charge and energy flow between constituent atoms in materials. These essential capabilities are not attainable using infrared or visible laser pulses, and will provide critical insight to correlated electron systems and molecular complexes with strong coupling between electronic and nuclear dynamics. Figure 79 illustrates two multi-dimensional X-ray spectroscopy schemes: stimulated X-ray Raman spectroscopy, and core-hole correlation spectroscopy.

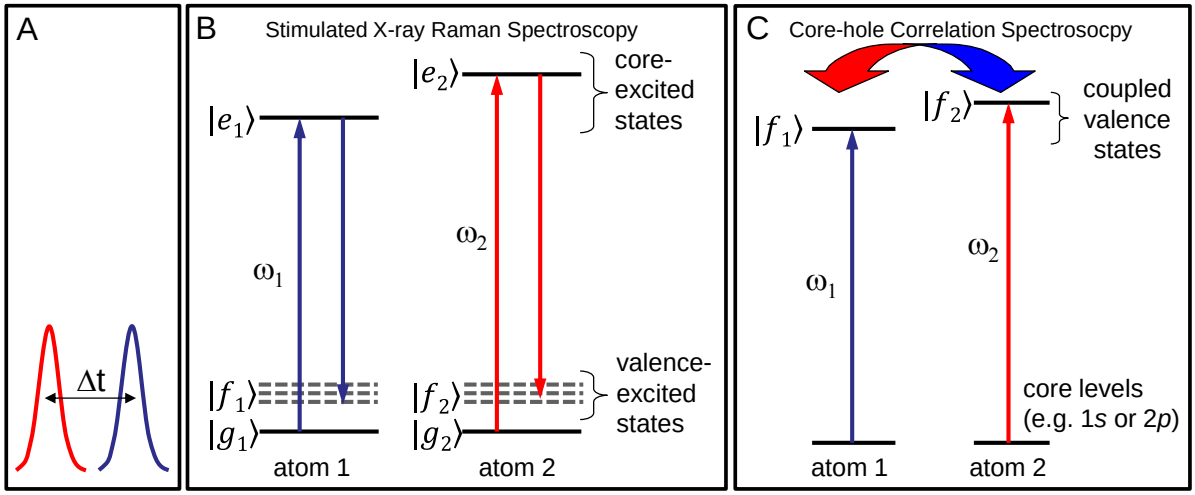

Figure 79. Multi-dimensional spectroscopy schemes using sequences of two-color pulses (A). (B) Illustrates stimulated or Stimulated X-ray Raman Spectroscopy (SXRS) in which localized valence excitations $<f_1|g_1>$ and $<f_2|g_2>$ are created and probed via resonant Raman processes at specific atoms. This approach creates a local valence excitation, and enables element-specific probing of charge flow. (C) Illustration of core-hole correlation spectroscopy in which resonant core-level excitation of two atoms is used to probe the coupling between their respective valence states f_1 and f_2.

Multi-Dimensional Spectroscopy – Stimulated X-ray Raman

Figure 79 presents an example and outlines the theoretical basis for coherent or Stimulated X-ray Raman Spectroscopy (SXRS)[6]. Whereas conventional optical Raman spectroscopy techniques exploit visible or infra-red laser fields to probe lower-frequency vibrational resonances in matter, SXRS uses X-rays to probe valence excitations in matter (Figure 79b). One may consider SXRS as a powerful extension (stimulated version) of spontaneous X-ray Raman processes such a RIXS (as discussed in sections 2.1 and 2.2).

The power of this multi-dimensional technique is that it creates a localized valence excitation, or coherent electronic wavepacket, via a resonant stimulated Raman scattering process originating from the core level of a specific atom (see Figure 79b). A probe pulse in resonance with a second atom can then follow the time evolution of the wavepacket, and the flow of valence charge between different atomic sites, via various interaction mechanisms, for example: X-ray absorption spectroscopy, photoelectron spectroscopy, or via a second SXRS process (as illustrated in Figure 79b). The potential impact of this new approach is illustrated in Section 2.1, Figure 2 which shows recent SXRS simulations of ultrafast energy transfer dynamics in a Zn/Ni porphyrin heterodimer which are of interest as model components in artificial light harvesting and photosynthetic complexes.[7]

In a multi-dimensional implementation, the initial excitation is created by a pulse-pair, and a third pulse (in a phase-matched geometry) reads out the scattered Raman signal. Thus, SXRS measures a third-order, $\chi^{(3)}$, four-wave mixing process whereby a sequence of three incident pulses (three fields): $E_n(k_n,\omega_n)|_{n=1,2,3}$, generate a stimulated signal, e.g., $E_{sig}(-\omega_1+\omega_2+\omega_3)$, in the momentum-matched direction, $k_{sig}=-k_1+k_2+k_3$. The Fourier transform of the signal with respect to the time delays of the pulses creates a two-dimensional map of the valence electronic states and their evolution. Importantly, since the final state is not core-excited, but only valence-excited, multidimensional signal-maps can be measured over much longer time scales than are possible with core-hole correlation techniques.

Multi-Dimensional Spectroscopy - X-ray Core-hole Correlation

A complement to core-hole correlation spectroscopy is core-hole correlation spectroscopy (Figure 79c)[3, 8] – essentially the equivalent of two-dimensional electronic spectroscopy the X-ray regime. It exploits nonlinear interactions with coherent X-ray pulses to probe correlation effects between pairs of valence electrons excited at different atomic sites in a molecule.

Figure 80 presents an example in which core-hole correlation spectroscopy probes the quantum coupling between nitrogen- and oxygen-associated valence states in different isomers of aminophenol. Here, two pulses probe the aminophenol molecule, one centered at 400 eV (ω_N) and the other at 535 eV (ω_O), in resonance with the 1*s* core excitations in N and O atoms, respectively. In the coherent four-wave mixing process, the target molecule interacts with three X-ray pulses separated by times t_{12} and t_{13} and emits a fourth pulse with temporal profile $S(t, t_{13}, t_{12})$. The two-dimensional Fourier transform of this signal with respect to t_{12} and t_{13} yields a two-dimensional electronic spectrum in frequency space. Off-diagonal features in this 2D spectrum are present only when there is correlation between the two excited valence electrons on the N and O atoms; no signal should be seen in the Hartree-Fock limit of independent orbitals. Calculations show that the extent of this correlation depends not only on molecular structure (i.e., it differs in ortho- and para- aminophenol, but also on the nature of the molecular orbitals excited within the energy envelopes (~10 eV) of ω_N and ω_O[8]. An important criterion for core-level correlation spectroscopy is that the X-ray pulse durations must be faster than the Auger decay time (~5 fs[9]), since Auger decay suppresses the correlation signal of interest.

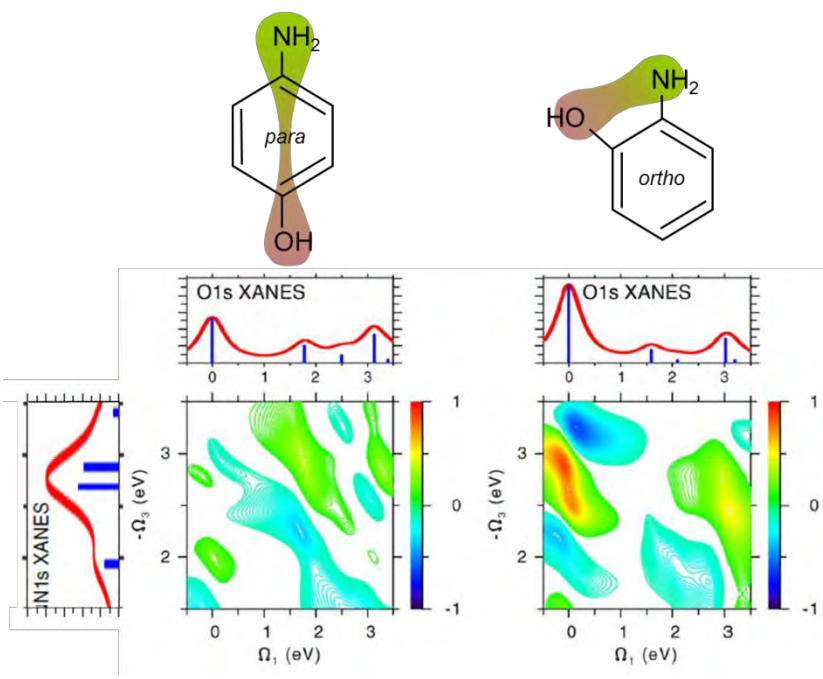

Figure 80. Valence and core-excited states of aminophenols of *para* and *ortho* isomers of aminophenol, and the predicted corresponding 2D X-ray core-hole correlation maps. The off-diagonal cross-peaks (right map) indicate the quantum mixing between nitrogen- and oxygen-associated valence states (mixing of the N-1*s* and O-1*s* XANES spectra). Such quantum effects are absent in the *para* isomer due to the separation of the O and N atoms. (from ref. 8).

Multi-Dimensional Spectroscopy – LCLS-II

Following is a broader description of some of the compelling advantages of investigating valence electron dynamics and correlated phenomena via multi-dimensional X-ray spectroscopy:

- ***Temporal (or phase) information***—unavailable from conventional RIXS measurements, which probe the spectral density-density correlation function $S(\boldsymbol{q},\boldsymbol{\omega})$ in the frequency domain but without phase information. Powerful capabilities of time/phase measurements include: (1) distinguishing different contributions to the density-correlation spectral distribution, e.g. homogeneous versus inhomogeneous

distributions of correlated states, and (2) following emergent properties as they evolve from perturbative non-equilibrium conditions created by tailored electronic or vibrational excitations ranging from the THz to the X-ray range (e.g., modulation or manipulation of correlated states via coherent vibrational modes or charge-transfer excitations).

- ***Element and chemical state specificity***—essential for understanding the correlation between valence states associated with particular atomic or molecular orbitals. For the first time it will be possible to directly follow the coherent flow of valence charge between different atomic sites in time, energy, and space. This ability will be extremely powerful for understanding mixed-valence molecular complexes, dilute-magnetic semiconductors, multiferroics, charge-transfer complexes, cuprates (electronic states coupled to Cu orbitals versus O orbitals), and much more. Although conventional RIXS is element specific, it is not able to distinguish coherences across different atoms.

- ***Symmetry selectivity***—sensitivity to specific valence states (e.g., 3*d* versus 2*p*) and the capability to distinguish spin and orbital moments via powerful soft X-ray dichroism effects.

- ***Access to the entire manifold of valence momentum sates*** — since the soft X-ray excitation wavelength is comparable to the unit-cell/molecular size (*k* vector large compared to the Brillouin zone), the strict dipole selection rules that mediate optical transitions are substantially relaxed. The momentum space spanning the entire Brillouin zone can be sampled with exquisite resolution. Soft X-ray transitions from core levels directly probe important *d-d* excitations that are optically forbidden.

- ***Quantum selectivity***—pulse sequences and momentum matching allow one to effectively isolate specific terms of the contributing Liouville-space pathways that comprise the theoretical description of coupled quantum systems based on a time-dependent perturbation approach. This selectivity makes it possible to distinguish for example coherent charge coupling from incoherent charge transfer, electronic relaxation from excited-state absorption etc. In combination with element specificity and ultrafast time resolution, this capability will constitute a major breakthrough for understanding correlated systems.

Multi-dimensional X-ray spectroscopy and nonlinear X-ray science will be hallmarks of LCLS-II as they require capabilities that are not available from any other X-ray source. High peak-power X-ray pulses are just one of several essential requirements. Equally important is the ability to *control* the degree of X-ray nonlinearity while resolving small signals with high fidelity. High repetition rate is absolutely essential to achieve this in order to avoid disrupting the electronic states (or other sample attributes) that are being investigated. An important benchmark to recognize is that the scientific impact of multi-dimensional laser techniques was realized only after the development of multi-kHz and MHz ultrafast laser sources. These lasers combined both high peak power and high average power to enable extremely sensitivity measurements of controlled near-equilibrium interactions of laser pulse sequences with matter.

Feasibility

Recent theoretical predictions and experimental results indicate that stimulated X-ray emission (and related nonlinear X-ray processes) are readily achievable with X-ray lasers. X-ray absorption cross-sections provide a starting point for rough feasibility estimates for nonlinear X-ray processes. Typical absorption cross-sections are ~10^{-18} cm^{-2} per atom (e.g. for 1*s* transitions in low-Z elements and 2*p* transitions in first-row transition metals). Thus, the "threshold" for nonlinear interaction is ~10^{17}-10^{18} photons/cm^{-2} in a pulse duration on the order of the core-hole lifetime (~5 fs[9]). This corresponds to ~10^{9}-10^{10} photons/pulse in a 1 μm focus (~10^{16} W/cm^{2} at 500 eV). Estimates based on X-ray nonlinear susceptibilities lead to similar conclusions for the required X-ray peak power density.[6, 8] Note that modern nonlinear optical spectroscopy experiments typically operate in the perturbative regime, ~0.1 photons per cross-section, in order to avoid distortion of the spectral signal of interest from saturation and other

unwanted effects. Thus the scientific impact of modern nonlinear and multidimensional optical spectroscopies relies substantially on high laser repetition rates to compensate low signal levels and enable experiments in the perturbative regime. LCLS-II will be the first laser to provide this capability in the X-ray regime.

Beyond these initial estimates, Haxton and McCurdy have applied multiconfiguration time-dependent Hartree-Fock methods to model a simulated Raman process in NO molecules with two pulses at 393 eV and 403 eV (3×10^{17} W/cm^2 and 5×10^{16} W/cm^2 respectively).[10] In this ultrafast two-color stimulated Raman process (via auto-ionizing states) a population transfer of ~41% into valence excited states of NO is predicted, with ~30% ionization of the initial ground state, as shown in Figure 81. In this strongly nonlinear regime, SXRS effectively competes with ionization and other nonlinear effects.

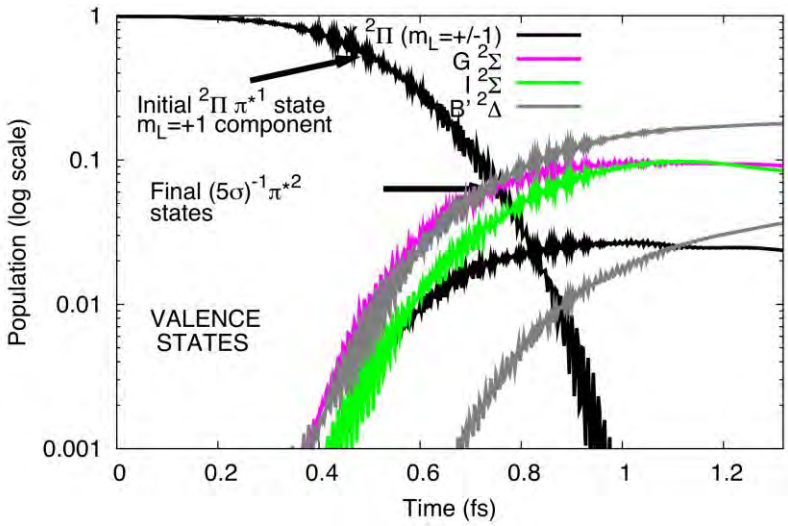

Figure 81. Simulated 2-color X-ray Raman simulation in NO molecules via multiconfiguration time-dependent Hartree-Fock methods. Population transfer of ~41% to valence states is observed, with ~30% ionization of the initial ground-state population.[10]

Predictions of SXRS in atomic sodium by Miyabe and Bucksbaum[11] using perturbation theory and time-dependent non-perturbative approaches show similar results, with a 10% saturation predicted at 5×10^{15} W/cm^2, and significant Rabi oscillation effects appearing for intensities $>2\times10^{16}$ W/cm^2. Since the coupled valence states in sodium are separated by ~3 eV, the Raman transition probability is quite sensitive to pulse bandwidth in these calculations. Simulations of resonant stimulated X-ray scattering at the Co L_3-edge by Stöhr and Scherz,[12] using the Bloch-Rabi formalism, predict observable effects at ~10^{13} W/cm^2. At this level, the stimulating X-ray field is comparable to the zero-point field responsible for spontaneous scattering. Finally, recent experimental studies at the Si L-edge (115 eV) show clear evidence of stimulated emission at peak power densities of ~5×10^{12} W/cm^2, as illustrated in Figure 82.[13] The stronger effects observed in Si are attributable in part to the larger absorption cross-section and longer core-hole lifetime, ~19 fs.

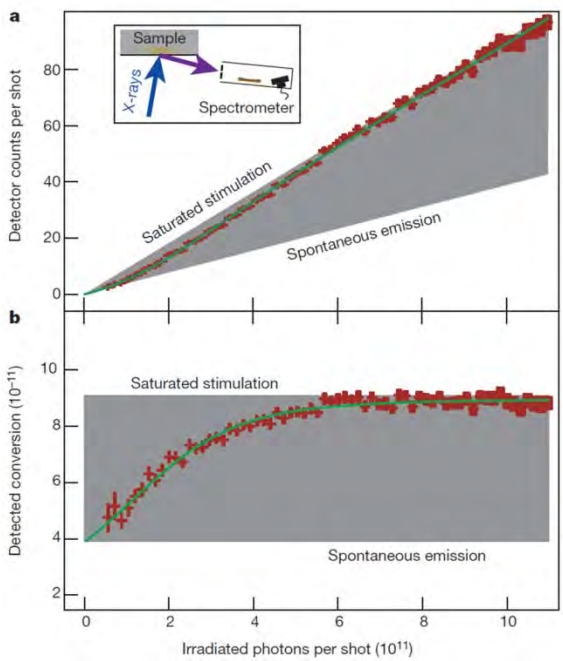

Figure 82. Stimulated non-resonant X-ray emission at 115 eV from the Si L_3-edge. The grey area identifies the region between spontaneous emission and saturate stimulated emission for the experimental geometry (inset). Red symbols show (a) the measured counts/shot as a function of incident photons/pulse, and (b) measured counts/shot normalized by the incident photons/pulse.[13]

References:

1. J. D. Hybl, A. W. Albrecht, S. M. G. Faeder, and D. M. Jonas, "Two-Dimensional Electronic Spectroscopy," Chem. Phys. Lett. **297**, 307 (1998).
2. M. C. Asplund, M. T. Zanni, and R. M. Hochstrasser, "Two-dimensional infrared spectroscopy of peptides by phase-controlled femtosecond vibrational photon echoes," PNAS **97**, 8219 (2000).
3. S. Mukamel, D. Abramavicius, L. Yang, W. Zhuang, I. V. Schweigert, and D. Voronine, "Coherent Multidimensional Optical Probes for Electron Correlations and Exciton Dynamics: From NMR to X-rays," Accounts of Chem. Res. **42**, 553 (2009).
4. X. Li, T. Zhang, C. N. Borca, and S. T. Cundiff, "Many-body interactions in semiconductors probed by optical two-dimensional fourier transform spectroscopy," Phys. Rev. Lett. **96**, 057406 (2006).
5. T. Brixner, J. Stenger, H. M. Vaswani, M. Cho, R. E. Blankenship, and G. R. Fleming, "Two-dimensional spectroscopy of electronic couplings in photosynthesis," **434**, 625 (2005).
6. S. Tanaka, and S. Mukamel, "Coherent X-ray Raman spectroscopy: A nonlinear local probe for electronic excitations," Phys. Rev. Lett. **89**, 043001 (2002).
7. J. D. Biggs, Y. Zhang, D. Healion, and S. Mukamel, "Watching energy transfer in metalloporphyrin heterodimers using stimulated X-ray Raman spectroscopy," Proceedings of the National Academy of Sciences **110**, 15597 (2013).
8. I. V. Schweigert, and S. Mukamel, "Coherent ultrafast core-hole correlation spectroscopy: X-Ray analogues of multidimensional NMR," Phys. Rev. Lett. **99**, 163001 (2007).
9. M. O. Krause, and J. H. Oliver, "Natural Widths of Atomic K and L Levels, Kα X-Ray Lines and Several KLL Auger Lines," J. Phys. Chem. Ref. Data **8**, 329 (1979).
10. D. J. Haxton, and C. W. McCurdy, "Ultrafast Population Transfer to Excited Valence Levels of a Molecule Driven by X-ray Pulses," submitted for publication (2014).
11. S. Miyabe, and P. Bucksbaum, "Transient Impulsive Giant Electronic Raman Redistribution," arXiv:1410.3161 (2014).
12. J. Stöhr, and A. Scherz, "Creation of X-Ray Transparency of Matter by Stimulated Elastic Forward Scattering," submitted (2015).
13. M. Beye, S. Schreck, F. Sorgenfrei, C. Trabant, N. Pontius, C. Schuszler-Langeheine, et al., "Stimulated X-ray emission for materials science," Nature **501**, 191 (2013).

3.2 Heterogeneous Ensembles: Fluctuations, Structure and Function

Synopsis

X-ray scattering is a well-utilized experimental technique in material, energy and mesoscale sciences that provides fundamental insights into the structure and organization of matter, from micrometer down to sub-nanometer-length scales. A fundamental assumption in many experiments and subsequent data analyses is that the sample is statistically isotropic. The availability of state-of-the-art X-ray sources and detectors redefine the limit of what can be considered isotropic. Fluctuation scattering provides the underlying theoretical and practical framework for scattering experiments from such samples. Although current and future X-ray sources will allow the acquisition of this type of scattering data in a routine fashion, there is a lack in understanding of both the theoretical and practical aspects of this method, preventing the optimal utilization of current X-ray sources.

Introduction

In the design of materials or engineered nanoparticles, knowledge of the structure of matter provides important clues to understanding the performance of the desired function and suggests directions about how to engineer further improvements by linking structure to property.[1-4] Small and Wide Angle X-ray Scattering (SAXS/WAXS) has become a standard technique for the characterization of materials.[5] Materials such as solutions, disordered polymers or other materials without long-range order have X-ray scattering patterns that are typically angularly isotropic.[6] The dependence of the mean intensity to the scattering angle is directly related to the average shape, local and long-range order of the material under investigation, as seen in Figure 83.

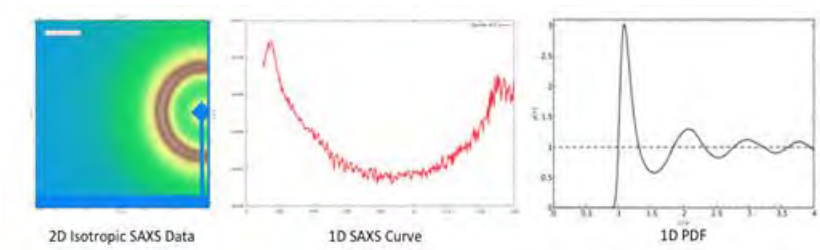

Figure 83: Traditional X-ray scattering analysis reduces a two-dimensional isotropic X-ray scattering pattern to a one-dimensional curve depicting the mean intensity versus resolution. The information contained in the data can be expressed as the radial pair distance distribution, expressing the distribution of interatomic distances in the material.

Scattering analyses of bulk materials provides researchers with a comprehensive technique that allows them to characterize the structure of matter in terms of correlation lengths in a material[7] often associated with specific structural features such as lamella, spherical or cylindrical morphologies. The analysis of single particle data is similar and provides an estimate of the radius of gyration, a low-resolution shape of the particle, or anisotropy and polydispersity of the scattering species[7]. The theoretical foundations of the analyses of X-ray scattering can be traced back to fundamental work performed by Debye,[8] Kratky and Porod,[9] Guinier & Fournet[10] and others. A fundamental assumption in the analyses of scattering data and derivation of X-ray scattering theory is concisely summarized by Porod:[7]

"The system is statistically isotropic"

The consequence of this assumption is that X-ray scattering data of statistically isotropic materials can be described by a single curve depicting the dependency between mean scattered intensity and the scattering angle. A SAXS curve I(q) can be described by the product of two components, namely a *structure factor* S(q) and a *form factor* $I_0(q)$. Whereas the form factor $I_0(q)$ captures the scattering behavior of the isolated particles, the structure factor describes the effects of the packing of the objects. In the case of dilute systems, the structure factor is gas-like and equal to 1 and the scattering curve depends fully on the shape of the particle via the form factor $I_0(q)$.

Under the assumption of a statistically isotropic material, the expression of the intensity, as stated above, can be described as the 0th order Hankel transform[11, 12] of the radial distribution function γ(r):

$$I(q) \propto \int_0^\infty \gamma(r) r^2 j_0(q,r)\, dr \tag{1}$$

where $j_0(q, r)$ is a spherical Bessel function of order 0. The radial distribution function provides an average overview of the surrounding of each scattering element. Because of the assumption of an isotropic system, this distribution depends on a radius only.

In the absence of additional information, apart from an experimental SAXS curve, the only real-space information that can be obtained from the SAXS curve of a statistically isotropic material is the one-dimensional radial distribution function γ(r). This function γ(r) can be obtained from the experimental data via an inverse Hankel transform and is practically accomplished via minimizing a trial distribution γ(r) such that its Hankel transform fits the experimental data.[13] Only when additional prior information is used to supplement the SAXS data, such as the notion of topologically connected scattering density or a basic idea of the shape or symmetry of the particle or material under investigation, additional higher-dimensional structural parameters can be derived. In the case of scattering from isolated, mono-disperse particles, for instance, restraints on the topological connectivity of the scattering mass can result in reasonable 3D reconstructions of the particles at low resolution.[14, 15]

The main success of X-ray scattering methods in the analyses of materials, particles and fluids stems from the fact that the experiment is relatively straightforward, providing a wide variety of research communities with the basic tools required to probe the structural and dynamical properties of their samples. In spite of the success of SAXS/WAXS, the information content in one-dimensional scattering data severely limits the amount of structural details that can reliably be extracted from experimental scattering curves. The availability of additional experimental data will allow one to probe different, more detailed spatial characteristics of materials and provide the research community with structural information with a higher degree of confidence than can be obtained with traditional scattering methods.

New Opportunities

The advent of ultra bright coherent X-ray sources, fast detectors, and high-performance computing opens up new avenues in X-ray scattering of materials. Specifically, ultra short femtosecond pulses from the LCLS and proposed LCLS-II redefine which type of materials can, from a scattering point of view, be considered to be statistically isotropic. In a traditional scattering experiment, with long exposure times and a large beam size, localized structural features resulting in diffraction anisotropy are buried in the noise of data. By reducing the beam size, these localized structural irregularities become more prominent in the scattering patterns. Furthermore, the ability to record scattering patterns at high-repetition rates allows researchers to collect a large number of scattering patterns, allowing one to overcome inherent signal to noise challenges.

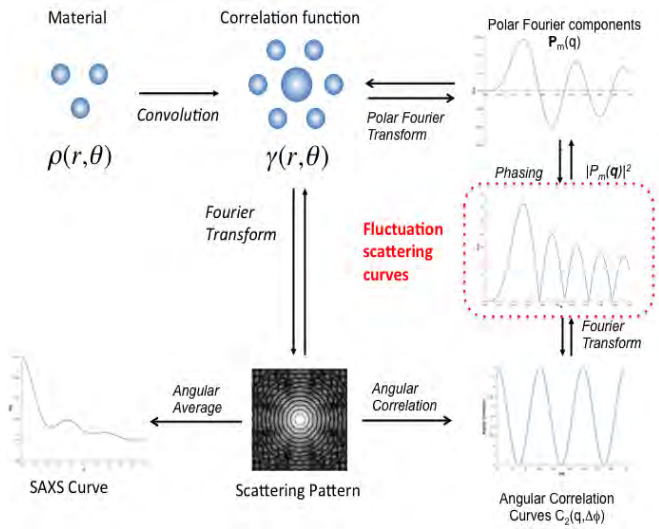

Figure 84: Fluctuation scattering curves of a 2D system are the squared amplitudes of a Polar Fourier Transform (PFT) of the 2D autocorrelation function $\gamma(r,\theta)$ of the material under investigation.

Under experimental conditions readily available at an FEL, a small focal spot, a coherence length that exceeds the length scale of interest and the ability to take exposures below rotational diffusion times, a number of experimental systems show signs of angular anisotropy in the scattering patterns.[3, 16-18] The angular anisotropy in scattering patterns of disordered systems can be detected by computing angular correlations of the scattering data,[19, 20] revealing average rotational symmetries in reciprocal space. Due to the presence of multiple scattering species in the beam and the presence of counting noise, a large number of images are required to guarantee statistical significance of the data.[17] This experimental technique, first conceived by Kam[20, 21] is known as fluctuation scattering.

Fluctuation scattering extends small and wide-angle scattering

To understand the nature of the data obtained from a fluctuation scattering experiment, it is instructive to consider the case of a two-dimensional scattering system, such a nanoparticles randomly oriented in the plane. Basic scattering theory shows[22] that the diffraction pattern of a 2D system is proportional to the Fourier Transform of the 2D-autocorrelation function $\gamma(r,\theta)$ of the sample. The angular average of this scattering pattern is equal to a traditional SAXS curve. If instead of a "standard" Fourier Transform in Cartesian coordinates, a Fourier transform in polar coordinates (a *Polar Fourier Transform*[11]) of the real-space autocorrelation function is performed, Polar Fourier expansion coefficients $P_l(q)$ are obtained.[11, 12] The square of the amplitudes of these complex expansion $|P_l(\boldsymbol{q})|^2$ coefficients comprises a fluctuation scattering data set, as seen in Figure 84. Experimentally, these squared amplitudes of the polar Fourier expansion coefficients are accessible by computing the average angular autocorrelation function $C_2(\boldsymbol{q},\Delta\phi)$[6] and decomposing it in orthogonal functions.

Although an overlap with traditional X-ray scattering is present, the practical difference between SAXS/WAXS and fluctuation scattering is very significant. Not only does fluctuation scattering require a radically different approach to data acquisition and analyses as compared to standard X-ray scattering, the resulting data provides insights in the average anisotropic distribution of scattering matter in disordered systems. The fundamental differences between X-ray scattering and fluctuation scattering demand the development of new approaches rather than mere incremental improvements of existing methods. A key difference between SAXS and FXS data collection is the number of images required. Whereas a complete SAXS dataset will typically be obtained in less than five exposures, a complete FXS dataset requires significantly more shots, ranging from 50 to more than 10,000 images, depending on the system. Given the availability of fast detectors and bright X-ray beams, these measurements can be performed relatively quickly.

The increased demand to understand materials at various length scales beyond the isotropic assumption can be fulfilled by the capabilities of the LCLS-II. The successful deployment of this method will have a large impact on a wide variety of scientific disciplines, as it will allow for a more thorough characterization of the samples under investigation, ultimately leading to new and improved materials that can play a pivotal role in addressing the nation's energy needs.

Current uses of fluctuation scattering data

The use of experimental angular correlations in the analyses of scattering data is currently limited to a few studies summarized below:

- In 1981, Kam, Koch and Bordas[21] show evidence of angular correlations from TMV scattering patterns.
- In 2009, Wochner, Dosch and coworkers[16] show the existence of angular correlations in disordered colloidal systems and utilize these correlations to determine local symmetries.
- In 2011, Saldin and coworkers[23] use angular correlation to determine the structure of a gold nanorod using direct phasing approaches.
- In 2011, Su, Kevan and coworkers[17] investigate the presence of angular correlations in 2D magnetic domains.
- In 2012, Chen, Zwart and coworkers[3] use angular correlations in the structure determination of Pt-coated Au-nanodumbbells.
- In 2013, Pedrini and coworkers[18] use angular correlations to determine the 2D structure of metallic nanoparticles.
- In 2013, Starodub and coworkers[24] use angular autocorrelations obtained from single particle scattering FEL experiments to determine the 3D structure of an object with cylindrical symmetry.
- In 2013 Malmerberg, Poon, Zwart and coworkers (to be published) have obtained angular autocorrelations from biological nanoparticle FEL scattering and use these in 3D structure determination, Figure 85.

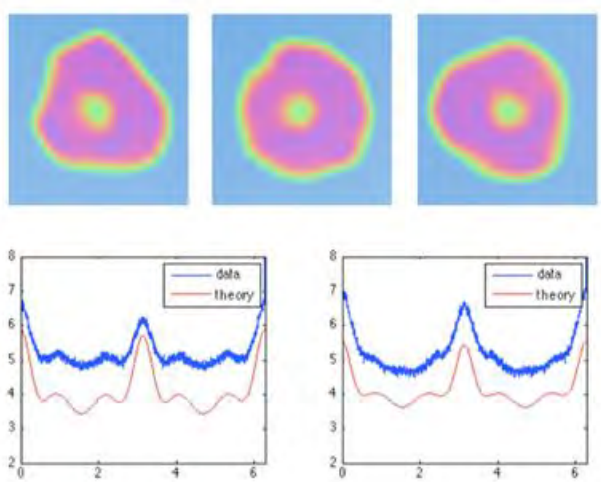

Figure 85. Top row: orthogonal sections of the mean model describing experimental carboxysomes fluctuation scattering data as obtained by our unconstrained real-space procedure. Bottom row: observed (blue) and model-based (red) angular autocorrelations for two q-values. Further analysis is ongoing (to be published).

As can be seen from these applications, the focus of the method has been largely on the use of angular correlations to determine the structure of nanoparticles and less on non-particulate systems. The work by Wochner *et al*[16] and Su *et al*[17] highlight the difficulties associated with the interpretation of angular autocorrelation data from non-particulate systems. The community at large is currently working on the development of methods to analyze non-particulate data from, for instance, block-copolymer-based organic photovoltaic materials. Fluctuation scattering on energy-related materials can be further enhanced

by performing the experiment across a resonant edge. This approach will allow for the spatio-chemical structure determination of novel materials, essential to the nation's energy needs.

Fluctuation scattering can provide a wealth of experimental information exceeding what can be obtained from traditional scattering methods. The proposed parameters of the LCLS-II instrument — high rep-rate and high flux — will result in an ultimate fluctuation scattering machine capable of generating the required number of exposures within a reasonable time.

References

1. P. Bassereau, D. Brodbeck, T. P. Russell, H. R. Brown, and K. R. Shull, "2-Dimensional Ostwald Ripening in Symmetrical Diblock Copolymer Films - Reply," Phys Rev Lett **74**, 4961 (1995).
2. C. H. Guo, Y. H. Lin, M. D. Witman, K. A. Smith, C. Wang, A. Hexemer, et al., "Conjugated Block Copolymer Photovoltaics with near 3% Efficiency through Microphase Separation," Nano Lett **13**, 2957 (2013).
3. G. Chen, M. A. Modestino, B. K. Poon, A. Schirotzek, S. Marchesini, R. A. Segalman, et al., "Structure determination of Pt-coated Au dumbbells via fluctuation X-ray scattering," Journal of synchrotron radiation **19**, 695 (2012).
4. A. Kusoglu, M. A. Modestino, A. Hexemer, R. A. Segalman, and A. Z. Weber, "Subsecond Morphological Changes in Nafion during Water Uptake Detected by Small-Angle X-ray Scattering," Acs Macro Lett **1**, 33 (2012).
5. B. R. Pauw, "Everything SAXS: small-angle scattering pattern collection and correction," J Phys-Condens Mat **25** (2013).
6. G. Fritz-Popovski, A. Bergmann, and O. Glatter, "Real space functions from experimental small angle scattering data," Phys Chem Chem Phys **13**, 5872 (2011).
7. O. Glatter, and O. Kratky, *Small angle x-ray scattering* (Academic Press, London ; New York, 1982).
8. P. Debye, "Zerstreuung von röntgenstrahlen," Annalen der Physik **351**, 809 (1915).
9. O. Kratky, and G. Porod, "Diffuse small-angle scattering of X-rays in colloid systems," Journal of Colloid Science **4**, 35 (1949).
10. A. Guinier, and G. Fournet, "Small Angle Scattering," International Tables for X-ray Crystallography, 324 (1955).
11. N. Baddour, "Operational and convolution properties of two-dimensional Fourier transforms in polar coordinates," J Opt Soc Am A **26**, 1767 (2009).
12. N. Baddour, "Operational and convolution properties of three-dimensional Fourier transforms in spherical polar coordinates," J Opt Soc Am A **27**, 2144 (2010).
13. O. Glatter, "Indirect Fourier Transformation - New Method for Data Evaluation in Small-Angle Scattering," Acta Crystallogr A **31**, S164 (1975).
14. D. I. Svergun, M. V. Petoukhov, and M. H. J. Koch, "Determination of domain structure of proteins from X-ray solution scattering," Biophys J **80**, 2946 (2001).
15. D. I. Svergun, V. V. Volkov, M. B. Kozin, H. B. Stuhrmann, C. Barberato, and M. H. J. Koch, "Shape determination from solution scattering of biopolymers," J Appl Crystallogr **30**, 798 (1997).
16. P. Wochner, C. Gutt, T. Autenrieth, T. Demmer, V. Bugaev, A. D. Ortiz, et al., "X-ray cross correlation analysis uncovers hidden local symmetries in disordered matter," Proceedings of the National Academy of Sciences of the United States of America **106**, 11511 (2009).
17. R. A. Kirian, K. E. Schmidt, X. Wang, R. B. Doak, and J. C. Spence, "Signal, noise, and resolution in correlated fluctuations from snapshot small-angle x-ray scattering," Physical review. E, Statistical, nonlinear, and soft matter physics **84**, 011921 (2011).
18. B. Pedrini, A. Menzel, M. Guizar-Sicairos, V. A. Guzenko, S. Gorelick, C. David, et al., "Two-dimensional structure from random multiparticle X-ray scattering images using cross-correlations," Nature communications **4**, 1647 (2013).
19. D. K. Saldin, V. L. Shneerson, R. Fung, and A. Ourmazd, "Structure of isolated biomolecules obtained from ultrashort x-ray pulses: exploiting the symmetry of random orientations," Journal of physics. Condensed matter : an Institute of Physics journal **21**, 134014 (2009).
20. Z. Kam, "Determination of Macromolecular Structure in Solution by Spatial Correlation of Scattering Fluctuations," Macromolecules **10**, 927 (1977).

21. Z. Kam, M. H. Koch, and J. Bordas, "Fluctuation x-ray scattering from biological particles in frozen solution by using synchrotron radiation," Proceedings of the National Academy of Sciences of the United States of America **78**, 3559 (1981).
22. C. Giacovazzo, *Fundamentals of crystallography* (International Union of Crystallography ; Oxford University Press, New York, 1992).
23. D. K. Saldin, H. C. Poon, M. J. Bogan, S. Marchesini, D. A. Shapiro, R. A. Kirian, et al., "New light on disordered ensembles: ab initio structure determination of one particle from scattering fluctuations of many copies," Phys Rev Lett **106**, 115501 (2011).
24. D. Starodub, A. Aquila, S. Bajt, M. Barthelmess, A. Barty, C. Bostedt, et al., "Single-particle structure determination by correlations of snapshot X-ray diffraction patterns," Nature communications **3**, 1276 (2012).

3.3 X-ray Cinematic Micro-Tomography with Chemical Imaging

The high repetition rate of the LCLSII lends itself to imaging dynamic processes. Being able to 3D image chaotic real time processes such as turbulent flame combustion, liquid jet breakup, fracture propagation in materials, and self-ordering in crystallization allows for digital recording of the entire process, which, in turn, allows for the validation of computational models. Validation of such models allows for development and optimization of the process under study at a rate much faster than that achieved by experimental development alone. This has clear economic and innovation advantages. Imaging with X-rays allows penetration through samples in environmental chambers and thus the creation of more realistic in-situ environments that can be used to validate the computational models.

Radiographic Imaging of Flames

Choice of suitable X-ray energy can selectively image chemical species of interest. Figure 86 shows the current state of the art for the soft X-ray spectroscopic imaging of a non-turbulent flame in laminar flow.[1] Figure 86 shows absorption radiographs of a flame obtained at different wavelengths that allow for reactant species identification. The conversion of CH_4 to CO to CO_2 is clearly monitored within the flame, but this two-dimensional imaging scan of a stable symmetric flame took many minutes to record by raster scanning a small synchrotron X-ray beam over the sample.

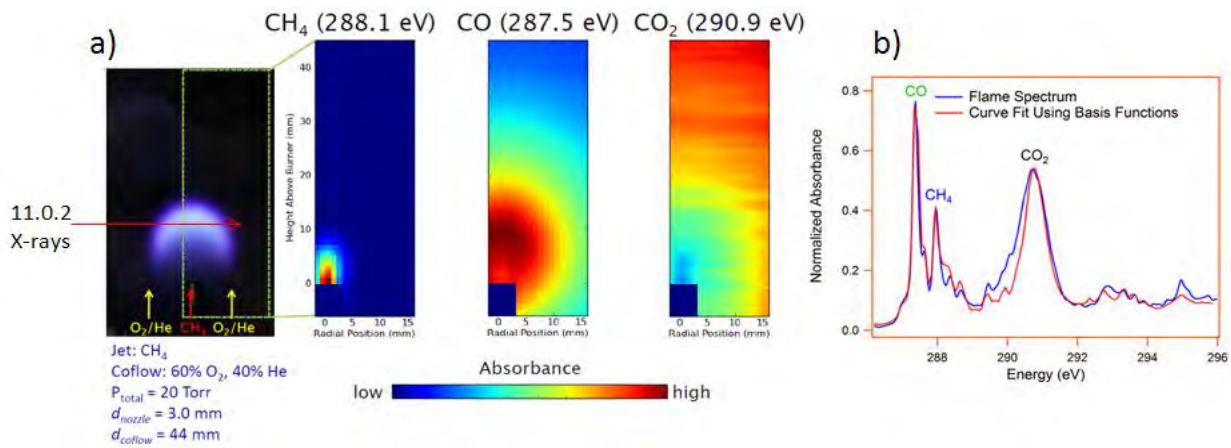

Figure 86. (a) Visible light image (left) and radiographs of a methane/oxygen stable symmetric flame at 30 torr at different wavelengths showing spatial distribution of starting, intermediate and final products. (b). Absorption spectrum of flame showing characteristic fingerprinting peaks that allow for chemical identification of the various gaseous reactants.[1]

3D Imaging of Stochastic Flames Using LCLS II

Gas flows in stochastic flames require temporal resolutions of ~10 µsec and spatial resolutions of ~10 µm. This implies gas velocities of ~1 m/sec. As such, the 0.1-1 MHz repetition rate of the LCLS II is well suited to the instantaneous imaging of flames and the soft X-ray energy of the source is well matched to spectroscopically identifying various combustion intermediates and products. The chemical reactions occurring in the turbulent flow of a flame is inherently three- dimensional in nature. Snapshot imaging of the flame in 3D is required. This can be achieved by limited view tomography and the application of the new computationally intensive iterative tomographic reconstruction codes [2] with the additional constraints imposed by motion-tracking algorithms such as optical flow, gradient approaches, and spatiotemporal analysis.[3-5] For example, a single-snapshot 3D reconstruction of the sample from a small number of views is inherently noisy; but with the use of motion tracking algorithms such as optical flow providing

additional constraints to the reconstruction algorithms, an improved signal to noise 3D movie will be practical despite limited sample views.

Figure 87 shows the schematic of one such experimental arrangement with soft X-rays illuminating a convex grating in conical diffraction geometry. The convex grating diverges the beam to provide a several-millimeter field of view for a sample flame. The conical diffraction provides multiple diffraction orders and, following reflection from a multilayer mirror, multiple instantaneous views of the sample can be recorded via the MHz cameras. Figure 87 shows five beams; but with appropriate choice of grating, the light energy can be directed into more diffraction orders and more sample views, dependent on the experimental requirements. Given 10^{10} hν/pulse with adequate spectral resolution to fingerprint reactants, a grating efficiency of ~10% for the weaker 2nd order, a multilayer reflectivity of ~30%, a sample absorbance of ~30% and a 1x1 K area detector, the estimated flux at the detector is ~100-500 hν/pixel/pulse, which is adequate for 3D imaging on the 10 μsec timescale. Other optical schemes in the soft X-ray range can be envisioned, such as the use of transmission gratings and whispering galleries.[6]

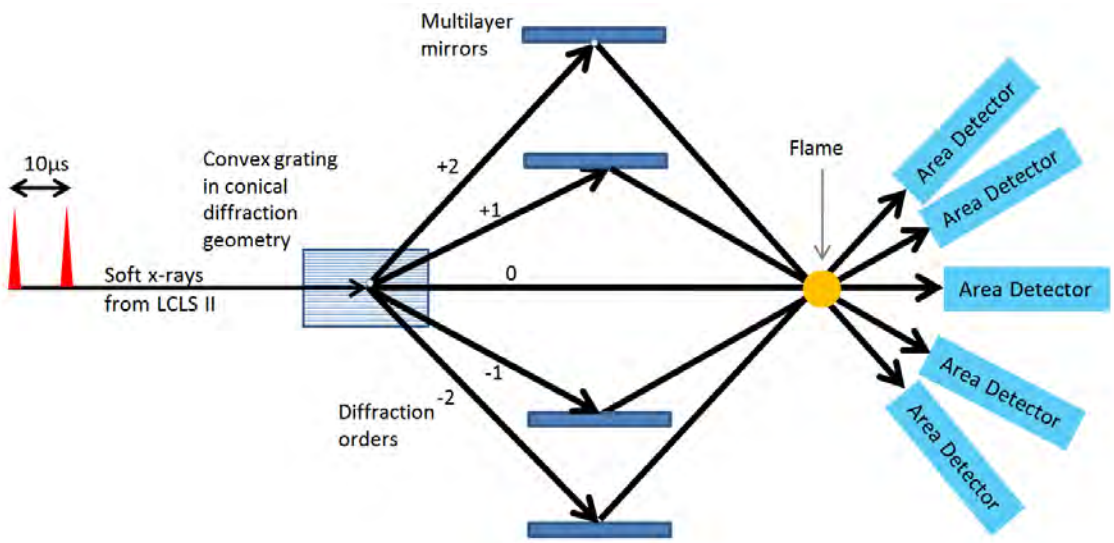

Figure 87: Schematic arrangement for the use of the LCLS II soft X-ray output to 3D image a flame. Plan view: the grating dispersion is out of the paper plane, as is the flame axis.

3D Imaging at Higher X-ray Energies

The use of harder X-rays allows for 3D imaging of denser samples such as liquid jets during breakup following injection to a combustion chamber [7] or thin materials undergoing structural fracture [8]. The same methodology applies where the optics are arranged to achieve multiple views. For hard X-rays, crystals are used. Figure 88 shows a schematic of such an arrangement where Si(111) and Si(220) crystals are used at different angles to provide five views of the sample at 5 keV. Additional crystals and crystal planes and Laue and Bragg diffraction can be used to increase the number of views or change energy. An energy of 5 keV shown here allows adequate penetration and absorption through a 200 μm thick octane jet sample being injected into a 10 mm diameter chamber of air at 10 bar. The small pressure container is made of thin walled beryllium.

Summary

The general theme of 3D cinematic tomographic is the simultaneous view of the sample from multiple directions. Newly developed iterative reconstruction routines allow for only a few views and the

additional constraints imposed by motion-tracking optical flow algorithms, gradient approaches, and spatiotemporal analysis constraint the individual images, improving reconstruction and reducing noise. Various optical schemes can be devised to optimize for a particular X-ray energy range of interest.

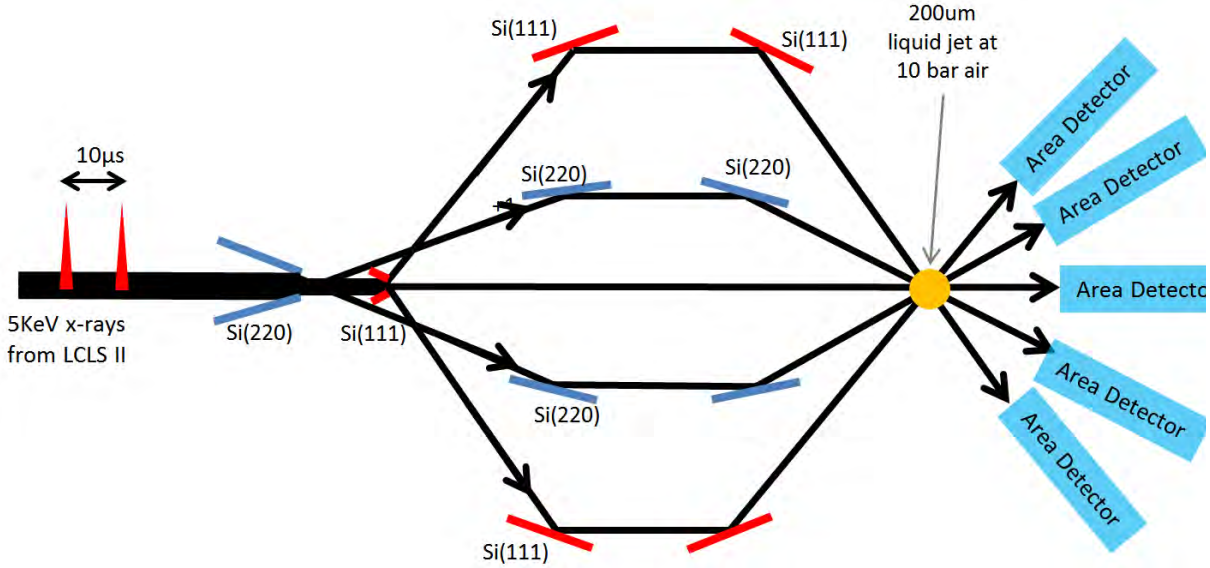

Figure 88: Schematic arrangement for the use of the LCLS II using 5 KeV X-rays to 3D image an octane liquid jet breakup inside a 10 mm diameter beryllium cylinder at 10 atmosphere of air simulating fuel injection into an internal combustion engine.

References

1. J. Frank, A. Shavorskiy, H. Bluhm, B. Coriton, E. Huang, and D. Osborn, "In situ soft X-ray absorption spectroscopy of flames," Appl. Phys. B **117**, 493 (2014).
2. S. V. Venkatakrishnan, L. F. Drummy, M. A. Jackson, M. De Graef, J. Simmons, and C. A. Bouman, "A Model Based Iterative Reconstruction Algorithm For High Angle Annular Dark Field-Scanning Transmission Electron Microscope (HAADF-STEM) Tomography," Image Processing, IEEE Transactions on **22**, 4532 (2013).
3. P. Merkle, A. Smolic, K. Muller, and T. Wiegand, "Efficient Prediction Structures for Multiview Video Coding," Circuits and Systems for Video Technology, IEEE Transactions on **17**, 1461 (2007).
4. B. D. Lucas, and T. Kanade, "An iterative image registration technique with an application to stereo vision," in *Proceedings of the 7th international joint conference on Artificial intelligence - Volume 2* (Morgan Kaufmann Publishers Inc., Vancouver, BC, Canada, 1981), pp. 121.
5. F. Nielsen, *Visual Computing: Geometry, Graphics, and Vision* (Charles River Media / Thomson Delmar Learning, 2005).
6. I. N. Bukreeva, I. V. Kozhevnikov, and A. V. Vinogradov, "Whispering Gallery Mirrors for the Soft X-Ray Region: Properties and Applications," Journal of X-Ray Science and Technology **5**, 396 (1995).
7. Y. Wang, X. Liu, K.-S. Im, W.-K. Lee, J. Wang, K. Fezzaa, et al., "Ultrafast X-ray study of dense-liquid-jet flow dynamics using structure-tracking velocimetry," Nat Phys **4**, 305 (2008).
8. D. L. Davidson, and J. Lankford, "Dynamic real time fatigue crack propagation at high resolution as observed in the scanning electron microscope," in *Fatigue Mechanisms*, J.T.Fong, ed. (Proc ASTM-NBS-NSF Symp, Kansas City, Mo, 1979), pp. 277.

4.0 Instrumentation

4.1 X-ray Optics & Beamlines

Approaches to mitigate wavefront distortion with high power beams

To preserve the X-ray wavefront both in and out of focus, the demands on mirror shape precision are very high. In the case of the LCLS II mirrors, a shape error of 0.5 nm rms is required. With the average power delivered by LCLS II, the preservation of such shape precision becomes even more challenging. Therefore, the cooling and holding schemes are very important. The need to preserve such a high quality on long mirror surfaces differentiates the LCLS II optics requirements from those at a synchrotron radiation facility.

For the LCLS II mirrors, liquid nitrogen cooling will not be employed to avoid mirror contamination issues. Instead, the mirrors will be side cooled with water. This cooling must also be compatible with a bender. Being nearly diffraction limited, the FEL X-ray beam divergence changes with photon energy. Moreover, the first mirror will reflect the third harmonic in some cases and at higher photon energy absorb it. Therefore, the power absorbed by the mirror can be very different at different photon energies.

The cooling of a mirror is optimized when the length of the cooling pad corresponds to the full width half maximum (FWHM) of the beam footprint on the mirror. For the LCLS II mirrors, this condition is not possible, because of the variable X-ray divergence. This effect can be mitigated by using three independent water circuits, providing flow to 5 separate cooling pads shown in Figure 89. The cooling is provided by fins entering into troughs machined into the side of the mirror. The troughs are then filled by Gallium-Indium eutectic in order to guarantee a good thermal contact between the silicon mirror and the cooling pads.

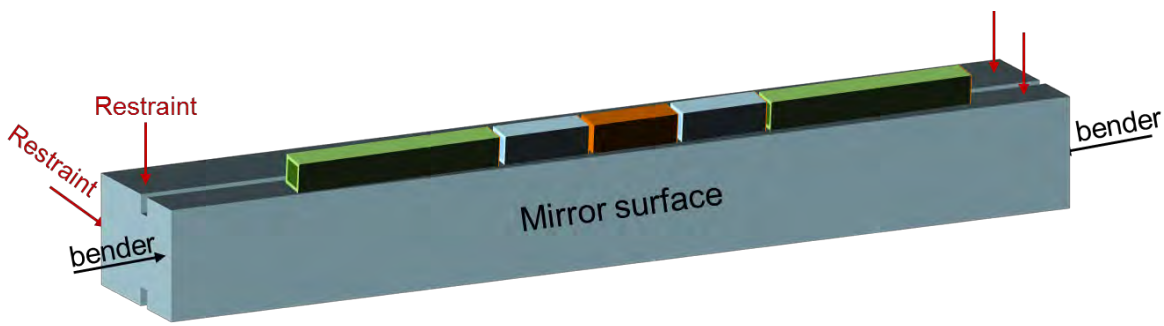

Figure 89: Illustration of the cooling system adopted for the 1 m long mirror. The cooling pads have fins, which enter into troughs. The different colors of the cooling pads indicate which pads share the same water circuit. The position of the bender is also shown.

With this variable cooling scheme, it is possible to preserve a shape error of 0.3 nm rms for an incident X-ray power of 40 W. Higher powers, up to 200 W can be accommodated without damage to the optics, but with somewhat reduced performance. Examples of the performance reduction at different powers are shown in Figure 90.

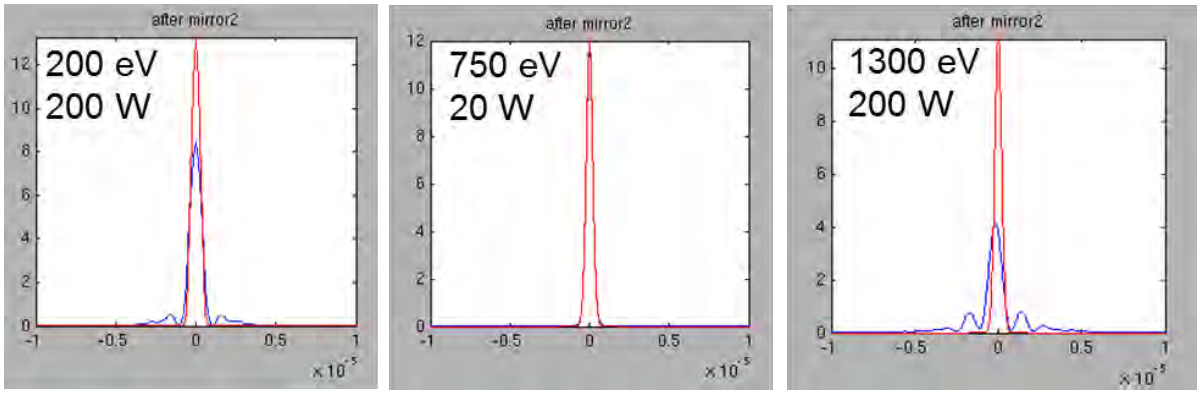

Figure 90: Focal spot profiles of the X-ray beam from perfect mirrors (red curves) and from mirrors irradiated by 20 or 200 W powers cooled in the manner described above. From left to right, are the cases of 200 eV photon energy and 200 W power, 750 eV and 20 W and 1300 eV and 200 W.

In addition to the aspherical deformation of the mirror due to the heat load, there is also a spherical thermal term. To correct this term, the mirror will be equipped with a motorized bender to remove the convex radius of curvature. The bender will employ an off-axis pusher close to the optical surface of the mirror shown in Figure 89. The two pushers will be controlled by a single motor and calibrated in the optical metrology laboratory.

Combined hard and soft X-ray beams

There are a few ways to combine the hard and soft X-rays into the same beamline. The soft and hard X-ray undulators are spatially separated by 2.5 m. If both beams are supplied by the superconducting linac, there is a 5 ns minimum delay between X-ray pulses from the separate undulators. The two beams must be matched in time (with a variable delay) and space. To bring the soft X-rays into the hard X-ray beamline, the lateral displacement should be covered in the near experimental hall (NEH). For photon energies from 0.3 to 3 keV and mirrors coated with B_4C, the grazing incidence angle may be 11 mrad. At this angle, four mirrors can make the hard X-ray and soft X-ray beams collinear within the NEH. The total delay from the deflecting mirrors is only ~300 ps. To reach 5 ns, the difference in path between the soft and hard X-rays has to be 1.5m. A four-crystal monochromator delaying the hard X-ray beam is a possible solution. The delay line must have variable diffraction angle and distance between crystal pairs. It requires a complicated, but feasible mechanical system.

Splitting and recombining X-ray beams

Multidimensional X-ray spectroscopy will require, in general, multiple X-ray beams intersecting the sample. A transient grating has been achieved by using an amplitude dividing mirror [1]. Here, a split and delay concept is described. Beam splitting can be realized by a mirror, which reflects half of the beam and lets pass the other half undisturbed. Such mirror is usually made by realizing a chamfer at end of the substrate and polishing the useful area until the edge of chamfer. This mirror is used as the first and last elements of a delay line, shown in Figure 91. This concept is a modification of the designs adopted at FLASH and Fermi@Elettra. Here, all the mirrors stay in the same plane and on the same side of the incoming optical path. This solution permits access to higher photon energies with a more compact system. The principle is the following: M1 (the beam splitter) deflect half of the beam upward. The other half follows the red path hitting the mirrors M5, M6, M7 and M8 (all of which are fixed). The deflected fraction of the X-ray beam goes along the blue path, reflecting from mirrors M2, M3, and M4. By moving together M2 and M3, one can vary the delay between the two X-ray beams. The two X-ray beams (red and blue) are recombined after M4. This mirror is identical to M1, with the chamfer toward the source.

By using an angle of incidence of 10 mrad for the fixed internal part of the delay line and of 14 mrad for the mobile external part, one can obtain delays fr0m -100 fs to more than 1 ps in a 4 m overall length.

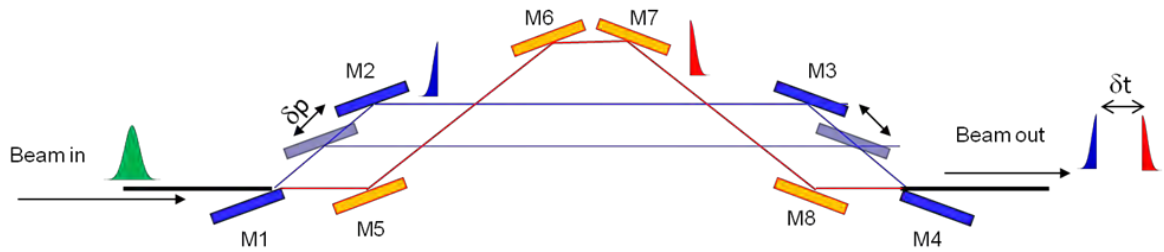

Figure 91: Delay line scheme. The X-ray beam is split in two by the M1 mirror and recombined by the M4 mirror. The time delay is varied by moving the M6 and M7 mirrors.

This split and delay design concept can be applied as the basis of a scheme for two crossing X-ray beams. By slightly changing the angle of incidence of the last mirror, by 5 mrad, one can obtain a separation of ~50 mm between the two X-ray beams. This displacement is sufficient to accommodate a group of mirrors to produce variable crossing angles (α) on the sample from 2 to 90° (Figure 92). For shallow angles, a mirror with a single optical coating can be used; while for larger angles some discrete multilayer-coated mirrors have to be employed.

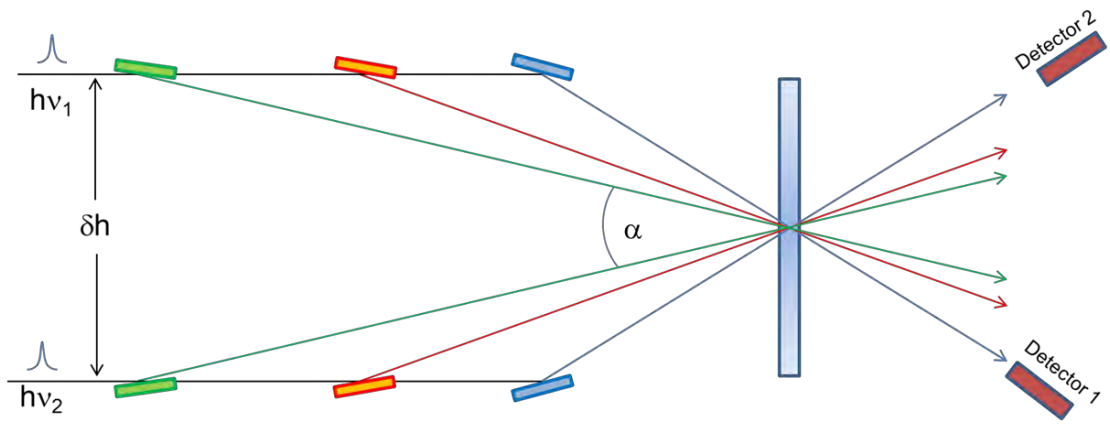

Figure 92: Scheme of the variable angle mirror system. To cover variable angles α from 2 to 90°, the length of the assembly is 1.5 m.

If three X-ray beams are needed, for example two beams to generate the standing wave and one beam as a probe, the optical system become more complex. A low resolution diffraction grating can be used to generate the third X-ray beam. In practice, the M6 and M7 mirrors are replaced by low groove density gratings and rotating flat mirrors.

Nano focusing

Very small focal spots, well below 1 µm, can be achieved in different ways. One approach is to use elliptical mirrors. To achieve a spot size of 100 nm, slope errors of ~50 nrad are required. An ellipse will strong curvature can be achieved by properly bending a flat and shaped substrate shown in Figure 93. A spot of 100 nm in diameter is achievable over most of the soft X-ray range. At low photon energy, the diffraction limit increases the spot size by a factor two at 300 eV. With a 2 mJ pulse energy, a calculated fluence of $>10^{21}$ W/cm^2 is achieved.

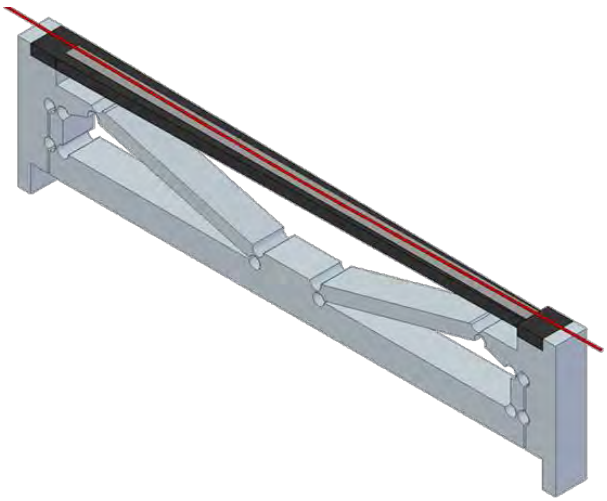

Figure 93: Schematic view of the mirror bender to achieve a short focal length elliptical mirror starting from a flat surface.

Fresnel zone plates are another attractive option. Recently, diamond zone plates were successfully tested at the LCLS at a photon energy of 8 keV.[2] The zone plates produced the predicted focal spot and did not suffer damage from the intense X-ray beam. Such lenses can be quite large, in terms of geometric and numerical aperture. The efficiency of these lenses is still limited by the aspect ratio of the zones, but it is well above 10% over a large photon energy range. A recent development at SLAC and Stanford University [3] increased the aspect ratio of a zone plate, but this technique is currently only applicable to silicon. The beam damage limit for such lenses has to be tested. A drawback of zone plates is the chromatic focusing, which requires several zone plates to cover a photon energy range and a translation of the lens or sample. In addition, the focal distance is relatively short; to achieve a 30 nm focus, the focal distance is several tens of cm for hard X-rays, but < 2 cm at the carbon K-edge.

Experimental approaches & impact of LCLS-II

RIXS Spectrometers

For Resonant Inelastic X-ray Scattering (RIXS), different science topics provide varying requirements. Experiments studying correlated materials, described in Section 2.3.1, require quite high resolution. A high resolution RIXS spectrometer is intended to reach a resolving power E/ΔE of 50,000 in the photon energy range between 250 eV to 1000 eV. A conceptual solution is presented in Figure 94. It is based on a single optical element, a blazed grating with variable groove density, ruled on a spherical substrate. The angle of incidence is constant (88.5° in this example), and the detector will move in an X-Y plane to follow the focal curve of the grating (also shown in Figure 94). The maximum distance from the sample to the detector is of the order of 10 m.

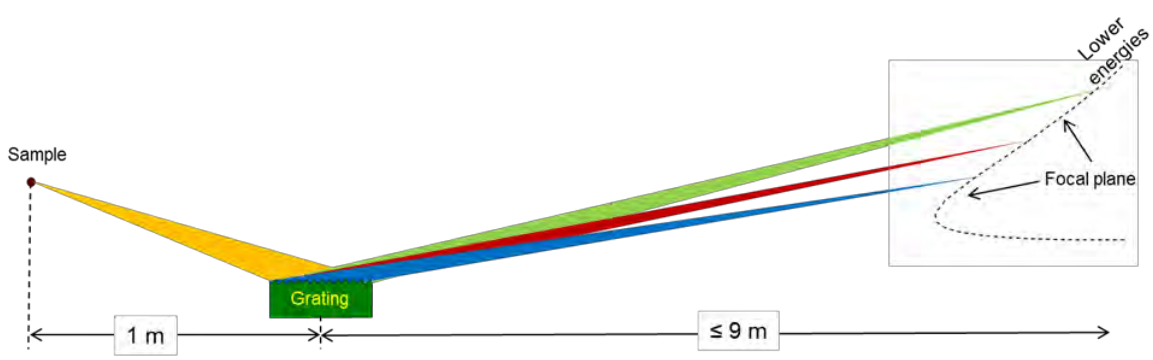

Figure 94: Schematic design of a high resolution RIXS spectrometer. The lower energies are diffracted at larger angles and focused slightly farther from the grating than the higher energies.

The use of a spherical VLS has some advantages. Only one optical element is needed to diffract and focus the radiation. In addition, the change of the focal distance with photon energy is limited, making the system easier to use and align. For high photon energy, above 550 eV, to reach the desired resolving power in a relatively limited space, a very high groove density grating (above 3000 lines/mm) would be required. Such a high groove density, with the required groove density variation, is not currently available. Therefore, the grating would be used in higher diffraction orders, the 2nd and 3rd order.

The expected grating efficiencies for the different diffraction orders are shown in Figure 95. This is a very important parameter in the RIXS spectrometers, since the expected count-rate (discussed later) is usually limited.

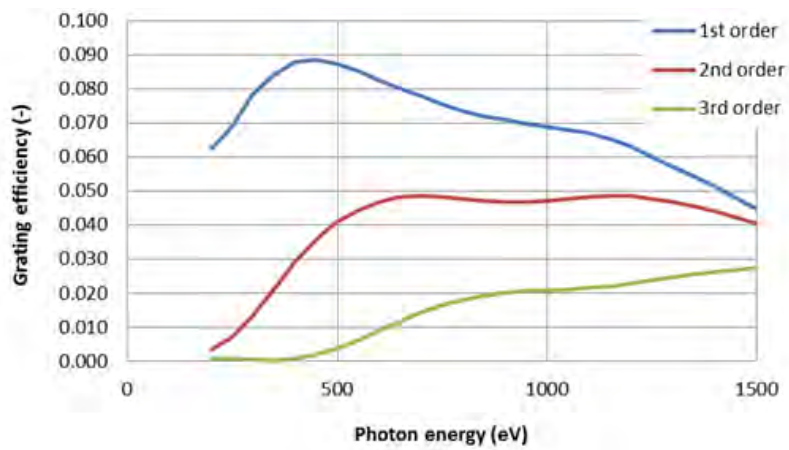

Figure 95: Predicted efficiency of the high resolution RIXS spherical VLS grating for a blaze angle of 2.3°.

In principle, the resolving power of a grating spectrometer can be very high, but there are limiting factors like the grating manufacturing precision and the detector spatial resolution. These limitations are in continuous evolution but, today, one can rely on 160 mm long gratings with the required precision and 20 μm spatial resolution for the detectors. The detector resolution can be increased by tilting the CCD. This rotation reduces the quantum efficiency, but several attempts to reduce the dead layer have been made and some good results were obtained.[4] Alternatively, there is detector development at LBNL, which promises to reach a spatial resolution of 6 μm.

Sample damage can also be a limiting factor. For instance, with the design described here, one needs a spot on the sample of the order of 10 μm in the dispersive direction and 2 mm in the other direction. The maximum power density that can be delivered to the sample is of the order of 1 mJ/cm^2, equivalent to 0.2 μJ. Nevertheless, even with this limiting factor, the expected count rate is 1,000 times higher than the count rate on an advanced synchrotron radiation source for the equivalent resolving power.

The beamline hosting the high resolution RIXS spectrometer must have a resolving power above 50,000. A monochromator is needed upstream of the sample because the soft X-ray self-seeding envisioned for LCLS II will not produce radiation with a narrow enough bandwidth. As a consequence of the long source distance, a monochromator having the required resolving power is possible. VLS plane gratings with 600 l/mm are sufficient. Mechanical and source stability can be the limiting factors and should be evaluated.

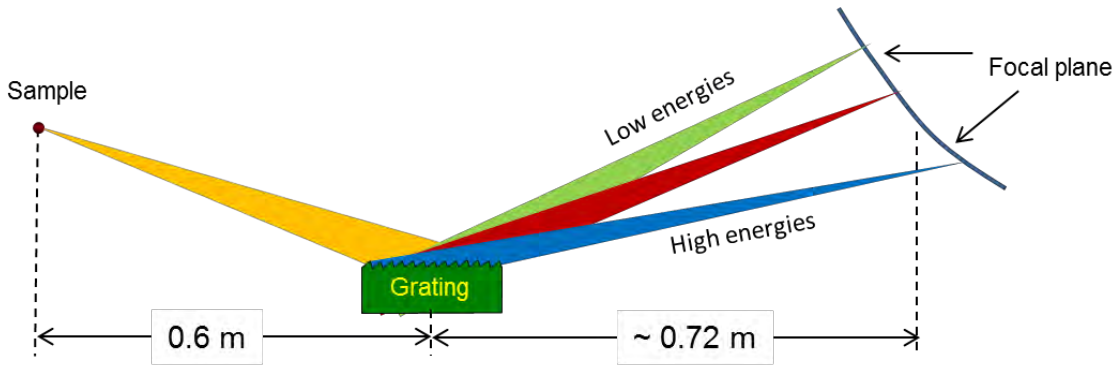

Figure 96: Layout of the Low Resolution Spectrometer. The focal plane is chosen to have the CCD always perpendicular to the incoming beam with the entire area in focus.

For experiments studying problems in catalysis, described in Section 2.2, there is a need for higher transmission at moderate resolution. Here, one can implement a lower resolution and more compact version of the spectrometer. The basic, design principle is the same, optimizing the photon collection while dispersing and focusing onto a position sensitive detector. As shown in Figure 96, the overall dimensions are reduced, which increases the angular collection of both the grating and the detector. To achieve a resolving power of 2,500-5,000, the grating shall demagnify the considerably. This can be achieved by a large ratio between the incident and the diffraction angle. By using a 1800 l/mm plane grating, with large groove density variation, one can, with a single grating and by using three diffraction orders, focus photon energies between 250 and 1200 eV at the detector.

In comparison with the high resolution spectrometer, the transmission of the moderate resolution spectrometer is improved by several factors. The shorter sample to grating and sample to detector distances increases the angular collection. The focus on the sample can be 100 µm in the dispersion direction allowing 10 times more photons while staying below the damage criterion. Overall, the count rate per area on the detector is expected to be 1,000 times larger in the moderate resolution spectrometer compared with the high resolution version.

References

1. F. Bencivenga, and C. Masciovecchio, Nuclear Instruments and Methods in Physics Research A **606**, 785 (2009).
2. C. David, S. Gorelick, S. Rutishauser, J. Krzywinski, J. Vila-Comamala, V. A. Guzenko, et al., "Nanofocusing of hard X-ray free electron laser pulses using diamond based Fresnel zone plates," Sci Rep-Uk **1** (2011).
3. C. Chang, and A. Sakdinawat, "Ultra-high aspect ratio high-resolution nanofabrication for hard X-ray diffractive optics," Nat Commun **5** (2014).
4. D. P. Woodruff, "Chapter 1 - Surface Structure," in *Chemical Bonding at Surfaces and Interfaces*, A. N. G. M. P. K. Nørskov, ed. (Elsevier, Amsterdam, 2008), pp. 1.

4.2 Lasers

Overview

Approximately 75 percent of all experiments at the LCLS require optical laser excitation to initiate a reaction or state within the sample under investigation. The vast majority of the physical phenomena under investigation by pump/probe techniques occur on a timescale of picoseconds to femtoseconds, requiring both optical and X-ray sources to have femtosecond pulse duration and a well-defined and controllable temporal separation. LCLS-II will present challenges for optical lasers primarily in two broad areas: (1) increasing the repetition rate of the lasers to match that of the LCLS-II X-ray beam (up to ~1 MHz) with suitable pulse energy and (2) maintaining low jitter and drift relative to the X-ray beam. Related challenges will include safely managing high average power beams, producing sufficient pulse energy at wavelengths of interest where the conversion efficiency is low (e.g., THz, deep-UV), and producing and maintaining increasingly shorter pulse durations to take full advantage of the high time fidelity of the X-rays and optical beams for experiments on extremely short time scales. New opportunities in high energy density (HED) science will drive demand for increased optical laser intensity.

High Repetition Rate

In the baseline design for the LCLS-II superconducting accelerator the maximum repetition rate for electron bunches (and therefore X-ray pulses) is ~1 MHz. While specific experiments may be limited by detectors or other considerations, the majority of science opportunities will require 10 to100 kHz lasers for pump-probe measurements at THz to EUV frequencies. This establishes an initial goal for LCLS-II of a 100 kHz laser system with ~1 mJ for frequency conversion (~100 W).

Ti:sapphire

The standard laser system for LCLS is based on Ti:sapphire lasers operating at repetition rates up to 120 Hz to match the LCLS X-ray beam repetition rate. Ti:sapphire is a very well developed platform with numerous commercial suppliers, versatility in wavelength and pulse duration, and with a broad range of accessories to extend the wavelength from UV to THz. The standard LCLS Ti:sapphire system is comprised of a MHz oscillator that seeds a regenerative amplifier ("regen"). Typically, a multipass amplifier (MPA) provides additional amplification up to ~25 mJ at 120 Hz.

Ti:sapphire is the technology of choice for scaling in repetition rates up to ~10 kHz for applications that do not require the highest pulse energy. The primary technical issue for scaling Ti:sapphire is degradation due to thermal effects from the pump laser. Cryogenic cooling of Ti:sapphire can extend the average power of regen and multipass amplifiers into the range of ~20 to 30 W of average power at 1 kHz, with demonstrations of up to 40 to 50 W[1] at 10 kHz. The existing Ti:sapphire MPAs at LCLS could be modified with cryogenic cooling to reach these average power levels.

At higher repetition rates (e.g., 100 kHz), commercial Ti:sapphire laser systems are available with an average power of ~5 W with conventional cooling. In principle higher average power at 50 to 100 kHz could be obtained with cryogenic cooling; but in practice such products are not currently offered due to a relatively low market demand and limited availability of high average power pump lasers at this repetition rate. While it is anticipated that there will be some development in these pump lasers, the combined disadvantages of pump availability and increasingly challenging cryogenic engineering leave Ti:sapphire as a material of second choice for high average power 100 kHz-class amplifiers.

OPCPA

Optical Parametric Chirped Pulse Amplification (OPCPA) is currently the most promising option for a high average power amplifier system scaling to 100 kHz with >100 W average power with short pulse duration and flexible center wavelength. Similar to Chirped Pulse Amplification (CPA), an ultrashort pulse is first stretched in time, amplified, and recompressed. In contrast to CPA, in which amplification is based on stimulated emission, OPCPA transfers energy from a pump beam to a seed beam in an optical parametric amplifier (OPA). The amplification bandwidth can span almost one octave, supporting sub-10-fs pulse durations in the visible spectrum. In contrast to traditional amplification via stimulated emission in pumped laser crystals, no energy is directly stored during the amplification process in the nonlinear material due to the instantaneous nature of the OPA process, thereby mitigating typical thermal effects and beam distortions and facilitating power and energy scaling of the OPA systems. A review of OPCPA technology can be found in ref. 2. Extensive development has been done on high power OPCPA in the past years.[3] The key enabling technology for high average power OPCPA is commercially available high power Yb:YAG amplifier technology[4] for OPCPA pumping.

LCLS has initiated an R&D program to develop a 100 W average power (1 mJ at 100 kHz or 0.1 mJ at 1 MHz) OPCPA laser system. The target of ≥1 mJ was selected to provide sufficient peak power to drive low-efficiency wavelength conversion processes such as THz generation by optical rectification, which has a 10^{-5} conversion efficiency. Other baseline performance parameters include 15 fs FWHM pulse duration, tunability from 0.7 to 1.0 µm, and timing synchronization jitter ≤20 fs RMS from 0.01 to 1 MHz. The configuration of the proposed laser system is shown in Figure 97.

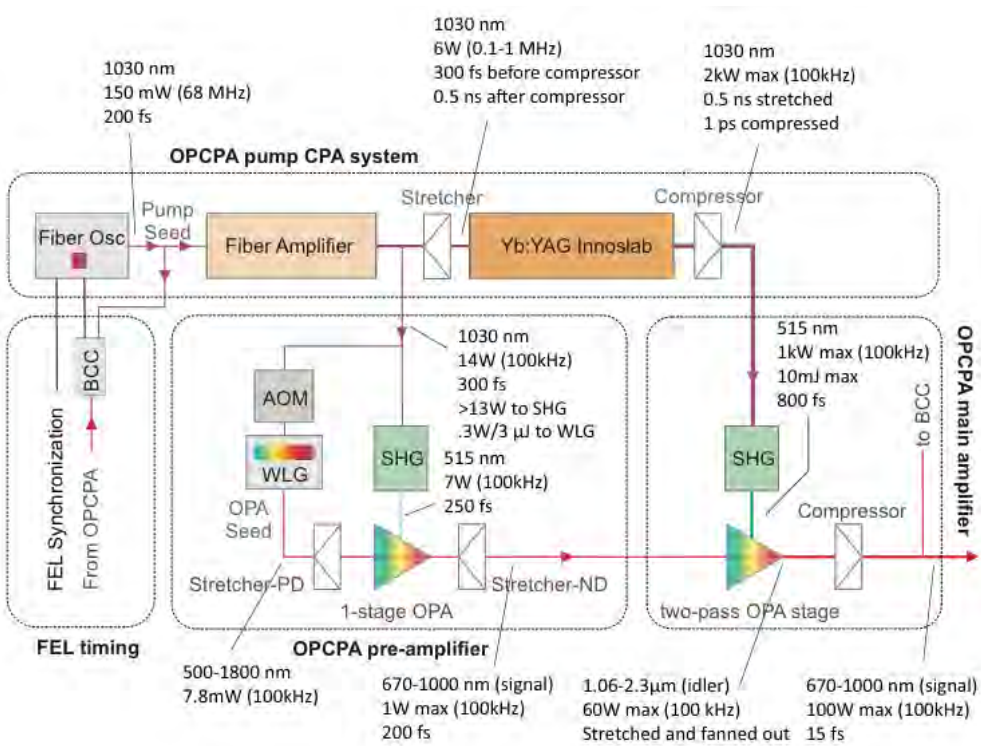

Figure 97: Laser setup and detailed beam parameters for the initial R&D laser amplifier.

The system will be based on a commercial oscillator for seeding the amplifier and the pump laser for passive synchronization, a commercial fiber pre-amplifier to achieve ~10 W average power, and several

stages of OPCPA pumped by a commercial Yb:YAG amplifier producing >1 kW average power with a few picosecond pulse duration.

The architecture of the system is designed to enable enhanced performance through upgrades or alternative modes of operation. Substantial development is also required in terms of investigating thermal properties of nonlinear optical crystals for OPCPA and modeling the amplification process prior to design and operation of an amplifier. Although OPCPA is inherently less influenced by thermal issues compared with standard energy-storage media, at the kW level of pump even a very small coefficient of absorption can result in significant heat dissipation in the OPCPA crystals.

Currently, sub-10 fs X-ray pulses available from the FEL and cross-correlation techniques allow the laser/X-ray delay to be measured with ~20 fs accuracy. One limit on the achievable time resolution in pump-probe measurements is effectively the pulse duration of the pump-probe laser system. We expect to deliver 15 fs for this proposed laser amplifier and sub-10 fs for a future upgrade. The pulse duration or gain bandwidth in optical parametric amplification is flexible to a certain extent. The pulse duration upgrade can be performed by extending the phase-matching bandwidth: 515 nm pumped BBO OPCPA can be used to amplify sub-7 fs pulses. Shorter pulses can be generated with spectral pulse broadening in a gas-filled capillary and subsequent compression with chirped mirrors.

A large spectral range is accessible with various OPCPA configurations pumped with either the fundamental or the second harmonic of the OPCPA pump amplifier. Different spectral regions can be addressed with OPCPA from the VIS range (0.7 to 1 µm, signal wave) to the mid-IR (1.1 to 4.5 µm, signal and idler wave) depending on the pump wavelength (e.g., 1.03 µm from Yb:YAG high power amplifiers or 0.515 µm, frequency doubled). A 0.515 µm pumped OPCPA system is planned for the initial R&D phase of the amplifier.

Lasers for High Energy Density Science

The field of High Energy Density (HED) science performed at the Matter in Extreme Conditions (MEC) instrument has laser requirements that emphasize high pulse energy and high peak power. The current MEC laser capability is comprised of two laser systems: an Nd:glass, high-energy, temporally-shaped, nanosecond laser system that fires at one shot per few minutes, and a Ti:sapphire, high intensity, femtosecond laser system capable of producing 30 TW peak power at 5 Hz. There are multiple, overlapping pathways for making improvements in laser systems to best take advantage of the new capabilities.

High peak power

The unique combination of a petawatt laser in close proximity to the LCLS MEC end station and X-ray beam will for the first time permit detailed pump-probe studies employing first-principles X-ray scattering techniques to measure and uncover the physical mechanisms underlying the interaction of ultra-intense laser radiation with matter. Commercial petawatt laser systems are available operating at "low" energy (~30 J) and short pulse duration (~30 fs) with repetition rates of up to 1 Hz. Similar systems operating at up to 10 Hz are promised for delivery to the Extreme Light Infrastructure (ELI) projects in the EU. Higher energy (>100 J), longer pulse (>100 fs) systems operating at one shot per few minutes are also commercially available. Within the user community there are proponents for both types of lasers depending on the specific science of interest. LCLS is engaging in community outreach through workshops and direct interactions to help articulate the case for both types of petawatt laser systems. This input will inform the selection of the specific laser technology at the time each project is approved and funded.

High pulse energy

For accessing the conditions of planetary interiors as well as for creating warm dense matter, it is important to get into the multi-Mbar regime with well-defined shock conditions. Currently in MEC, such shocks are driven by the second harmonic of a Nd:glass laser system, producing ~30 J in 10 ns pulses at a repetition-rate of 0.2 shots/minute. Due to the relatively low pulse energy of the drive laser a small laser focus is required to achieve high pressures. Higher laser pulse energy would allow for higher pressures to be reached with uniform shocks. One possible upgrade path would be achieved by replacing the final glass amplifier rods with a commercially available amplifier, in conjunction with larger aperture LBO crystals, enabling the generation of up to 100J in a 10ns pulse at up to 1 shot/minute. Additional improvements in the system may also be achieved by upgrading the seed laser and front-end amplifier chain. These upgrades would significantly enhance the possibilities for shock physics studies at LCLS-II.

Laser Synchronization and Timing

Taking full advantage of the temporal resolution of femtosecond X-ray pulses and femtosecond optical lasers in pump-probe experiments requires timing measurement and control of the variable delay between the pulses on a timescale of a few 10 fs or better. At present, LCLS has a pulse-to-pulse timing jitter relative to the accelerator radio-frequency (RF) distribution of approximately 60 fs RMS, integrated over a bandwidth of 0.1 to 100 kHz. Optical lasers must be locked to the accelerator RF distribution with similar or better timing jitter, and drifts in the laser beam path and RF distribution must be controlled to approximately the 1 ps level. A detailed description of the timing distribution and oscillator locking electronics developed at SLAC is given in ref. 5.

The CW RF drive and high Q of the superconducting accelerator cavities of LCLS-II promises to significantly reduce the timing jitter between the low-level RF and the electron bunches and corresponding X-ray pulses, possibly to as low as a few femtosecond. This improvement will drive corresponding demand for improvements in the jitter of the pump-probe lasers, particularly in experiments that probe ultrafast dynamics of transient systems.

In all cases it will be highly beneficial to have an out-of-loop monitor of the time of arrival of the optical laser pulses at the interaction point with the X-rays. One promising option for this out-of-loop monitor is based on pulsed femtosecond timing distribution technology utilizing optical balanced cross-correlators for timing detection.[6] In this work, remote two-color optical-to-optical synchronization was demonstrated with 3.3 fs rms slow drift over 24 hours between a Ti:sapphire oscillator and an Er-doped fiber laser. Similar systems are already in use (DESY/FLASH) or planned (European XFEL and the PAL FEL) for precision synchronization of optical laser with FEL X-ray beams.

Cross-correlation techniques have been developed at LCLS and other facilities that rely on X-ray-induced material changes that cause prompt (few-femtoseconds) changes in the optical properties of the material (typically silicon nitride). These techniques include changes in the reflectivity of a thin membrane illuminated by a laser pulse at a 45 degree angle[7] or changes in the transmission and reflection of a membrane illuminated by a temporally chirped laser pulse[8]. Both methods have measured temporal accuracy on the order of 25 fs RMS and both are currently in operation at LCLS. LCLS is investigating methods of scaling cross-correlation techniques up to the 100 kHz repetition rate of LCLS-II. Nevertheless, LCLS II requires the development of methods for reducing the jitter and drift of the optical lasers to the minimum achievable level.

References

1. I. Matsushima, H. Yashiro, and T. Tomie, "10 kHz 40 W Ti:sapphire regenerative ring amplifier," Opt. Lett. **31**, 2066 (2006).

2. A. Vaupel, N. Bodnar, B. Webb, L. Shah, and M. Richardson, "Concepts, performance review, and prospects of table-top, few-cycle optical parametric chirped-pulse amplification," OPTICE **53**, 051507 (2013).
3. R. Riedel, J. Rothhardt, K. Beil, B. Gronloh, A. Klenke, H. Höppner, et al., "Thermal properties of borate crystals for high power optical parametric chirped-pulse amplification," Opt. Express **22**, 17607 (2014).
4. D. J. Richardson, J. Nilsson, and W. A. Clarkson, "High power fiber lasers: current status and future perspectives [Invited]," J. Opt. Soc. Am. B **27**, B63 (2010).
5. K. Gumerlock, J. Frisch, B. Hill, J. May, D. Nelson, and S. Smith, in *FEL2014*(Basel, Switzerland, 2014).
6. H. Li, L. J. Chen, H. P. H. Cheng, J. E. May, S. Smith, K. Muehlig, et al., "Remote two-color optical-to-optical synchronization between two passively mode-locked lasers," Opt. Lett. **39**, 5325 (2014).
7. S. Schorb, T. Gorkhover, J. P. Cryan, J. M. Glownia, M. R. Bionta, R. N. Coffee, et al., "X-ray–optical cross-correlator for gas-phase experiments at the Linac Coherent Light Source free-electron laser," Appl. Phys. Lett. **100**, 121107 (2012).
8. M. R. Bionta, H. T. Lemke, J. P. Cryan, J. M. Glownia, C. Bostedt, M. Cammarata, et al., "Spectral encoding of x-ray/optical relative delay," Opt. Express **19**, 21855 (2011).

4.3 Detectors

LCLS II presents several challenges for detectors, the primary ones being the very-high pulse repetition rate. Secondary exigent demands include the expanded high-energy reach at low repetition rates and possible damage associated with the greater radiation fluence.

Depending on the experiment, pulse-to-pulse images will have to be read out with a speed matching the LCLS-II repetition rate or multiple pulses will be accumulated in the detector before readout. Besides the obvious challenge of developing very fast readout cameras, it is worth pointing out that also detectors operating in accumulation mode will have to perform with a very high degree of uniformity and provide a large dynamic range.

Large, fast, two-dimensional cameras for imaging are key to the success of the LCLS II experimental program and the most challenging to develop.

Direct detection charged-coupled devices (CCDs) have proven their value as scientific detectors in astronomy, synchrotron-based research, and lately also at FELs. In particular the fCCD developed at LBNL has seen extensive use at LCLS.[1] A new version, the very-fast CCD (vfCCD), is currently under development. It will maintain the current version's performance, but increase the frame rate to 5-10 kHz. The vfCCD will provide single-photon sensitivity down to the oxygen edge and its auto-ranging gain ability will offer significant dynamic range, all within 30-50 μm pixels. Use with photon energies up to 5 keV is foreseen limited only with concerns about radiation damage. Several options for fabricating a thin entrance window to achieve high quantum efficiency for soft X-rays are being worked on.

Complementary-metal-oxide-semiconductor (CMOS) image sensors are very popular for visible-light cameras. They have been pursued within high-energy physics and more recently for soft X-rays.[2] They may be able to provide similar performance as CCDs at very competitive cost. As for CCDs their upper photon energy is determined by the effective sensitive thickness while the entrance window defines the quantum efficiency at low photon energy.

Both technologies (CCD and CMOS) are capable of providing the small pixels (ca. 5 μm) required for cameras coupled with grating or crystal-based spectrometers and offer the most viable solution for high-resolution spectroscopy. For chemistry requiring resolution on the order of 1 eV direct measurements using superconducting Transition-Edge-Sensors (TES), with improved channel counts and counting rates, are possible.[3]

Hybrid pixel array detectors have revolutionized photon science detectors and been very successful at X-ray facilities all around the world. New cameras are being developed to match the beam characteristics of the various FELs under construction.[4-7] At SLAC, the ePix series of detectors have been designed and built for LCLS.[8] The ePix100 hybrid pixel detector features small 50 μm pixels with low noise capability (<100e) and is targeted towards XPCS experiments and as a detector in wavelength dispersive spectrometer setups. The ePix10k hybrid pixel detector features 100 μm pixels with auto gain ranging (two gains) and a large signal range of up to 10^4 8keV photons. This makes the detector a perfect choice for X-ray diffraction experiments. Both variants target the tender (2-5 keV) and hard X-ray (5-12 keV) regime at LCLS. Other variants are also being considered. Although the current generation of cameras can be read out at 120 Hz, frame rates between 2 and 10 kHz are expected for the next generation. An advantage of this technology is the possibility to implement "smart" cameras, which allow triggered event selection together with in-pixel storage. Therefore, the very high pulse repetition rate of LCLS II may be accommodated without the need to read and store every single frame. Further, a region of interest mode of operation will allow for a smaller area of the camera to be read out at higher speed.

At the highest photon energies to be delivered by LCLS II, silicon becomes partially transparent reducing the quantum efficiency and increasing the vulnerability of downstream electronics to radiation damage. Within the sensor-circuit-chip hybrid paradigm this can be addressed by replacing the silicon sensor with one composed of a material with a higher photon cross section. Sensors based on GaAs, Germanium, as well as thick silicon, are being explored. Alternatively, a phosphor screen coupled via an optical fiber array to an optical CMOS imager operating at 120 Hz would provide a solution, which could be modular for ease of construction, repair, and operational flexibility.

References

1. D. Doering, Y. D. Chuang, N. Andresen, K. Chow, D. Contarato, C. Cummings, et al., "Development of a compact fast CCD camera and resonant soft x-ray scattering endstation for time-resolved pump-probe experiments," Rev Sci Instrum **82** (2011).
2. C. B. Wunderer, A. Marras, M. Bayer, L. Glaser, P. Gottlicher, S. Lange, et al., "The PERCIVAL soft X-ray imager," J Instrum **9** (2014).
3. K. D. Irwin, and G. C. Hilton, "Transition-edge sensors," Top Appl Phys **99**, 63 (2005).
4. B. Henrich, J. Becker, R. Dinapoli, P. Goettlicher, H. Graafsma, H. Hirsemann, et al., "The adaptive gain integrating pixel detector AGIPD a detector for the European XFEL," Nuclear Instruments and Methods in Physics Research Section A: Accelerators, Spectrometers, Detectors and Associated Equipment **633, Supplement 1**, S11 (2011).
5. M. Porro, L. Andricek, L. Bombelli, G. De Vita, C. Fiorini, P. Fischer, et al., "Expected performance of the DEPFET sensor with signal compression: A large format X-ray imager with mega-frame readout capability for the European XFEL," Nuclear Instruments and Methods in Physics Research Section A: Accelerators, Spectrometers, Detectors and Associated Equipment **624**, 509 (2010).
6. A. Koch, M. Hart, T. Nicholls, C. Angelsen, J. Coughlan, M. French, et al., "Performance of an LPD prototype detector at MHz frame rates under Synchrotron and FEL radiation," J Instrum **8** (2013).
7. A. Mozzanica, A. Bergamaschi, S. Cartier, R. Dinapoli, D. Greiffenberg, I. Johnson, et al., "Prototype characterization of the JUNGFRAU pixel detector for SwissFEL," J Instrum **9** (2014).
8. G. Blaj, and e. al., J Synchrotron Radiat **22**, xx (2015).

4.4 Diagnostics

The X-ray FEL pulses produced from SASE or self-seeded operation exhibit intrinsic pulse-by-pulse fluctuations in pulse energy[1], spectral content, temporal profile, transverse profile, coherence, and degree of polarization. Additional jitter and drift originating from the electron bunch itself such as the arrival time and average photon energy also exist. Diagnostic systems that characterize each and every pulse or an ensemble of pulses provide the enhanced and sometimes necessary sensitivity required by many of the scientific opportunities at LCLS-II. With the greatly improved stability of the LCLS-II SC linac, many experiments may be feasible in an accumulating detection mode where all experimental parameters are stable to within the required precision during the detection accumulation time. In this case the diagnostics can measure an average or ensemble of pulses. However, when experimental parameters change between pulses and over time, averaging is no longer the efficient path to sufficient sensitivity and pulse-by-pulse diagnostics will be required.

Diagnostics devices for machine tuning can often be destructive to the beam whereas diagnostics for experimental operation must (nearly) transparently characterize the FEL pulses. Here we describe in a prioritized order how each fluctuating parameter can be characterized sufficiently to enable the scientific opportunities described in Chapter 3. These devices will be developed or refined/enhanced if existing on LCLS to handle the LCLS-II transformative capabilities in terms of better performance such as coverage of a wider photon energy range, high repetition rate operation using faster readout electronics, and most importantly mitigation of potential performance degradations associated with the non-negligible thermal load on beam intercepting components.

Pulse Energy

Nearly every FEL experiment relies on knowing the number of photons in each pulse (pulse energy) incident on the sample. Moreover, filtering of other fluctuations (e.g. spectral content) often results in additional fluctuations in the pulse energy. Consequently a high dynamic range, high sensitivity pulse energy diagnostic is a priority. For hard X-rays, the LCLS single-shot transmissive energy monitor based on measuring the near-UV fluorescence of N_2 gas[1] will be upgraded for high repetition rate operation with faster readout electronics, and for higher photon energies above 10 keV the Compton scatterings from thin solid targets [2] can be used. For the high repetition rate soft X-ray FEL beam, the ion and/or electron yield from a dilute noble gas[3] will be employed for the higher quantum efficiency and thus lower operating pressure which is critical to minimizing thermal effects by the high beam power, and is single-shot capable.

Photon Energy and Spectral Content

Measurements of the absolute photon energy and spectral distribution are vital to advanced spectroscopic methods, especially without the use of a monochromator, or in a two-color experiment. With hard X-rays a bent Si thin crystal single-shot spectrometer [4] has been successfully employed on LCLS operating at 120 Hz for photon energies above 5 keV. The same technique using a thin and more transmissive diamond crystal will function below 5 keV. For higher repetition rate operation cooling of the diamond crystal is required as well as a high frame-rate imaging detector for the spectrograph. For soft X-rays the kinetic energy of the primary photoelectrons from a dilute noble gas (e.g. He or Ne) system can be

[1] In the self-seeded operation using the current LCLS schemes, the FEL bandwidth is much reduced, but the intensity fluctuation increases compared to that of SASE operation because of the jitter in the strength of the seed which itself depends on the SASE process before the seeding chicane.

measured and used to infer the absolute photon energy to within 100 meV [5] and when fully optimized this method will provide a viable transmissive and shot-to-shot spectral diagnostic. Furthermore, if external seeding schemes are used, SASE-induced spectral jitter will abate. Coupled with the improved electron beam energy stability of the LCLS-II SC linac, a multi-shot average will likely to be sufficient for a variety of experiments.

Arrival Time and Temporal Profile

X-ray pulse arrival time jitter measurements are critical to all time-resolved experiments. Various single-shot optical-X-ray cross-correlation techniques have been successfully developed at LCLS for measuring the relative timing between a laser pump and the X-ray FEL, and a temporal resolution approaching the X-ray pulse duration has been achieved.[6] These timing tools should continue to serve well for LCLS-II if they can be upgraded to operate at higher repetition rate by mitigating potential thermal effects in the solid target. Relative timing between X-ray pulses remains a challenge due to the diminishingly small cross-section of non-linear interactions at X-ray wavelengths; typical schemes used in the visible regime are no longer feasible. However the advanced technology of the superconducting RF linac will improve electron bunch stability entering the undulators. This will significantly reduce some of the electron beam-related fluctuations in the FEL pulses, especially the arrival time, thus possibly alleviating single-shot timing requirements in certain cases.

There has been no direct X-ray FEL temporal profile measurement of sufficient resolution to date. However, a single-shot electron streaking technique has been successfully demonstrated on LCLS by spatially mapping out the energy loss of the spent beam imprinted by the lasing process for both soft and hard X-rays with resolution approaching a few fs [7]. For LCLS-II, this technique will be employed for the Cu linac at 120 Hz and the SC linac but operating at lower repetition rate. High repetition rate operation will require significant upgrades currently not planned.

In the long term, to fully help realize the scientific potential of the LCLS-II X-ray FEL, especially in the area of multidimensional X-ray spectroscopy, enhanced capabilities in spatial, temporal, and spectral diagnostics need development to completely characterize the phase space of the FEL radiation. In particular, the frequency, duration, delay, relative intensity ratio, carrier and envelope phases of the wave packets of the multi-color and/or multi-bunch are important parameters for measuring attosecond time scales characteristic of electronic motion and quantum coherences in atoms and molecules.

Transverse profile and Beam position

The transverse profile of the FEL beam not only serves the most basic needs of any user for alignment, but also provides important information of the lasing process, which could be used for machine tuning. For the former, capturing/displaying a time averaged beam image will suffice, whereas single-shot capability is required for diagnosing the FEL performance. For LCLS single-shot beam profile measurement based on X-ray scintillation and optical imaging (albeit destructive) is capable of revealing imperfections of any upstream X-ray optics such as mirrors and monochromators.[8] For LCLS-II high repetition rate operation, two important upgrades will be implemented for cooling the scintillator and sub-μs camera exposure control and readout for single-shot image capturing in burst mode.

The beam centroid position can be monitored non-destructively for hard X-rays on LCLS using quadrant detection form Compton scatterings [2], and for soft X-rays in a low-density noble gas using the photoelectrons and ions detected on split electrode [9]. Pointing jitter measurement can be accomplished by using multiple devices with sufficient separation along the beam. The high repetition rate operation of the LCLS-II will require upgrades in cooling the target for hard X-rays and using faster readout electronics for both techniques. However the improved electron beam stability of the LCLS-II SC linac will reduce

the both the shot-to-shot positional and pointing jitter and long time scale drift, relegating the single-shot requirement.

Wavefront and Transverse Coherence

The FEL wavefront and transverse coherence of an often focused beam at the sample exhibits fluctuations due to the partial coherence of a SASE beam as well as static and dynamic effects induced by X-ray optics. Developments in the area of wavefront and transverse coherence measurements on a single-shot basis will help achieve the best possible performances, e.g. sub-nm spatial resolution in single particle imaging experiments, or obtaining femtosecond time-scale dynamics of disordered systems at atomic length scales for X-ray correlation spectroscopy experiments by resolving minuscular speckle contrast. Wavefront measurements can be achieved with traditional Hartmann type sensors or by measuring the coherent scattering from well-characterized nanoparticles [10, 11], although both techniques are destructive, thus providing only the typical or "average" information on the beam wavefront. Soft and hard X-rays transverse coherence measurements based on Young double-slits [12] and the Hanbury Brown Twiss effect [13] have been demonstrated are either destructive or multi-pulse ensemble averages. Development of minimally invasive and single-shot capable wavefront and coherence measurements should continue and will reap scientific benefits as more and newer experimental opportunities provided the transformative LCLS-II FEL performances.

State and Degree of Polarization

The possibility of variable polarization FEL beam at LCLS-II with a DELTA undulator [14] will permit additional new studies of novel magnetic systems, especially in a time-resolved manner. Tuning and optimizing the DELTA-undulator performance and using the polarized FEL requires a diagnostic capable of measuring the state (linear, elliptical, or circular) and degree of polarization, ideally on a single-shot basis to properly take into account the jitters in the lasing process. For soft X-rays, an angle-resolved time of flight (TOF) electron spectrometer system mapping the anisotropic emission distribution from a dilute gas has been in development by a European XFEL team [15] and successfully tested at LCLS. The baseline design of this device is single-shot capable, but was intended to measure only the relative change in the degree of polarization assuming a predominant polarization state[2], and when complimented by scanning type of reflection-based polarimeter systems, it should provide the needed capability of polarization analysis of the LCLS-II with sufficiently high sensitivity.

These envisioned upgrades represent significant technical challenges in certain cases, but preliminary analyses indicate that there are clear paths forward to successful implementation. As the variety, complexity, and intricacy of the FEL-based experiments evolve X-ray diagnostics along with X-ray optics will grow in sophistication, to enable new experimental approaches for addressing the scientific opportunities at LCLS-II.

[2] In the case of a completely un-polarized beam, the emission distribution will be isotropic and identical to that of either left or right circularly polarized beam thus is not differentiated. An enhanced design seeks to analyze the spin of the photoelectron wavefunction, which depends on the chirality of the polarization.

References

1. S. P. Hau-Riege, R. M. Bionta, D. D. Ryutov, R. A. London, E. Ables, K. I. Kishiyama, et al., "Near-Ultraviolet Luminescence of N2 Irradiated by Short X-Ray Pulses," Physical Review Letters **105**, 043003 (2010).
2. Y. Feng, J. M. Feldkamp, D. M. Fritz, M. Cammarata, R. Aymeric, C. Caronna, et al., "A single-shot intensity-position monitor for hard x-ray FEL sources. ," in *Proc. SPIE 8140, X-Ray Lasers and Coherent X-Ray Sources: Development and Applications IX,* (2011), p. 81400Q
3. K. Tiedtke, J. Feldhaus, U. Hahn, U. Jastrow, T. Nunez, T. Tschentscher, et al., "Gas detectors for x-ray lasers," Journal of Applied Physics **103**, 094511 (2008).
4. D. Zhu, M. Cammarata, J. M. Feldkamp, D. M. Fritz, J. B. Hastings, S. Lee, et al., "A single-shot transmissive spectrometer for hard x-ray free electron lasers," Applied Physics Letters **101**, 034103 (2012).
5. C. Bostedt, "Unpublished," (2015).
6. N. Hartmann, W. Helml, A. Galler, M. R. Bionta, J. Grunert, S. L. Molodtsov, et al., "Sub-femtosecond precision measurement of relative X-ray arrival time for free-electron lasers," Nat Photonics **8**, 706 (2014).
7. C. Behrens, F. J. Decker, Y. Ding, V. A. Dolgashev, J. Frisch, Z. Huang, et al., "Few-femtosecond time-resolved measurements of X-ray free-electron lasers," Nat Commun **5**, 3762 (2014).
8. Y. Feng, "Unpublished," (2015).
9. K. Tiedtke, "Gas Based Detectors for FEL Photon Diagnostics," (2015), http://www.xfel.eu/sites/site_xfel-gmbh/content/e63594/e65073/e243602/e249682/08-KaiTiedtke_eng.pdf.
10. B. Floter, P. Juranic, S. Kapitzki, B. Keitel, K. Mann, E. Plonjes, et al., "EUV Hartmann sensor for wavefront measurements at the Free-electron LASer in Hamburg," New J. Phys. **12**, 13 (2010).
11. N. D. Loh, D. Starodub, L. Lomb, C. Y. Hampton, A. V. Martin, R. G. Sierra, et al., "Sensing the wavefront of x-ray free-electron lasers using aerosol spheres," Opt. Express **21**, 12385 (2013).
12. I. A. Vartanyants, A. Singer, A. P. Mancuso, O. M. Yefanov, A. Sakdinawat, Y. Liu, et al., "Coherence Properties of Individual Femtosecond Pulses of an X-Ray Free-Electron Laser," Physical Review Letters **107**, 5 (2011).
13. S. Song, D. L. Zhu, A. Singer, J. H. Wu, M. Sikorski, M. Chollet, et al., "Intensity Interferometry Measurements with Hard X-ray FEL Pulses at the Linac Coherent Light Source," X-Ray Free-Electron Lasers: Beam Diagnostics, Beamline Instrumentation, and Applications Ii **9210**, 10 (2014).
14. H.-D. Nuhn, "Unpublished," (2015).
15. M. Ilchen, "Unpublished," (2015).

5.0 Overview of LCLS-II

The LCLS-II is an X-ray Free-Electron Laser (FEL) designed to deliver photons between 200 eV and 5 keV at repetition rates as high as 1 MHz using a superconducting RF linac (SCRF) while still providing pulses at short wavelengths and high X-ray pulse energy over the photon range of 1 to 25 keV using the existing copper RF (CuRF) LCLS linac at 120 Hz.[1] To cover the full photon-energy range, the facility will include two variable-strength (gap-tunable) undulators, one dedicated to the production of soft X-rays (SXU) from 0.2 – 1.3 keV and one dedicated to production of Hard X-rays (HXU) from 1.0 – 25.0 keV. The facility will also introduce the possibility of generating near transform-limited pulses using self-seeding as well as photon beamline monochromators. The LCLS-II project scope is illustrated schematically in Figure 98.

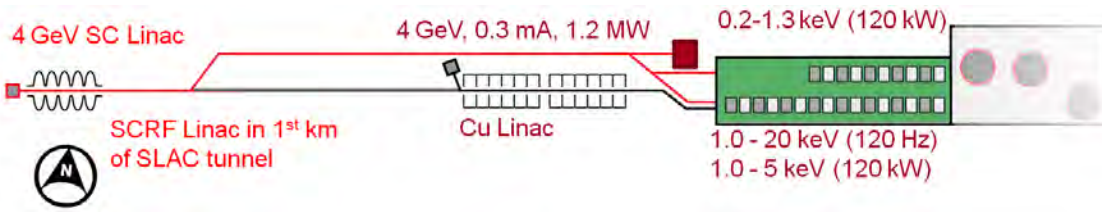

Figure 98: Schematic layout of the LCLS-II project scope

The facility is constructed to deliver either high-rate beam from the SCRF linac to both the SXU and HXU undulators, or to deliver the high-rate beam to the SXU undulator and deliver beam from the existing copper CuRF linac at 120 Hz to the HXU undulator. As illustrated in Figure 99, the SXU undulator is designed to lase in SASE mode over the photon energy range from 0.2 to 1.3 keV when supplied with beam from the SCRF linac. The HXU undulator is designed to lase in SASE mode over the photon energy range from 1.0 keV to 5.0 keV when supplied with beam from the SCRF linac, and over the energy range from 1.0 to 25.0 keV when supplied with beam from the existing CuRF linac. Both undulators will include the option for self-seeding, with SXU self-seeding over the photon energy range from 0.2 to 1.3 keV when fed by the SCRF linac and HXU self-seeding covering the photon energy range from 4.0 to 12.0 keV when supplied beam from the CuRF linac. The HXU self-seeding system is not designed to operate with high power beam from the SCRF linac but may be upgraded to do so.

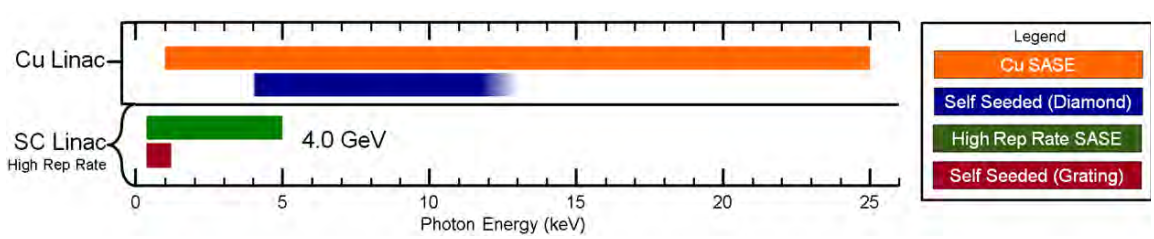

Figure 99: Photon energies from the SCRF and CuRF linacs for both SASE and self-seeded operation, assuming 4.0 GeV SCRF electrons and 3-to-15 GeV CuRF electron beams. Self-seeding for photon energies between 1.3 and 4 keV is possible with an upgrade.

5.1 Unique LCLS-II Capabilities

The LCLS-II will have the high peak brightness capability and flexibility of LCLS while also having the ability to provide MHz rate beams from a CW SCRF linac. As described, the operating regimes are:

1. Soft X-ray photons from SASE and self-seeding between 0.2 and 1.3 keV at MHz rates, with an average X-ray power as high as 200 Watts;

2. Hard X-ray photons from SASE between 1.0 and 5.0 keV at MHz rates with an average X-ray power as high as 200 Watts and with the possibility of a future upgrade to self-seeding operation at energies between 1 and 4 keV;

3. Hard X-ray photons with SASE between 1 and 25 keV and self-seeding between 4 keV and 13 keV at 120 Hz, with mJ-class pulses and performance comparable to or exceeding that of LCLS.

The SCRF linac will be intrinsically more stable than the LCLS linac and the energy stability of the electron beams is specified to be <0.01% rms which is >10x more stable than that from the CuRF linac. The timing stability in the initial implementation of LCLS-II is specified to be better than 20 fs rms and is expected to be roughly 10 fs rms. The transverse stability and pointing stability are specified to be better than 10% of the beam sizes. It is expected that the stability of the SCRF beams will be improved after the initial operation with the implementation of additional feedback systems that are possible due to the very high repetition rates of the linac.

The beams from the CuRF linac at 120 Hz will retain all of the flexible operating modes that are being developed at LCLS. These include pulse-length control, two-color pulses and two pulses with delay at the 100 fs scale. New techniques are being developed as well which may allow pulse-by-pulse pulse length control and limited shaping of the X-ray pulses. Many of these techniques will be implemented on the SCRF linac as well however these capabilities are beyond the baseline project and will take time after initial operation to develop the full capability.

5.2 Overview: Linacs, Undulators/FELs

The beam parameters from the SCRF linac, listed in Table 1, include performance specifications for the nominal bunch charge of 100 pC as well as the performance ranges and jitter limits. To optimize the FEL performance for a variety of experimental requirements, the LCLS-II is being designed to operate with a wide range of bunch charges ranging from 10 to 300 pC. The maximum repetition rate of the SCRF linac is 0.929 MHz.

Table 1. Electron beam operational parameters at SCRF linac end, including rms stability requirements.

Electron Beam Parameters	**symbol**	**nominal**	**range**	**units**
Final electron energy (operational)	E_f	4.0	2.0-4.14	GeV
Electron bunch charge (limited by beam power)	Q_b	0.10	0.01-0.3	nC
Max. bunch repetition rate in linac (CW)	f_b	0.62	0-0.93	MHz
Average electron current in linac	I_{av}	0.062	0.001-0.3	mA
Average electron beam power at linac end (limit)	P_{av}	0.25	0-1.2	MW
Norm. rms transverse slice emittance at undulator	$\gamma\varepsilon_{\perp\text{-}s}$	0.45	0.2-0.7	μm
Final peak current (at undulator)	I_{pk}	1000	500-1500	A
Estimated RMS Beam Stability Goals:				
Relative rms electron energy stability (at und.)	$(\Delta E/E_f)_{rms}$	< 0.01	-	%
Relative rms peak current stability (at und.)	$(\Delta I/I_{pk})_{rms}$	< 5	-	%
Bunch arrival time stability (rms, at und.)	$(\Delta t_b)_{rms}$	< 20	-	fs
Transverse centroid stability (rms, at und., 100 pC)	$\Delta x_{rms}/\sigma_x$	< 10	-	%

The SCRF linac is being designed to accelerate 300 μA up to >4GeV for 1.2 MW of beam power, which is sufficient to ultimately generate more than 100 Watts of X-rays to each of ten individual undulator beamlines. The initial LCLS-II configuration will be limited to a maximum power of 250 kW by the downstream beam dump capacity. The baseline SCRF linac only includes sufficient RF power to accelerate 100 μA up to 4 GeV.

The electron beam parameters of the existing CuRF linac, listed in Table 2, are based on those of the LCLS. The LCLS-II project requires no modifications to the existing LCLS injector, linac or bunch compressor systems. The beam transport in the Beam Switch Yard (BSY), downstream of the LCLS linac, will be modified as part of an Accelerator Improvement Project (AIP) to allow a connection to the transport line from the LCLS-II SCRF linac. A DC dipole will be used to direct the beam from either the SCRF or the CuRF linac into the transport line to the HXU undulator.

Table 2. Electron beam parameters from the CuRF linac in the LCLS-II; the beam from the CuRF linac will be very similar to that produced currently in the LCLS

Electron Beam Parameters	**symbol**	**nominal**	**range**	**units**
Final electron energy (operational)	E_f	13.6	2.5-15	GeV
Maximum upgrade energy (or reduced duty factor)	E_{max}	17	-	GeV
Electron bunch charge (limited by beam power)	Q_b	0.13	0.02 - 0.30	nC
Bunch repetition rate in linac (CW)	f_b	120	0 - 120	Hz
Normal rms transverse slice emittance (nom. charge)	$\gamma\varepsilon_{\perp\text{-}s}$	0.45	0.2 - 0.7	μm
Final peak current	I_{pk}	3000	500 - 4500	A

As noted, the SXU undulator can be fed from the SCRF linac, while the HXU undulator can be fed from either the SCRF or the CuRF linacs, although not from both simultaneously. The undulators will be installed in the existing LCLS Undulator Hall. A schematic of the undulator layout appears in Figure 100.

Both undulators are variable-gap hybrid permanent-magnet undulators. The HXU undulator has a period of 26 mm, close to that of the existing LCLS undulator, while the SXU undulator has a period of 39 mm. The maximum length of the existing LCLS Undulator Hall is roughly 150 meters. This will allow for the installation of up to 35 segments for the HXU, with each segment being 3.4 meters long followed by an interspace of 1.0 meters for a quadrupole, phase shifter, RF BPM, and *x* and *y* steering coils, To support self-seeding, two of these undulator slots will be reserved for self-seeding monochromators. The baseline will include 32 HXU segments plus two self-seeding slots, one of which contains the existing HXU self-seeding monochromator; the other is reserved for a future upgrade.

The SXU undulator can be shorter, and there will be 21 SXU undulator segments plus one empty slot for the self-seeding monochromator which will be based on the LCLS SXUSS monochromator but modified for higher average power with a resolving power of 10,000. Development of the SXUSS monochromator is ongoing. The last three SXU undulator slots are reserved for the future installation of polarization control undulators, and the space upstream of the SXU undulator may be used for future seeding installations or additional undulators for two-color X-ray generation or other upgrades.

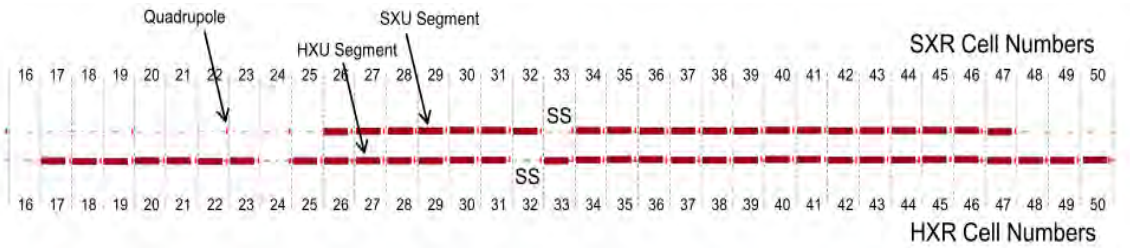

Figure 100: Schematic of the undulator layout. The total length represented in this figure is roughly 150 m, and the two undulators are separated horizontally by 2.5 m. The undulator layout includes space for the baseline self-seeding monochromators at slots 33 (SXU and 32 (HXU) as well as space a future monochromator upgrade in slot 24 (HXU), polarization control upgrade (slots 48-50 (SXU), future installation for undulators or beam manipulation in slots 16-25 (SXU).

At the nominal SCRF energy of 4.0 GeV, the HXU can cover the photon energy range of 1.5 to 5 keV in SASE mode. For the HXU to access lower photon energies, such as 1 keV, the linac energy would be decreased to 3.3 GeV. Over most of the photon energy range, the HXU undulator length is >20% longer than that required to saturate. However with 100 pC bunch charge, there is little margin at 5 keV, and the photon pulse energy is decreased to a few μJ. In this case, the 20% margin in undulator length can be gained by operating the SCRF linac at the maximum energy of roughly 4.2 GeV or operating at lower bunch charge and thereby lower beam emittance. With 20 pC per bunch, more than 20 μJ of X-rays per pulse are expected.

Figure 101 illustrates the estimated X-ray pulse energies for the SXU and HXU as a function of the photon energy when fed by the SCRF linac with 100 pC per bunch.

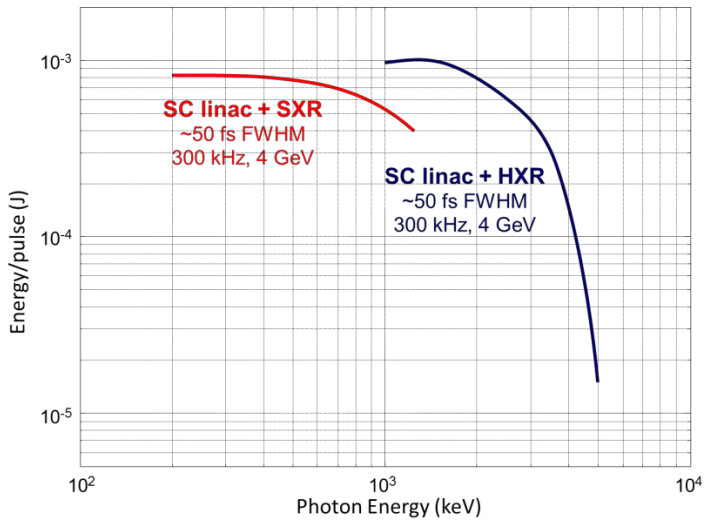

Figure 101: Calculated X-ray pulse energies versus photon energy for the SXU (red) and the HXU (blue) undulators for 100 pC per bunch.

Figure 102 illustrates the calculated X-ray pulse energy versus the photon energy for the HXU FEL when fed by the CuRF linac with 130 pC per bunch and compressed to 3 kA (similar to the LCLS operation). Because of the shorter undulator period, the X-ray pulse energy from the HXU FEL will be slightly lower than that of the LCLS at photon energies of a few keV. However, the LCLS-II HXU will be able to generate X-rays over a much wider range of wavelengths than the LCLS.

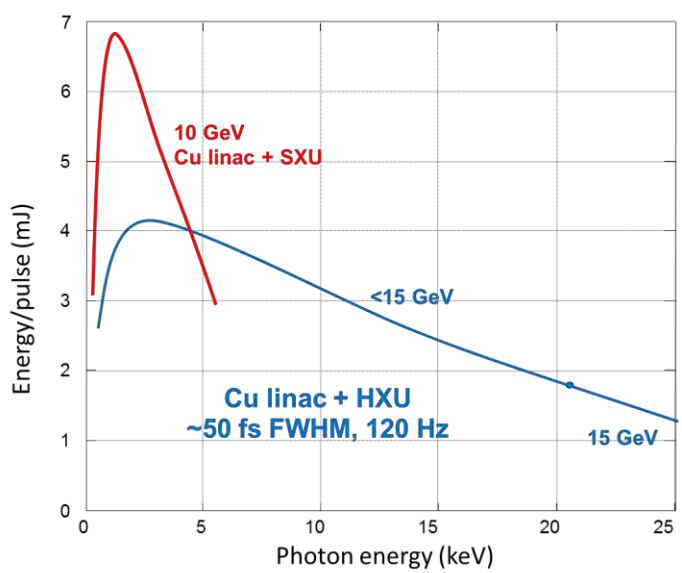

Figure 102: Calculated output per pulse from Hard X-ray Undulator when driven by the CuRF Linac.

5.3 Operating Modes

The LCLS-II will be flexible in its operating modes. As noted above, the HXU can be fed from either the SCRF linac or the CuRF linac, while the SXU can be fed only from the SCRF linac. The BSY Beam Spreader can direct the SCRF linac beam arbitrarily toward either undulator or to the BSY dump. The design does not presently include the capability of delivering different bunch charges or peak currents to the two undulators simultaneously, however that capability may be developed in the future. .

The very high average power of the accelerated CW SCRF electron beam makes it undesirable to terminate the beam anywhere other than in specially-designed beam dumps. Materials struck by the full-

power beam in a persistent manner for more than roughly 100 microseconds may be damaged, possibly leading to a breach of the vacuum chamber. For this reason, several accelerator operating modes are envisioned for initial low-power commissioning, recovery from RF trips, recovery from beam-loss trips, and startup from shut-down periods. These modes are configured to allow machine setup and diagnosis, but are defined at much lower average-power levels to protect the beamline components during these less controlled, more transient startup periods. Beams sent to different destinations may operate in different modes at the same time. For example, it should be possible to tune up low-power beams going to one undulator while simultaneously delivering full-power beams to the other. Examples of possible operating SASE modes are listed in Table 3 below.

Table 3. Examples of possible operating modes in the LCLS-II.

Configuration	**Linac Parameters**	**SXU**	**HXU**
High rate to SXU and HXU	*SCRF: 4 GeV, 0.929 MHz; 60 pC* *CuRF: off*	50-200 W at 1 keV (120-450 uJ at 460 kHz)	20 W at 3 keV (43 uJ at 460 kHz)
High rate to SXU and medium pulse energy at HXU	*SCRF: 4 GeV, 0.240 MHz; 100 pC* *CuRF: off*	80-200 W at 250 eV (350-900 uJ at 210 kHz)	20 W at 1.5 keV (1 mJ at 20 kHz)
Medium rate and pulse energy at SXU and HXU	*SCRF: 4 GeV, 0.490 MHz; 100 pC* *CuRF: off*	20 W at 500 eV (1 mJ at 20 kHz)	125 W at 4 keV (0.4 mJ at 310 kHz)
High rate to SXU and high pulse energy at HXU	*SCRF: 4 GeV, 0.410 MHz; 100 pC* *CuRF: 15 GeV, 120 Hz, 130 pC*	200 W at 250 eV (500 μJ at 400 kHz)	0.5 W at 3 keV (4 mJ at 120 Hz)
High rate to SXU and short wavelength at HXU	*SCRF: 4 GeV, 0.929 MHz; 30 pC* *CuRF: 15 GeV, 120 Hz, 130 pC*	50 - 200 W at 1.2 keV (50-200 uJ at 920 kHz)	0.1 W at 25 keV (500 uJ at 120 Hz)

All of the flexibility, including X-ray pulse length and two-color techniques that are being developed at LCLS, will continue to exist. The SCRF linac is designed to operate over a range of bunch charges and peak currents. The charge and repetition rate are limited by the maximum electron beam power delivered to an undulator of 120 kW. The nominal parameters are 100 pC per bunch at up to 300 kHz with a 60 fs FWHM pulse length. The pulse length decreases to 20 fs FWHM with a 20 pC bunch (and the repetition rate can be increased to roughly 900 kHz) and increases to 150 fs FWHM with a 300 pC bunch (but the maximum repetition rate is decreased to 100 kHz). Techniques that are being developed at LCLS will be used to control the pulse length in LCLS-II, reducing it from the nominal values listed above. It is expected that these techniques will be able to provide few fs FWHM pulses. In this case, the energy per pulse will decrease in proportion to the pulse length. The generation of shorter pulses is an ongoing topic of R&D.

5.4 Future Options/Capabilities

Although not explicitly part of the baseline capability, the FEL facility as constructed will likely be able to support many enhanced modes of operation.

Self-Seeding

The current LCLS soft X-ray self-seeding scheme[2] is, in practice, a monochromator and electron chicane, inserted into the section 9 of the undulator. It collects the SASE radiation produced by the first 8 undulator sections, selects a narrower bandwidth and uses the resulting monochromatic beam to seed the electron beam in the following undulator section. The self-seeding monochromator is composed by a

toroidal grating dispersing the light horizontally, and some mirrors to refocus and super-impose the X-ray and electron beams in the following undulator section. The current monochromator has a resolution around 5,000 and is mainly limited by the number of illuminated grooves of the grating, i.e. by the diffraction limit.

After the experience of the soft X-ray self-seeding commissioning, it is clear that the power generated by the first 8 undulator sections is more than sufficient to provide enough photons for seeding the electron beam in the downstream undulator sections. Therefore, the resolving power can be increased by lengthening the distance from the SASE source to the grating, as shown in Figure 103, and by using a larger groove density grating, 1800 l/mm in this case. In practice, one can open the gaps of the undulators upstream of the self-seeding monochromator, which illuminates more grooves and increases the resolving power. Considering the needed seeding power, one can expect a resolving power between 20,000 and 40,000.

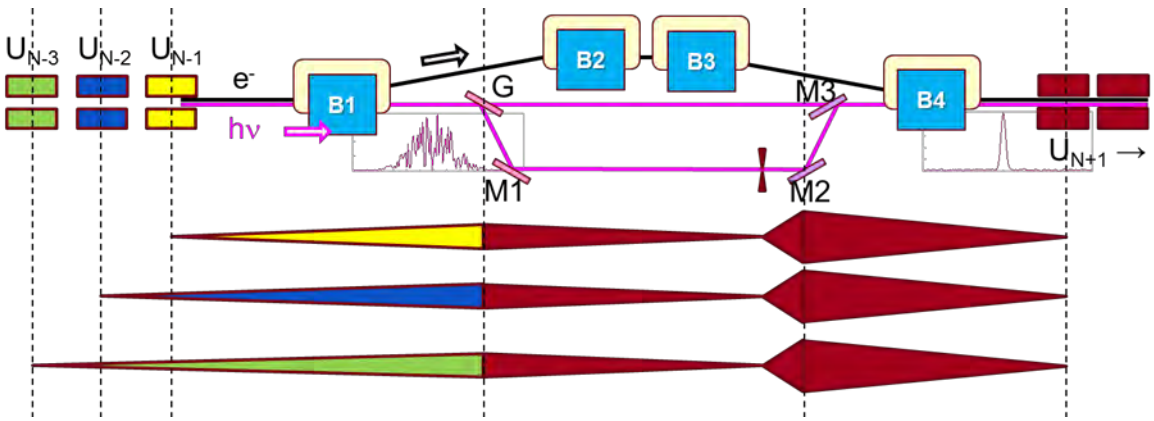

Figure 103: Schematic view of the soft X-ray self-seeding. The grating is designed to accommodate variable source distances. The small defocusing resulting from the variation of the source distance is negligible because of the length of the photon-electron interaction region.

Additional Operating Modes and Options

There are a number of enhanced operating modes which may provide access to additional capabilities. It is possible that some of these might be implemented as part of the baseline project or added shortly after construction. Two-color operation may be accomplished with different schemes tailored to the experimental requirement. Photon energies differing by up to 1-2% are currently generated by operating the FEL in a double bunch scheme.[3] Double bunch operation is ideal for two color experiments requiring only a few eV difference in photon energies and delays between 0-100 fs. Two color pulses that could differ by the entire spectral range of the undulator (0.2-1.3 keV for the SXU) are possible with the split undulator scheme.[4] Here the first and second halves of the undulator are tuned to the desired respective X-ray energies, and a chicane in the middle of the undulator is used to generate a time delay.

A unique capability afforded by the co-location of undulators at LCLS is the potential to combine hard and soft X-ray pulses, originating from respective undulators, on a sample within an endstation. This form of hard X-ray, soft X-ray two color experiment could be accomplished with two pulses originating from the SC linac or one from each of the respective linacs. This would enable one to simultaneously probe the dynamics of electronic and nuclear structure.

External laser seeding (and more general laser manipulation of the e-beam) on the soft X-ray undulator would provide control over the bandwidth and pulse duration (at close to the Fourier transform limit) at sub-keV photon energies. This will be particularly powerful for spectroscopic methods such as time-resolved RIXS. The potential for creating large coherent spectral bandwidth, and pulse durations ~1 fs or

less will enable non-linear X-ray spectroscopies in a similar manner to what has been achieved for optical non-linear spectroscopy. Accelerator methods to provide multiple X-ray pulses for four-wave mixing experiments have also been proposed.[5]

Driving the soft X-ray undulator with the high-energy electron beam from the warm copper SLAC linac will generate pulses with very high energy (>5 mJ) in the tender (2-5 keV) X-ray regime at 120 Hz. The peak power levels from this source could reach the TW level opening up new capabilities for single particle imaging.

Extending high repetition rate operation to photon energies of 6-9 keV via electron energies of 4.5-6 GeV could be enabled by increasing cryoplant capacity (to support higher accelerating gradients), by increasing the number of cryomodules, or by a reduced duty cycle operating mode. High repetition hard X-rays from the undulator fundamental would transform hard X-ray scattering and spectroscopy.

References

1. T. Raubenheimer, "LINAC Coherent Light Source II (LCLS-II) Project " (SLAC, 2015).
2. D. Cocco, R. Abela, J. W. Amann, K. Chow, P. J. Emma, Y. Feng, et al., "The optical design of the soft x-ray self seeding at LCLS," (2013), pp. 88490A.
3. A. Marinelli, D. Ratner, A. A. Lutman, J. Turner, J. Welch, F. J. Decker, et al., "High-intensity double-pulse X-ray free-electron laser," Nat Commun **6** (2015).
4. A. A. Lutman, R. Coffee, Y. Ding, Z. Huang, J. Krzywinski, T. Maxwell, et al., "Experimental Demonstration of Femtosecond Two-Color X-Ray Free-Electron Lasers," Physical Review Letters **110**, 134801 (2013).
5. G. Marcus, G. Penn, and A. A. Zholents, "Free-Electron Laser Design for Four-Wave Mixing Experiments with Soft-X-Ray Pulses," Phys Rev Lett **113** (2014).

Appendix 1: X-ray Interactions and Non-Disruptive Probing

Soft X-rays are an incisive probe of electronic structure. However, an important requirement is that the probe pulse not disrupt the system that we seek to understand. This is equally true for systems in a correlated ground state, and for systems prepared in a perturbative near-equilibrium excited state by a tailored excitation pulse. The X-ray *probe* interaction with the material under study must remain in the *linear* regime, and this places restrictions on the tolerable pulse fluence for ultrafast probes.

Nonlinear X-ray probe interaction may be manifest in several forms depending on the experimental technique, and on the material properties under investigation. For example, photoelectron spectroscopy is one of the most informative probes of electronic structure - reporting on both the energy and momentum of the electronic states of an ordered solid. However, at fluences above ~5×10^6 ph/pulse (50 μm spot) space-charge effects distort the photoelectron spectrum and degrade the energy resolution. Thus high repetition rate at moderate flux per pulse is essential to achieve the required count rates for photoemission spectroscopy.

Photon-in photon out techniques can tolerate somewhat higher pulse fluence and still remain in the *linear* interaction regime. For example, XES measurements on Si samples at FLASH indicate an acceptable upper pulse fluence limit on the order of 10 mJ/cm^2. Recent resonant diffraction studies of charge-ordering in nickelate samples at LCLS indicate a safe upper bound of ~1 mJ/cm^2. These fluence levels are consistent with ultrafast visible spectroscopy research over the past several decades, where the importance of maintaining a linear probe interaction is well established. For 1 keV photons and characteristic spot sizes of 50 μm (e.g. for probing heterogeneous materials even smaller focal spots may be required), this corresponds to an upper limit on the usable fluence of ~10^8 photons per pulse.

However, photon-in photon-out spectroscopy techniques are photon hungry, owing to the small inelastic cross-sections. The most demanding experiments at 3rd generation soft X-ray synchrotron sources require an average flux in excess of ~10^{12} ph/s/(10 meV bandwidth). In order to achieve these average flux levels with soft X-ray lasers (while restricted to less than 10^8 ph/pulse as described above), they must operate in the 10-100 kHz regime. The most demanding and most informative experiments of the future, experiments that are presently well beyond our reach, will push this requirement into the MHz regime, and will require even better energy resolution.

Similar estimates on the appropriate fluence limit can be derived based on simple considerations of the X-ray absorption cross-section, and the deposited energy per atom. In the soft X-ray range (0.1-1 keV), typical atomic absorption cross-sections are on the order of 10^{-18} cm^2. If one considers 10^9 photons/pulse at 1 keV, in a 30 μm focal spot (10^{-5} cm^2 area), this corresponds to 10^{17} eV/cm^2 (16 mJ/cm^2), or 0.1 eV per atom. The typical energy of a covalent bond is ~1 eV per atom, so this fluence level is sufficient to break ~10% of the covalent bonds in a molecule or solid. This interaction level is far from linear or non-disruptive.

From another perspective, this fluence level corresponds to ~10% valence to conduction band excitation in a 1 eV gap semiconductor. This is the nominal threshold at which "non-thermal" melting is known to occur in semiconductors. These electronic excitation levels are sufficiently high to directly destabilize the lattice. Based on these considerations, the incident fluence per pulse should be ~1 mJ/cm^2 or less in order to be safely in a linear interaction regime. High repetition rate will be essential to provide the high average X-ray flux required by the experiments, while keeping the flux per pulse safely in the *linear* interaction regime.

SLAC National Accelerator Laboratory, 2575 Sand Hill Road, Menlo Park, California 94025-7015